



UNIVERSIDADE ESTADUAL DE CAMPINAS
Instituto de Física Gleb Wataghin (IFGW)

Fernando Henrique de Sá

Estudo de Impedâncias e Instabilidades Coletivas aplicado ao Sirius.

**Study of Impedances and Collective Instabilities
applied to Sirius.**

Campinas

2018

Fernando Henrique de Sá

**Estudo de Impedâncias e Instabilidades Coletivas
aplicado ao Sirius.**

Tese apresentada ao Instituto de Física Gleb Wataghin (IFGW) da Universidade Estadual de Campinas (UNICAMP) como parte dos requisitos exigidos para a obtenção do título de Doutor em Física, com ênfase em Física de Aceleradores.

Orientador: Prof. Dr. Antônio Rubens Britto de Castro

Co-orientador: Prof. Dr. Silvio Antonio Sachetto Vitiello

Este exemplar corresponde à versão final da tese defendida pelo aluno Fernando Henrique de Sá, e orientada pelo Prof. Dr. Antônio Rubens Britto de Castro

Campinas

2018

MEMBROS DA COMISSÃO JULGADORA DA TESE DE DOUTORADO DE
FERNANDO HENRIQUE DE SÁ RA: **133940** APRESENTADA E APROVADA AO
INSTITUTO DE FÍSICA “GLEB WATAGHIN”, DA UNIVERSIDADE ESTADUAL DE
CAMPINAS, EM 27/02/2018.

COMISSÃO JULGADORA:

- Prof. Dr. Antônio Rubens Britto de Castro - (Presidente) - IFGW/UNICAMP
- Prof. Dr. José Antônio Brum - IFGW/UNICAMP
- Prof. Dr. Varlei Rodrigues - IFGW/UNICAMP
- Prof. Dr. Peter Kuske - HELMHOLTZ-ZENTRUM BERLIN
- Prof. Dr. Ricardo Magnus Osório Galvão – UNIVERSIDADE DE SÃO PAULO - USP

A Ata de Defesa, assinada pelos membros da Comissão Examinadora, consta no processo de vida acadêmica do aluno.

CAMPINAS
2018

ABSTRACT

Sirius is the new fourth generation light source that is being built in Campinas, Brazil, by the Brazilian Synchrotron Light Laboratory (LNLS). With a natural emittance of 250 pm rad, extremely high-brightness synchrotron light will be generated by, at most, 18 insertion devices (IDs) installed in the straight sections of the storage ring and by 20 superbends (3.2 T) present in the center of each achromat of the magnetic lattice. The standard vacuum chamber will be round, made of copper, with a radius of 12 mm, which is small compared to third generation light sources chambers, and the first IDs planned will be out of vacuum and will have a very reduced gap, with chambers as small as 2.4 and 3.0 mm, in most cases. Additionally, vacuum pumping will be distributed, through the use of NEG coating at the inner surface of the chambers in the whole ring. All these factors intensify the impedance related effects of the machine, which can generate coherent oscillations, compromising the quality of the light, cause total or partial beam loss and influence the equilibrium dynamics of the electrons. In this work some of the main components of the vacuum chamber were modelled and their wake fields were calculated with semi-analytical and numerical methods and added to the total impedance budget of the machine. With the application of this model to the first phase of operation, it was found that the beam will suffer from transverse coupled bunch resistive wall instability, making it necessary the installation of transverse bunch-by-bunch feedback systems in both planes. It was also predicted stability without feedback action provided that the ring operates with chromaticity larger than 2.2 in both planes. The thresholds for intra-bunch instabilities are much above the nominal operation current and will not be a problem in any of the three planes and there will be no longitudinal coupled-bunch motion as long as the ring operates with superconducting RF cavities. The installation of a Landau cavity is planned for the phase two of operation, which will allow higher total current in the machine and even high single-bunch current in the middle of the train. Even though it was not done any calculations for these future operation conditions, the methods and codes developed in this work can be directly applied for those cases.

Keywords: Sirius; impedances; beam instabilities; beam dynamics.

Resumo

Sirius é a nova fonte de luz síncrotron de quarta geração que está sendo construída em Campinas, Brasil, pelo Laboratório Nacional de Luz Síncrotron (LNLS). Com uma emissânci natural de 250 pm rad, radiação síncrotron de altíssimo brilho poderá ser gerada por até 18 dispositivos de inserção (DI) instalados nos trechos retos do anel de armazenamento e por 20 dipolos de alto campo (3.2 T) presentes no centro de cada arco cromático da rede magnética. A câmara de vácuo padrão do anel será cilíndrica, feita de cobre e terá 12 mm de raio, que é um valor pequeno comparado às câmaras de fontes de luz síncrotron de terceira geração, e os primeiros DIs previstos serão fora do vácuo e terão uma abertura bastante reduzida, com câmaras de apenas 2.4 e 3.0 mm de raio, na maioria dos casos. Adicionalmente, o sistema de vácuo do anel será distribuído, através da deposição de NEG na superfície interna das câmaras ao longo de todo o anel. Todos esses fatores intensificam os campos de arraste, ou impedâncias, da máquina, que podem gerar oscilações coerentes, deteriorando a qualidade da luz gerada, e causar perda total ou parcial do feixe, além de influenciar na dinâmica de equilíbrio dos elétrons. Neste trabalho alguns dos principais componentes da câmara de vácuo foram modelados e seus campos de arraste calculados por meios semi-analíticos e numéricos e adicionados ao modelo total de impedância do anel. Com a aplicação de tal modelo para a primeira fase de operação, constatou-se que o feixe será instável nos planos transversais devido a oscilações causadas por acoplamento entre pacotes gerados pela impedância de parede resistiva, tornando necessária a instalação de sistemas de retroalimentação pacote por pacote para manter a estabilidade. Também foi previsto que o feixe ficará estável se o anel for operado com uma cromaticidade nominal de 2.2 em ambos os planos transversais. Os limiares das instabilidades relacionadas a oscilações intra-pacote estão muito acima da corrente nominal de operação e não serão um problema. Não há previsão de instabilidades longitudinais de acoplamento entre pacotes, haja vista que a máquina operará com cavidades de RF supercondutoras. Na segunda fase de operação está prevista a instalação de uma cavidade Landau, que permitirá operação com corrente total mais alta, inclusive com pacotes bastante intensos no meio do trem. Apesar de não terem sido feitos cálculos para esse tipo de operação, os principais métodos e códigos desenvolvidos nesse trabalho podem ser diretamente usados para tal fim.

Palavras-chaves: Sirius; impedâncias; instabilidades de feixe; dinâmica de feixe.

LIST OF FIGURES

Figure 1 – Schematic of a storage–ring–based light source.	24
Figure 2 – Illustrations of a dipole magnet.	26
Figure 3 – Illustrations of a quadrupole magnet.	27
Figure 4 – Illustrations of a sextupole magnet.	28
Figure 5 – Comparison of machines emittances.	33
Figure 6 – One fourth of the unit cell of the Sirius storage ring.	38
Figure 7 – Twiss functions of the Sirius storage ring.	38
Figure 8 – Sirius building layout.	39
Figure 9 – Frenet-Serret reference frame of a storage ring	42
Figure 10 – Scheme of a tapered transition.	75
Figure 11 – Neg effect on impedance.	101
Figure 12 – Effect of NEG on TMCI	102
Figure 13 – Effect of NEG on loss factor and effective longitudinal impedance . . .	103
Figure 14 – Low frequency impedance for different values of distance of the mag- netic poles of dipoles to the exterior part of the vacuum chamber. . . .	104
Figure 15 – Cross section of the kicker window–frame magnet that will be used in Sirius storage ring.	106
Figure 16 – Coupled flux impedance of the dipole kicker magnet as a function of the frequency for several values of capacitance (left) and resistance (right). .	108
Figure 17 – Tsutsui model for the window–frame kicker magnet.	108
Figure 18 – Transverse impedances of the four models of kicker analysed.	109
Figure 19 – Titanium coating thickness effect on impedance.	110
Figure 20 – Geometric impedance from the tapered transitions of the undulators. Solid lines represent numerical calculations performed with ECHOz1 and ECHOz2 for the Delta undulator and with ECHOzR for the Ad- justable Phase Undulator (APU). Dashed lines are the prediction by the analytic formulas studied in subsection 3.9.1.	113
Figure 21 – Wall impedance of the four types of undulators planned for Sirius. . . .	115
Figure 22 – Scheme of the keyhole–shaped chamber for the BC magnet.	116
Figure 23 – Comparison of the vertical dipolar impedance among different models of BC chamber.	116
Figure 24 – Comparison of impedances of different models of BC chamber.	118

Figure 25 – (a) behavior of $Y_k(x)$ as a function of $3x/k^{3/2}$ showing its smooth dependency. (b) Sum of the two terms of the coherent synchrotron radiation (CSR) impedance: the free-space contribution, W'_0 and the shielding term, W'_1 , where it becomes clear the cancellation of the long tail at positions ahead of the source particle (z negative)	119
Figure 26 – CSR driven longitudinal instability (adapted from Bane <i>et al.</i> (2010))	121
Figure 27 – CSR effective wake functions and impedances calculated using the parameters of the Sirius low-field dipoles. Solid lines represent the real part of the impedance and dashed lines, the imaginary part. In both plots the blue line coincides with the red one and, therefore, it is not visible.	123
Figure 28 – Total CSR impedance (left) and wake (right) models for Sirius, considering the two types of dipoles. Solid lines represent the real part of the impedance and dashed lines represent the imaginary part.	123
Figure 29 – Longitudinal impedance budget for Sirius.	128
Figure 30 – Single-bunch loss factor (left, blue) and effective impedance (right, orange) calculated for the nominal operation mode of phase1 for Sirius.	128
Figure 31 – Horizontal dipolar impedance budget for Sirius.	130
Figure 32 – Vertical dipolar impedance budget for Sirius.	131
Figure 33 – Horizontal kick factors for single-bunch operation mode.	131
Figure 34 – Vertical kick factors for single-bunch operation mode.	131
Figure 35 – Tune shift normalized by the bunch current as a function of the number of bunches in uniform filling.	132
Figure 36 – Longitudinal PETRA 7-Cell cavity impedance compared with the minimum shunt impedance needed to drive coupled-bunch instabilities for several values of total beam current.	134
Figure 37 – The horizontal axis indicates the mapping of the RF cavity longitudinal impedance peak frequencies in the coupled-bunch modes. Vertical axis indicates the fractional part of one revolution frequency in the ring. Black horizontal lines are $\pm\nu_z$ and the interval defined by the dots is the interval in which sampling by the synchrotron tune corresponds to instability at the indicated current.	135
Figure 38 – Transverse PETRA 7-Cell cavity impedance compared with the minimum shunt impedance needed to drive coupled-bunch instabilities for several values of total beam current.	137

Figure 39 – The horizontal axis indicates the mapping of the RF cavity transverse impedance peak frequencies in the coupled–bunch modes. Vertical axis indicates the fractional part of one revolution frequency in the ring. Black solid horizontal line is the fractional part of ν_x and black dashed line is the fractional part of ν_y . The interval defined by the dots is the range in which sampling by the betatron tune corresponds to instability at the indicated current.	138
Figure 40 – Stationary parameters of the longitudinal plane, calculated from the solution of the Haissinski equation.	139
Figure 41 – Fitting of the impedance budget of the storage ring.	140
Figure 42 – Mode–coupling instability for two different bunch lengths for phase one of operation. The black lines indicate where different azimuthal modes couple.	141
Figure 43 – Longitudinal beam parameters obtained from tracking.	143
Figure 44 – Time evolution of the energy spread for different bunch currents close to the threshold of the sawtooth–like instability.	143
Figure 45 – Discrete Fourier transform of the time–dependent bunch centroid, as a function of frequency in units of the zero–current synchrotron frequency.	144
Figure 46 – Tracking results, showing the effect of noise as a function of current for different numbers of macroparticles in the simulation.	145
Figure 47 – Normalized energy spread increase in Simulations induced by noise. . .	148
Figure 48 – Application of equation (7.16) to account for energy spread increase. .	149
Figure 49 – Longitudinal beam distribution and its discrete Fourier transform for a CSR simulation with beam current of 1.2 mA.	150
Figure 50 – Time evolution of the bunch size for a beam current of 4.0 mA under the effect of the microbunching instability driven by CSR.	151
Figure 51 – Time evolution of the energy spread and bunch length for different bunch currents in the simulation with CSR and the machine impedance budget.	151
Figure 52 – Transverse coupled–bunch instabilities for the first phase of operation of the Sirius storage ring.	152
Figure 53 – Effect of chromaticity on the most unstable mode of the transverse coupled–bunch instabilities for the first phase of operation of the Sirius storage ring.	154
Figure 54 – Transverse single–bunch instabilities for the first phase of operation of the Sirius storage ring, considering the unperturbed longitudinal distribution, without the effects of intrabeam scattering (IBS) and potential well distortion.	155

LIST OF TABLES

Table 1 – Main Parameters of the Sirius Storage Ring.	40
Table 2 – Wall Impedance parameters.	99
Table 3 – Main parameters of the kicker magnet for impedance modeling	106
Table 4 – Main parameters for the fast correctors impedance model.	111
Table 5 – Main parameters of the undulators impedance modeling.	112
Table 6 – Main parameters used for modeling the CSR impedance and effective wake function	121
Table 7 – Sirius storage ring impedance budget for phase 1. RW stands for Resistive wall and Trans for transitions.	126
Table 8 – Broad band resonators model of the Sirius longitudinal impedance budget.	140
Table 9 – Transverse coupled–bunch instability thresholds at zero chromaticity for the phase one of operation for different assumptions on the Insertion Devices (IDs) effects.	153

ACRONYMS

3rd GLS Third Generation Light Sources.

4th GLS Fourth Generation Light Sources.

APU Adjustable Phase Undulator.

BBR broad band resonator.

BPM Beam Position Monitor.

BSC Beam Stay Clear.

CERN European Organization for Nuclear Research.

CNPEM National Center for Research in Energy and Materials.

CSR coherent synchrotron radiation.

DC direct current.

DSP direct space charge.

FOFB Fast Orbit Feedback System.

HOM higher order mode.

IBS intrabeam scattering.

ID Insertion Device.

ISP indirect space charge.

l.h.s. left hand side.

LINAC Linear Accelerator.

LNLS Brazilian Synchrotron Light Laboratory.

MAC Machine Advisory Committee.

MBA Multi-Bend-Achromat.

ME Maxwell Equations.

NEG Non-Evaporable Getter.

PEC Perfect Electric Conductor.

PIC particle in cell.

r.h.s. right hand side.

rms root-mean-square.

SC-RF Superconducting RF Cavity.

SI International System of Units.

SLS Synchrotron Light Source.

TMCI Transverse Mode-Coupling Instability.

VFP Vlasov Fokker Planck.

CONTENTS

Acronyms	17
1 Introduction	23
1.1 Synchrotron Light Sources	23
1.2 Storage Ring Main Devices	25
1.2.1 Magnetic Lattice	25
1.2.2 RF Cavity	28
1.2.3 Vacuum System	30
1.3 Light Source Generations	31
1.3.1 Multi-Bend-Achromat (MBA)	34
1.4 Collective Effects	35
1.4.1 Interaction Mechanisms	35
1.4.2 Wake Fields	36
1.5 The Sirius Project	37
2 Single-Particle Dynamics	41
2.1 Reference System	41
2.2 Transverse Dynamics	43
2.2.1 Linear Equations of Motion	44
2.2.2 Betatron Function and Phase Advance	45
2.2.3 Dispersion Function	47
2.2.4 Action–Angle Variables	48
2.2.5 Linear Map Formulation: Matrix Theory	49
2.2.6 Chromaticity and Action Dependent Tune shift	49
2.3 Longitudinal Dynamics	50
2.3.1 Changes in Revolution Time	51
2.3.2 The Energy Balance	51
2.3.3 Phase Stability Principle	52
2.3.4 The Potential Well	53
2.4 Radiation Damping and Equilibrium Parameters	54
2.4.1 Fokker-Planck Equation	55
3 Wakes and Impedances	59
3.1 Wake Fields	59
3.2 Wake Functions	62
3.3 The Wake Potential	63
3.4 The "Causality" Principle	64
3.5 Expansion of the Wakes	65
3.6 Impedances	67

3.7	Potential of Bunches of Particles	68
3.7.1	Multi-Turn and Multi-Bunch Effects	69
3.7.2	Relation with Impedance	70
3.8	Models for Impedances and Wakes	72
3.9	Impedance Calculation	73
3.9.1	Tapered Transitions	74
3.9.2	Multi-Layer Resistive Wall	78
3.9.3	Numeric Methods	80
3.9.3.1	Finite Line Density Issue	81
3.9.3.2	ECHO Code	82
3.9.3.3	GdfidL Code	84
4	Collective Effects	85
4.1	Sum of the Wakes	85
4.2	Energy Loss	86
4.3	Current Dependent Hamiltonian	88
4.4	Stationary Effects	89
4.4.1	Potential Well Distortion	89
4.4.2	Incoherent Tune Shifts	90
4.5	Coherent Motion (Instabilities)	91
4.5.1	Longitudinal Plane	94
4.5.2	Transverse Plane	95
4.6	Tracking Code	97
5	Impedance Modeling	99
5.1	Standard Chamber	99
5.1.1	Effect of Non-Evaporable Getter (NEG) Coating	99
5.1.2	Low-Frequency Impedance	103
5.2	Kicker Chambers	105
5.3	Fast Correctors Chambers	111
5.4	Undulators Chambers	112
5.5	BC Chamber	115
5.6	Coherent synchrotron radiation (CSR)	117
6	Impedance Budget	125
7	Instability Studies	133
7.1	The PETRA 7-Cell Cavity	133
7.2	Longitudinal Plane	138
7.2.1	Standard Impedance Budget Effects	139
7.2.2	Noise in Tracking Simulations	145
7.2.2.1	Estimative of Numerical Noise	147
7.2.3	Inclusion of CSR in the Budget	149

7.3	Transverse Plane	152
7.3.1	Multi-Bunch Instabilities	152
7.3.2	Single-Bunch Instabilities	155
Conclusions	159
Bibliography	163

1 INTRODUCTION

The first objective of this work was to study the subject of wake fields and impedances in accelerators and their effects on the beam dynamics of electron storage rings. The following goal was to apply this knowledge gathered from the literature to the Sirius storage ring, building the impedance budget with semi-analytic and numeric calculations of the impedances of the main components¹, with special care to the characterization of the effect of the NEG coating on the total impedance; and to perform calculations to predict the beam instabilities thresholds and study the possible cures for them.

This thesis is organized in the following manner:

- in this Chapter general concepts related to the work necessary to understand its relevance for the Sirius project as well as a brief description of the main mechanisms involved will be discussed;
- in Chapter 2 the main concepts of the single particle dynamics, important for the development of the rest of the work, will be introduced;
- in Chapter 3 the key of the wake field theory will be presented with focus to the physical interpretation of the quantities introduced;
- in Chapter 4 the methodology for computation of the impedance effects on the beam will be briefly described, with references for more detailed works and explanation of the derivation of the equations;
- in Chapter 5 the models applied to the impedance calculation of some of the main components of the storage ring will be presented and justified;
- in Chapter 6 the whole impedance budget gathered so far for the storage ring will be presented;
- in Chapter 7 the instabilities studies performed with the impedance budget will be discussed;

1.1 Synchrotron Light Sources

Synchrotron Light Sources (SLSs) are scientific facilities where the interaction between light and matter is used to study properties of a variety of materials. Through

¹ This part of the work was done together with other members of the Brazilian Synchrotron Light Laboratory (LNLS) team.

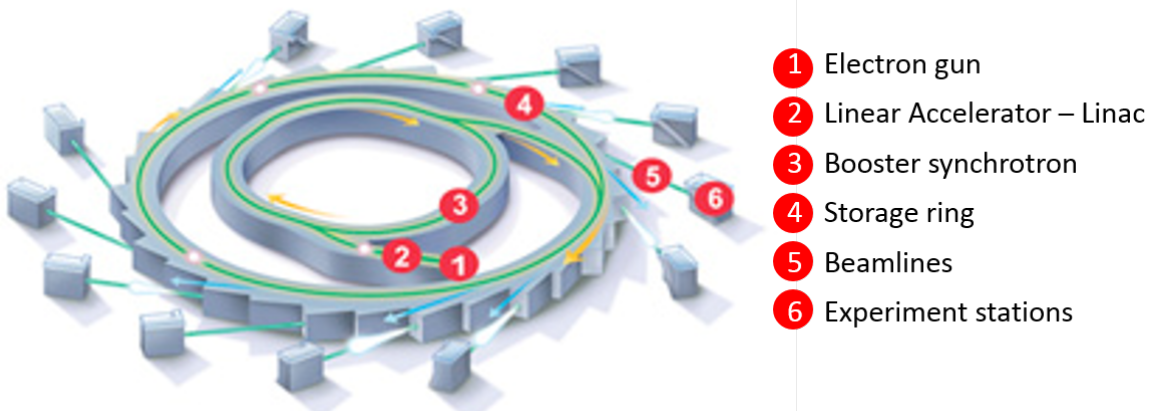


Figure 1 – Schematic of a storage–ring–based light source showing the three main systems: the injection systems, composed of an electron gun, a Linear Accelerator (LINAC) and a booster; the storage ring and the beamlines, with the experiment stations at their ends.

techniques involving absorption, reflection, refraction and scattering of light of different ‘colors’ and polarizations by the materials under study, their atomic structure, composition and chemical activity can be determined. The frequency of the light used in these facilities ranges from tera-hertz to hard X-rays and its origin is always related to the emission created by centripetal acceleration of ultra-relativistic charged particles (generally electrons), which has unique properties for use in scientific investigation: broad spectrum, high total flux and the strong collimation are among them.

These facilities always rely on particle accelerators to create the ideal conditions for the electrons emission and there are several different types of accelerators (a brief description can be found in Wiedemann (2007)). Among them, we highlight the ones based on synchrotron storage rings. In this type of SLS the electrons are grouped in several bunches that fill the whole storage ring and are confined for hours in approximately circular orbits by deflecting and focusing magnetostatic fields. The radiation used in experiments can be generated by the same fields that deflect the beam (dipoles) or by special devices called IDs that are installed in element-free sections of the ring, called straight sections. The ring topology of these machines allows dozens of beamlines to work simultaneously, performing completely different experiments, where the emitted light periodically hit the samples under study and the interaction patterns are recorded for as long as needed to achieve the desired resolution for the experiment.

Figure 1 shows a generic scheme of a storage ring based light source. It has three main subsystems: an injector, the storage ring and the beamlines. The injector is responsible for generating and accelerating the particles up to the ultra-relativistic energy of the storage ring and in most light sources it is composed of a gun, a LINAC and a booster synchrotron. In the case of electron storage rings the electron beam is emitted from cath-

odes in the gun, via thermionic or photoelectric effect, and are compressed in bunches and accelerated by the LINAC, generally up to energies of hundreds of MeV. After this, the electrons are transported to the booster synchrotron where they are accelerated up to the energy of the storage ring, generally a few GeV, and extracted from it to be injected into the storage ring. This whole process can happen with a repetition rate of a few Hz.

The storage ring is a synchrotron just like the booster in which the average energy of the electron beam is constant, while they perform dozens of billions of turns in the few hours they remain there. After injection, the bunches of electrons oscillate around the ideal orbit in the storage ring, but in a few dozens of thousands of turns they are damped, reaching the storage ring equilibrium values of transverse emittances (size and divergence), longitudinal length and energy spread. In ideal storage rings they stay stable in stationary closed orbits emitting radiation that is collected by the beamlines. The radiation exits the storage ring through holes in the external part of the vacuum chamber, called exit ports, and propagate to the beamline in straight trajectories, tangent to the electrons orbit in the point where it was generated.

1.2 Storage Ring Main Devices

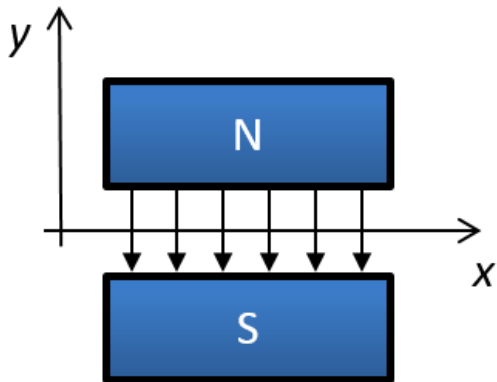
This work will focus on the study of the dynamics of the particles while they are in their equilibrium regime inside the storage ring, without considering the details of the injection process. For this reason, in this subsection we will present the main subsystems of a storage ring and discuss their main contributions to the task of keeping particles in stable confinement for such long times. Throughout this whole work the approximation $v \propto c$ will be assumed in the formulas, given the ultra-relativistic regime of the particles. Besides, all the equations are presented using the International System of Units (SI).

1.2.1 Magnetic Lattice

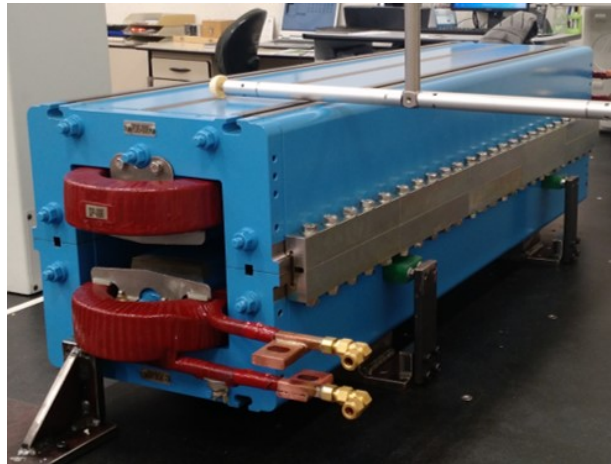
Magnetic lattice is the series of static magnets that are placed along the beam trajectory to deflect and focus it to keep the motion stable. It is composed of a reduced number of distinct types of magnets that have specific functions for the beam confinement:

Dipoles: or bending magnets, are the devices responsible for deflecting the beam in such a way that its net deflection in one turn is 2π rad. They generate an almost constant vertical field, B_y , along the beam path that curves its horizontal trajectory (see Figure 2). At each point of the trajectory inside a dipole the curvature, $G(s)$, is given by:

$$G(s) = \frac{1}{\rho(s)} = \frac{e}{p_0} B_y(s) \approx \frac{ec}{E_0} B_y(s) \quad (1.1)$$



(a) Schematic figure of a dipole magnet, where N and S indicate the North and South poles of the magnet and the vertical down arrows indicate the magnetic field lines



(b) Picture of a real dipole magnet.

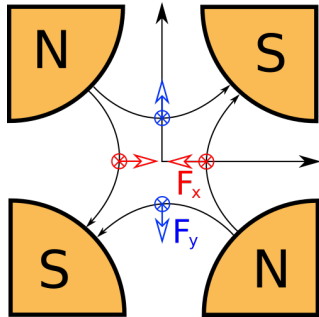
Figure 2 – Illustrations of a dipole magnet.

where s is the longitudinal position along the ring, $\rho(s)$ is the radius of curvature, e is the absolute value of the particle's charge, c is the speed of light, p_0 is the absolute value of the average linear momentum of the beam and E_0 is the corresponding average beam energy. Notice in the equation above that dipoles work as spectrometers, if the beam has an energy spread and in the absence of other types of magnets, particles with higher/lower energy will spiral out/in because their total deflection angle will be different than 2π rad, which means eventually all particles will hit the vacuum chamber and be lost;

Quadrupoles: are responsible to focus the beam, keeping oscillating around the ideal orbit. They achieve this by creating a field that grows linearly in intensity with the displacement from its center (see Figure 3), in such a way that they work as lenses. They are characterized by their strength, defined by:

$$K(s) = \frac{e}{p_0} \left. \frac{\partial B_y}{\partial x} \right|_{y=0} (s) \quad (1.2)$$

where x and y are the horizontal and vertical displacement from the center of the quadrupole. The strength defined above is directly related to how much the quadrupole deflect off-centered particles, being its integral along the quadrupole length directly related to the focal length of the magnet. One intrinsic limitation of quadrupoles imposed by Maxwell Equations (ME) and the Lorentz force is that they cannot focus the beam simultaneously in the horizontal and vertical directions. This means that two types of quadrupoles are needed in a magnetic lattice, one to focus in the horizontal, called focusing quadrupoles by convention, and another to focus in the vertical, the defocusing quadrupoles, in such a way that net focusing



(a) Schematic figure of a quadrupole magnet, where the curved arrows indicate the magnetic field lines and the red/blue arrows indicate the direction of the horizontal/vertical forces felt by an electron entering the sheet. Notice this quadrupole focuses in the horizontal, so it is a focusing quadrupole.

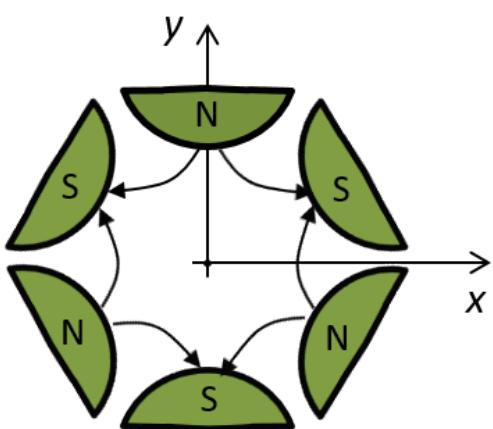


(b) Picture of a real quadrupole magnet, with the coils that generate the magnetic field and the iron core that guide and shape the field lines inside the gap.

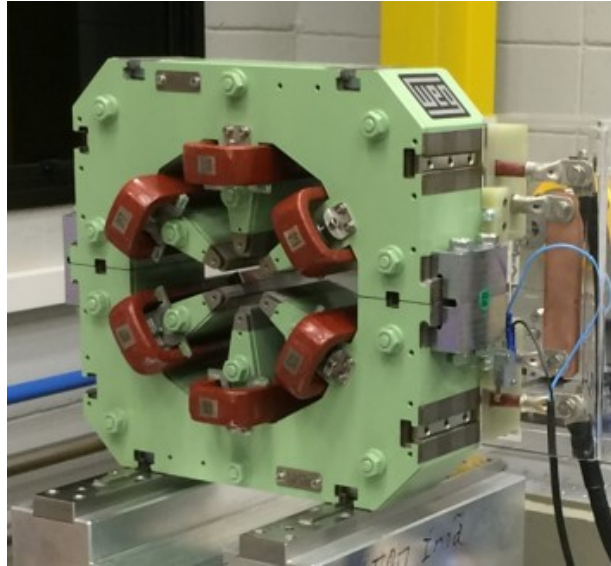
Figure 3 – Illustrations of a quadrupole magnet.

in both planes can be achieved with intelligent positioning of the magnets. Besides, quadrupoles are arranged along the ring to correct the intrinsic limitation of the dipoles regarding the energy dispersion, as discussed above, adding/subtracting net deflection in one turn for particles with more/less energy. This causes particles to have different closed orbits depending on their energy, the chromatic closed orbits. Quadrupoles and dipoles are the most important multipoles in a storage ring because together they define its main equilibrium properties, such as the particles average energy, the transverse beam natural emittance, and beam sizes along the ring, as well as the fundamental frequency of oscillation of the particles, the tune.

Sextupoles: quadrupoles also suffer from chromatic aberrations, focusing more or less the particles depending on their energy. This difference in focusing makes particles oscillate differently around their closed orbit, changing their fundamental resonant frequency. This is not a conceptually fundamental problem, but a practical one because in almost all modern storage rings it is impossible to store particles with only dipoles and quadrupoles. Sextupoles can correct that effect if placed at the right positions along the ring because of their non-linear magnetic field, which grows quadratically with the distance from its center, see Figure 4. Just like quadrupoles, it is needed two types of sextupoles, focusing and defocusing, to correct the horizontal and vertical frequency of oscillation of the particles. Sextupoles are needed, but they introduce several complications for the design of a storage ring, because their non-linear fields introduce chaos in some regions of the particles phase space. More sextupoles or higher order multipoles can be introduced to avoid chaos as much as possible and also to help correcting higher order chromatic effects.



(a) Schematic figure of a sextupole magnet, where N and S indicate the North and South poles of the magnet and the curved arrows indicate the magnetic field lines.



(b) Picture of a real sextupole magnet.

Figure 4 – Illustrations of a sextupole magnet.

Higher order multipole magnets, such as octupoles and decapoles, can be used to correct higher order chromatic and geometric aberrations, but their use is not very common in the design of storage ring for light sources as they are in colliders, even though this tendency is changing with the new light sources that are being designed, such as MAX IV (LEEMANN *et al.*, 2009), ESRF upgrade (FARVACQUE *et al.*, 2013), APS-U (SUN; BORLAND, 2013), SLS upgrade (SOUTOME *et al.*, 2016) and Spring-8 upgrade (SOUTOME *et al.*, 2016). Nevertheless, they are always present in storage rings as errors of the main magnets and their effect must be taken into account in detailed single particle dynamics analysis.

Generally, lattices have high periodicity, being the repetition of a unit cell along the whole extension of the ring. This periodicity simplifies the design of the ring, the dynamics of the electrons and reduces the number of dangerous resonances that can harm the beam stability. Unit cells generally can be divided in two parts, an arc section, where the dipoles are placed, interleaved by focusing elements to control the dispersion and focus the beam from one dipole to another, and a straight section, with a dedicated space for the installation of IDs for light generation and other machine equipment. The straight sections also have focusing elements to match the beam to the arcs.

1.2.2 RF Cavity

At each turn, the electrons lose energy due to synchrotron radiation which must be replenished periodically in order for them to remain in stable orbits, with energy close to the nominal energy of the storage ring. The magnetostatic components described above cannot perform such a task neither any other component or method relying on static

electromagnetic fields of any kind, because according to the ME and the Lorentz force, the net energy transferred to a charged particle by static fields in one turn over the ring must be zero. This means that the laws of physics constraint that it is necessary to rely on time dependent electromagnetic fields to replenish the energy of the electrons. The way this is accomplished in a storage ring is through the use of devices called RF cavities.

The RF cavity is a cylindrical electromagnetic cavity with the lowest Transverse Magnetic mode (TM010) in the range of radiofrequency. Cavities for use in storage rings must have at least two small holes in its axis for the beam passage and one other hole to couple the cavity with an external source to feed the mode TM010 with energy. This energy is transferred to the particles when they pass through the cavity by the almost homogeneous longitudinal electric field of this mode. The frequency of this particular mode is always exactly equal to a multiple, h , of the revolution frequency of the beam along the ring, in such a way that the phasing between the electric field and the beam entrance in the cavity remains constant over several passages and, once initially adjusted when the beam is injected in the ring, will be such that the average energy lost in one turn is replenished. This special phase is called the synchronous phase. Moreover, this synchronicity mechanism, that, by the way, is the responsible for the name of this type of accelerator, creates h points in the ring's longitudinal phase space around which the electrons can form stable bunches.

Besides the mode used to feed energy to the beam, a cavity can have several other modes of higher resonant frequencies with a high quality factor, Q , that can be excited by the beam. When the beam passes through the cavity it leaves electromagnetic fields with a very wide spectrum of frequencies. Most of these frequency components are rapidly scattered and dissipated, but some of them, close to the resonant frequency of these modes, can last for very long times and, assuming the beam is constantly feeding them, strong electric potentials, or wake fields, can be formed. These potentials, in turn, influence the beam dynamics, causing energy loss, distortion of the bunches and instabilities.

There are some methods to avoid this problem with cavities. For example, it is possible to insert couplers in the cavity, similar to the one that feeds the fundamental mode, but designed and positioned specially to interact with one or a group of these higher order modes (HOMs) to absorb the energy deposited by the beam, which is later transformed in thermal energy by resistors outside the cavity, or to design wave guides in the cavity, through which the modes can propagate and be dissipated in the resistive endings. Another method involves shifting the frequency of the modes, via thermal or mechanical deformation, in such a way that they do not couple with any frequency of the beam.

The superconducting RF cavities also do not have this problem because they are built with very large tubes for the beam passage, in such a way that the HOMs

can propagate through them. Even though for the main mode the ratio of the shunt impedance by the quality factor, R_s/Q , which depends only on the geometry of the cavity, as explained by Wiedemann (2007, Sec. 15.4), is strongly reduced by this approach, the zero resistivity of the wall still provides very large values for Q and R_s . Sirius will adopt this type of cavity and, based on the operation reports of other laboratories which also employed this solution, we do not expect to have problems with HOMs.

1.2.3 Vacuum System

The vacuum system is used to create a compact region around the reference orbit in the whole machine with very low pressure, and thus minimize collisions of the stored charged particles with residual gas molecules, increasing the lifetime, which is the average time particles can be stored with stable movement, and minimizing the production of bremsstrahlung radiation. As an estimative, the average pressure of a storage ring must be lower than 1 nTorr for the average stored time of the particles to be of the order of a few dozens of hours.

The vacuum system is composed of two main subsystems, the vacuum vessel, which defines the boundaries of the electron's environment, and vacuum pumps, which maintain the desired difference in pressure between the two regions. Most of the extension of the vacuum vessel is composed of straight and long chambers with a specific cross section, constant along the extension of the chamber. They are made of metals due to several desirable properties of these materials, such as high heat and electrical conductivities, high acceptance to welding and braising, high resistance to pressure and low cost. Among them we highlight implications of the high electrical conductivity, due to its importance for this work. Besides the standard vacuum chamber there are several other structures that compose the vacuum vessel, for example:

Bellows: are sanfonated elements that connect two vacuum chambers in order to accommodate longitudinal thermal expansions and transverse misalignments between them, as well as the assembly to the vacuum components themselves;

Valves: devices that are used to isolate the vacuum in different sections of the ring. Generally they remain open, creating a single vacuum region along the ring, but can be closed automatically in case of accidents, or for maintenance;

Flanges: are the components responsible for coupling two different vacuum components together in a leakage-free manner;

Dipole Chambers: are special curved chambers used in the regions where there are dipoles. In some cases they have exit ports to extract the photon beam to the beamlines;

Radiation Masks: are small protuberances in the vacuum chamber designed to shadow more sensitive elements from synchrotron radiation.

Diagnostic Elements: are components used both to measure the electromagnetic signals generated by the beam to determine its properties, such as intensity, position and oscillations and act back on it either as a feedback or feedforward corrections to perturbations. They must be inside the chamber because the high frequency components they measure cannot propagate out the chamber;

Transitions: there are some sections of the vessel that have different cross sections than the standard chamber, generally to accommodate special devices such as RF cavity, IDs, some magnets, ceramic chambers, collimators, etc. Transitions are smooth longitudinal variations of cross section from one chamber to the other.

These are only some examples of the different components of the vacuum vessel of a storage ring. All these components introduce variations in the inner cross sections of the chamber which interact with the electromagnetic fields of the beam, creating other fields, called wake fields, that causes not only heating of the components, in addition to the radiation heating, but also act back on the beam itself affecting its dynamics with the potential of causing instabilities that can severely limit the machine performance. The study of this last interaction applied to the new Sirius light source in Brazil will be the main subject of this work.

1.3 Light Source Generations

Brightness is the main figure of merit used to characterize a synchrotron light source (HETTEL, 2014b), the larger its value the better the radiation. It is a measure of the intensity and collimation of the radiation at a given frequency or wavelength and can be mathematically defined by the following expression, according to Huang (2013):

$$B(\omega) = \frac{1}{\Delta\omega} \frac{F(\omega)}{\Sigma_x(\omega)\Sigma_y(\omega)} \quad (1.3)$$

where ω is the photon frequency, $F(\omega)$ is the flux, the average number of photons per second, Σ_x and Σ_y correspond to the volume the photon beam occupies in the horizontal and vertical phase space, respectively, and $\Delta\omega$ is a frequency bandwidth that is proportional to the central frequency (usually 0.1%). The volume occupied by the photon beam in phase space is convolution of the electron beam distribution and the photon distribution emitted by a single electron. This last term depends on the radiation frequency and on how it was generated. On the other side, the volume occupied by the electron beam in phase space is called emittance and it depends only on the storage ring properties.

Equation (1.3) shows that to increase the brightness of a given light source it is necessary to increase the number of stored electrons, which linearly impacts the total photon flux, and minimize the emittance of the electron beam. Consequently, together with the electrons energy, the emittance and the current are the main figures of merit of a storage ring. New machines always try to push the limit of these factors to obtain gains in synchrotron light quality and, from time to time, new ideas and breakthroughs in accelerator technology create large scale advances.

These discontinuities in the otherwise small and incremental improvements of the radiation quality happened three times along the history of storage ring based light sources, classified as four generations of machines. The first breakthrough was the construction of machines dedicated to the generation of synchrotron radiation from dipoles, which marked the difference from the first generation of light sources, which were parasitical to particle colliders.

The second breakthrough was the construction of machines specialized to operate with IDs, which are special devices that are installed along the straight trajectory of the beam and generate a transverse magnetic field with an amplitude that varies sinusoidally along the longitudinal direction. When the beam passes through this field it wiggles, and synchrotron emission of radiation happens due to its deflection at each wiggle. The light emitted from successive wiggles interferes in such a way that only photons with specific frequencies survive and the resulting radiation has a spectrum where all the energy is concentrated at very thin peaks around multiples of this resonant frequency. The intensity of these peaks is proportional to the number of particles in the beam and the number of wiggles of the ID field and their bandwidth is proportional to the inverse of the number of wiggles. Additionally, the polarization of the radiation is defined by the direction of the magnetic field of the ID. For example, if the field is vertical, the electrons will oscillate horizontally and the radiation will be horizontally polarized. In specially designed IDs, circular and elliptical polarizations can also be achieved by changing not only the intensity of the field but also its direction as a function of the longitudinal position. All these properties of the light can be tuned according to the needs of the experiment to be carried out at the experimental station, which makes these devices a very powerful tool for scientific investigations.

Currently, another generation of light sources is rising. With much smaller emittances, these machines are being called Fourth Generation Light Sources (4th GLS). This search for smaller emittance becomes clear when we observe the graph shown in Figure 5 which compares the 3rd and 4th GLS. To interpret this figure it is important to know that the emittance of a storage ring roughly scales with

$$\varepsilon \propto \frac{\gamma^2}{N_b^3}, \quad (1.4)$$

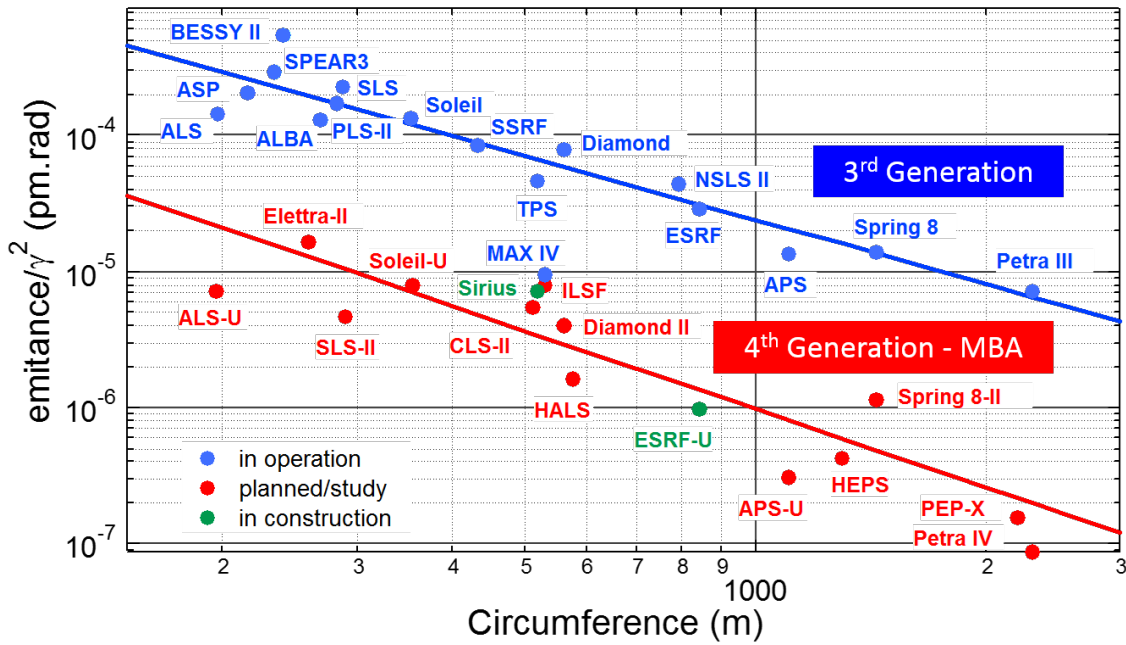


Figure 5 – Natural emittance normalized by relativistic energy squared as a function of ring circumference for several existing Third Generation Light Sources (3rd GLS) and future 4th GLS. The blue solid line is a fitting among the 3rd GLS and the red solid line is a fitting among the 4th GLS. Note the only 4th GLS in operation today is MAX-IV. Updated from (LIU; WESTFAHL, 2017).

where $\gamma = E/m_0c^2$ is the relativistic energy and N_b is the number of dipoles, or bending magnets, of the storage ring. Besides, higher energy storage rings generally imply in larger circumferences and, consequently more dipoles. Given the scaling presented above, it is clear that in general the emittance is reduced with the increase of the ring circumference, as shown by the tendency lines in the figure.

The 4th GLS will enable new science to be made, according to Eriksson *et al.* (2014): "The significant improvement provided by the DLSRs (Diffraction Limited Light Sources, or 4th GLS) under construction and in the design stage will enlighten our view of the world and allow science which is not possible, or not even thinkable, today.". In section 4 of his article, Eriksson *et al.* provides a very good review of the possible scientific studies that will be enabled by such machines. Here we highlight the advances in imaging techniques, such as ptychography (THIBAULT *et al.*, 2014), and diffraction (HITCHCOCK; TONEY, 2014), that will be possible due to the increase in the transverse coherent part of the flux ².

² For a brief and didactic description of coherence, we recommend the work of Huang (2013).

1.3.1 Multi-Bend-Achromat (MBA)

The main reason for the 4th GLS to achieve such small emittances is the use of Multi-Bend-Achromat (MBA) lattices. In 3rd GLS the number of dipoles in one unit cell of the magnetic lattice is two or three depending on the machine, but in 4th GLS this number is larger than five, hence the name multi-bend. The achromat part of the name MBA is due to the fact that energy dispersion errors introduced by dipoles are corrected locally and do not affect the trajectories and transverse bunch sizes inside the IDs.

Even though this change does not seem to be harmful or difficult in a first analysis, it requires several developments in almost all the areas involved in designing, constructing and operating a light source (ERIKSSON *et al.*, 2014; LIU; WESTFAHL, 2017). The larger number of dipoles in a short space requires strong focusing from the quadrupoles to achieve low emittances. These strong quadrupoles require strong sextupoles to correct their chromatic errors, which, in turn, require other strong sextupoles to increase the stability region around the fixed point of the one-turn map (BORLAND *et al.*, 2014). In order to produce all these strong magnets, they need to be closer to the beam, their gap must be smaller (JOHANSSON *et al.*, 2014), which implies the vacuum chambers must be smaller too. The smaller vacuum chamber decreases the vacuum conductance³, making it necessary to adopt different solutions for vacuum pumping (AL-DMOUR *et al.*, 2014), generally distributed along the whole ring, such as the use of NEG coating inside the chambers, first proposed by Benvenuti (1983). The proximity of the vacuum chamber and all the other in-vacuum components to the beam, increase the beam coupling impedance, which leads to higher heating of the components and to instabilities (NAGAOKA; BANE, 2014). The stronger magnets also imply more sensitivity of the lattice to errors, such as construction errors of the magnets, misalignments and residual multipoles (NEUENSCHWANDER *et al.*, 2015; HETTEL, 2014a), and, together with the very small transverse sizes of the beam, require tight tolerances power supply stability and vibration, not only of the magnets and Beam Position Monitors (BPMs), but also of the components of the beamlines, such as the monochromators (SUSINI *et al.*, 2014; SIEWERT *et al.*, 2014) and also for the detectors at the experimental stations (DENES; SCHMITT, 2014). Underlying all these intricacies is the need of very detailed design, characterization and, in some cases measurement, of all the components that are installed in the light source. Besides, detailed single particle models of the storage ring are fundamental to evaluate the effect of each new design on the global properties of the ring, such as beam lifetime and dynamic aperture. All this requires very detailed simulations and high computational power (BORLAND *et al.*, 2014).

Regarding the beam coupling impedance, the last 3rd GLS that were built already demonstrated a need to evaluate the budget of the ring, simulating and, more importantly,

³ The vacuum conductance is proportional to the third power of the vacuum chamber radius, as described by Al-Dmour *et al.* (2014).

designing the components to minimize heating and other impedance related issues (NAGOKA, 2004a; GÜNZEL; PEREZ, 2008; BLEDNYKH; KRINSKY, 2007; BLEDNYKH *et al.*, 2009). For 4th GLS this approach is practically mandatory because the predictions for thresholds for strong instabilities are much lower for these machines than they were for 3rd GLS (KLEIN *et al.*, 2013; LINDBERG; BLEDNYKH, 2015; PERSICHELLI *et al.*, 2017; WANG *et al.*, 2017a; WANG *et al.*, 2017b). Additionally, the use of NEG technology extended along the whole ring requires more detailed analysis of its effect on the impedance.

1.4 Collective Effects

Collective effects can cause severe deterioration of the brightness of a machine because they can lead to the increase of the effective emittance of the electron beam, through coherent oscillations of the bunches, increase of the energy spread and the beam sizes in all three planes. Besides, they can cause beam loss, which limits the maximum current that can be stored and consequently the total photon flux of the machine. In this section we will introduce the main mechanisms that drive collective effects in a storage ring.

1.4.1 Interaction Mechanisms

One of the most important interaction in storage ring light sources is the collision of particles in the beam, generally referred to as Coulomb scattering or IBS, which is highly chaotic and its effects on the beam resembles the properties of the emission of radiation, causing emittance and energy spread increase (PIWINSKI, 1974; BJORKEN; MTINGWA, 1983; KUBO *et al.*, 2001). Additionally, the collision process also leads to particle loss through a mechanism called Touschek scattering, first explained by Bruno Touschek (BERNARDINI *et al.*, 1963), described in details by Piwinski (1998), where the transverse energy of oscillation is transferred to the longitudinal plane and the particles gain/lose an energy deviation so large that they are lost. All these effects are very detrimental to new light sources, being the Touschek lifetime their main source of particle loss, as pointed out by Nagaoka & Bane (2014).

The direct space charge (DSP) is another type of interaction among the particles, being the result of the action of the cloud of electromagnetic field existent inside the beam on individual particles. Each particle generates an electric and a magnetic field that, when averaged among all particles, result in a net potential dependent on the shape and sizes of the bunch. This potential acts like an external field on the movement of the particles, leading to tune-shifts with amplitude and possible excitation of resonances. However, for ultra-relativistic electron beams such as the ones of a light source storage

ring, with energies on the order of a few GeV, this effect is very small and can be neglected. This happens because in this limit the non-radiating field generated by each particle is concentrated in a plane transverse to its movement and the electric and magnetic forces that act on other particles moving parallel to it cancel each other out.

The Coherent synchrotron radiation (CSR) is another type of direct interaction between particles in a beam. The radiation emitted by the particles travels forward with the velocity of light and, due to the fact that the particles are moving on a curved trajectory when they emit light, this radiation catches up with the particles ahead of the emitting particle (DERBENEV *et al.*, 1995). If the wavelength of the radiation is of the same order of or larger than the bunch length, the average of this effect is non-zero and the head of the bunch feels a net force. As this effect depends on the radiated field, in contrast to the DSP, it does not tend to zero as the energy on the particles increases and can be very harmful, depending on the bunch length of the beam, causing energy spread increase and bunch lengthening or even microbunching (BYRD *et al.*, 2002).

All mechanisms described above are examples of direct interactions among the particles, they do not depend on the immersive environment to happen. The wake fields and the indirect space charge (ISP) on the other hand, results from the interaction with the vacuum chamber. The contact of the non-radiating field of the beam with the metallic walls of the chamber induces currents in the surface of the metal that travels with the beam, these surface currents also generate an electromagnetic field that propagates to the center of the vacuum chamber and influences the movement of the particles, as described by Laslett (1963). This electromagnetic field can have properties of non-radiating and radiating field, depending on the characteristics of the vacuum chamber. If we consider the chamber is perfectly conducting and with translational symmetry in the longitudinal direction, then the surface charges travel in straight lines with the beam speed, which means they will produce only non-radiating fields with the same properties of those of the DSP. This is the origin of the ISP, that for the same reasons as the DSP is negligible for high energy storage rings⁴.

1.4.2 Wake Fields

If any of the two conditions considered for the vacuum chamber does not hold, then the surface charges also generate radiating fields or fields that are dragged behind the source particle, namely wake fields. For example, if the vacuum chamber has no longitudinal translational symmetry, then the surface charges must follow curved paths, which makes them suffer accelerations and hence, radiate electromagnetic fields. Notice

⁴ This statement is not true for static (or quasi-static) fields, because the electric and magnetic components of the force decouples and they depend on whether or not the boundary is a good electric conductor or a high- μ magnetic material. This problem was first studied by Laslett (1963) and will be addressed later in this work.

that this is only one of the several possible ways of introducing this mechanism, it would be equivalent to say that the surface of the metal scatter the fields generated by the particles in the beam and when the surface of the vacuum chamber has longitudinal symmetry the reflection is specular but when it has corrugations or transitions, the scattering is diffuse. Precisely what happens is that the walls of the vacuum chamber impose boundary conditions on the fields that exist inside the vacuum vessel, univocally defining its time and spatial dependency.

The wake fields can be very harmful to the beam, changing the properties of the static distribution of particles and creating instabilities above a given current threshold, which can lead to coherent oscillations of the bunches, emittance and energy spread increase and even beam loss. All these effects cause serious deteriorations of the brightness of the radiation, limiting the photon flux and bringing deterioration of its phase space average distribution.

1.5 The Sirius Project

The National Center for Research in Energy and Materials (CNPEM) is a Brazilian institution located in Campinas-SP that gathers four national laboratories, being the LNLS one of them. This laboratory was created in 1987 to design, construct and operate a SLS. Such goals were successfully achieved with UVX, a second generation light source that was opened to external users in 1997. Since then, the Brazilian community of synchrotron users has grown and studies of a new, more competitive machine, started in 2008.

By the end of 2011, Sirius was a well-developed project and it consisted on a permanent magnet-based 3rd GLS, with an energy of 3 GeV, an emittance of the order of 2 nm rad and circumference of 480 m, as described by Liu *et al.* (2010) and Liu *et al.* (2011). This scenario changed after the first meeting of the Machine Advisory Committee (MAC), in June 2012, when the committee recommended leaders to follow the idea of MAX-IV (LEEMANN *et al.*, 2009) and pursue sub-nanometer emittances. This challenge was accepted and Sirius became the second project to fit the category of what today is called 4th GLS, with a natural emittance even lower than the first projected machine of this kind, the MAX-IV (LIU *et al.*, 2013).

After several changes in the magnetic lattice (LIU *et al.*, 2014; LIU *et al.*, 2015; LIU *et al.*, 2016a) to improve the brightness of the light generated by the IDs that are being planned for Sirius (SIRIUS, 2013; VILELA *et al.*, 2017), the current lattice of the storage ring is the one presented in Figure 6 and the current optical functions are presented in Figure 7. The arc of the cell, composed of all the elements from the first to the second B1 dipoles, inclusive, is repeated twenty times to form the ring. The straight sections alternate

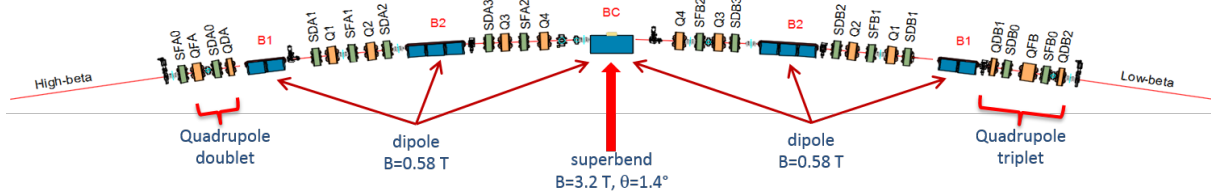


Figure 6 – One fourth of the unit cell of the Sirius storage ring. Dipoles are shown in blue, quadrupoles in orange and sextupoles in green. The vacuum pumps and valves are also shown. Only half of the high-beta (A) and of the low-beta (B) straight sections are shown. The arc and the straight sections are repeated to form the unit cell in the following way: A-B-B-B. The unit cell is then, repeated five times to form the ring.

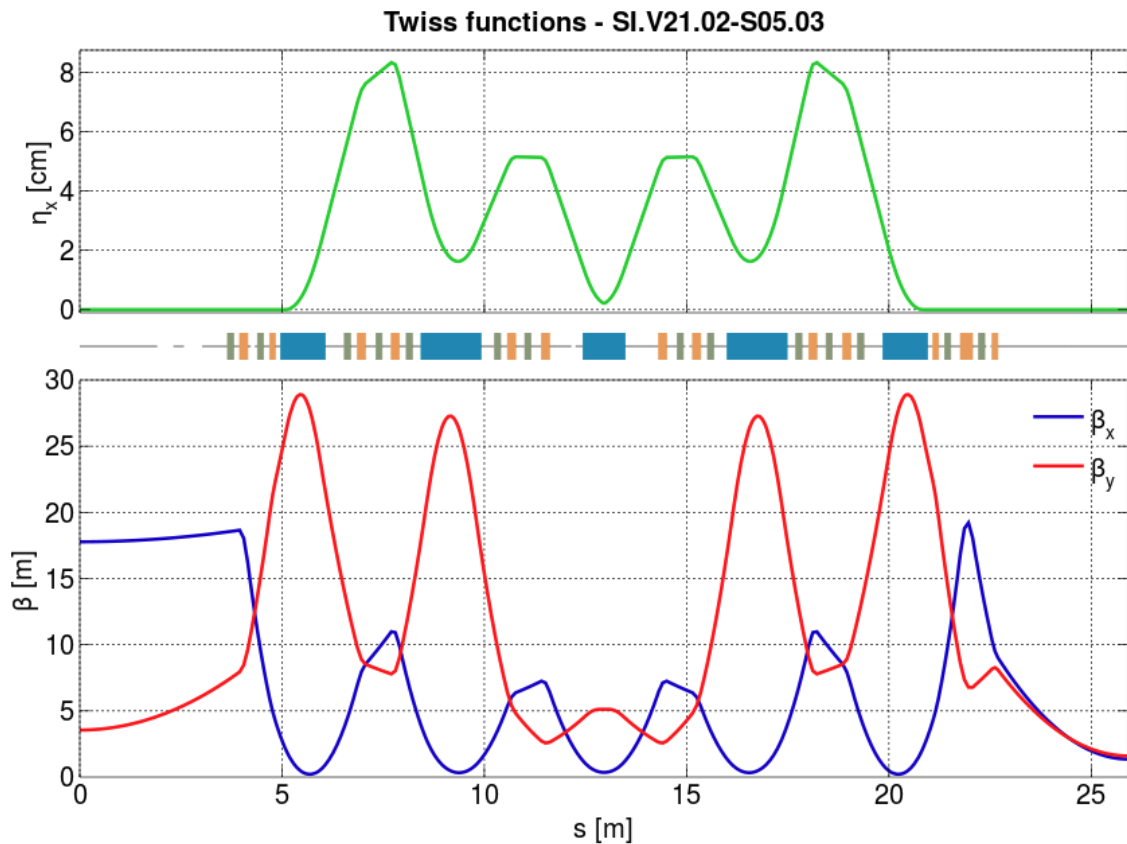


Figure 7 – Optical (twiss) functions for one fourth of a period of the Sirius lattice. In green is shown the dispersion function. In red, the vertical betatron function is shown and in blue, the horizontal betatron function. Notice the strong focusing of the betatron functions at the center of the low-beta (B) sections. (copied from Sirius (2013).)

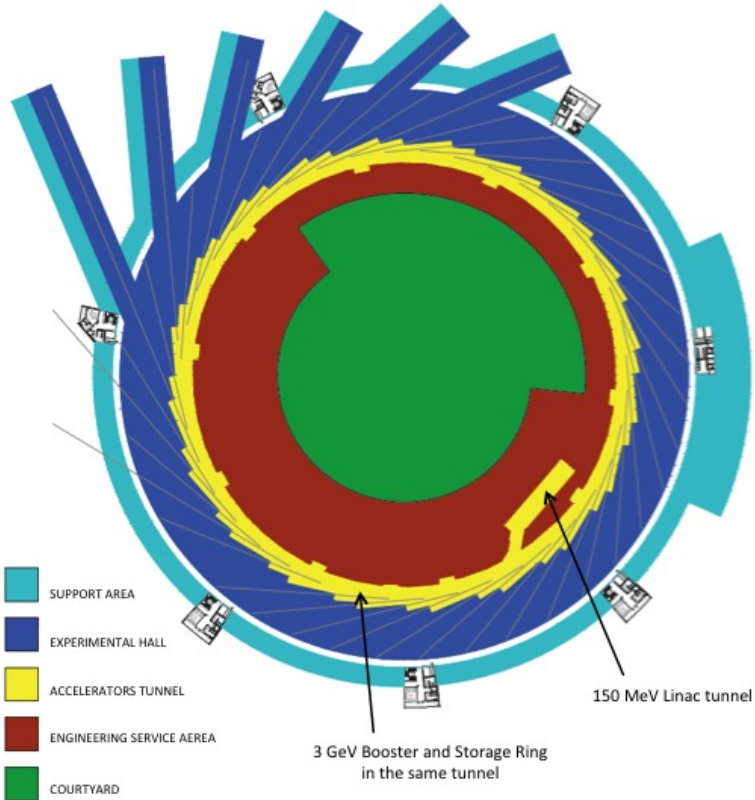


Figure 8 – Sirius building layout, showing all the important areas of the light source, with emphasis on the booster sharing the same tunnel as the storage ring and the 150 MeV LINAC tunnel. The experimental hall will be able to accommodate beamlines up to 100 m long and the requirement for longer beamlines, with possible length up to 450 m, is anticipated. (copied from Sirius (2013).)

in sections with two quadrupoles in each matching extremity (A), and sections with three quadrupoles (B), in the following manner: A-B-B-B, in such a way that the ring has five A sections and fifteen B sections. The difference between these two types of sections is that beam is strongly focused in both directions, horizontal and vertical, in the B sections, to improve the radiation generated by the undulators which will be installed there and the A sections are optimized for off-axis injection in the horizontal plane. This way the ring has twenty straight sections, from which eighteen will be available for installation of IDs. However the real symmetry of the ring is only five, which difficulties the optimization of the single particle non-linear optics (SÁ *et al.*, 2016; DESTER *et al.*, 2017). In the center of each arc there is a special dipole magnet, with longitudinal gradient and a strong peak field of 3.2 T in its center that will provide hard x-rays, with critical energy of 19.2 keV, for additional 20 beamlines (LIU *et al.*, 2016a; SIRIUS, 2013).

The whole accelerator complex of the Sirius SLS, shown schematically in Figure 8, will be composed of a 150 MeV LINAC, a full energy booster synchrotron, that will ramp the electrons from the LINAC energy to the storage ring nominal energy with a cycling rate of 2 Hz, and the storage ring, as described in Sirius (2013) web page. The injection

Table 1 – Main Parameters of the Sirius Storage Ring.

Parameter	Symbol	Operation Phases			Unit
		Commiss.	Phase 1	Phase 2	
Energy	E_0		3.0		GeV
Circumference	L_0		518.4		m
Revolution period	T_0		1.73		μs
Revolution frequency	f_0		578		kHz
Angular rev. freq.	ω_0		3.632		Mrad s^{-1}
Harmonic number	h		864		
Momentum compaction	α		1.7×10^{-4}		
Transverse tunes (H/V)	$\nu_{x/y}$		49.11/14.17		
Energy loss per turn	U_0		473		keV
Natural emittance	ε_0		252		pm rad
Natural energy spread	σ_δ		8.5×10^{-4}		
Damping times (H/V/L)	$\tau_{x/y/z}$		16.9/22.0/12.9		ms
Damping rates (H/V/L)	$\alpha_{x/y/z}$		59.2/45.5/77.5		Hz
Nominal total current	I_0	30	100	350	mA
Current per bunch	I_b	34.7	116	405	μA
RF cavity		1 7-Cell		2 SC-RF	
Voltage gap	V_0	1.8		3.0	MV
Natural bunch length	σ_z	3.2(10.7)		2.5(8.2)	mm (ps)
Synchrotron Tune	ν_z	3.56×10^{-3}		4.6×10^{-3}	

system will operate in top-up mode, where the total current of the storage ring is kept nearly constant during the whole user's shift, because periodic injection cycles along the day are performed without the need of interrupting the operation of the machine. The booster will be concentric to the storage ring and placed inside the same tunnel, which minimizes costs related to the construction of a separate shielding and helps diminishing its emittance, only 3.5 nm rad at 3 GeV (SÁ *et al.*, 2014), which is important to maximize the injection efficiency in the storage ring (LIU *et al.*, 2016b).

Table 1 shows the main global parameters of the storage ring for the planned operation phases of the machine. Even though the commissioning will be performed with a normal conducting PETRA 7-Cell RF cavity, in the users operation phases of the storage ring the RF cavities will be Superconducting RF Cavity (SC-RF). The installation of a 3th harmonic passive landau cavity to lengthen the bunches and increase the lifetime is foreseen, allowing multi-bunch operation with higher currents. Even though the expected filling pattern of the machine is uniform, other arbitrary filling patterns are possible and, in particular, gaps may be needed to cure ion instabilities (WANG *et al.*, 2013; NAGAOKA; BANE, 2014).

2 SINGLE-PARTICLE DYNAMICS

In this chapter the main concepts of single particle dynamics that will be useful for the rest of the work will be introduced without any intention to be complete or rigorous in the presentation. There are good books, for example the ones written by Lee (1999) and by Wiedemann (2007), and also one outstanding report written by Sands (1970) that cover all the topics presented here and much more, with thoughtful didactics. Besides, Borland *et al.* (2014) give a quick overview on all the topics relevant for single particle dynamics.

2.1 Reference System

Connected to the concept of a storage ring is the one of the reference orbit. This special closed orbit is the one that an ideal particle, the synchronous particle, with the storage ring nominal energy would follow if it had the correct initial conditions. All the components of a storage ring are aligned according to this special orbit in such a way that their center, symmetry points or axis coincide with it and, in practice, the trajectories of all particles stored in the machine will be close to it. For this reason, the reference orbit is chosen to be the origin of the reference frame, defining a curved coordinate system that moves along the ring, with one longitudinal coordinate tangent to the local orbit and two transverse coordinates perpendicular to it. This type of co-moving coordinate system is a particular case of a Frenet-Serret frame (FRENET, 1852; SERRET, 1851; Wikipedia Contributors, 2017d), where the torsion is always zero, since storage rings are usually designed only with dipoles that deflect in the horizontal plane. Such a coordinate system can be defined in the following way (LEE, 1999, chap. 2):

$$\begin{aligned}\hat{\mathbf{s}}(s) &= \frac{d\mathbf{r}_0(s)}{ds}, \\ \hat{\mathbf{x}}(s) &= -\rho(s) \frac{d\hat{\mathbf{s}}(s)}{ds}, \\ \hat{\mathbf{y}}(s) &= \hat{\mathbf{s}}(s) \times \hat{\mathbf{x}}(s),\end{aligned}\tag{2.1}$$

where s is the arc length of the reference orbit starting from an arbitrary point, \mathbf{r}_0 is the position of the reference orbit in relation to a static, cartesian reference frame, $\hat{\mathbf{s}}$ is the Frenet-Serret vector tangent to the orbit, $\hat{\mathbf{x}}$ is the negative of the normal vector, generally known in accelerator physics literature as radial or horizontal coordinate, $\hat{\mathbf{y}}$ is the standard binormal versor, often called vertical direction in accelerator physics. The scalar ρ is the local radius of curvature of the reference orbit, which is equal to the one introduced by the dipoles, as defined in equation (1.1). This means that the reference

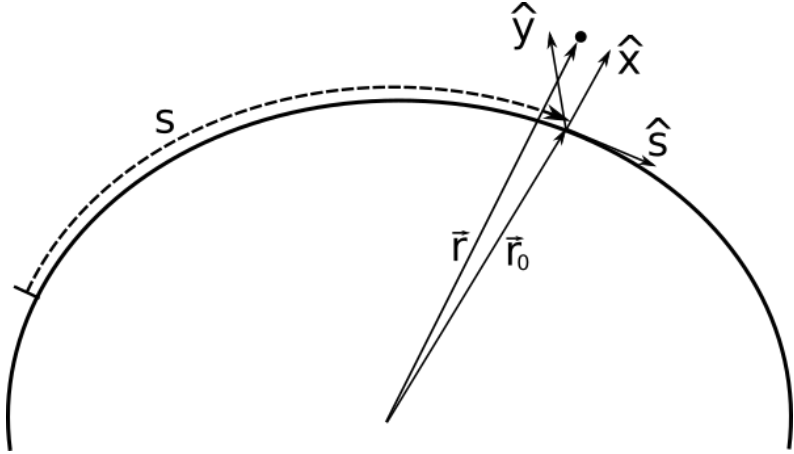


Figure 9 – Frenet-Serret reference frame of a storage ring, with right-handed coordinate system $\{\hat{x}, \hat{y}, \hat{s}\}$. Adapted from (LEE, 1999, pp. 123).

frame of an accelerator is piecewise straight with curvature different from zero only at the dipole field regions.

With the definitions above, the position of an arbitrary particle can be described as small deviations from the reference orbit (see Figure 9)

$$\mathbf{r}(s) = \mathbf{r}_0(s) + x\hat{x}(s) + y\hat{y}(s) \quad (2.2)$$

with x and y being the horizontal and vertical displacements of the particles in relation to the reference orbit. In this reference frame, the dynamics of each particle can be represented by its position in the six dimensional phase space defined by:

$$\{x, x', y, y', z, \delta\} \quad (2.3)$$

with

$$x' = \frac{dx}{ds} \approx \frac{p_x}{p}, \quad y' = \frac{dy}{ds} \approx \frac{p_y}{p}, \quad \delta = \frac{p}{p_0} - 1 \quad (2.4)$$

where p_0 is the storage ring nominal linear momentum, $\delta \approx \Delta E/E_0$ is the energy deviation of the particle in relation to the nominal energy of the storage ring and x' and y' are the normalized transverse components of the linear momentum of the particle. The coordinate z is defined as the relative longitudinal position of the particle in relation to the synchronous particle

$$z(t) := s_{\text{sync}}(t) - s(t) \quad (2.5)$$

where t is the wall-clock time and $s_{\text{sync}}(t)$ is the trajectory arc-length of the synchronous particle. Note that if the particle is ahead of the synchronous particle z will be negative. This convention is very important and will be consistently adopted throughout this work.

2.2 Transverse Dynamics

At this point it is convenient to describe in general terms the movement of the stored particles in storage rings similar to Sirius'. The particles are ultra-relativistic electrons with energy of the order of a few GeV, and most of their velocity is always locally tangent to the ideal orbit. There are typically hundreds of billions electrons grouped in several bunches along the reference orbit, each bunch having length of a few milimiters and transverse sizes of the order of dozens of microns. Each electron is under the influence of a variety of electromagnetic fields (gravity can be neglected), coming from the static magnetic fields of the dipoles and multipoles, the radiofrequency field of the RF cavity, the direct fields of other electrons in the same bunch and the fields scattered by the vacuum vessel, generated by other electrons in the same bunch, in other bunches or even by themselves in previous turns. Also, they emit synchrotron radiation in a random manner, which makes them lose energy and perturbs their movement with a recoil effect.

The description of the dynamics of the stored particles begin with an approximation that neglects the effects of their self-generated fields, i.e. their interaction with each other, with the vacuum chamber and with the residual molecules in their atmosphere. In this framework the only forces acting on the particles are the magnetic fields of the dipoles and multipoles and the longitudinal electric field of the RF Cavity and the only way they can lose energy is through synchrotron radiation emission. Under such conditions, the one-turn map of the ring defines a fixed point in the phase space defined in equation (2.3) and the particles oscillate around it, being the oscillations in the planes $\{x, x'\}$, $\{y, y'\}$ and $\{z, \delta\}$ practically uncoupled. The oscillations in the first two planes are called transverse oscillations, while the one in the third plane is denominated longitudinal oscillation.

For current synchrotrons, the dynamics of the longitudinal motion is much slower than the dynamics of the transverse motion. As an example, in the Sirius storage ring particles take approximately 215 revolutions around the ring to complete one turn around the fixed point in the longitudinal direction while they oscillate 49 times per revolution around the fixed point in the transverse plane. This property makes it possible to separate the study of the longitudinal plane from the transverse one, considering the energy deviation of one particle as a constant parameter in the transverse equations of motion. The effects of the radiation energy loss are even slower than the longitudinal motion, taking a few thousands of turns in the ring to significantly change the transverse motion.

Neglecting the energy variations of the particles, and the randomness of the radiation emission, the motion of the particles can be described by a Hamiltonian in the Frenet-Serret coordinate system defined by the ideal orbit. Considering the paraxial motion of the particles around the closed orbit, this Hamiltonian can be simplified to a quadratic form in the momentum coordinates. See, for example, the second chapter of Lee (1999, pp. 32) book.

This Hamiltonian generates four first-order coupled and non-linear equations of motion for the transverse coordinates that accurately describe the short and mid-term stability of the particles. Most of the non-linearities and coupling in these equations come from the magnetic fields of the magnets along the ring, being the other contributor the curvature of the reference orbit and the energy deviation of each particle. At this stage of the simplification of the problem the dynamics of the electrons still is very complicated, mainly for storage rings such as Sirius, with several and very strong sextupoles that introduce chaos in the system in regions of the phase space that are surrounding the fixed point.

2.2.1 Linear Equations of Motion

With further approximations, considering only the terms of the equations of motion that are linear with the phase-space coordinates and ignoring all coupling between the two transverse directions, the analysis of the dynamics becomes simple, with analytic solutions to the equations of motion and physically significant parameterizations, that describes a given machine. With this simplification, the transverse movement of the electron is only dependent on the fields of dipoles and quadrupoles. Under such considerations, the Hamiltonian of an arbitrary particle stored in the ring is given by

$$H \approx \frac{x'^2}{2} + \frac{y'^2}{2} + \frac{G^2(s)}{2}x^2 + \frac{K(s)}{2}(x^2 - y^2) - G(s)x\delta \quad (2.6)$$

where it was normalized by the total momentum of the particle, p , and expanded up to second order in the transverse phase space coordinates, in such a way that only dipoles, $G(s)$, and quadrupoles, $K(s)$, contribute to the dynamics. Besides, the independent variable was changed from time to the longitudinal position of the particle along the Frenet-Serret frames, which is possible because it is a monotonic function of time in storage rings, allowing for easy inversion of derivatives. All the steps to get the equation above are described in detail in the literature (BENGTSSON, 1997; LEE, 1999; WIEDEMANN, 2007). The equations of motion will be:

$$\begin{aligned} x'' &= -\frac{\partial H}{\partial x} = -\left(K(s) + G^2(s)\right)x + G(s)\delta \\ y'' &= -\frac{\partial H}{\partial y} = K(s)y \end{aligned} \quad (2.7)$$

where the energy deviation dependent term in the horizontal equation of motion is the dispersion generated by the dipole.

Looking back at the beginning of this section and reviewing all the approximations, at first sight it seems that the region of validity of these linear equations is so limited that their understanding is useless. However that is not what is observed in practice, because storage rings are carefully designed to maximize the validity of this linear behavior: the

position, number and strength of all magnets are so well tuned that nonlinearities cancel each other. Another important point to justify the study of these linear equations is that for synchrotron radiation generation, the smaller the transverse size and divergence of the electron beam the better, which means most particles will stay for most of the time in a very small region of approximately hundreds of microns around the fixed point, where only the linear part of the one-turn map have a significant effect on the dynamics. Besides, if a particle experience large transverse oscillations and happens not to be lost, damping effects that arise due to synchrotron radiation emission will bring them close to the fixed point in a few dozens milliseconds.

2.2.2 Betatron Function and Phase Advance

The homogeneous part of the equations of motion presented in equation (2.7) can be cast in the following way:

$$u'' + K_u(s)u = 0 \quad (2.8)$$

where u can be both, x and y and $K_x = K(s) - G^2(s)$ and $K_y = -K(s)$. These equations are known as Hill equations and their solutions can be parametrized in the following form, as shown by Courant & Snyder (1958):

$$u(s) = \sqrt{2J\beta_u(s)} \cos(\mu_u(s) - \phi) \quad (2.9)$$

where $\beta_u(s)$ is called the betatron function and depends only on the magnetic lattice and $\mu_u(s)$ is called phase advance and its relation to the betatron function is given by

$$\mu'_u(s) = \frac{1}{\beta_u(s)}. \quad (2.10)$$

The constants ϕ and J depend on the initial conditions. It can be shown that:

$$J = \mathcal{H}(u(s), u'(s)) := \gamma_u(s)u^2(s) + 2\alpha_u(s)u(s)u'(s) + \beta_u(s)u'^2(s), \quad (2.11)$$

$$\text{with } \alpha_u(s) = -\frac{\beta'_u(s)}{2} \quad \text{and} \quad \gamma_u(s) = \frac{1 + \alpha_u^2(s)}{\beta_u(s)},$$

which represents the equation of an ellipse in phase space with J being the invariant area of such ellipse.

The relevance of this parameterization is that it conveys very important practical information regarding the properties and responses to perturbations of the beam that can be extracted directly from the betatron function. It can be seen from equation (2.9) that the maximum excursion a given particle can experience in a fixed longitudinal point of the ring is proportional to the square root of the betatron function. Analogously, the beam size of a distribution in equilibrium will also be proportional to the square root of the local

betatron function. Thus, the ratio between the amplitudes of movement in two different positions is proportional to the ratio of the square root of the betatron functions at the two locations, a property that is fundamental in the process of defining the transverse sizes of the vacuum chamber of a storage ring. For example, let us suppose the maximum betatron function of a lattice is 16 m at a place where the vacuum chamber has an internal dimension of 12 mm. This means that in another place where the betatron function is only 1 m the vacuum chamber can be much smaller, only 3 mm, without affecting the stored beam, which would allow the installation of devices that require smaller apertures. The name of this curve that defines the minimum aperture the vacuum chamber can have along the ring is called Beam Stay Clear (BSC).

Another important property that is related to the betatron function is the response of the beam to spurious electromagnetic fields. It can be shown that the larger the betatron function the larger the effect of such field in the beam dynamics. In the special case of dipolar fields, which are constant in the transverse plane, this dependency goes with $\sqrt{\beta(s_0)}$, for a quadrupolar field it is proportional to $\beta(s_0)$, for a sextupole $\beta^{3/2}(s_0)$ and so on. For example, the strategy of focusing the betatron function is commonly used in storage rings in straight sections where IDs are installed to minimize their effect on the optics. Besides, this also reduces the BSC which allow them to have smaller gaps and, consequently, stronger magnetic fields, which is desirable for radiation emission. In the case of Sirius, the focusing will happen in both planes, which will allow the installation of new types of devices, called the Delta undulators, with small gap in the vertical and the horizontal directions.

Besides the betatron function, another important advantage of the parameterization presented in equation (2.9) is the interpretation of the integral of the phase advance in one turn around the ring. This integral normalized by 2π defines the tune of the machine:

$$\nu_u = \frac{1}{2\pi} \oint ds \frac{1}{\beta_u(s)}. \quad (2.12)$$

The integer part of this number corresponds to the number of complete oscillations in the phase space the particles make after completing one turn in the ring. To interpret the fractional part it is important to note in equation (2.9) that the dislocation of a particle in a fixed longitudinal position in successive turns is a perfect senoid, independently of the parameterization:

$$u_i(s_0) = A_{u,0} \cos(2\pi\nu_u i - \phi_0). \quad (2.13)$$

where $A_{u,0}$ is a constant and the fractional part of the tune is identified as the natural frequency of oscillation. This means that resonances can be excited by any electromagnetic field along the ring with a frequency equal to the tune times the revolution frequency. This observation is paramount to understand the collective instabilities that will be studied in

this work. The electromagnetic fields generated by a bunch of particles interacts with other bunches and, because they have the same oscillation frequency, a collective oscillation emerges due to resonance. This mechanism can even happen in a single bunch, where oscillations of the head of the bunch drives the tail to ever larger oscillations.

Additionally, resonances are also excited by static fields if the tune is a rational number, as long as these fields have the correct transverse spatial dependency. For example, if the fractional part of the tune is $1/2$ and there is a spurious constant quadrupolar field in some point of the ring, the kicks received by the particles in successive turns would always sum constructively and a resonance behavior would be excited. If both transverse planes of motion are considered it can be shown that if the tunes satisfy the equation:

$$m\nu_x + n\nu_y = p \quad (2.14)$$

where m , n and p are integers, resonances can be excited by static magnetic field around the ring. The number $r^2 = m^2 + n^2$ is called the order of the resonance, and the lower the order is, the higher its strength. If both m and n must be non-zero for the equation (2.14) to be true, then the resonance depends on the existence of coupling fields, where the position of the particle in one direction influences the kick in the other direction.

2.2.3 Dispersion Function

The inhomogeneous solution of the linear equations of motion can be written in the following form:

$$x_\delta(s) = \eta(s)\delta \quad (2.15)$$

where $\eta(s)$ is called dispersion function and, like the betatron function, depends only on the magnetic lattice. Note that this is a particular solution of the equation, where periodic conditions are imposed. This choice has an advantage over other solutions because of the meaning of the dispersion function: its value along the ring gives the shape of the averaged trajectory of a particle with non-zero energy deviation. In other words, this particular solution of the inhomogeneous equation gives the closed orbit for off-momentum particles.

The dispersion function is very important to determine the equilibrium emittance of a storage ring (WIEDEMANN, 2007, pp. 304),

$$\varepsilon_0 \propto \oint ds \frac{\mathcal{H}(\eta(s), \eta'(s))}{|\rho^3(s)|} \quad (2.16)$$

where the minimization of the functional $\mathcal{H}(\eta(s), \eta'(s))$ in the dipoles of the ring is one of the main goals when designing a storage ring. The dispersion function is also important for the calculation of the momentum compaction factor, α , which is the relative difference

in closed orbit path length per unit of energy deviation, δ ,

$$\frac{\Delta L}{L} \approx \delta\alpha := \delta \oint ds \frac{\eta(s)}{\rho(s)}. \quad (2.17)$$

This parameter, which in general is positive, is of fundamental importance for the longitudinal dynamics, because it couples linearly the time it takes for the particles to complete one turn in the ring with their energy deviation. Notice that the only sections of the ring which contribute to the integral those are where the reference orbit is curved (in other places the radius is infinity) and this is because particles with more/less energy generally follow paths with larger/smaller radius in the dipoles, which increases/decreases the path length.

2.2.4 Action–Angle Variables

Finding the action angle variables for a given Hamiltonian is equivalent to solving the equations of motion, due to the simple time, or s , evolution of such variables. For Hamiltonians with one elliptic fixed point, this task is achieved by performing canonical transformations in the phase space variables that brings them to the normal form, where the movement is a simple harmonic oscillator. Then, the radius in phase space is an invariant of motion and is recognized as the action. This procedure can be applied to the Hamiltonian of equation (2.6) by recognizing the dispersion orbit as a canonical transformation that changes the origin of the phase space (BERG, 1996, Appendix A2)

$$x(s) \rightarrow \overbrace{x(s) - x_\delta(s)}^{x_\beta}, \quad (2.18)$$

where $x_\delta(s)$ is given by equation (2.15), in such a way that the new Hamiltonian is purely a quadratic form, without the crossed term $x\delta$. This pure betatronic Hamiltonian can than easily be written in action-angle variables in the following way:

$$K = \frac{J_x}{\beta_x(s)} + \frac{J_y}{\beta_y(s)} \quad (2.19)$$

where J_x and J_y , defined by equation (2.11) are recognized as horizontal and vertical actions and the equation of motion shows that the angle variable, θ , is the phase advance, defined in equation (2.10):

$$J'_u = \frac{\partial K}{\partial \theta_u} = 0 \quad \text{and} \quad \theta'_u = \frac{\partial K}{\partial J_u} = \frac{1}{\beta(s)} = \mu'_u \quad (2.20)$$

These variables will be very important for this work, because the wake-fields will be included in the electron dynamics as perturbations to the Hamiltonian presented above.

2.2.5 Linear Map Formulation: Matrix Theory

An alternative way to describe the linear dynamics of a storage ring is via symplectic transfer matrices, where the evolution of the coordinates in phase space can be always written in the following form

$$\mathbf{u}(s) = \mathcal{M}_{s \leftarrow s_0} \mathbf{u}(s_0) \quad (2.21)$$

where $\mathbf{u}(s) = (u(s), u'(s))$ is vector of the coordinates in phase space and $\mathcal{M}_{s \leftarrow s_0}$ is the transfer matrix from points s_0 to s . This form of the time evolution of the coordinates can be obtained from equation (2.9) by derivation with respect to s and substitution of J and ϕ by the initial conditions $\mathbf{u}(s_0)$. After this procedure, it can be verified that \mathcal{M} can be written in normal form (BENGTSSON, 1997)

$$\mathcal{M}_{s \leftarrow s_0} = \mathcal{A}(s) \cdot \mathcal{R}(\mu_{s \leftarrow s_0}) \cdot \mathcal{A}^{-1}(s_0) \quad (2.22)$$

where \mathcal{A}^{-1} is a transformation matrix to the normalized coordinates and R is a rotation matrix in these coordinates, given by

$$\mathcal{A}(s) = \begin{bmatrix} \sqrt{\beta_u} & 0 \\ -\frac{\alpha}{\sqrt{\beta_u}} & \frac{1}{\sqrt{\beta_u}} \end{bmatrix}, \quad \text{and} \quad \mathcal{R}(\theta) = \begin{bmatrix} \cos(\theta) & \sin(\theta) \\ -\sin(\theta) & \cos(\theta) \end{bmatrix}, \quad (2.23)$$

and also satisfy the composition rule

$$\mathcal{M}_{s_2 \leftarrow s_0} = \mathcal{M}_{s_2 \leftarrow s_1} \cdot \mathcal{M}_{s_1 \leftarrow s_0} \quad (2.24)$$

where $\{s_0, s_1, s_2\}$ in this order are sequential positions along the ring. Besides, successive turns around the ring at some position s_0 are completely described by the one turn matrix, $\mathcal{M}(s_0)$:

$$\mathbf{x}_n = \mathcal{M}^n \cdot \mathbf{x}_0, \quad \text{with} \quad \mathcal{M}^n = \mathcal{A} \cdot \mathcal{R}^n(2\pi\nu) \cdot \mathcal{A}^{-1} = \mathcal{A} \cdot \mathcal{R}(2\pi n\nu) \cdot \mathcal{A}^{-1}. \quad (2.25)$$

This formulation of the linear transverse motion is very useful for numeric calculation of the evolution of the particles.

2.2.6 Chromaticity and Action Dependent Tune shift

The quadrupoles correct the chromatic effects in the orbit of the beam that are generated in the dipoles and the result of such a correction is the finite value of the dispersion function. However quadrupoles themselves are dispersive components, which means their focusing strengths depend on the energy of the particles. This dependency comes from higher-order terms of the Hamiltonian, not shown in equation (2.6), and causes an effect on the beam where particles with different relative energy offsets have different tunes.

The linear part of this dependency is called linear chromaticity, which, if not corrected, reduces the lifetime of the beam to a few seconds in most storage rings. For example, for the case of Sirius the chromaticity of the ring without sextupoles is ≈ -130 for the horizontal direction. This means that particles with an energy deviation of only 0.15 % would have a tune that is 0.2 smaller than the tune of a particle with zero energy deviation. As the energy deviation oscillates in the scale of hundreds of turns, this particle would almost certainly cross a resonance that would induce its loss. Considering the equilibrium energy spread of the Sirius storage ring is only half of this value, approximately 0.09 %, without chromaticity correction all particles with energy deviation above two sigma of this distribution would be lost. Besides this mechanism, negative chromaticities, even when they are small, make the beam more sensitive to collective instabilities driven by wake fields, as will be analysed later in this work.

The sextupoles are introduced in the machine to correct the linear chromaticity to positive values close to zero. After correction, these sextupoles change the higher-order chromatic terms and also introduce geometric aberrations, non-linearities in the dynamics of all particles that reduce the region around the fixed point where the beam is stable. The main contribution of this effect for the dynamics in the vicinity of the fixed point is the generation of a linear dependency of the tune of each particle with its action variable, J_u . Writing the linear expansion of the tune as a function of the energy deviation and the action we get:

$$\begin{aligned}\nu_x(\delta, J_x, J_y) &\approx \nu_{x,0} + \xi_x \delta + A_{xx} J_x + A_{xy} J_y \\ \nu_y(\delta, J_y, J_x) &\approx \nu_{y,0} + \xi_y \delta + A_{yy} J_y + A_{yx} J_x\end{aligned}\tag{2.26}$$

where ξ_x and ξ_y are the horizontal and vertical chromaticities, and A_{xx} , A_{yy} and $A_{xy} = A_{yx}$ are the action-dependent tune shifts.

These are the most important one-turn effects that impact on the mid and long-term dynamics of the electrons at small oscillation amplitudes, in such a way that if we average the Hamiltonian of equation (2.19) in one turn,

$$H_t(J_x, J_y) = \frac{1}{L_0} \oint ds K(s) = \frac{\omega_0}{c} (\nu_x J_x + \nu_y J_y),\tag{2.27}$$

they can be added to it simply by writing

$$\begin{aligned}H_t(J_x, J_y, \delta) &= \frac{\omega_0}{c} \left((\nu_{x,0} + \xi_x \delta) J_x + (\nu_{y,0} + \xi_y \delta) J_y + \right. \\ &\quad \left. A_{xx} \frac{J_x^2}{2} + A_{xy} J_y J_x + A_{yy} \frac{J_y^2}{2} \right).\end{aligned}\tag{2.28}$$

2.3 Longitudinal Dynamics

In the study of the transverse dynamics the time scale involved was of a few turns in the storage ring, which allowed us to treat the energy deviation of the particles

as another constant of motion. In this section the dynamics of the electrons in a few hundreds of turns will be analysed. In this scale the transverse betatron oscillations are averaged out and the longitudinal dynamics, which describes the path length and energy oscillations around the fixed point, has a well-defined natural frequency. The main factors that influence the movement in this scale are the small unbalances between the energy loss of the particles and their energy gain in the RF cavity and the revolution time variation due to the energy offset of the particles.

2.3.1 Changes in Revolution Time

When the energy of a particle changes its velocity is also modified, which contributes to the change of the revolution time. For most storage rings of SLSs this effect is negligible when compared to the change in path length described by equation (2.17), due to the ultra-relativistic regime in which these machines operate. This allows us to approximate the left hand side (l.h.s.) of equation (2.17) to the relative change in revolution time. Then, from one turn to another, the relative position of a particle will change by:

$$z_{n+1} = z_n + \delta_n \alpha L_0 \quad (2.29)$$

where n refers to the current turn and $n + 1$ to the next. L_0 is the nominal circumference of the ring.

2.3.2 The Energy Balance

It can be shown that the rate of energy loss of a particle due to synchrotron radiation emission is proportional to the inverse of square of the local curvature radius of the particle times the fourth power of its total energy (JACKSON, 1962, pp. 661: eq. 14.31). Translating this dependency to a storage ring, the energy loss in one turn depends on the magnetic fields of the lattice and on the energy deviation of the particle. For the ideal particle the average energy loss depends only on the magnetic field of the dipoles, but as the closed orbit for particles with non-zero energy deviation is different, its energy loss is also different, not only because of the intrinsic dependence of the emission, but also because of the slightly different magnetic fields it will experience in one turn. The combination of these effects can be modeled in the following linear approximation:

$$\Delta E_{\text{Rad}} \approx -U_0 - E_0 L_0 \alpha_z \delta_n \quad (2.30)$$

where U_0 is the energy loss of the ideal particle in one turn, E_0 is the nominal energy of the storage ring and the coefficient α_z includes both effects, the intrinsic dependence on the energy and the different orbit fields.

The energy gain of a particle in the RF cavity is given by the integral of the longitudinal electric field, $E_{||}$, along the path of the particle and depends only on the

initial phase of the field when it enters the cavity:

$$\Delta E = V(t_0) = q \int_0^{L_c} ds E_{\parallel}(s, t)|_{t=s/c+t_0} \quad (2.31)$$

where $V(t_0)$ is called the gap voltage of the cavity and L_c is its length.

Now let us assume the frequency of oscillation of the electromagnetic field inside the cavity, ω_{RF} , is exactly a multiple of the revolution frequency of the synchronous particle, ω_0 :

$$\omega_{RF} = h\omega_0 \quad (2.32)$$

where h is called harmonic number. With this assumption, even though the fields are time dependent, the synchronous particle will always see the same conditions as it enters the cavity. Now let us make a further assumption that the synchronous particle reaches the cavity in the exact time to gain energy U_0 from the cavity:

$$V(0) = U_0 \quad (2.33)$$

where the time reference on l.h.s. is relative to the position of the synchronous particle. Considering both assumptions and combining the energy gain in the cavity with the energy loss in one turn, given by equation (2.30), we get the following one turn energy balance for a storage ring:

$$\delta_{n+1} = \delta_n - L_0 \alpha_z \delta_n + \frac{V(z_{n+1}) - U_0}{E_0}. \quad (2.34)$$

where the subscript $n + 1$ in the particle position means that it will go around the ring first and then pass through the cavity.

2.3.3 Phase Stability Principle

Combining equations (2.29) and (2.34) we get the one turn map for the longitudinal plane for which the synchronous position and the nominal energy defines a fixed point. To analyse the stability of this fixed point let us linearize the map in its vicinity:

$$\begin{bmatrix} z_{n+1} \\ \delta_{n+1} \end{bmatrix} = \underbrace{\begin{bmatrix} 1 & \alpha L_0 \\ -V'_0 & 1 - L_0 \alpha_z - V'_0 \alpha L_0 \end{bmatrix}}_M \begin{bmatrix} z_n \\ \delta_n \end{bmatrix}. \quad (2.35)$$

where V'_0 is the derivative of the voltage gap in relation to the arrival time of the particles at the synchronous position normalized by the nominal energy of the ring, E_0 . It can be shown that the eigenvalues of the matrix M are given by the solution of the characteristic equation

$$\lambda^2 - \text{Tr}(M)\lambda + \text{Det}(M) = 0 \quad (2.36)$$

with $\text{Tr}(M) = 2 - L_0(\alpha_z - V'_0\alpha)$ and $\text{Det}(M) = 1 - L_0\alpha_z \approx 1$. This means that for the matrix to be stable, $|\text{Tr}(M)| \leq 2$ (COURANT; SNYDER, 1958), the derivative of the gap voltage must be positive/negative if α is positive/negative. To illustrate this condition, consider that initially a particle arrives at the cavity ahead of the synchronous particle, the positive derivative means it will gain more energy, which makes it take longer to go around the ring if the momentum compaction is positive, diminishing the difference of its arrival time to the synchronous particle for the next turn. This way all particles remain in an oscillatory movement around the fixed point with frequency given by

$$\text{Tr}(M) = 2 \cos(2\pi\nu_z) \approx 2 - (2\pi\nu_z)^2 \implies \nu_z \approx \frac{1}{2\pi} \sqrt{L_0\alpha_z + V'_0\alpha L_0}, \quad (2.37)$$

where ν_z is called synchrotron tune in analogy to the betatron tunes defined in subsection 2.2.2.

Additionally, the determinant of the one-turn matrix is $(1 - L_0\alpha_z)$, which implies the oscillations are damped, with α_z being the damping factor. In most storage rings this effect is small compared to the oscillation time, requiring thousands of turns to influence the dynamics.

The voltage gap has the same harmonic composition as a function of the arrival time as the electric field as a function of time. This means that the condition imposed in equation (2.32) implies that there are at least h stable fixed point along the ring and, as in general the voltage is a pure senoid, these are the only stable points. This means that it is possible to store up to h agglomerations of electrons, called bunches, in a storage ring.

2.3.4 The Potential Well

There is an important approximation to the map equations derived in the previous sections that consists in considering the turn by turn iterations as infinitesimal transformations and taking the limit to the continuum, considering differences between turns as derivatives. With this considerations, the equations of motion becomes:

$$\begin{aligned} \frac{dz}{ds} &= \alpha\delta(s) \\ \frac{d\delta}{ds} &= \alpha_z\delta(s) + \frac{V(z(s)) - U_0}{L_0E_0}. \end{aligned} \quad (2.38)$$

If the damping term is not considered, the equations of motion can be derived from a static Hamiltonian, given by:

$$H_{||} = \frac{\alpha}{2}\delta^2 - \overbrace{\int_0^z dw \frac{V(w) - U_0}{L_0E_0}}^{U(z)} \quad (2.39)$$

where the first term of the right hand side (r.h.s.) is the kinetic term and $U(z)$ is called the potential well, in an analogy with a potential energy. When the oscillations are small the potential well can be expanded in power series of the longitudinal position. Generally the RF cavity of storage rings are adjusted with each other in such a way that their potentials always sum constructively, creating a practically linear gap voltage $V(z)$ around the fixed point, which implies the Hamiltonian can often be approximated by

$$H_{\parallel} = \frac{\alpha}{2}\delta^2 + \frac{V'}{2L_0}z^2 \quad (2.40)$$

which is an harmonic oscillator, equivalent to the linear map of equation (2.35), if the damping is not considered. This harmonic Hamiltonian is often used for analytic treatments of instabilities because it is a good approximation for most RF systems and also due to the simple expressions of its action-angle variables (LINDBERG, 2016, sec. III):

$$H_{\parallel} = \frac{\omega_z}{c}J_z \quad \text{with} \quad z = \sqrt{\frac{2J_z\alpha c}{\omega_z}} \cos \theta_z \quad \text{and} \quad \delta = \sqrt{\frac{2J_z\omega_z}{\alpha c}} \sin \theta_z, \quad (2.41)$$

where $\omega_z = \omega_0\nu_z = \omega_0/2\pi\sqrt{V'_0\alpha L_0}$ is the synchrotron frequency.

2.4 Radiation Damping and Equilibrium Parameters

The synchrotron radiation emission is a quantum process that happens uncorrelatedly among all the electrons in the beam. While the average emission has a well defined and smooth behavior, such as the spectra that are calculated with classical electrodynamics for dipoles and IDs, a closer look into the individual emissions reveals the random nature of these events. As expected the effect this process generates on the beam is also dual, the average emission is responsible for energy loss and damping of the longitudinal and transverse oscillations, while the random character of single emission events generates uncorrelated motion in all planes that heat up the beam.

Both effects have very different dependencies on the parameters of the particles. For example, in the last section we used the fact that the energy loss depends linearly with the energy deviation of the particles, which caused an exponential damping of the oscillations, i.e. a damping proportional to the amplitude of the oscillation, while the heating in the longitudinal plane happens because the emissions are instantaneous and uncorrelated among electrons or in time, having no short term dependency on any parameter of the electrons, which generates random walks for the energy deviations. Because these effects have such different dependencies they always compete with each other, if the amplitude of oscillation is large the damping dominates, if it is small there is a blow up. It is this competition that generates the equilibrium energy distribution of the beam and consequently, due to the potential well, the longitudinal distribution. While the amplitude

of oscillation of each electron is in an endless variation, the average of all electrons in a bunch remains stationary, with both effects balancing each other out.

In the transverse plane the effect of the radiation emission on the dynamics is not as direct as in the longitudinal plane. Damping in the transverse plane is a two-fold effect: first the electrons lose transverse momentum due to radiation emission because the emission is mostly on the direction of motion. This does not change the normalized momentum of the electron, because the longitudinal momentum is also affected by this emission. In a second moment the electron passes through the RF cavity, where the longitudinal momentum is replenished but the transverse momentum is unchanged, which means the normalized transverse momentum is decreased. The net effect is an exponential damping of the transverse oscillations, proportional to the betatron action of the movement.

The excitations of oscillations happen in the horizontal plane because of the dispersion function in the dipoles. When an electron emits radiation its closed orbit abruptly changes, because its energy deviation has changed, however, as the position of the electron is the same as before, a betatron oscillation around the new closed orbit is excited. Again, both effects balance each other out in the equilibrium, defining a distribution and consequently the natural emittance of the storage ring. In the vertical plane, as the dispersion is ideally zero, the excitations are created by a much weaker mechanism and the natural vertical emittance is practically zero. This mechanism is related to the fact that the photon emission is not exactly in the direction of the momentum of the electrons, but with an angular aperture around it proportional to $1/\gamma$, which slightly changes the vertical momentum of the electron, exciting betatron oscillations. In real storage rings, residual vertical dispersion function from magnet errors and coupling fields that transfer part of the horizontal emittance to the vertical plane completely overshadow this process and define the vertical emittance of the beam.

2.4.1 Fokker-Planck Equation

All the arguments described in the last section can be mathematically described by modeling the evolution of the beam distribution in terms of the Fokker-Planck equation. In this framework we can consider the interaction of the electrons with the radiation they emit as large particles subjected to a weak random and Markovian force, with an approximately white spectrum. These are the conditions imposed on a system by the kinetic theory in order for the distribution function to be described by such equation, according to Landau & Lifshitz (1981), Wang & Uhlenbeck (1945), Zwanzig (2001).

There are several works that explain the use of the Fokker-Planck equation in storage rings (LINDBERG, 2016; SUZUKI, 1983; SUZUKI, 1986; LEE, 1999; WIEDEMANN,

2007). Here, only the main results will be presented:

$$\frac{\partial \Psi}{\partial s} + \{\Psi, H\} = \mathcal{F}(\Psi) \quad (2.42)$$

where $\Psi = \Psi(\mathbf{q}, \mathbf{p}, s)$ is the beam distribution in phase space, $\mathbf{q} = (x, y, z)$ and $\mathbf{p} = (x', y', \delta)$ are the position and momentum vectors,

$$\{\Psi, H\} = \frac{\partial \Psi}{\partial \mathbf{q}} \cdot \frac{\partial H}{\partial \mathbf{p}} - \frac{\partial \Psi}{\partial \mathbf{p}} \cdot \frac{\partial H}{\partial \mathbf{q}} \quad (2.43)$$

is the Poisson bracket between the Hamiltonian and the particle distribution, where the operators $\frac{\partial}{\partial \mathbf{q}}$ and $\frac{\partial}{\partial \mathbf{p}}$ are the gradients in relation to the positions and momenta of the phase space, and $\mathcal{F}(\cdot)$ is the Fokker-Planck operator for the accelerator, explicitly given by (LINDBERG, 2016, eq. 33)

$$\begin{aligned} \mathcal{F}(\Psi) = & \frac{2\alpha_z}{c} \left(\Psi + \delta \frac{\partial \Psi}{\partial \delta} \right) + D_z \frac{\partial^2 \Psi}{\partial \delta^2} + \\ & \frac{2\alpha_x}{c} \left(\Psi + J_x \frac{\partial \Psi}{\partial J_x} \right) + D_x \left(J_x \frac{\partial^2 \Psi}{\partial J_x^2} + \frac{\partial \Psi}{\partial J_x} + \frac{1}{4J_x} \frac{\partial^2 \Psi}{\partial \theta_x^2} \right) + \\ & \frac{2\alpha_y}{c} \left(\Psi + J_y \frac{\partial \Psi}{\partial J_y} \right) + D_y \left(J_y \frac{\partial^2 \Psi}{\partial J_y^2} + \frac{\partial \Psi}{\partial J_y} + \frac{1}{4J_y} \frac{\partial^2 \Psi}{\partial \theta_y^2} \right) \end{aligned} \quad (2.44)$$

where c is the speed of light, $\{J_x, \theta_x\}$ and $\{J_y, \theta_y\}$ are the action-angle variables of the horizontal and vertical planes, as defined in equation (2.11), and α_u and D_u are the damping and diffusion terms introduced by the radiation emission in the three planes of motion, for which Sands (1970) and Wiedemann (2007) derive explicit expressions.

Notice that equation (2.42) separates the hamiltonian forces in the l.h.s. and the dissipative and random forces in the r.h.s.. If the effect of radiation emission were not taken into account, the r.h.s. would be zero and the l.h.s. would be a statement of the Liouville Theorem for Hamiltonian flow, which in the accelerators physics community is also known as Vlasov Equation. For machines that operate with heavy particles, such as the colliders that use protons or ions, this is approximately true and the beam never reaches the equilibrium, but for storage rings of synchrotron light sources, which mostly employ electrons, the Fokker-Planck terms are very important to describe the behavior of the beam in time scales of the order of ms or higher, which are the scales where impedance related collective instabilities happen.

The Fokker-Planck equation can be used to calculate the equilibrium distribution of the beam. Considering the total Hamiltonian of the ring is given by the sum of equations (2.39) and (2.19),

$$H = \frac{J_x}{\beta_x} + \frac{J_y}{\beta_x} + \frac{\alpha}{2} \delta^2 + U(z), \quad (2.45)$$

the equilibrium distribution is a separable function in the three planes of motion because the H does not couple them. Besides, the horizontal distribution must be a function only

of the invariant J_x , the vertical of J_y and the longitudinal of H_{\parallel} , because they are the invariants of motion:

$$\Psi(\mathbf{q}, \mathbf{p}) = f_x(x, x')f_y(y, y')f_z(z, \delta) = f_x(J_x)f_y(J_y)f_z(H_{\parallel}). \quad (2.46)$$

With these considerations the distribution commutes with the total Hamiltonian and the l.h.s. of the Fokker-Planck equation, (2.42), is zero. From the r.h.s. it can be shown that

$$\Psi(\mathbf{q}, \mathbf{p}) = \overbrace{\frac{f_x}{\exp(-J_x/\varepsilon_x)} \cdot \frac{f_y}{\exp(-J_y/\varepsilon_y)}}^{2\pi\varepsilon_x} \cdot \overbrace{\frac{f_{\delta}}{\exp\left(-\frac{\delta^2}{2\sigma_{\delta}^2}\right)}}^{\sqrt{2\pi}\sigma_{\delta}} \cdot \overbrace{\frac{\lambda}{\exp\left(-\frac{1}{2\sigma_{\delta}^2}\frac{2}{\alpha}U(z)\right)}}^A \quad (2.47)$$

with

$$\varepsilon_x = \frac{cD_x}{2\alpha_x}, \quad \varepsilon_y = \frac{cD_y}{2\alpha_y}, \quad \sigma_{\delta} = \frac{cD_z}{2\alpha_z}, \quad (2.48)$$

where ε_x and ε_y are the horizontal and vertical emittances, σ_{δ} is the energy spread of the beam and A is a normalization constant such that

$$\int dz' \lambda(z') = 1 \quad (2.49)$$

It is easy to see that the beam vertical size is given by

$$\sigma_y^2(s) = \langle y^2 \rangle = 2\beta_y(s) \int d\theta_y \cos^2(\theta_y) \int dJ_y f_y(J_y) J_y = \beta_y \varepsilon_y \quad (2.50)$$

and that for the horizontal plane the canonical transformation that shifted the off-momentum fixed point, represented by equation (2.18), must be taken in account:

$$\sigma_x^2 = \langle (x + \eta\delta)^2 \rangle = \langle x^2 \rangle + \langle 2x\eta\delta \rangle + \eta^2 \langle \delta^2 \rangle = \beta_x \varepsilon_x + \eta^2 \sigma_{\delta}^2. \quad (2.51)$$

For the longitudinal plane, in the simple case of a quadratic potential well, as described by equation (2.40), we have

$$\sigma_z^2 = \int dz' \lambda(z') z'^2 = \frac{1}{A} \int dz' \exp\left(-\frac{V'}{2L_0\alpha\sigma_{\delta}^2} z'^2\right) z'^2 = \sigma_{\delta}^2 \frac{L_0\alpha}{V'} = \sigma_{\delta}^2 \frac{c^2\alpha^2}{\omega_z^2}. \quad (2.52)$$

3 WAKES AND IMPEDANCES

The main aspects of single-particle dynamics, governed by the guiding electromagnetic fields generated by the magnets and the RF cavity, were analysed in the last chapter. The effects of the radiation emission on the particle that generated this radiation were also considered, and concepts such as equilibrium distribution of particles, emittance and energy spread were introduced; however, no interaction among the particles in this distribution was considered. Besides the external fields, the self-generated fields, fields induced by the stored particles, are important to characterize the dynamics when the intensity of the beam becomes large. These fields have different effects on the beam depending on how the interaction happens. In this chapter we will study the theory of wake fields, analysing its main definitions and modeling.

3.1 Wake Fields

Even though the mechanism behind the interaction among the stored particles through wake fields is very simple to describe qualitatively, a quantitative self-consistent description is very difficult. The main difficulty comes from the fact that ME should be solved using the vacuum chamber of the whole ring being subjected to a source, the beam, that is varying due to external fields and the self-generated fields we want to determine. In order to tackle this problem self-consistency must be forgotten and approximations must be done.

The first approximation is to consider that all the properties of the materials that compose the vacuum chamber are linear in relation to the intensity of the fields. This linearity combined with the linearity of the ME allow us to solve the electromagnetic fields for a single source particle and sum over the beam to get the desired result. Another approximation consists in breaking the storage ring in several small parts that do not interact with each other, which allow us to solve ME for each part independently. This approximation is valid for storage rings because generally the irregularities or transitions in the vacuum chamber are far from each other in such a way that the fields generated in one of them cannot propagate to the other.

The two approximations described above already greatly simplifies the problem, but in order to make it tractable other two are needed: the rigid beam and the impulse approximations. The rigid beam approximation consists in considering that when the particles are passing through a component that generates wake fields they always move in straight lines parallel to each other with constant and equal speeds. Applying this approximation to the particles that generates the wake fields allows for a simple algorithm

to solve the ME for any structure, because it defines that the source of the fields is a particle moving straight in the longitudinal direction with constant speed. As the boundary conditions are imposed by the walls of the chamber, the whole problem becomes well defined. The impulse approximation consists in saying that the effect of the wake fields of a structure on the particles is only to change their momentum after the whole process and this change in momentum is given by the integral from minus infinity to infinity of the Lorentz Force on the unperturbed trajectory of the particle. Combining this approximation with the rigid beam, we see that the integral must be performed parallel to the source particle at a fixed distance from it.

To clarify these approximations, let us express them mathematically. First, consider a particle with charge Q and velocity v moving in the vacuum chamber. The ME for the fields generated by this particle are given by:

$$\begin{aligned}\boldsymbol{\nabla} \cdot \mathbf{D} &= Q\delta(x - x_0)\delta(y - y_0)\delta(s - vt) \\ \boldsymbol{\nabla} \cdot \mathbf{B} &= 0 \\ \boldsymbol{\nabla} \times \mathbf{E} &= -\frac{\partial \mathbf{B}}{\partial t} \\ \boldsymbol{\nabla} \times \mathbf{H} &= Qv\hat{\mathbf{s}}\delta(x - x_0)\delta(y - y_0)\delta(s - vt) + \frac{\partial \mathbf{D}}{\partial t}\end{aligned}\tag{3.1}$$

where $\delta(\cdot)$ is the Dirac's Delta function, x_0 and y_0 defines the transverse displacement of the source particle, $\hat{\mathbf{s}}$ is the unitary vector that defines the longitudinal direction and

$$\mathbf{D}(t) = \int_{-\infty}^{\infty} dt' \varepsilon(t - t') \mathbf{E}(t')\tag{3.2}$$

$$\mathbf{B}(t) = \int_{-\infty}^{\infty} dt' \mu(t - t') \mathbf{H}(t'),\tag{3.3}$$

where ε and μ simplifies to the electric permittivity and magnetic permeability of the vacuum in the region inside the vacuum chamber where the source particle is, but can be any causal function that describes the dynamics of the materials of the wall. Combining these equations with the boundary conditions of continuity of the perpendicular components of \mathbf{D} and \mathbf{B} and of the tangential components of \mathbf{H} and \mathbf{E} , the problem is well defined and there is an unique solution for \mathbf{E} and \mathbf{B} inside the vacuum chamber. For the case when the chamber is considered as a Perfect Electric Conductor (PEC), the fields inside the wall are zeroed by surface charge and currents in the inner wall, as described by Jackson (1962, sec. I.5).

If a witness particle with charge q experiences these fields in agreement to the approximations made before, its momentum change is expressed by

$$\Delta \mathbf{p}(\rho_s, \rho_w, z) = \int_{-\infty}^{\infty} dt \mathbf{F}(\rho_s, \rho_w, s, t)|_{s=vt-z},\tag{3.4}$$

where ρ_w and ρ_s are the transverse positions of the witness and source particles, respectively, and z is the distance the witness particle is behind the source. The Lorentz force

in this case is given by

$$\mathbf{F} = q(E_s \hat{\mathbf{s}} + (E_x + vB_y) \hat{\mathbf{x}} + (E_y - vB_x) \hat{\mathbf{y}}). \quad (3.5)$$

All the conditions imposed above to simplify the problem are referred as zeroth-order approximations by Stupakov (2000), which indeed they are in the sense that they define the minimum level of complexity the analysis of wake fields must contain to explain the behavior of the beam. However, most of the considerations are well justified, for example, the assumption of linearity of the materials is justified by the fact that the intensities of the fields involved are not large compared to the saturation curves of the materials, in such a way that linearization of the responses is always possible. For example, the magnetic field of in-vacuum IDs is generated by ferromagnetic blocks placed with alternating magnetization direction along the beam trajectory. Generally there is a very thin copper foil between the blocks and the beam environment shielding the blocks from the self-generated fields of the beam, however very low frequency fields can penetrate the foil and reach the blocks, which makes them important for the determination of such fields and the effects on the beam. This was the case presented by Blednykh *et al.* (2016) where a model for the wakes was built from the linearization of the response of such materials and a good agreement with beam measurements was achieved.

The approximation of breaking the ring in small parts which contribute independently to the whole budget of wake in the machine is always revisited by people responsible for simulating the components of new machines. In several occasions, where elements that introduce variations in the vacuum chamber transverse profile are close to each other, they are simulated together to check if there is mutual interference. Apart from some cases where the elements have resonances with similar frequencies, the results show that one simulation with both components is equal the sum of them simulated separately.

The impulse approximation is also justified by the small effect these fields have on the dynamics of the beam in a single pass. Actually this approximation is recurrent in accelerator physics simulations; models for IDs and multipoles, such as quadrupoles and sextupoles, are very common under this assumption. Even for these components, which are stronger than wake fields, the results are a good approximation to the more detailed simulation with thick components.

There are two different aspects of the rigid-beam approximation that must be analysed separately in order to justify it. The first is the consideration that the witness particle is always at a fixed distance z behind the source particle. This approximation is very good for any storage ring because as the particles are ultra-relativistic, their velocity is close to the light speed and even with a considerable energy difference between the particles, their velocity difference is negligible. Additionally, the typical energy variation inside a bunch is very small, on the order of 0.1 %.

The second aspect is related to the consideration that the particles traverse the structure parallel to the axis, because, in principle, sloping straight trajectories could also be considered and the momentum gain would be dependent on the angles x' and y' of the source and the witness particle. An inclined trajectory of the source particle could generate different electromagnetic fields in the structure, because the coupling between the two would be affected. Besides, an inclined trajectory of the witness particle would make it sample different fields, yielding different momentum changes. There is a study in the literature by Danilov (2000) where the author calculates the angular wake for a stripline and an experimental work from the same author (DANILOV *et al.*, 1993) where a current-dependent damping of the oscillations is measured at the 120 MeV injection energy for the BEP electron storage ring. There are also some other related studies in the literature (JONES *et al.*, 1998). However, there is no strong experimental evidence of the importance of such effect in the total impedance budget of a storage ring, probably because of the paraxial nature of the movement of the particles.

One interesting feature of the impulse approximation is that, even though the interaction between two particles via wake fields does not respect Newton's third law (action-reaction) and, consequently, cannot be cast into an Hamiltonian formulation, the mean-field interaction, where the degrees of freedom of all the source particles of the beam are averaged out, does respect the Hamilton equations, because, as can be seen in equation (3.4), the change in momentum of the witness particle depends only on its position.

3.2 Wake Functions

The approximations performed in the last section led to a formula to describe the change in momentum of the witness particle and to a method of how to include this momentum change in the dynamics of this particle. In summary, everything we need to know in order to compute the effect of the wake fields are already defined, we just need to compute the total momentum variation for each particle due to the action of all the other particles. In this process it is useful to define functions that are independent of the charge of the particles involved, being dependent only on the structure that generates the wake fields. These functions are called wake functions, or simply wakes, and are defined by

$$(w_x, w_y, w_s) = \frac{v}{qQ} (\Delta p_x, \Delta p_y, -\Delta p_s), \quad (3.6)$$

where the components of $\Delta \mathbf{p}$ are given by equation (3.4). The wake function has units of energy per square charge, which is VC^{-1} in SI. The minus sign in the definition of the longitudinal wake is introduced so that positive values have an interpretation of energy loss when both charges have the same sign.

3.3 The Wake Potential

With the approximations performed in the section 3.1 together with the restrictions imposed on the electromagnetic fields by the ME it is possible to show that the wake functions can be derived from a scalar potential function, called wake potential. To show this, we will use the same approach described by Stupakov (2000), that is credited to Alex Chao. The Lagrangian of the witness particle is

$$L = -mc^2\sqrt{1 - \frac{v^2}{c^2}} + q\mathbf{A} \cdot \mathbf{v} - q\phi, \quad (3.7)$$

where \mathbf{A} is the potential vector of the electromagnetic fields defined in equation (3.1) and ϕ is the scalar potential of the same fields. Inputting this Lagrangian into the Euler-Lagrange equation we get

$$\frac{d}{dt}(\mathbf{p} + q\mathbf{A}) = q\nabla(\mathbf{A} \cdot \mathbf{v} - \phi), \quad (3.8)$$

where ∇ denotes derivation with respect to the witness particle position. Integrating the equation above with the considerations made in section 3.1 we get

$$\frac{qQ}{c}\nabla_R W := \Delta\mathbf{p} = q \int_{-\infty}^{\infty} dt \nabla(vA_s - \phi). \quad (3.9)$$

where $\mathbf{R} = (x_w, y_w, -z)$ and $W = W(\boldsymbol{\rho}_s, \boldsymbol{\rho}_w, z)$ is the wake potential and it is assumed that the velocity of the particle is in the longitudinal direction. It was also considered that the fields go to zero at infinity. It can be checked that the wake functions as defined in equation (3.6) are obtained from the wake potential:

$$w_s = -\frac{\partial W}{\partial(-z)} = \frac{\partial W}{\partial z}, \quad \mathbf{w}_{\perp} = \nabla_{w,\perp} W, \quad (3.10)$$

and, as $W \in \mathbb{C}^\infty$, we have the following equality

$$\frac{\partial \mathbf{w}_{\perp}}{\partial z} = \nabla_{w,\perp} w_s. \quad (3.11)$$

which is known as Panofsky-Wenzel theorem. It is also possible to show that in the ultra-relativistic limit, $v \rightarrow c$, the wake potential is an harmonic function of the transverse coordinates of the witness particle (STUPAKOV, 2000)

$$\nabla_{w,\perp}^2 W = \frac{\partial^2 W}{\partial x_w^2} + \frac{\partial^2 W}{\partial y_w^2} = 0, \quad (3.12)$$

and, if perfect conducting walls are assumed at the ends of the structure, it is also an harmonic function with respect to the transverse coordinates of the source particle (ZAGORODNOV *et al.*, 2015)

$$\nabla_{s,\perp}^2 W = \frac{\partial^2 W}{\partial x_s^2} + \frac{\partial^2 W}{\partial y_s^2} = 0. \quad (3.13)$$

These properties are very important for calculating wake functions numerically and will be used later in this work. The Panofsky-Wenzel theorem, for example, is employed in three-dimensional simulations to calculate all wake functions from the longitudinal electric field, because the longitudinal wake function depends only on this component of the field, as given by equation (3.5). Then, from equation (3.11) we have:

$$\mathbf{w}_\perp = \int_{-\infty}^z dz' \nabla_\perp \left(\frac{c}{qQ} \int_{-\infty}^{\infty} dt E_s|_{s=ct-z'} \right). \quad (3.14)$$

3.4 The "Causality" Principle

When we take the ultra-relativistic limit, $v \rightarrow c$, all the wake fields generated by a particle can only influence particles that are behind it, no particle ahead will suffer its influence. This is equivalent to saying that the wake potential must satisfy the condition

$$W(\boldsymbol{\rho}_s, \boldsymbol{\rho}_w, z) = 0, \quad \forall z < 0, \quad (3.15)$$

which also directly applies to the wake functions. This condition is known in literature as causality principle and, even though it is only an approximation for the real machine, most calculations of wake functions for the ring components are performed under this assumption, including all the refined results obtained of the solutions of the ME by numeric solvers.

The main idea of this approximation is that, since the direct field of an ultra-relativistic particle is in the same transverse plane as the particle itself, the wake fields generated by an imperfection in the vacuum chamber are created at the exact same time this particle passes through the longitudinal position where this imperfection is located. As both, particle and wake field wave front have the same speed, the latter cannot catch up with the first.

Even though this is a good approximation for real beams stored in SLS storage rings and it generally simplifies the calculations and even enables the use of specific algorithms to compute the effects on the beam, in this work we will not assume this approximation for any of the wakes used and all the algorithms to be developed will work with causal and non-causal wakes. The main reason for this consideration is that all the raw effective wakes from the time domain solvers of the ME do not respect the causality condition, because they are calculated from finite-length charge distributions. The causal impedances are only obtained after post-processing the data and the point-charge wakes, or Green functions, can only be accessed through fitting, which makes it very practical to use the raw effective wakes in simulations.

Besides, this formalism of wake functions is very general and can be applied in the modeling of other sources of collective effects, such as the interaction of the beam with ions

in the vacuum chamber (WANG *et al.*, 2013) or to model the effect of CSR on the beam. While the wakes of the former case also respect causality, the later case, in a completely the opposite way, is zero behind and non-zero ahead the source particle (DERBENEV *et al.*, 1995).

3.5 Expansion of the Wakes

For most applications we are interested in knowing the wake functions only in a domain very close the center of the vacuum chamber, with ρ_s and ρ_w much smaller than the characteristic transverse dimension of the vacuum chamber, which allow us to expand the wake potential in its transverse coordinates and keep only the low-order terms

$$W(\rho_s, \rho_w, z) \approx W_0 + \rho_s^T \cdot \mathbf{M}_s + \rho_w^T \cdot \left(\mathbf{M}_w + \mathcal{D} \cdot \rho_s + \frac{1}{2} \mathcal{Q} \cdot \rho_w \right) \quad (3.16)$$

where W_0 , \mathbf{M}_s , \mathbf{M}_w , \mathcal{D} and \mathcal{Q} are coefficients of the expansion that depend only on the longitudinal position z , being \mathcal{Q} and \mathcal{D} symmetric matrices and $Q_{11} = -Q_{22}$ due to equation (3.12). Expanding the wake functions in first order we get

$$w_s \approx W'_0 + \rho_s^T \cdot \mathbf{M}'_s + \rho_w^T \cdot \mathbf{M}'_w \quad (3.17)$$

$$\mathbf{w}_\perp \approx \mathbf{M}_w + \mathcal{D} \cdot \rho_s + \mathcal{Q} \cdot \rho_w \quad (3.18)$$

where the prime indicates derivation with respect to z .

All these components have different effects on the beam and some of them are more important than others. The component W'_0 generally is the only term of the expansion of w_s that is considered in calculations because it dominates the rest of the expansion. So this term is responsible for all the longitudinal effects on the beam, including average energy loss, potential well-distortion, hence bunch-lengthening and bunch-shortening, coupled bunch oscillations, and even energy spread increase in some cases. For this reasons, from now on, the term longitudinal wake will always refer to W'_0 unless otherwise specified.

The vectors \mathbf{M}_s and \mathbf{M}_w are generally referred to as monopolar wakes, because they generate a transverse wake that is independent of the transverse displacement of the particles. The effect these wakes can cause on the beam is to change its closed orbit as a function of the beam current which is a static effect and cannot lead to instabilities. In addition, for most practical cases these terms are zero due to symmetries in the vacuum chamber.

The elements of the matrix \mathcal{D} are referred to as dipolar wakes, because they are generated due to dipole displacements of the source particle. Specifically \mathcal{D}_{11} and \mathcal{D}_{22} are called horizontal and vertical dipolar wakes, respectively. They are responsible for all the transverse instabilities that leads to coupled oscillations of the bunches, emittance deterioration and even beam loss. Besides, they can also induce coherent tune shifts, a

concept that will be described later. These terms are dangerous because they create a mechanism for oscillations of the source particles to induce oscillations on the witness particle and this force is always resonant because both particles have approximately the same tune. The term $\mathcal{D}_{12} = \mathcal{D}_{21}$ is zero in most cases due to symmetries in the vacuum chamber, but even when it is non-zero it does not induce any significant effect on the beam because, as generally the fractional part of the horizontal and vertical tunes are different, oscillations in one plane do not drive oscillations in the other.

The coefficients \mathcal{Q}_{11} and \mathcal{Q}_{22} are called detuning or quadrupolar wakes because the force they induce has the same characteristics of a quadrupole. In the ultra-relativistic limit $\mathcal{Q}_{11} = -\mathcal{Q}_{22}$ which is the basic property of the quadrupole strengths in the horizontal and vertical plane and, as expected from a quadrupole, they generate tune shifts in the beam as a function of current. The same analysis made for the coefficient \mathcal{D}_{12} applies for the term \mathcal{Q}_{12} .

As mentioned above, some components of the wake expansions are zero depending on the properties of the vacuum chamber. This is a consequence of the fact that the wake potential must preserve all the symmetries of the vacuum chamber. For example, the standard vacuum chamber used in the Sirius storage ring is a round straight tube, which is a particular case of a cylindrical symmetry. For this type of symmetry all the components of \mathbf{M}_s , \mathbf{M}_w and \mathbf{Q} must be zero and the only components of \mathbf{D} different from zero are the horizontal and vertical dipolar wakes and they must be equal to each other. Thus we conclude that most of the resistive wall of the Sirius storage ring will not induce quadrupolar wakes nor any type of skew effect and that there will be no significant orbit distortions as a function of current. Besides, considering that most of the components installed in the ring, such as bellows and BPMs only slightly break this symmetry, we can expect that the behavior of the beam in the horizontal and vertical planes will be very similar, where the differences will mostly be due to asymmetries in the single-particle dynamics.

Taking into consideration what was discussed above, we can rewrite the expansion of the wakes in equations (3.16) and (3.17) keeping only the most important terms:

$$W(\rho_s, \rho_w, z) = W_0(z) + x_w (W_X^D(z)x_s - W^Q(z)x_w) + y_w (W_Y^D(z)y_s + W^Q(z)y_w) \quad (3.19)$$

and, consequently

$$\begin{aligned} w_s(z) &= W'_0(z) \\ w_x(x_s, x_w, z) &= W_X^D(z)x_s - W^Q(z)x_w \\ w_y(y_s, y_w, z) &= W_Y^D(z)y_s + W^Q(z)y_w \end{aligned} \quad (3.20)$$

where $W_X^D = D_{11}$, $W_Y^D = D_{22}$ and $W^Q = -Q_{22}$ and the ultra-relativistic approximation was considered.

3.6 Impedances

As already mentioned in the beginning of section 3.2 all the tools needed to model the effect of the wake fields on the beam are described in section 3.1, however it is useful to define some other concepts such as the wake functions or the wake potential because they facilitate and uniformize the formalism. The impedance is another one of these concepts, introduced by Vaccaro (1966) to explain instabilities in the ISR ring at European Organization for Nuclear Research (CERN). It is proportional to the Fourier transform of the wake functions with respect to the longitudinal coordinate, z , and it is very useful in any kind of analytic calculation of instabilities, or even in the determination of the wake functions. Besides, due to the fact that we are interested in the effects of wake fields for storage rings which are intrinsically periodic, the impedance reveals properties that are difficult to infer looking at the wake itself.

There are several different definitions of impedances in the literature. In this work we will adopt the definitions of Chao (1993), Stupakov (2000), Heifets & Kheifets (1991):

$$\begin{aligned} Z_{\parallel}(\omega) &:= \frac{1}{c} \int_{-\infty}^{\infty} dz W'_0(z) e^{i\omega z/c} \\ Z_x^D(\omega) &:= -\frac{i}{c} \int_{-\infty}^{\infty} dz W_X^D(z) e^{i\omega z/c} \\ Z_y^D(\omega) &:= -\frac{i}{c} \int_{-\infty}^{\infty} dz W_Y^D(z) e^{i\omega z/c} \\ Z^Q(\omega) &:= -\frac{i}{c} \int_{-\infty}^{\infty} dz W^Q(z) e^{i\omega z/c} \end{aligned} \quad (3.21)$$

where $Z_{\parallel} \equiv Z_s \equiv Z_L$ is the longitudinal impedance, Z_x^D and Z_y^D are the horizontal and vertical dipolar impedances and Z^Q is the quadrupolar, or detuning, impedance. In other references, such as in the book of Zotter & Kheifets (1998), the impedance is the conjugate complex of the definitions presented here. The wakes can be obtained back from the impedances by the inverse transforms

$$\begin{aligned} W'_0(z) &= \frac{1}{2\pi} \int_{-\infty}^{\infty} d\omega Z_{\parallel} e^{-i\omega z/c} \\ W_t(z) &= \frac{i}{2\pi} \int_{-\infty}^{\infty} d\omega Z_t e^{-i\omega z/c}, \end{aligned} \quad (3.22)$$

where W_t and Z_t denote any of the transverse wakes and impedances. Considering that the wakes are real functions, the impedances must satisfy

$$Z_{\parallel}(\omega) = Z_{\parallel}^*(-\omega) \quad (3.23a)$$

$$Z_t(\omega) = -Z_t^*(-\omega), \quad (3.23b)$$

or simply, the real part of the longitudinal impedance must be an even function of the frequency and the imaginary part must be an odd function, while for the transverses impedances the opposite is valid: the real part is odd and the imaginary part is even.

Impedances have several other interesting mathematical properties, as presented by Chao (1993). For example, when the wakes satisfy the causality condition the real and imaginary parts of the impedance obey Kramers–Kronig relations (KRONIG, 1926), also known as Hilbert transforms.

It is interesting to note that instead of defining the impedances by the set of equations (3.21) we could have defined one generalized impedance from the wake potential

$$Z(\boldsymbol{\rho}_s, \boldsymbol{\rho}_w, \omega) = -\frac{i}{c} \int_{-\infty}^{\infty} dz W(\boldsymbol{\rho}_s, \boldsymbol{\rho}_w, z) e^{i\omega z/c} \quad (3.24)$$

and the impedances could be derived simply by considering its expansion in the transverse coordinates:

$$Z(\boldsymbol{\rho}_s, \boldsymbol{\rho}_w, \omega) = \frac{c}{\omega} Z_{\parallel} + x_w (Z_x^D x_s - Z^Q x_w) + y_w (Z_y^D y_s + Z^Q y_w). \quad (3.25)$$

3.7 Potential of Bunches of Particles

Now that all the important tools for describing the wake field effects were introduced we will calculate the change in momentum that a specific particle inside a bunch will feel due to the action of all the other particles. To do that we will assume that in the whole ring there is only one source of impedance, localized at a given point of the accelerator, and that the vacuum chamber is perfectly aligned with the reference orbit of the storage ring in such a way that a particle that is on the reference orbit also is at the origin of the expansion made in equation (3.16). The synchronous position will be adopted as the origin of the longitudinal coordinate and the positions of the particles will be measured with respect to it, in agreement to the definitions of section 2.3.1, specifically to equation (2.5), where particles behind the synchronous particle have positive deviations. Under such assumptions we get:

$$V(\boldsymbol{\rho}_i, z_i) = \sum_j W(\boldsymbol{\rho}_j, \boldsymbol{\rho}_i, z_i - z_j) \quad (3.26)$$

where $V(\boldsymbol{\rho}_i, z_i)$ is denominated effective wake potential, because it is the net effect of the average of the point-charge wake potential over the bunch and the indices i and j are related to the witness and the source particles respectively. Notice the summation above is very difficult to evaluate for a real beam, because in every bunch there are dozens of billions of electrons. Moreover, this sum does not highlight properties of the beam such as time dependence. If the beam is in equilibrium or is slowly varying the l.h.s. of equation (3.26) is approximately the same for successive turns in the ring, or over several passages by the impedance source, but each term of the r.h.s. can be very different from one turn to another, which means the sum must always be carried out. For all these reasons, it is important to make an approximation and consider that the effective wake

potential experienced by each particle is an integral over the beam distribution:

$$V(\boldsymbol{\rho}, z, s) = \int d\boldsymbol{p} \int d\boldsymbol{\rho}' \int dz' \Psi(\boldsymbol{p}, \boldsymbol{\rho}', z'; s) W(\boldsymbol{\rho}', \boldsymbol{\rho}, z - z') \quad (3.27)$$

where $\boldsymbol{p} = (x', y', \delta)$ represents the momentum coordinates and Ψ is beam probability density distribution function in phase space, which is time dependent in the general case and is normalized to one.

3.7.1 Multi-Turn and Multi-Bunch Effects

The equation (3.27) is not general enough to take into account all the wake field forces on the particles. In some cases the wakes persist for so long that they last for a time equivalent to several turns in the ring, acting on the same particles that generate the fields in successive turns. Generally these wakes are generated by cavity-like structures in the vacuum chamber that trap their electromagnetic eigen-modes for long times. In this situation we must add a sum over the distribution in previous turns

$$V(\boldsymbol{\rho}, z, s) = \sum_{k=-\infty}^{\infty} \int d\boldsymbol{p} \int d\boldsymbol{\rho}' \int dz' \Psi(\boldsymbol{p}, \boldsymbol{\rho}', z'; s - kL_0) \times \\ W(\boldsymbol{\rho}', \boldsymbol{\rho}, z - z' + kcL_0) \quad (3.28)$$

where the sum can be extended to infinity because the wake-potential is zero for relative positions between the source and the witness particles when there is no interaction between them. For example it does not make sense for a particle to feel the wake field it generates in the next turn. This means the wake potential must be zero for large negative values of $z - z'$. Yet, in the most general case, there is more than one bunch stored in the ring, which means it is also necessary to take the influence of other bunches into account

$$V_n(\boldsymbol{\rho}, z, s) = \sum_{l \in \mathcal{B}} \frac{I_l}{\langle I \rangle} \sum_{k=-\infty}^{\infty} \int d\boldsymbol{p} \int d\boldsymbol{\rho}' \int dz' \Psi_l(\boldsymbol{p}, \boldsymbol{\rho}', z'; s - s_r) \times \\ W(\boldsymbol{\rho}', \boldsymbol{\rho}, z - z' + s_r) \quad (3.29)$$

where

$$s_r = kL_0 - (s_l - s_n) \quad (3.30)$$

is the retarded position defining when the wakes were generated, I_l is the current and s_l is the synchrotron position of the l -th bunch in the ring, $\langle I \rangle = \sum_{l \in \mathcal{B}} I_l / M$ is the average current per bunch, M is the number of buckets filled, and \mathcal{B} is a set of integer numbers to identify which bunches are filled with particles. For example, if the bunches 1, 10, 500 and 735 are filled and the rest is empty, then $\mathcal{B} = \{1, 10, 500, 735\}$ and for sure $n \in \mathcal{B}$. Also, V_n needs the subscript n in order to identify it as the wake potential felt by the n -th bunch in the ring.

Combining equation (3.29) with the expansion of equation (3.20) we can derive expressions for each component of the effective wake functions of the beam

$$(V_0)_n(z, s) = \sum_{l \in \mathcal{B}} \frac{I_l}{\langle I \rangle} \sum_{k=-\infty}^{\infty} \int dz' \lambda_l(z'; s - s_r) W'_0(z - z' + s_r) \quad (3.31a)$$

$$(V_X^Q)_n(x, z, s) = x \sum_{l \in \mathcal{B}} \frac{I_l}{\langle I \rangle} \sum_{k=-\infty}^{\infty} \int dz' \lambda_l(z'; s - s_r) W^Q(z - z' + s_r) \quad (3.31b)$$

$$(V_X^D)_n(z, s) = \sum_{l \in \mathcal{B}} \frac{I_l}{\langle I \rangle} \sum_{k=-\infty}^{\infty} \int dz' d_l(z'; s - s_r) W_X^D(z - z' + s_r) \quad (3.31c)$$

where λ_l is the longitudinal line distribution and d_l is the horizontal dipole moment of the l -th bunch defined by

$$\lambda_l(z; s) = \int d\mathbf{p} \int d\boldsymbol{\rho}' \Psi_l(\mathbf{p}, \boldsymbol{\rho}', z; s) \quad (3.32)$$

$$d_l(z; s) = \int d\mathbf{p} \int d\boldsymbol{\rho}' x \Psi_l(\mathbf{p}, \boldsymbol{\rho}', z; s) \quad (3.33)$$

and V_0 , V_X^D and V_X^Q are the effective longitudinal, horizontal dipolar and horizontal detuning wake functions of the bunch. The expressions for the vertical effective wakes V_Y^D and V_Y^Q are very similar to the horizontal ones, just changing x for y .

3.7.2 Relation with Impedance

In order to demonstrate how the concept of impedance is useful in the beam dynamic calculations and its interpretation, let us consider that the beam is stationary, which means its distribution does not depend on time, and that all bunches in the ring are identical and equally spaced. When we apply the last assumption to equation (3.31a) we notice the double sum can be replaced by a single one, if we define a variable

$$j = kM + l - n$$

where M is the number of bunches stored in the ring. This way the sum reads

$$V_0(z) = \sum_{j=-\infty}^{\infty} \int dz' \lambda(z') W'_0(z - z' + jc \frac{T_0}{M}). \quad (3.34)$$

where the symbols l and n can be dropped due to the symmetry among bunches and the potential is time-independent. Additionally, if we substitute the wake function by its representation in terms of the impedance given in equation (3.22) the equation above becomes

$$V_0(z) = \frac{1}{2\pi} \sum_{j=-\infty}^{\infty} \int d\omega \tilde{\lambda}(\omega) Z_{||}(\omega) e^{-i\omega(z/c + j \frac{T_0}{M})} \quad (3.35)$$

where the line density $\lambda(z')$ was also substituted by its Fourier Transform, defined as

$$\tilde{\lambda}(\omega) = \int_{-\infty}^{\infty} dz \lambda(z) e^{i\omega z/c}. \quad (3.36)$$

Finally, using the Fourier Series expansion of the Dirac's delta comb:

$$\sum_{p=-\infty}^{\infty} \delta(\omega - pM\omega_0) = \frac{1}{M\omega_0} \sum_{j=-\infty}^{\infty} e^{-i2\pi j \frac{\omega}{M\omega_0}} = \frac{1}{M\omega_0} \sum_{j=-\infty}^{\infty} e^{-i\omega(j \frac{T_0}{M})}, \quad (3.37)$$

where $\omega_0 = 2\pi/T_0$ is the angular revolution frequency of the ring, equation (3.35) can be written as

$$V_0(z) = \frac{M\omega_0}{2\pi} \sum_{p=-\infty}^{\infty} \tilde{\lambda}(pM\omega_0) Z_{\parallel}(pM\omega_0) e^{-ipM\omega_0 z/c}. \quad (3.38)$$

where we notice the beam will only sample the impedance at multiples of the revolution frequency. Similar expressions can be obtained for the dipolar and quadrupolar effective wake functions:

$$V_x^D(z) = -\frac{iM\omega_0}{2\pi} \sum_{p=-\infty}^{\infty} \tilde{d}(pM\omega_0) Z_x^D(pM\omega_0) e^{-ipM\omega_0 z/c} \quad (3.39a)$$

$$V_x^Q(x, z) = -x \frac{iM\omega_0}{2\pi} \sum_{p=-\infty}^{\infty} \tilde{\lambda}(pM\omega_0) Z^Q(pM\omega_0) e^{-ipM\omega_0 z/c} \quad (3.39b)$$

and analogously for the vertical plane. Notice in the equations above that the dipolar impedance does not generate any effective wake function if the beam is stable and well centered in the vacuum chamber, because in this condition the dipole moment of the beam is zero. This is the main characteristic of a coherent mechanism, it depends on the values of specific properties of the beam, in this case the longitudinal distribution of the dipole moment, and its effects are only visible through averages on the distribution. On the other hand, the detuning wake generates a z -dependent quadrupole strength on individual particles of the beam even if the beam is stationary, which is characteristic of an incoherent effect: it affects the intra-bunch dynamics but it is not necessarily reflected in the averages on the distribution.

Equation (3.38) can be exploited in order to clarify the meaning behind the concept of impedance and its analogy with an electric circuit impedance. Notice that the equation can be interpreted as the Fourier expansion of the wake in the interval T_0/M and the coefficient that multiplies the exponential in the sum is the Fourier component of this expansion

$$\tilde{V}_0 = \tilde{\lambda} Z_{\parallel}, \quad (3.40)$$

where $\tilde{\lambda}$ is the analog of the current in a circuit and \tilde{V}_0 is the voltage induced by this current. The same analogy can be extended to the impedance in other planes. Actually, the modeling of the vacuum chamber as a circuit is a resource widely used to model the low frequency part of the impedance, as done by Sessler & Vaccaro (1967), Davino & Hahn (2003), for example.

3.8 Models for Impedances and Wakes

Even though the impedance of each component is result of a complex interaction between one particle and its environment, they often can be represented by simple physical models. A good example that is widely used, either to model the interaction of the beam with a trapped mode of a RF cavity, as described by Zotter & Kheifets (1998, Appendix 1.B), or to represent the whole impedance budget of a storage ring, is the resonator impedance, given by the RLC circuit in parallel

$$\frac{1}{Z_{\parallel}} = \frac{1}{R_s} + \frac{i}{\omega L} - i\omega C \Rightarrow Z_{\parallel} = \frac{R_s}{1 + iQ \left(\frac{\omega_R}{\omega} - \frac{\omega}{\omega_R} \right)} \quad (3.41)$$

where R_s is called the shunt resistance of the cavity, $Q = R_s \sqrt{C/L}$ is the quality factor, $\omega_R = 1/\sqrt{LC}$ is the resonant frequency and L and C are the inductance and the capacitance. The wake function associated with this impedance is given by the damped harmonic oscillator¹

$$W'_0(z) = \begin{cases} 0 & z < 0 \\ \alpha R_s & z = 0 \\ 2\alpha R_s e^{-\alpha z/c} \left(\cos \left(\frac{\bar{\omega}_R z}{c} \right) - \frac{\alpha}{\bar{\omega}_R} \sin \left(\frac{\bar{\omega}_R z}{c} \right) \right) & z > 0 \end{cases}, \quad (3.42)$$

where $\alpha = \omega_R/2Q$ is the damping factor and $\bar{\omega}_R = \sqrt{\omega_R^2 - \alpha^2}$. When Q is large, the damping factor is small and the wake rings for several periods, extending to large z distances behind the source particle. Such type of wakes are called narrow-band, because in the frequency domain the impedance has a sharp peak around the resonant frequency, with maximum amplitude equal to R_s . In the context of a storage ring, where several bunches are stored in the machine, wakes like this, generated by one bunch can last long enough to influence other bunches behind it or even itself in the following turns, if the resonance condition of the sequential bunches spacing and the wake period is approximately met. On the other hand, if Q is small, generally close to one, the damping factor is large, and the wake decays fast. This type of resonator is called broad band resonator (BBR), because its impedance has a very wide spectrum.

The periodicity of the storage ring was considered in the calculation of the effective wakes in section 3.7.1 and expressed by the infinite sum in equations (3.31). When the impedances are narrow-band, only a few of those sampling lines are relevant for the convergence of the sum. This is a result of the multi-turn buildup of the electromagnetic fields in the device that generates the impedance. When the wake is broad-band, the impedance does not change much from successive lines in the summation, in such a way that the sum can be replaced by an integral, and the whole information regarding the

¹ This expression is valid for $Q > 1/2$. The general formula can be found in Zotter & Kheifets (1998, sec. 3.2.4).

periodicity of the system is lost, because the interaction only occurs in a short-time interval. The reasoning above suggest that the attribution of narrow or broad-band term depends on the size of the ring and, more specifically, on the bunch spacing.

There are some degenerate cases of the resonator impedance which are very useful to model sort-range wakes. They are the resistive impedance, Z_{Res} , and the inductive impedance, Z_{Ind} , given by

$$\begin{aligned} Z_{\text{Res}} &= R \\ Z_{\text{Ind}} &= -iL\omega \end{aligned} \Rightarrow \begin{aligned} W'_{0,\text{Res}} &= R\delta(z) \\ W'_{0,\text{Ind}} &= iL\delta'(z) \end{aligned} \quad (3.43)$$

where $\delta(z)$ is the Dirac's delta function and $\delta'(z)$ its first derivative. While the resistive impedance is related to energy loss and instabilities, the imaginary creates tune shifts and potential well distortion. It is common in the related literature to attribute the word capacitive to negative inductive impedances, even though it does not have the correct ω -dependence.

The analogous of the longitudinal resonator model for the transverse plane is given by

$$Z_t = \frac{\omega_R}{\omega} \frac{R_s}{1 + iQ \left(\frac{\omega_R}{\omega} - \frac{\omega}{\omega_R} \right)}, \quad (3.44)$$

where the factor $1/\omega$ must be introduced for the impedance to satisfy the symmetry properties and the Panofsky–Wenzel theorem. The corresponding wake function is²

$$W_t(z) = \begin{cases} 0 & z < 0 \\ \frac{2\alpha\omega_R}{\bar{\omega}_R} R_s e^{-\alpha z/c} \sin\left(\frac{\bar{\omega}_R z}{c}\right) & z > 0 \end{cases}. \quad (3.45)$$

3.9 Impedance Calculation

For most practical cases, determining the impedance of a given component of the storage ring is a very difficult task because of the complexity of the boundary conditions involved. The exact analytic solution of the ME can only be performed for a limited number of cases, and even in these cases some idealization of the real system must be performed. In order to tackle this problem, the accelerator physics community resorts to various possible ways of finding approximate results and all these efforts can be grouped in two categories: the analytic treatments and the numeric solutions.

An adequate description of the analytic methods for finding such solutions is beyond the scope of this work and can be found in the book written by Zotter & Kheifets (1998) and the report written by Gluckstern (2000). Besides, Chao (1993) and Palumbo *et*

² Same as described in footnote 1. The general expression is in Zotter & Kheifets (1998, sec. 3.3.2).

al. (1994) also discuss some of the approximate methods in a very intuitive way; and Ng & Bane (2010) presents a table with some of the most important results for common types of accelerator structures. Not covered in any of these references is the explanation of the use of the parabolic equation, which is a paraxial approximation of the ME, to the impedances calculation, presented by Stupakov (2006). From these equations it can be shown that the wakes must satisfy a very interesting scaling feature that is very useful for numeric simulations (STUPAKOV *et al.*, 2011).

Most analytic methods are employed in frequency domain, which means the result of the calculation is an expression for the impedance, not for the wake, which generally is valid for a certain range of frequencies and most common approximations consider either frequencies much lower than the cutoff frequency³ of the pipe ($\omega \sim 2.4c/b$) or very high frequencies. While the first kind of approximations is valid for bunches longer than the characteristic transverse dimension of the structures, the latter is a good approximation for very short bunches.

In the case of Sirius, the standard vacuum chamber has a radius of 12 mm while the bunch will have approximately 3 mm in length. This combination of dimensions is delicate because the bunch is not long enough for the low frequency approximations to be valid nor short enough for the high frequency regime to dominate, which means we cannot rely only on these methods to compose the Sirius impedance budget.

Below we will describe two cases of analytic impedance calculations of fundamental importance to this work: the first is the tapered transition, which is an example for the arguments presented above, indicating that numerical solvers are the most accurate way of calculating impedances, and the other is the resistive wall, which is a big exception to this rule. Finally, we will introduce the main concepts important for numerical simulations.

3.9.1 Tapered Transitions

Some components in a storage ring require transverse apertures that are different from the standard vacuum chamber. For example, most undulators need narrower chambers because their magnetic gap is small in order to achieve larger fields. The beam ports of the RF cavities, on the other hand, can be larger than the standard pipe. These two types of structures in the vacuum chamber are called collimators⁴ and cavities, respectively, and have a strong impact on the total impedance budget of a storage ring, mainly in the transverse plane. See for example a paper by Günzel (2006) which describes the impedance budget of the ESRF storage ring or another work of the same author, Günzel & Perez (2008), where the impedance budget of ALBA is analysed.

³ Cutoff frequency is the frequency of the lowest eigen-mode of the pipe, above which the fields can propagate through the tube.

⁴ Actually there is a device called collimator which have the same concave geometry of the pairs of transitions defined with this name here. Their function is to screen the transverse tail of the beam.

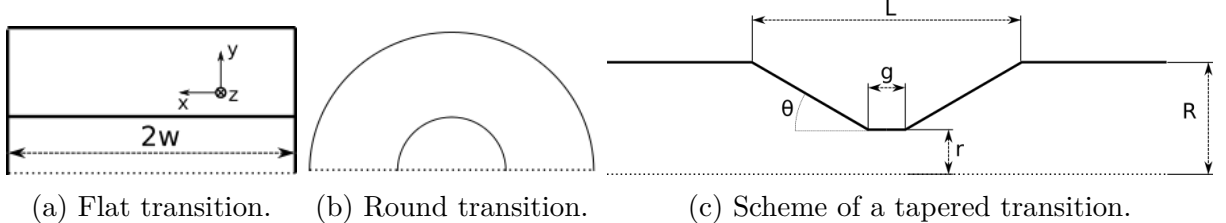


Figure 10 – When $r > R$ the element is called cavity and when $r < R$ it is called collimator. The tapers are the smooth transition regions of the chamber, region where the radius varies. When the transition has no tapers it are called step-in or step-out, depending on the relation between the initial and final radius.

Figure 10c shows a scheme of such type of geometry, with the important parameters for the impedance calculation. Such geometry can be separated in two independent contributions from the two cross section variations if the gap, g , is large, according to Bane *et al.* (2007). As discussed by Heifets & Kheifets (1991), when the beam passes through transitions two forces act on it: one from the change of the energy stored in the synchronous component of the field that travels with the beam, Z_s , originated due to the difference in the cross sections, and another one due to the radiation emitted by the image charges on the wall, Z_r ,

$$Z_0^{\text{out}} = Z_r + Z_s \quad (3.46a)$$

$$Z_0^{\text{in}} = Z_r - Z_s \quad (3.46b)$$

where Z_0^{out} is the total impedance of the transition where the beam goes from a smaller chamber to a larger one (step-out), Z_0^{in} is the impedance from a larger chamber to a smaller one (step-in) and the equality of the terms Z_r in both cases is a consequence of the beautiful theorem of directional symmetry of the impedance, demonstrated by Heifets (1990). The term Z_s is constant regardless of the frequency and tapering of the transition, and causes energy gain in the step-in case and energy loss for the step-out. For a transition with round cross-section this contribution to the impedance is given, according to Palumbo *et al.* (1994), by

$$Z_s \approx \frac{Z_0}{2\pi} \ln \left(\frac{r_1}{r_2} \right), \quad (3.47)$$

where $Z_0 = 120\pi \Omega$ is the impedance of free space and r_1 and r_2 are the radius of the chamber before and after the transition, respectively. Besides, for the step-in case the total energy loss by the beam must be approximately zero, $Z_0^{\text{in}} \approx 0$, because the radiation emitted propagates in the opposite direction of the beam. This means that all the energy of the radiation must be taken from the synchronous field, which yields that in the high frequency limit $Z_r = Z_s$.

Notice that the average influence of the source term, Z_s , on the impedance in one turn around the ring is zero, because of the periodicity of the vacuum chamber.

Thus, the term that really matters is the contribution from radiation, which depends on the characteristics of the transition, such as the tapering. Analytic studies of this component were carried out by Yokoya (1990) for a round geometry (Figure 10b), where the author derived expressions for the low frequency range of smoothly varying tapered transitions. Later Stupakov (1996) corrected the upper frequency limit of the validity of these expressions and extended the lower limit to zero frequency. The result is the following:

$$\frac{\omega r^2}{cl} \ll 1 : \quad Z_{\parallel} = -\frac{i\omega Z_0}{4\pi c} \int_{-\infty}^{\infty} dz (r')^2, \quad Z_t = -\frac{iZ_0}{2\pi} \int_{-\infty}^{\infty} dz \left(\frac{r'}{r}\right)^2, \quad (3.48)$$

where $r = r(z)$ is the radius of the chamber, $r' = r'(z)$ is the derivative of the radius and $t = (L - g)/2$ is the taper length. This impedance is imaginary while the one from the high frequency limit is real. This happens because below the cutoff frequency no radiation can propagate, suggesting that above this threshold a real part of the impedance will arise and approach the high frequency limit, while the imaginary part will tend to zero, after a complex frequency range where the transition between the two limiting behaviors dominates. Another feature of the equation above is that the impedance tends to zero with the taper length. For example, for a linear taper the formulas above simplify to

$$\frac{\omega r^2}{cl} \ll 1 : \quad Z_{\parallel} = -\frac{i\omega Z_0}{4\pi c} \frac{|r_1 - r_2|}{t}, \quad Z_t = -\frac{iZ_0}{2\pi} \frac{1}{t} |r_1^{-1} - r_2^{-1}|, \quad (3.49)$$

where $t = \tan^{-1} \theta = l/|r_1 - r_2|$ is the transition factor of the taper.

Stupakov (2007) developed a method to find the low frequency impedance of tapers with general cross sections and derived explicit formulas for a flat taper, consisting on a rectangular geometry with varying vertical gap and constant horizontal aperture, as shown in Figure 10a. His results are:

$$\begin{aligned} Z_{\parallel} &= -0.43 \frac{i\omega Z_0}{\pi c} \int_{-\infty}^{\infty} dz (h')^2 \\ \frac{\omega w^2}{2cth} \ll 1 \text{ and } h \ll w \ll l : \quad Z_y &= -\frac{iZ_0 w}{4} \int_{-\infty}^{\infty} dz \frac{(h')^2}{h^3} \\ Z_x^D &= -Z_x^Q = -\frac{iZ_0}{4\pi} \int_{-\infty}^{\infty} dz \left(\frac{h'}{h}\right)^2 \end{aligned} \quad (3.50a)$$

where w is the chamber half-width and $h(z)$ is the half-gap. It is worth noting that the dipolar horizontal and the quadrupolar impedances are equal to each other and a factor of 2 smaller than the transverse impedance in a conical taper, while the longitudinal impedance is approximately 7/4 of its counterpart. The most interesting result, however, is the linear dependence of the vertical dipolar impedance with the width of the chamber, which makes this impedance approximately $\pi/2w / \langle h \rangle_{\text{harm}}$ larger than the round chamber

one. For example, for a linear taper these expressions become

$$\begin{aligned} Z_{\parallel} &= -0.43 \frac{i\omega Z_0}{\pi c} \frac{|h_1 - h_2|}{t}, \\ \frac{\omega w^2}{2cth} \ll 1 \text{ and } h \ll w \ll l : \quad Z_y &= -\frac{iZ_0}{2} \frac{w}{t} (h_1^{-1} + h_2^{-1}) |h_1^{-1} - h_2^{-1}|, \\ Z_x^D &= -Z_x^Q = -\frac{iZ_0}{4\pi} \frac{1}{t} |h_1^{-1} - h_2^{-1}|, \end{aligned} \quad (3.51)$$

where we note that $Z_y^{\text{flat}}/Z_y^{\text{round}} = \pi w(h_1^{-1} + h_2^{-1})$.

Podobedov & Krinsky (2007) studied the low frequency limit of confocal⁵ elliptical transitions and found results very similar to the expressions above for the flat geometry, which gives some confidence in trying to extend the qualitative results discussed here for approximated geometries.

Even though the low-frequency impedance of long and short collimators and cavities are the same, because the equations showed above can be applied to both limits, Heifets (1990) found different limits for the high frequency impedances of a round cavity, depending on the length of their gap. Besides, Stupakov *et al.* (2007) found equal limit values for the longitudinal impedance, but different for the transverse dipolar impedance in a round collimator. While for the longitudinal limit the value is two times the quantity in equation (3.47), for the transverse plane they found

$$\text{short: } Z_x^D = \frac{Z_0 c}{2\pi\omega r^2} \left(1 - \frac{r^4}{R^4}\right) \quad \text{long: } Z_x^D = \frac{Z_0 c}{\pi\omega R^2} \left(1 - \frac{R^4}{r^4}\right) \quad (3.52)$$

where the notation of Figure 10c was used. Besides, there is a very large frequency gap between the two limiting cases that are of great importance, mainly for storage rings such as Sirius, which have bunch lengths that sample these frequencies. For the round collimator, Stupakov & Podobedov (2010) used the parabolic equation to calculate the impedance from a few dozens GHz up to a few THz, with excellent agreement with results from numerical solvers. However, so far the impedance for other geometries, or even the detailed behavior of one of the round transitions, can only be accessed with the aid of numerical solvers.

For example, Blednykh (2006) studied the impedance of the flat collimator-type chamber of a mini-gap undulator and found very intense narrow-band mode just above the cutoff of the pipe, that depended very strongly on the width of the cross-section. For all these reasons the formulas studied here, even though very useful to the study of this type of impedance and qualitative analysis of the relevant parameters for impedance optimization, will not be used quantitatively for any device of the impedance budget.

⁵ Confocal ellipses means they have the same *foci*. In the case of the transition cited here, the equation $a^2(z_1) - b^2(z_1) = a^2(z_2) - b^2(z_2)$ is valid for any longitudinal position z_1 and z_2 , where a and b are the larger and smaller axes of the ellipse.

3.9.2 Multi-Layer Resistive Wall

The standard resistive wall effect has been known for a long time. It was first observed to generate coherent oscillations in electron streams coupled to circuits by Pierce (1951) and then used to create a resistive-wall amplifier by Birdsall *et al.* (1953). This idea was first applied to the study of collective effects in accelerators by Neil & Sessler (1965) and Laslett *et al.* (1965) to explain longitudinal and transverse coherent oscillations of coasting beams and then by Courant & Sessler (1966) to describe instabilities of bunched beams. Since then the theory for calculation of the now called resistive-wall impedance evolved (CHAO, 1993), being exactly solved by Bane (1991) for a round and infinitely thick and long vacuum chamber, where the author provided analytic formulas for the short-range wake-fields, and for an arbitrary transverse cross section by Yokoya (1993), who based its work on a formalism developed by Gluckstern *et al.* (1993). In his work, Yokoya also showed that the spectral dependency of the longitudinal and transverse dipolar and quadrupolar impedances of elliptic chambers with equal smaller axis, but different eccentricities, are identical, in such a way that their wake functions differ from each other only by a constant factor. In the special cases of a round and a flat chamber, which are degenerated cases of an ellipse, with eccentricities equal to 0 and 1 respectively, the so called Yokoya factors are given by

$$(Z_{\parallel})_{\text{flat}} = (Z_{\parallel})_{\text{round}} \quad (3.53)$$

$$(Z_x^D)_{\text{flat}} = \frac{\pi^2}{24} (Z_x^D)_{\text{round}} \quad (3.54)$$

$$(Z_y^D)_{\text{flat}} = \frac{\pi^2}{12} (Z_x^D)_{\text{round}} \quad (3.55)$$

$$(Z^Q)_{\text{flat}} = \frac{\pi^2}{24} (Z_x^D)_{\text{round}}, \quad (3.56)$$

where the net horizontal force felt by the witness particle with the same horizontal position as the source particle is zero for the flat chamber. Actually, this is a particular case of the general result that the wake potential of this structure must not depend individually on the horizontal positions of the source and witness particles, but only on their difference

$$W_{\text{flat}}(x_s, y_s, x_w, y_w, z) = W_{\text{flat}}(y_s, y_w, x_s - x_w, z),$$

so that the condition of translational symmetry in the horizontal direction is respected.

It is very recurrent in accelerators to have chambers that are composed of different laminar layers of materials. For example, the chambers of fast time-varying magnets, such as the injection kickers of a storage ring, must be made of a bad conductor, generally a ceramic, to allow the penetration of the fields. To avoid discontinuities in the path of the image current of the beam⁶, which could lead to excessive heating and consequent

⁶ This is equivalent to say: "to decrease the impedance of the beam".

melting or burning of the magnet components and the accumulation of static charges in the ceramic, a thin layer of metal is coated in the inner surface of the chamber. The thickness of the coating must be of a few microns: thin enough not to distort the external field as it penetrates the walls, which has frequencies of the order of hundreds of kilo Hertz, and thick enough to shield most of the frequencies of the beam, which extend to a few dozens of giga Hertz. Specifically for the kicker magnet, outside the ceramic vacuum chamber, there is a layer of ferrite, which is used to guide the external field of the kicker. In the low frequency part of the spectrum, all these different layers of materials are seen by the self-generated fields of the beam and contribute to the impedance.

Besides, the multi-layer chamber model also applies in the simple case of a standard vacuum chamber of an accelerator, where the finite thickness of wall can be interpreted as a multi-layer chamber composed of metal and air. For low frequencies, the skin depth of the material becomes larger than the thickness of the chamber, which decreases the losses by the beam. As a consequence, the real part of the impedance goes to zero and the imaginary part goes to a constant value as the frequency tends to zero. This behavior is correctly predicted by the multi-layer model, while the infinitely thick formula predicts that both impedances diverge to plus and minus infinity, respectively. This low frequency of the resistive wall has a very narrow band nature and influences the long-range wake fields, which are directly related to the coupled bunch resistive-wall instability and the incoherent tune shifts caused by chambers without circular symmetry, as explained by Chao *et al.* (2002).

The multi-layer chambers problem was first tackled by Zotter (1969a), who created an algorithm that solved the problem for an arbitrary number of layers of materials with arbitrary electric and magnetic properties, as long as they were linear, homogeneous and isotropic (ZOTTER, 1969a; ZOTTER, 1969b; ZOTTER, 1970). Even though his method was general enough to be applied to any azimuthal mode m of the source, he only calculated the fields for the azimuthal modes $m = 0$ and $m = 1$ ⁷. This allowed him to derive explicit analytic formulas, under some approximations, for the longitudinal impedance of simplified configurations, such as a single wall with finite thickness, and a metallized ceramic chamber surrounded by a PEC. In this latter case, the author concluded that the effectiveness of the coating in the inner wall was much higher than what is intuitively thought by comparing the thickness of the coating with the skin depth of the fields for a given frequency.

Later Piwinski (1977) calculated the impedance generated by a gaussian bunch in a four-layer round chamber composed of metal, ceramic, ferrite and PEC, in that order, and confirmed what Zotter (1970) had previously found: for this type of multi-layer chambers,

⁷ It is remarkable that his method goes beyond the rigid beam approximation, considering the source of the wake fields as an infinitely long beam oscillating in the transverse plane to calculate the mode $m = 1$.

the fields will not penetrate through the coating if its thickness, t , satisfies

$$t > \frac{\delta^2}{d}, \quad \text{with} \quad \delta = \sqrt{\frac{2}{\mu_0 \omega \sigma_c}} \quad (3.57)$$

where δ is the skin depth, σ_c is the conductivity of the coating, μ_0 is the magnetic permeability of vacuum, ω is the angular frequency of the fields and d is the thickness of the ceramic. This means that, since generally $d \gg t$, the coating is efficient down to frequencies much lower than what is intuitively thought.

In a more recent work, Zotter (2005) rederived his formalism for a point like charge, which was used by Mounet & Métral (2009) to derive formulas for the electromagnetic fields and impedances of any azimuthal mode m , under the assumption of a rigid beam. Later, the same authors also derived expressions for a multi-layer flat chamber with possible different layers in the top and bottom plates (MOUNET; MÉTRAL, 2010a) which allowed them to generalize the Yokoya factors (MOUNET; MÉTRAL, 2010b). Then, in his PhD thesis, Mounet (2012) developed a general method to perform Fourier integrals, which allowed him to compute the exact short and long-range wake functions using the impedances. All these developments in 2D impedance theory were implemented by Mounet in a code called ImpedanceWake2D (MOUNET, 2011) that is available as free software for the accelerator community. It is important to mention that other authors also solved the problem of multi-layer impedances using different methods, for example Hahn (2008) and Al-Khateeb *et al.* (2005) also derived general methods valid for arbitrary energies and frequencies in round chambers and Burov & Lebedev (2002a), Burov & Lebedev (2002b) also solved the problem under the assumption of long wavelengths, $c/\omega \ll a$, for round and flat geometries.

In summary, the theory of smooth multi-layer infinitely long round chambers is completely solved. In this work we implemented Mounet & Métral formulas to calculate the impedances for round chambers for the azimuthal modes $m = 0$ and $m = 1$ in Matlab® and Python3 and the wake functions were obtained using the code Impedance-Wake2D. In cases where the eccentricity of the chamber is large, the Yokoya Factors are applied to the round chamber results.

3.9.3 Numeric Methods

The numerical solvers can be grouped in two categories: 1) the frequency domain codes, that are more indicated for calculation of resonant modes below the cutoff of the chamber, and 2) time domain solvers. While the first class computes the eigen-values and eigen-modes of the structures and the user must identify which ones can be excited by the beam passage, the latter solves ME computing directly the fields that are generated by the beam. In this type of solvers the beam is modeled by a line density of charge, λ , that traverses the structure at the speed of light with a constant transverse displacement,

ρ'_0 , and then, by discretization of the space-time in grids and approximations of the derivatives by linear operators on the fields in the vertices and faces of each grid, the electromagnetic field can be calculated up to the desired distance behind the source, so the integral defined in equation (3.4) can be carried out. Depending on the methods employed in the discretization and the properties of the linear operators in each grid, different convergencies of the solutions related to the finesse of the grids can be achieved. There are several different methods and codes in the literature dedicated to this purpose. For a good review on numeric methods Niedermayer & Gjonaj (2016) and its references are recommended.

3.9.3.1 Finite Line Density Issue

This procedure employed to find the impedances has an intrinsic limitation: the line density used as source particle in simulations must always spread over a few grids, which means a delta-like function can never be used and the wake functions, or wake potential, cannot be obtained. Instead, the effective wake potential, given by

$$V(\rho'_0, \rho, z) = \int dz' \lambda(z') W(\rho'_0, \rho, z - z'), \quad (3.58)$$

is the result of the simulations. In principle this equation could be inverted with the aid of the convolution theorem (Wikipedia Contributors, 2017c), where after the Fourier transform on both sides of the equation one could get

$$\tilde{W} = \frac{\tilde{V}}{\tilde{\lambda}}. \quad (3.59)$$

However, this procedure fails to give the values of the impedance at large frequencies due to two effects: the most obvious is the limitations imposed by the Nyquist theorem applied to the grid length of the simulation and the other comes from the fact that the line density Fourier transform has a tail at large frequencies that makes the denominator of equation (3.59) very small, which, in turn, increases the effect of the noise of the simulations for this frequency range. This limitation on the knowledge of the impedance for high frequencies makes it impossible to obtain the wake function accurately for short distances from the source.

The line density generally used for such calculations is the gaussian distribution:

$$\lambda(z) = \frac{1}{\sigma\sqrt{2\pi}} \exp\left(-\frac{(z - n\sigma)^2}{2\sigma^2}\right), \quad (3.60)$$

where n is an integer generally equal to 5 or 6. due to its minimal duration-bandwidth product (NIEDERMAYER; GJONAJ, 2016). A rule of thumb for these calculations is to consider the impedance only up to frequencies $\omega \leq 2\sigma/c$ thus avoiding strong influences of the numerical noises as discussed above, which is much more limiting than the Nyquist

requirement, given that in simulations the bunch length must be at least five times larger than the grid size.

The authors Podobedov & Stupakov (2013) found a way to overcome this problem, as long as the bunch length used in the simulation is short enough. However, a more practical approach comes from the fact that a real bunch also has a finite length and cannot excite wakes with arbitrarily large frequencies, which means if the line density used to obtain the wakes is smaller than the smallest longitudinal structure in the bunch expected to generate any macroscopic significant effect we want to study, then the impedance extracted from that simulation is close enough. Notice this method is intrinsically non-consistent, because we must know *a priori* how the beam will behave to compute the impedance that will drive this behavior. However, the knowledge gathered by the accelerator physics community in the last fifty years, through several experiments and confrontation of these results with simulated and analytic calculated beam dynamics, led to some rules of thumb that determines the maximum frequency that can be expected to influence the dynamics of a bunch with a given natural bunch length.

This approach may be conflicting in some situations when the high frequency content of the wake is desired but the structure being analysed has strong resonant modes that take hundreds of meters behind the source to damp. Running a simulation with a short line density will drastically increase the complexity of the simulation because of the smaller mesh size. The solution for these cases is running two simulations, one with a short bunch and small wake length and other with a longer bunch and long wake length, to characterize the resonant mode. Another approach is to simulate the resonant modes with a frequency domain code.

3.9.3.2 ECHO Code

There are some solvers in the literature that were developed specifically for rotationally symmetric geometries, such as ABCI (CHIN, 1994), since this type of structure is rather common in accelerators. In this type of systems the wake potential in the ultra-relativistic approximation can be partially solved without the need of specifying the boundary conditions, only by the application of the Panofsky-Wenzel theorem and equation (3.12). It can be shown (STUPAKOV, 2000) that the most general form for the wake potential in such conditions is:

$$W(\rho_s, \rho_w, \theta, z) = \sum_{m=0}^{\infty} W_m(z) \rho_w^m \rho_s^m \cos(m\theta) \quad (3.61)$$

where $\rho = |\boldsymbol{\rho}|$ is the distance of the particles to the center of the chamber, θ is the angle between the source and the witness particles and the source particle is assumed to lie in the $\hat{\mathbf{x}}$ direction. The wake functions can be obtained from the gradient of the wake

potential. Expanding the wake functions in the leading order we have

$$w_s(z) \approx W'_0(z) \quad (3.62)$$

$$\mathbf{w}_t(x_s, z) \approx W_1 \rho_s(\hat{\mathbf{r}} \cos(\theta) - \hat{\boldsymbol{\theta}} \sin(\theta)) = W_1 x \hat{\mathbf{x}} \quad (3.63)$$

where the force is in the same direction that of the displacement of the source particle.

This partial solution of the wake potential allows us to solve each azimuthal component of the wake potential separately, which implies the numerical solution can be found for a single plane of the structure, for example, the plane $x-s$, or $y=0$. This bidimensional mesh drastically reduces the simulation time for such components and this class of codes are called 2D solvers. Among such codes we highlight ECHOz1 and ECHOz2 (ZAGORODNOV *et al.*, 2003; ZAGORODNOV; WEILAND, 2005; ZAGORODNOV, 2006), which are distributed as free software by the author. While ECHOz1 calculates only the azimuthal mode $m = 0$, ECHOz2 provides the longitudinal and transverse wake functions for an arbitrary mode m . This code employs several solutions to common problems of numeric simulations that makes it the state of the art for impedance calculation. Among the advantages of this code we highlight:

- zero dispersion in the longitudinal plane. Longitudinal dispersion is a typical numeric artifact that introduces a non-physical dependency of the phase velocity of the electromagnetic waves with their frequency, which deteriorates the precision of the wakes;
- fast convergence of the ratio between bunch size and grid length, σ/h : in other codes this ratio must be one order of magnitude larger than ECHO's value for the results to have the same precision. In ECHO a ratio of 5 already gives convergent results, which greatly reduces the simulation time for a given frequency requirement on the knowledge of the impedance;
- moving mesh: instead of discretize the whole structure, the grids move with the source and this region extends behind it only down to the desired length of the wake. This approach helps reducing the simulation time in cases where the structure is larger than the wake length and is applied in other codes too, such as GdfidL;
- indirect integration: for the wake calculation, the infinite integral in the longitudinal direction can be substituted by finite integrals in closed contours that span the structure longitudinally. The first method proposed by Weiland (1983) was valid only for cavity-like structures, but then it was generalized for any rotationally symmetric structure by Napoléon *et al.* (1993), and finally generalized for any 3D structure by Zagorodnov (2006). This procedure greatly reduces the computational time because otherwise it would be necessary to propagate the beam for a very long distance

only for the integral to converge. Besides, it improves the precision of the results, because the long integral in the direct method suffers from accumulation of numerical errors.

There is another code provided by the same author, ECHOzR, that calculates the wakes for structures with rectangular cross sections (ZAGORODNOV *et al.*, 2015). The conditions imposed on the geometry are that the lateral walls are composed of infinite vertical and perfectly conducting parallel plates separated by a distance w and that the horizontal walls that define the vertical gap has an arbitrary longitudinal profile and electrical conductivity. Employing the harmonic properties of the wake potential (equations (3.12) and (3.13)) on the transverse coordinates of the source and witness particles, the author solves partially the wake potential by expanding it in trigonometric functions that automatically satisfy the boundary conditions in the vertical plates. This way, similarly to the rotationally symmetric case, the numerical computation is reduced to a bidimensional problem that is solved independently for each term of the expansion. All the advantages presented for ECHOz2 regarding the precision of the results and simulation time also applies for ECHOzR. The main difference between the two codes is that for the rectangular code significant post-processing of the results is needed, because the lowest order longitudinal and transverse wake functions are an infinite sum of the modes of the expansion. However, close to center of the chamber, convergence can be achieved by summation of approximately the first ten modes.

There is also a generic version of the ECHO code, called ECHO3D, that can be used to compute the wakes for an arbitrary geometry. This code has all the advantages of the bidimensional codes, but lacks a key feature: it is not parallelized. For 3D structures this limitation imposes great restrictions on the type of simulation that can be performed, due to the extremely large required computational time.

3.9.3.3 GdfidL Code

When the components of the vacuum chamber do not respect the symmetries required by the 2D solvers or cannot be approximated by one that does, 3D codes must be used. They are also used when a detailed simulation is needed to compute not only the wake potential but also the distribution of the electromagnetic field density in the structures, to calculate heating effects and also the transmission of the fields through ports. The most well-known applications for this type of simulations are GdfidL (BRUNS, 1997; BRUNS, 2017) and CST Particle Studio (CST, 2017), being the first code the adopted choice for Sirius components design and simulation.

4 COLLECTIVE EFFECTS

In the previous chapter the mechanism of interaction between particles was modeled and formulas for the momentum change of an arbitrary particle due to the action of all the other particles in the beam were derived. In this chapter we will try to include these interactions in the dynamic model of the particles and analyse how the beam will behave as a whole.

4.1 Sum of the Wakes

With the theory developed so far it is formally possible to calculate the wake potential for all the structures of the ring and include their effects on the beam dynamics assuming the impulse approximation, which considers the variation of the particle momentum must be applied at the position in the ring equivalent to the center of the impedance source. However, a further approximation is usually done for the calculation of the effect of wake-fields in global parameters of the machine, such as tune-shifts, energy loss and even instabilities. This approximation considers all the impedance sources are located at a single point in the ring, in other words, it neglects the phase advances between each wake source. This way the total longitudinal wake of a machine can be given by:

$$W'_0(z) = \sum_i (W'_0(z))_i \quad (4.1)$$

where i refers to the i -th impedance source of the ring.

For the transverse plane it is important to remember that the transverse amplitude of the displacements of the source and witness particles varies along the ring, which means the transverse components of the wake potential must be scaled according to the local betatron functions at their positions

$$\begin{aligned} W_u^D &= \frac{1}{(\beta_u)_T} \sum_i \sqrt{(\beta_u)_i^s (\beta_u)_i^w} (W_u^D(z))_i \\ W_u^Q &= \frac{1}{(\beta_u)_T} \sum_i (\beta_u)_i^w (W_u^Q(z))_i \end{aligned} \quad (4.2)$$

where u represents x or y , $(\beta_u)_T$ refers to the value of the betatron function at the position where all the impedances are being lumped, $(\beta_u)_i^w$ is the value of the betatron function at the location where the witness particle feels the kick and $(\beta_u)_i^s$ is the betatron function where the source particle generated the wake.

This scaling can be easily understood by the analysis of the wake potential terms of the quadrupolar and dipolar wakes. For example, the horizontal dipolar term of the wake

potential corresponds to $x_s x_w W_x^D(z)$, which means it depends linearly on the displacement x_s at the point a where it induces the wake fields. If we want to displace the position where this wake was generated from positions a to b and, on average, keep its value unchanged, it is necessary to consider that the amplitude of movement of the source particle were $\sqrt{\beta_x^a/\beta_x^b}$ larger when it excited the fields and we have to multiply our equivalent wake function by this value. In the same way, the witness particle felt the fields generated by the source at a position c downstream from the point where they were generated and, if we want to consider the position of the witness particle in b , it is important to multiply the effective wake by $\sqrt{\beta_x^c/\beta_x^b}$, to keep the average strength unchanged.

All references in literature consider that the position where the wake is generated and the position where the particles feel these wakes are the same, so in this work we will consider it too. Under such condition, the equations (4.2) reduce to

$$\begin{aligned} W_u^D &= \frac{1}{(\beta_u)_T} \sum_i (\beta_u)_i (W_u^D(z))_i \\ W_u^Q &= \frac{1}{(\beta_u)_T} \sum_i (\beta_u)_i (W_u^Q(z))_i \end{aligned} \quad (4.3)$$

where $(\beta_u)_i$ is the value of the betatron function at the position of the wake source. However, depending on the transverse sizes of the chamber the fields can only catch up with the witness at distances of the order of centimeters away from the point where the fields were generated. For 4th GLS, where the focusing is very strong, such a distance is enough for the betatron function to have changed considerably. The effect of this consideration can be a topic for future studies.

4.2 Energy Loss

One of the most important effects of wake fields is the energy loss by the beam. It can be computed considering only the leading order term in the momentum change expansion

$$\Delta E \approx c \Delta p \approx c \left(\frac{p_s}{p} \Delta p_s + x' \Delta p_x + y' \Delta p_y \right) \approx c \Delta p_s. \quad (4.4)$$

This way the energy variation of a given particle due to wake-fields depends on which bunch it is and on its longitudinal deviation from the synchronous particle and is given, in the most general form, by equation (3.31a) multiplied by the average charge of the bunches and the charge of the particle. If we consider the distributions are stationary and the ring is uniformly filled with charge, then the expression for the wake-potential is reduced to equation (3.38).

Under this approximation, the energy variation of a particle after passing through the impedance source would be given by:

$$\Delta E(z) = -eI_bT_0V_0(z) = -eI_bT_0 \frac{M\omega_0}{2\pi} \sum_{p=-\infty}^{\infty} \tilde{\lambda}(pM\omega_0) Z_{\parallel}(pM\omega_0) e^{-ipM\omega_0 z/c}. \quad (4.5)$$

where $I_b = Q_b/T_0 = N_b e/T_0$ is the current per bunch, T_0 is the revolution time, N_b is the number of particles per bunch and e is the absolute value of the elementary charge of the electron. The average total energy lost by one bunch is given by

$$\langle \Delta E \rangle_b = N_b \int_{-\infty}^{\infty} dz \lambda(z) \Delta E(z) = - (I_b T_0)^2 \overbrace{\frac{M\omega_0}{2\pi} \sum_{p=-\infty}^{\infty} |\tilde{\lambda}(pM\omega_0)|^2 \Re \{Z_{\parallel}(pM\omega_0)\}}^{\kappa_{\parallel}} \quad (4.6)$$

where $\kappa_{\parallel} \equiv \kappa_L$ is called the longitudinal loss factor, $|\tilde{\lambda}(\omega)|^2 = \tilde{\lambda}(\omega) \tilde{\lambda}^*(\omega)$ must be an even function of the frequency, given that λ is real. Notice that only the real part of the impedance contributes to the energy loss, because the imaginary part is an odd function of the frequency. The average energy loss per particle can be defined as

$$\langle \Delta E \rangle_p = \frac{\langle \Delta E \rangle_b}{N_b} = -eI_bT_0\kappa_{\parallel}. \quad (4.7)$$

For impedances that vary smoothly with the frequency compared to the interval $M\omega_0$, the sum in the definition of the loss factor can be replaced by an integral

$$\kappa_{\parallel} = \frac{1}{2\pi} \int_{-\infty}^{\infty} d\omega |\tilde{\lambda}(\omega)|^2 \Re \{Z_{\parallel}(pM\omega_0)\} = \frac{1}{\pi} \int_0^{\infty} d\omega |\tilde{\lambda}(\omega)|^2 \Re \{Z_{\parallel}(pM\omega_0)\}. \quad (4.8)$$

The sum of the energy loss in each impedance source of the ring results in an additional energy loss per turn for the particles. This means the new fixed point of the longitudinal one turn map is not given by equation (2.33), but by

$$V(z_0) = U_0 + \langle \Delta E \rangle_p \quad (4.9)$$

instead, where z_0 is the new synchronous position, measured in relation to the zero current one.

Another important parameter to consider in the design of several components of the vacuum chamber is the power deposited in the wall per unit area by the beam due to wake fields. To calculate such quantity we need the power loss of the whole beam, which is obtained from equation (4.6) by multiplying it by the number of bunches and dividing by the revolution time of the ring,

$$P_w = \frac{\langle \Delta E \rangle_T}{T_0} = \frac{M}{T_0} \langle \Delta E \rangle_b = T_0 \frac{I_0^2}{M} \kappa_{\parallel} \quad (4.10)$$

where $I_0 = MI_b$ is the total current stored. Now, to compute the power density one needs to know the distribution of the tangential component of the electric field on the

walls of the geometry. For complex geometries simulated in numerical solvers, this is done automatically by the codes, through the computation of the tangential magnetic field and application of the Leontovich boundary conditions (LANDAU; LIFSHITZ, 1960, pp. 280) to get the tangential electric field. When the calculation is performed analytically, not only the impedance, but also the fields in all regions of space must be known. For the round chamber, the symmetry helps and the power per unit area, D_s , is given simply by

$$(D_s)_{\text{circle}} = \frac{P_w}{2\pi bL} \quad (4.11)$$

where L and b are the length and radius of the chamber. For flat chambers, which can be approximated by two infinitely large parallel plates, this problem was solved by Piwinski (1992), whose results were used by Nagaoka (2006) to derive a formula that relates the power density of the parallel plates, at a distance b from the particle, with the one from the round chamber,

$$D_s(x) = \frac{\pi^2}{4 \cosh^2\left(\frac{\pi x}{2b}\right)} (D_s)_{\text{circle}}, \quad (4.12)$$

where x is the transverse position on the plate from the point of minimum distance between the particle and the plate. This function has a maximum value of 2.5 at $x = 0$ and decays to negligible values above $x \approx 4b$.

4.3 Current Dependent Hamiltonian

The usual approach to calculate the effects of the wakes on the beam is by introducing the total wake potential of the machine in the one turn averaged Hamiltonian (BERG, 1996; LINDBERG, 2016). This is justified by the fact that the wake forces are weak and their effects on the beam are very slow, in such a way that the evolution of the beam parameters are counted in a turn by turn basis. In section 4.1 it was defined a method to sum all the wakes of the machine and the average transverse Hamiltonian was defined in section 2.2.6, specifically in equation (2.28), and the average longitudinal Hamiltonian was defined in subsection 2.3.4, by equation (2.39).

The wakes strongly couple the evolution of the transverse dynamics with the longitudinal plane and for this reason, the transverse analysis of collective effects usually deal with the longitudinal Hamiltonian too. On the other hand, the coupling between both transverse planes is very small in normal conditions of machine operation and the wakes do not change this scenario, because of the generally weak coupling contributions from the impedance budget, due to the symmetries of the vacuum chambers. This property allows the simplification of the problem by neglecting the degrees of freedom of one transverse plane when the analysis of the other is being carried out. The analysis of the longitudinal motion is again simplified, without the need of considering both transverse

degrees of freedom of the particles. With these considerations, the one turn Hamiltonian of the particles that is generally considered for collective effects studies is

$$H_n = J_u \left(\nu_u + \xi_u \delta + J_u \frac{A_{xx}}{2} \right) + H_{\parallel} - \frac{\langle I \rangle T_0 V_n(u, z, s)}{(E_0/e)L_0} \quad (4.13)$$

where $\langle I \rangle T_0$ is the average charge per bunch, the subscript n indicates the n -th bunch and the effective wake potential is given according to the ideas developed in section 3.7, specifically by equations (3.31),

$$\begin{aligned} V_n(u, z, s) = \sum_{l \in \mathcal{B}} \frac{I_l}{\langle I \rangle} \sum_{k=-\infty}^{\infty} \int dz' & \left(\lambda_l(z'; s - s_r) W_0(z - z' + s_r) + \right. \\ & u d_l(z'; s - s_r) W_u^D(z - z' + s_r) + \\ & \left. \frac{u^2}{2} \lambda_l(z'; s - s_r) W^Q(z - z' + s_r) \right), \end{aligned} \quad (4.14)$$

where s_r is the retarded position defined in equation (3.30), λ_l and d_l are the longitudinal distribution and dipole moment of the beam, defined in equations (3.32), and W_0 is the primitive function of the longitudinal wake, W'_0 .

4.4 Stationary Effects

4.4.1 Potential Well Distortion

All the effects of the wakes on the beam can be calculated from the Hamiltonian defined in equation (4.13). One particular effect is the distortion of the potential well created by the RF cavities, which changes the equilibrium distribution of the particles and the intrabunch dynamic properties such as the synchrotron tune.

To calculate such effect, we consider a static distribution for the beam and neglect the effects of W_u^D and W^Q , because they are small for a well centered beam in the vacuum chamber. Besides, apart from the effect of cavities, the distortions are dominated by short-range wakes, in such a way that we can neglect the multi-bunch and multi-turn contributions. Under such considerations, the Hamiltonian of the particle becomes

$$H = \frac{\alpha}{2} \delta^2 + U(z) - \frac{I_b T_0}{(E_0/e)L_0} \int dz' \lambda(z') W_0(z - z'), \quad (4.15)$$

which is time-independent. Following the same reasonings performed in section 2.4.1 we notice that equation (2.47) is still valid if we substitute the expression for the longitudinal distribution by

$$\begin{aligned} \lambda(z) = \mathcal{H}(\lambda, z) &:= A \exp \left(\frac{1}{\alpha \sigma_{\delta}^2} \left(-U(z) + \frac{I_b T_0}{(E_0/e)L_0} \int dz' \lambda(z') W_0(z - z') \right) \right), \\ \text{with } A \in \mathbb{R} \left| \int_{-\infty}^{\infty} dz \mathcal{H}(\lambda, z) = 1 \right., \end{aligned} \quad (4.16)$$

which is a transcendental integral equation for the longitudinal distribution. This equation was first proposed and solved by Haïssinski (1973) and for this reason carries his name. Even though analytic solutions exist for some special impedances, such as the one presented by Shobuda & Hirata (1999), in general it must be solved numerically.

The method we adopted to solve this equation was based on an iterative approach. Starting from a very low I_b and an initial guess

$$\lambda_0^{I_b}(z) = A \exp\left(-\frac{U(z)}{\alpha\sigma_\delta^2}\right), \quad (4.17)$$

we iterate

$$\lambda_n^{I_b}(z) = \begin{cases} \mathcal{H}(\lambda_0^{I_b}, z) & \text{if } n = 1 \\ \mathcal{H}\left(\frac{\lambda_{n-1}^{I_b} + \beta\lambda_{n-2}^{I_b}}{1+\beta}, z\right) & \text{if } n > 1 \end{cases}, \quad (4.18)$$

where β is a positive convergence control variable. For each iteration the difference

$$d_n^{I_b} = \int_{-\infty}^{\infty} dz \left(\lambda_n^{I_b} - \lambda_{n-1}^{I_b} \right)^2 \quad (4.19)$$

is calculated and compared to a threshold, ϵ . When $d_n^{I_b} < \epsilon$, convergence is assumed and we set $\rho^{I_b} = \rho_{n_c}^{I_b}$. Then, the current is incremented by a small value $I_b + \Delta I$, with $\Delta I \ll I_b$, and the process is repeated with the initial guess $\rho_0^{I_b + \Delta I} = \rho^{I_b}$. This method does not require the wakes to respect causality and can also be applied to generic RF cavity potentials. The current version of the code implemented cannot handle wake functions that are given by distributions, such as the Dirac's delta function, $\delta(z)$, and its derivative, $\delta'(z)$, which corresponds to the resistive and the inductive wakes, respectively, but it could easily be extended to manipulate such operators. Currently, when we want to simulate these wakes, the effective wake given by the convolution of these distributions with a small gaussian beam is used. For example, in the Sirius simulations, where the bunch length is of the order on a few millimeters, a gaussian bunch of approximately $\sigma_z = 20 \mu\text{m}$ is more than enough to reproduce the results of the $\delta(z)$ and the $\delta'(z)$ wakes.

This implementation was benchmarked with the results presented by Bane & Ruth (1989) for the inductive and resistive impedances, but it fails to converge for the capacitive wakes (negative inductance) when the strength of the perturbation gets close to the well known singularity point of such impedance, as explained by Shobuda & Hirata (1999). However this was not a problem for all the practical cases studied in this work.

4.4.2 Incoherent Tune Shifts

The variation of the transverse oscillation frequency of the bunch as a function of the current is another effect which can be derived from the Hamiltonian of equation (4.13):

$$\Delta\nu_u^n = \frac{(\Delta\mu'_u)^n}{\omega_0/c} = \frac{1}{\omega_0/c} \left(\frac{\partial H_n}{\partial J_u} \Big|_{\langle I \rangle} - \frac{\partial H_n}{\partial J_u} \Big|_{\langle I \rangle=0} \right) \quad (4.20)$$

where the superscript n was used because the tune shift is different for different bunches if the filling pattern is not uniform and the wakes that generates it last for multiple turns. If the distributions are in equilibrium, we can show that:

$$\Delta\nu_u^n = \frac{\langle I \rangle T_0}{2\pi(E_0/e)} \sum_{l \in \mathcal{B}} \frac{I_l}{\langle I \rangle} \sum_{k=-\infty}^{\infty} \int dz' \left(\sqrt{\frac{\beta_u}{2J_u}} \cos(\mu_u) d_l(z') W_u^D(z - z' + s_r) + \right) \quad (4.21)$$

$$\beta_u \cos^2(\mu_u) \lambda_l(z') W_u^Q(z - z' + s_r) \right), \quad (4.22)$$

where it was used $u = \sqrt{2J_u\beta_u} \cos(\mu_u)$. For a well centered beam, $d_l = 0$ and the dipolar wake does not influence the tune, and even in the case when the beam is off centered its average effect is zero, because the term $\cos(\mu_u)$ averages to zero for each particle in the beam. The quadrupolar wake, on the other hand, creates a z dependent tune shift given by,

$$\Delta\nu_u^n = \beta_u (1 + \cos(2\mu_u)) \frac{\langle I \rangle T_0}{4\pi(E_0/e)} \sum_{l \in \mathcal{B}} \frac{I_l}{\langle I \rangle} \sum_{k=-\infty}^{\infty} \int dz' \lambda_l(z') W_u^Q(z - z' + s_r). \quad (4.23)$$

For uniform filling patterns, with M bunches, we can follow the reasonings presented in subsection 3.7.2 and use equation (3.39b) to show that:

$$\Delta\nu_u = -\beta_u (1 + \cos(2\mu_u)) \frac{I_b T_0}{4\pi(E_0/e)} \frac{iM\omega_0}{2\pi} \sum_{p=-\infty}^{\infty} \tilde{\lambda}(pM\omega_0) Z_u^Q(pM\omega_0) e^{-ipM\omega_0 z/c}, \quad (4.24)$$

where I_b is the current per bunch. Averaging this result with the bunch distribution and using the impedance property described in equation (3.23b), we get the average incoherent tune shift of an arbitrary particle in one synchrotron period, or simply, the incoherent tune shift of each bunch:

$$\langle \Delta\nu_u \rangle = \beta_u \frac{I_b T_0}{4\pi(E_0/e)} \overbrace{\frac{M\omega_0}{2\pi} \sum_{p=-\infty}^{\infty} |\tilde{\lambda}(pM\omega_0)|^2 \Im \{ Z_u^Q(pM\omega_0) \}}^{\kappa_u^Q}, \quad (4.25)$$

where κ_u^Q is the quadrupolar kick factor.

4.5 Coherent Motion (Instabilities)

The single-particle dynamics of a typical SLS storage ring was studied in chapter 2, where it was seen that the forces used to control the beam are highly harmonic. This harmonicity makes the beam very susceptible to coherent oscillations against any source of resonant perturbation. The wake fields are a type of perturbation that is always in resonance with the beam because it is self-driven, which also gives an exponential character to the amplitude growth of the coherent oscillations.

The most common way to analyse these instabilities analytically is through the Fokker-Planck equation. Actually, most works in literature do not take into account the

damping and diffusion terms of radiation emission, considering only the Liouville flow of the particles. Under this assumption, the r.h.s. of equation (2.44) is zero and the resulting equation is commonly known in the accelerator community as Vlasov equation. Sacherer (1973) developed a method to solve this equation for low currents and then generalized it for high currents (SACHERER, 1977). This method is widely used and was rederived in several subsequent works, using different basis functions for expansion of the coherent modes. The standard book for study of collective effects, Chao (1993), and the book written by Ng (2006) have a compilation of the solution of Sacherer integral equation for several different types of basis functions.

In this work we will use the solution found by Suzuki (1983) for the longitudinal Fokker-Planck equation and another work of the same author (SUZUKI, 1986) to the transverse plane for the estimates of single and multi-bunch instabilities. We will not follow in detail the derivation of his formulas here, but only highlight the main approximations made, in order to establish an easy interpretation of the results which will be presented in chapter 7. We recommend to the interested reader the original works and the more recent paper written by Lindberg (2016), where all the steps of the derivation are very well justified. Besides, since the Hamiltonian terms of this approach are identical to the solution of the Vlasov equation, all the references presented in the last paragraph are very helpful in understanding the method.

The main idea of the method is to describe the beam distribution as the equilibrium solution of the Fokker-Planck equation, Ψ_0 , plus a small perturbation, Ψ_1 , and analyse its time evolution. If the perturbation increases with time, the beam is considered unstable. Expressing this expansion mathematically we get

$$\Psi(\mathbf{J}, \boldsymbol{\theta}, s) = \Psi_0(\mathbf{J}) + \Psi_1(\mathbf{J}, \boldsymbol{\theta}, s) \quad (4.26)$$

where $\mathbf{J} = (J_u, J_z)$ and $\boldsymbol{\theta} = (\theta_u, \theta_z)$ are the action-angle variables in both planes considered (one transverse and the longitudinal planes). The subscript n was not used in the equation above to identify the bunch number only to simplify the notation, but the expansion above must be made for each bunch separately. Substituting this expression in the Fokker-Planck equation we obtain

$$\frac{\partial \Psi_1}{\partial s} + \{H_0, \Psi_0\} + \{H_0, \Psi_1\} + \{H_1, \Psi_0\} \approx \mathcal{F}(\Psi_0) + \mathcal{F}(\Psi_1) \quad (4.27)$$

where H_0 is the static part of the Hamiltonian defined in equation (4.13), calculated considering the effective wake potential generated by Ψ_0 , and H_1 is the dynamic part of the Hamiltonian, with effective wake potential generated by Ψ_1 . The term $\{H_1, \Psi_1\}$ was neglected in the equation above because it is non-linear in Ψ_1 , thus, much smaller than the other terms.

The next step is to assume a specific form for the distributions:

$$\Psi_0(\mathbf{J}) = f_0(J_u)g_0(J_z) \quad \Psi_1(\mathbf{J}, \boldsymbol{\theta}) = f_1(J_u, \theta_u)g_1(J_z, \theta_z)e^{-i\Omega s/c}, \quad (4.28)$$

where c is the light speed and Ω is the complex frequency which defines the stability of the beam. If the imaginary part of Ω is larger than zero, the beam will be unstable. This expansion is substituted in the Fokker-Planck equation

$$\begin{aligned} & -i\frac{\Omega}{c}f_1g_1 + g_0\frac{df_0}{dJ_u}\frac{\partial H_1}{\partial\theta_u} + f_0\frac{dg_0}{dJ_z}\frac{\partial H_1}{\partial\theta_z} + \\ & g_1\frac{\partial f_1}{\partial\theta_u}\frac{\partial H_0}{\partial J_u} + f_1\frac{\partial g_1}{\partial\theta_z}\frac{\partial H_0}{\partial J_z} = g_1\mathcal{F}(f_1) + f_1\mathcal{F}(g_1) \end{aligned} \quad (4.29)$$

where the facts that Ψ_0 is the equilibrium distribution of the Fokker-Planck equation and that the static Hamiltonian is function only of the action variables were used.

Assuming the ring is uniformly filled with M equally spaced bunches, by symmetry, their equilibrium distribution must be the same and the time evolution of the perturbations in each bunch must be equal, only a phase difference between them is allowed. Since the system is periodic, we can express an arbitrary phase among the bunches in the coupled-bunch basis, in such a way that, for a pure eigen-mode of this basis, the distribution of the l -th bunch can be written as a function of the distribution of the n -th bunch by

$$\Psi_{1l} = (f_1g_1)_n e^{-i\Omega s/c} e^{i\mu(l-n)/M} \quad (4.30)$$

where $\mu \in [0, M - 1]$ is the coupled-bunch mode. With this consideration, in order to solve the problem, instead of solving the Fokker-Planck equation for M bunches in the ring, we need to solve for the M coupled-bunch modes. This transformation does not change the form of equation (4.29) because the terms affected are the ones related to the wake potential, which are implicitly defined through H_0 and H_1 . The eigen frequency Ω also changes the implicit subscript n to the implicit subscript μ .

Several approximations are performed at this point. First, the stationary effects of the effective wake potential are neglected and the quadratic potential well of equation (2.40) is considered in the longitudinal plane. This perfectly harmonic potential defines a gaussian distribution for g_0 and a constant synchrotron tune, as shown in section 2.4.1. Even though this is a good approximation for low bunch currents, which is the case of multi-bunch operations in storage rings, the terms neglected here can have a significant contribution in the current range where single-bunch instabilities happen. Besides, this approximation exclude the possibility of using the equations derived here to study instabilities in the presence of a lengthening cavity in the ring, which creates a quartic potential well. There are generalizations of this method in literature to include synchrotron tune shifts, such as the work of Chin *et al.* (1983), or to consider the quartic potential well, by Chin (1983), but they will not be used in this work.

4.5.1 Longitudinal Plane

Another approximation consists in breaking the analysis in two, one for each plane. When the longitudinal plane is analysed, the effects of the dipolar and quadrupolar terms of the wake potential are neglected and the transverse perturbation f_1 can be set to unit. Under this approximation, the Fokker-Planck equation reads

$$\left(-i \frac{\Omega}{c} + \frac{\omega_z}{c} \frac{\partial}{\partial \theta_z} \right) g_1 + \frac{dg_0}{dJ_z} \frac{\partial H_1}{\partial \theta_z} = \mathcal{F}(g_1). \quad (4.31)$$

This equation can be solved expanding the function g_1 in azimuthal modes m and radial modes k :

$$g_1(I_z, \theta_z) = e^{-I_z} \sum_{k=0}^{\infty} \sum_{m=-\infty}^{\infty} a_k^{(m)} f_k^{(|m|)}(I_z) e^{im\theta_z}, \quad (4.32)$$

where $I_z = J_z / (\sigma_z \sigma_\delta)$ is the normalized action,

$$f_k^{(|m|)}(I_z) = \sqrt{\frac{k!}{(|m|+k)!}} I_z^{|m|/2} L_k^{|m|}(I_z), \quad (4.33)$$

and $L_k^{|m|}(I_z)$ is the generalized Laguerre polynomial (Wikipedia Contributors, 2018). The important property of this basis functions is their orthogonality. The azimuthal expansion is orthogonal under the interval $(0, 2\pi)$, which is the domain of the phase-space angle θ_z , and the functions $f_k^{(|m|)}$ are orthogonal under

$$\int_0^\infty dx e^{-x} f_k^{(|m|)}(x) f_l^{(|m|)}(x) = \delta_{kl}, \quad (4.34)$$

where δ_{kl} is the Kronecker delta function.

With this expansion it is possible to show that the Fokker-Planck equation can be written as an infinite matrix equation and Ω is given by its eigenvalues:

$$\left(\frac{\Omega}{\omega_z} - m + i \frac{|m| + 2k}{\tau_z \omega_z} \right) a_k^{(m)} = i \sum_{n=-\infty}^{\infty} \left(M_{k,l}^{m,n} + O_{k,l}^{m,n} \right) a_l^{(n)}, \quad (4.35)$$

where

$$M_{k,l}^{m,n} = \frac{I_b M \omega_0 \alpha}{2\pi(E_0/e)(\omega_z \sigma_z/c)^2} i^{(m-n)} m \sum_{p=-\infty}^{\infty} \frac{Z_L(\omega_p)}{\omega_p} g_{mk}(\omega_p) g_{nl}(\omega_p) \quad (4.36)$$

is the mode-coupling matrix and $O_{k,l}^{m,n}$ is a real matrix, called diffusion matrix, and is given by Suzuki (1983). The modes of oscillation of the beam are given by:

$$g_{mk}(\omega_p) = \frac{1}{\sqrt{k!(|m|+k)!}} \left(\frac{\omega_p \sigma_z}{\sqrt{2c}} \right)^{|m|+2k} \exp \left(- \left(\frac{\omega_p \sigma_z}{\sqrt{2c}} \right)^2 \right), \quad (4.37)$$

with

$$\omega_p = \omega_0 (pM + \mu + m\nu_z). \quad (4.38)$$

This eigenvalue equation must be truncated at some value of radial and azimuthal modes in order to be handled numerically. The specific truncation value, in general, depends on the impedance spectrum.

There are two types of instabilities which can be explained by the equation (4.35): the mode-coupling instabilities, which are generated by the broad-band impedance of the machine, and the coupled-bunch instabilities, generally created by RF cavities. The former is characterized by the coupling between two different modes. For low beam intensities, the real part of the frequency of two adjacent azimuthal modes differ from each other by the synchrotron frequency. As the beam current increases, these frequencies are shifted by the imaginary part of the impedance and, when they are close to each other, the real part of the impedance couple them. The two real frequency becomes complex, one being the conjugate complex of the other, which means one of them becomes unstable, if the value of the imaginary part is larger than the radiation damping effect. This instability is also known as microwave instability or turbulent bunch-lengthening and is characterized by the increase of the energy spread of the beam above given current threshold.

The coupled-bunch instabilities generally happen at small bunch currents, because they depend on the total current of the ring. This instability is caused by narrow-band impedances and it happens due to the asymmetry in the sampling of the real part of the impedance, caused by the shift $\mu + m\nu_z$ in the expression for ω_p . Since this type of instability happens at low values of bunch current, it is often not necessary to solve the eigenvalue problem defined by equation (4.35), in such a way that only the diagonal terms of the most prominent radial mode of the mode-coupling matrix are enough to calculate the threshold:

$$\frac{\Omega}{\omega_z} - m + i \frac{|m|}{\tau_z \omega_z} = \frac{I_b M \omega_0 \alpha}{2\pi(E_0/e) (\omega_z \sigma_z/c)^2} m \sum_{p=-\infty}^{\infty} \frac{Z_L(\omega_p)}{\omega_p} g_{m0}^2(\omega_p). \quad (4.39)$$

Actually, the diagonal terms of the mode-coupling matrix are used in a much more general scope than the estimative of the coupled-bunch instabilities. The quantity

$$\left. \frac{Z}{n} \right|_{\text{eff}} = \frac{\sum_{p=-\infty}^{\infty} \frac{Z_L(\omega_0(Mp+\nu_z))}{(Mp+\nu_z)} g_{m0}^2(\omega_0(Mp + \nu_z))}{\sum_{p=-\infty}^{\infty} g_{m0}^2(\omega_0(Mp + \nu_z))} \quad (4.40)$$

is called effective impedance and is used together with the loss factor, defined in section 4.2, as a figure of merit to characterize the impedance budget of a storage ring.

4.5.2 Transverse Plane

The effects of the longitudinal impedance are neglected in the transverse plane analysis and even though there are some works in literature which consider the quadrupolar impedance (LINDBERG, 2016), in this work we will only take into account the dipolar

impedance. In general, the quadrupolar wake helps increasing the threshold of the instabilities, but only when its strength is comparable with the dipolar wake. Since this is not the case for the Sirius storage ring, this approach is well justified.

Without the longitudinal impedance, the term involving the derivative of H_1 with respect to the longitudinal angle variable θ_z can be neglected because it is much smaller than the other terms in equation (4.29). With this simplification, a solution for f_1 can be found:

$$f_1 = D\sqrt{J_u} \frac{df_0}{dJ_u} e^{i\theta_x} \quad (4.41)$$

which is a rigid dipole motion of in the transverse phase space. This dipole mode varies longitudinally according to the function g_1 , which remains to be defined. After inserting the solution for f_1 in equation (4.29), the resulting equation for g_1 is very similar to the one of the longitudinal plane, in such a way that the solution is given by:

$$\left(\frac{\Omega - \omega_u}{\omega_z} - m + i \left(\frac{1}{\omega_z \tau_u} + \frac{|m| + 2k}{\tau_z \omega_z} \right) \right) a_k^{(m)} = -i \sum_{k=0}^{\infty} \sum_{m=-\infty}^{\infty} (M_{k,l}^{m,n} - O_{k,l}^{m,n}) a_l^{(n)} \quad (4.42)$$

where $O_{k,l}^{m,n}$ is the same diffusion matrix of the longitudinal plane analysis and

$$M_{k,l}^{m,n} = \frac{I_b M \omega_0}{4\pi(E_0/e)\omega_z} i^{m-n} \sum_{p=-\infty}^{\infty} \beta_u Z_u^D(\omega_p) g_{mk}(\omega_p - \omega_\xi) g_{nl}(\omega_p - \omega_\xi). \quad (4.43)$$

where we notice the local betatron function multiplies the impedance, as expected from the reasonings of section 4.1. In the case of the transverse planes the sampling frequency changes to include the effect of the transverse betatron oscillations of the beam,

$$\omega_p = \omega_0(Mp + \mu + \nu_u + m\nu_z), \quad (4.44)$$

Analogously to the longitudinal plane, two types of instabilities are explained by the equation above, one driven by the broad-band impedance, and another by narrow-band impedances. In this case, however, the former type, which is known as Transverse Mode-Coupling Instability (TMCI), generally is associated with beam loss, imposing a limit to the maximum current which can be stored in the ring. The same approximation made in the last section, can be done here too in order to calculate the multi-bunch instabilities:

$$\left(\frac{\Omega - \omega_u}{\omega_z} - m + i \frac{1}{\omega_z \tau_u} + i \frac{|m| + 2k}{\tau_z \omega_z} \right) = -i \frac{I_b M \omega_0}{4\pi(E_0/e)\omega_z} \sum_{p=-\infty}^{\infty} \beta_u Z_u^D(\omega_p) g_{m0}^2(\omega_p - \omega_\xi). \quad (4.45)$$

From the diagonal terms of the mode-coupling matrix we can define the dipolar kick factor of the impedance as:

$$\kappa_u^D = \frac{M \omega_0}{2\pi} \sum_{p=-\infty}^{\infty} Z_u^D(\omega_0(Mp + \nu_u)) g_{00}^2(\omega_0(Mp + \nu_u)) \quad (4.46)$$

which is the main figure of merit to represent an impedance budget.

4.6 Tracking Code

The structure of the tracking code used is very similar to the one described in Ref. Sá *et al.* (2015), with the additional feature of including damping and quantum excitation terms for the single particle dynamics. Wake field kicks can be included in two different ways:

General Wakes: In this case the wakes do not need to respect the causality condition and are passed to the code as interpolation tables. The code uses the particle in cell (PIC) approach, where the total simulation length for the longitudinal direction, L_c , is segmented into N_c intervals and the approximate beam distribution is calculated from the number of macroparticles in each cell. Then, the convolution theorem is used to calculate the kick curve(BASSI *et al.*, 2016b), which is interpolated according to each particle's position;

Resonators: The parameters of the resonators, (R_s, ω_r, Q) , are used as input. The code does not use the PIC approach, each of the N_p macroparticles being simulated interact with each other and the wake is calculated through the sum of the potentials left by each particle in each resonator.

In the second method N_p is the only variable to be tested for the result convergence analysis, while for the first method the additional variable N_c is also important. This inconvenience can be avoided if the number of slices is set in such a way that the grid length satisfies the Nyquist theorem for the highest relevant frequency of the impedance used in tracking,

$$\Delta z_c = L_c/N_c > \frac{2}{f_{\max}}. \quad (4.47)$$

This code was benchmarked with SPACE(BASSI *et al.*, 2016b) and Elegant(BORLAND, 2000).

5 IMPEDANCE MODELING

In this chapter the impedance modeling of some storage ring components will be discussed. The components described below are the ones for which the modeling is not trivial and required detailed analysis of some key aspects. The gathering of all the components and analysis of the whole impedance budget will be performed in the next chapter.

5.1 Standard Chamber

Sirius standard vacuum chamber will be made of copper with a round cross-section with 12 mm internal radius, b , which is considerably smaller than the chambers of 3rd GLS, as shown by Nagaoka & Bane (2014). This small chamber does not only affect the resistive wall impedance, which scales with $1/b^3$ for the transverse planes, but also all the other components' impedances, because of the proximity of the walls with the beam (NAGAOKA; BANE, 2014). In this section we will describe the adopted model for the impedance of the standard chamber of the storage ring, focusing on the effect of the NEG and the low-frequency contribution from the Laslett incoherent impedance generated by the magnetic poles of the dipoles. Table 2 shows the values of the main parameters of this model.

5.1.1 Effect of NEG Coating

The solution adopted for the vacuum in Sirius employs the mixed and concomitant use of localized and distributed pumping, where the last is achieved through coating the vacuum vessel with NEG (BENVENUTI *et al.*, 1998; PRODROMIDES, 2002). In 2012 the

Table 2 – Wall Impedance parameters.

Parameter	Value	Unit
Copper conductivity	59.0	MS m ⁻¹
Copper relaxation time	27	fs
NEG conductivity	1.0	MS m ⁻¹
NEG thickness	1.0	μm
Chamber radius	12.0	mm
Chamber thickness	1.0	mm
Total length	500	m
Dipole length	100	m
Chamber shape	round	

LNLS signed a license agreement with CERN to develop NEG coating in-house and since then the Vacuum Group has been working on the development of the infrastructure and improvement of techniques for production, deposition and in-situ activation of NEG in order to produce coatings with low surface roughness and good thickness uniformity in all vacuum chambers of the ring (SERAPHIM *et al.*, 2015; ROCHA, 2017).

The presence of NEG changes the electromagnetic properties of the inner surface of the chamber and contributes to the impedance increase. This effect was first noticed in an impedance measurement made in ELETTRA by Karantzoulis *et al.* (2003), where the authors described an anomalous increase of the tune shift with current after the installation of NEG-coated aluminum chambers for IDs. Nagaoka (2004b) tried to explain the measured results using the multi-layer formulas for the transverse impedance, but quantitative agreement was only obtained using excessively large resistivities for NEG. Such experimental results created some concern in the community and the effect of the roughness of the inner surface of the chamber was hypothesized as a possible explanation. Nagaoka *et al.* (2007) studied such an effect when analysing Soleil storage ring measurements, where the impedance budget of the machine was not enough to account for the bunch lengthening observed, and concluded that the impedance of the measured roughness could not explain the additional impedance necessary to fit the experimental results.

There are expressions in the literature to estimate the impedance of a rough surface, such as those of Bane *et al.* (1997) which are based on numeric calculations, and those of Stupakov *et al.* (1999) that are calculated analytically. Their predictions account for an inductive impedance in low frequency, where the characteristic length of the surface protrusions is much smaller than the bunch length, and real impedance for very large frequencies. However, one of the considerations for the derivation of such formulas is that the surface is perfectly conducting, which means all the image charges will flow by the rough surface. It seems reasonable that for finite conductivity chambers, the wall currents will penetrate the material and the effect of the roughness should be even smaller.

Given all the considerations presented above, the initial model adopted for the standard Sirius vacuum chamber is a round smooth infinite three-layer pipe, consisting of: 1 μm of NEG coating, 1 mm of copper and air to infinity. As shown in Table 2 the value used for NEG conductivity was 1 MS m^{-1} . This value is the measurement average of the NEG resistivity as a function of the frequency made by Koukovini-Platia *et al.* (2014). Since this measurement was performed for a very short frequency range, only from 10 to 11 GHz, and considering that other factors may influence the NEG conductivity, such as the activation process and aging effects, we calculated the impedance for several values of conductivity, as shown in Figure 11a. Also shown in the figure is the spectrum, in arbitrary units, of a gaussian bunch with $\sigma = 2.5\text{mm}$, which is the natural bunch length of the Sirius storage ring. Notice that the dependency of the impedance for the frequency

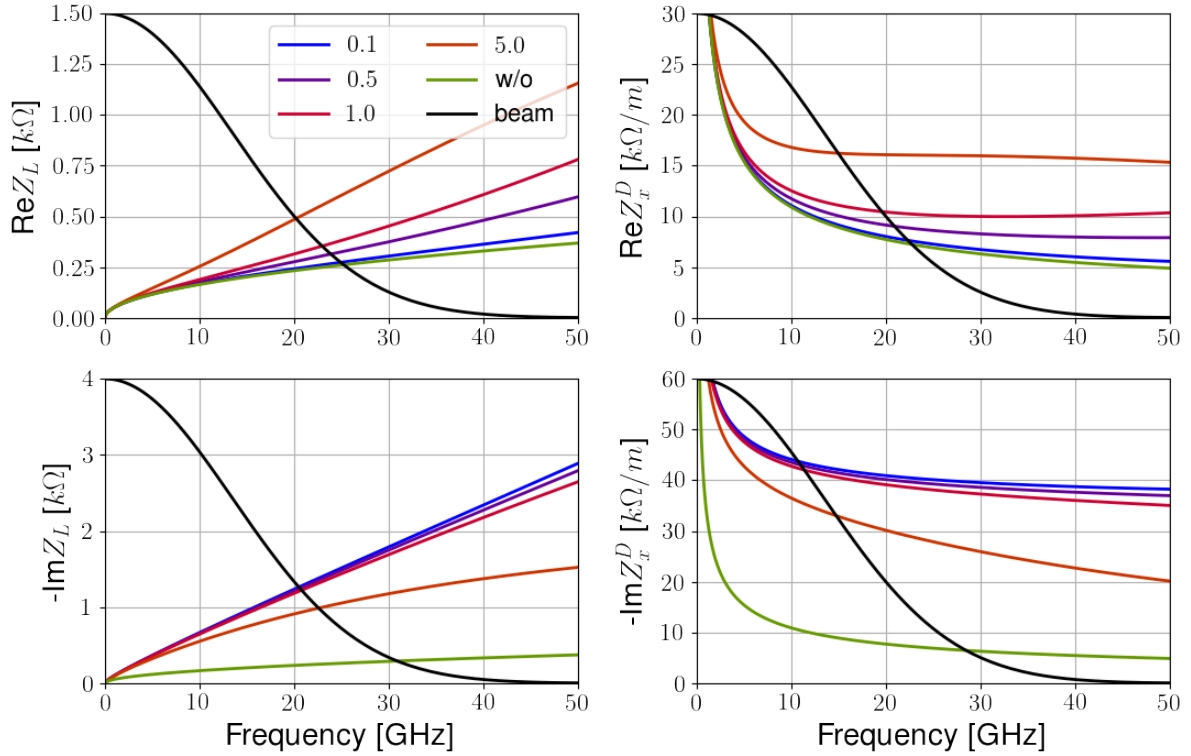
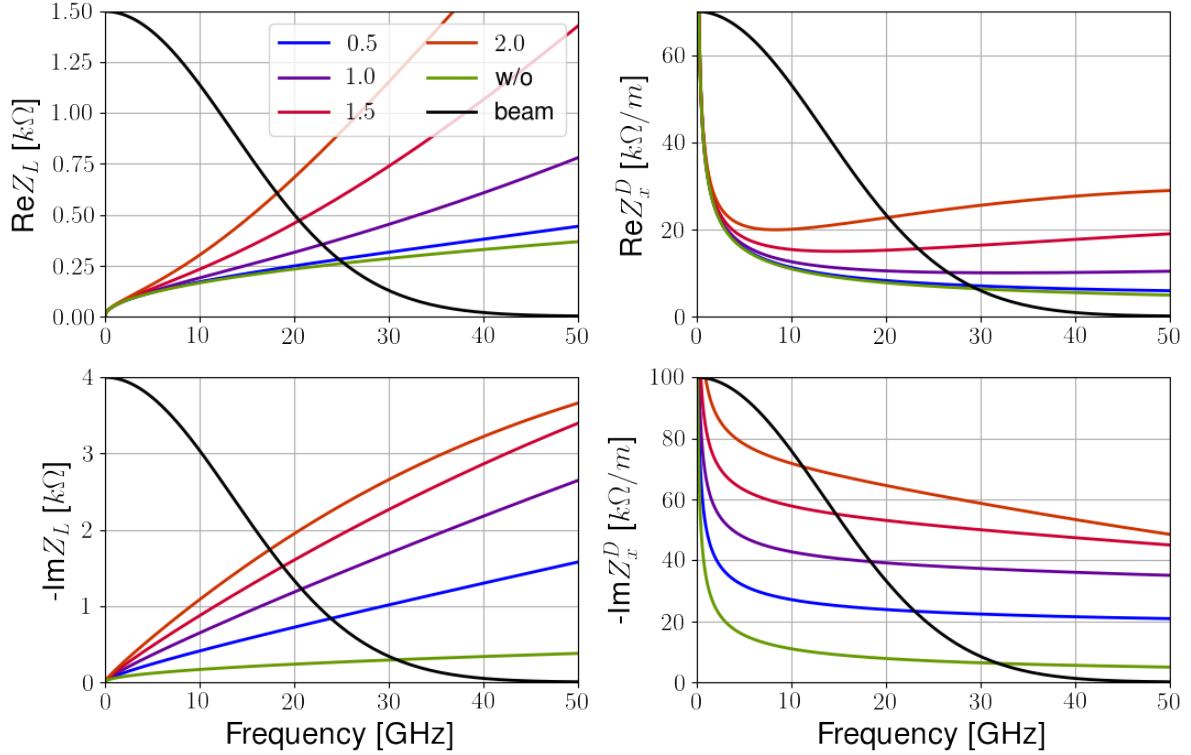
(a) Wall Impedance as a function of NEG conductivity (in MS m^{-1}).(b) Wall Impedance as a function of NEG thickness (in μm).

Figure 11 – Wall impedances as a function of the frequency for several values of NEG conductivity (a) and coating thickness (b). The nominal values for both are presented in Table 2. Also shown in black is the spectrum of a 2.5 mm gaussian bunch.

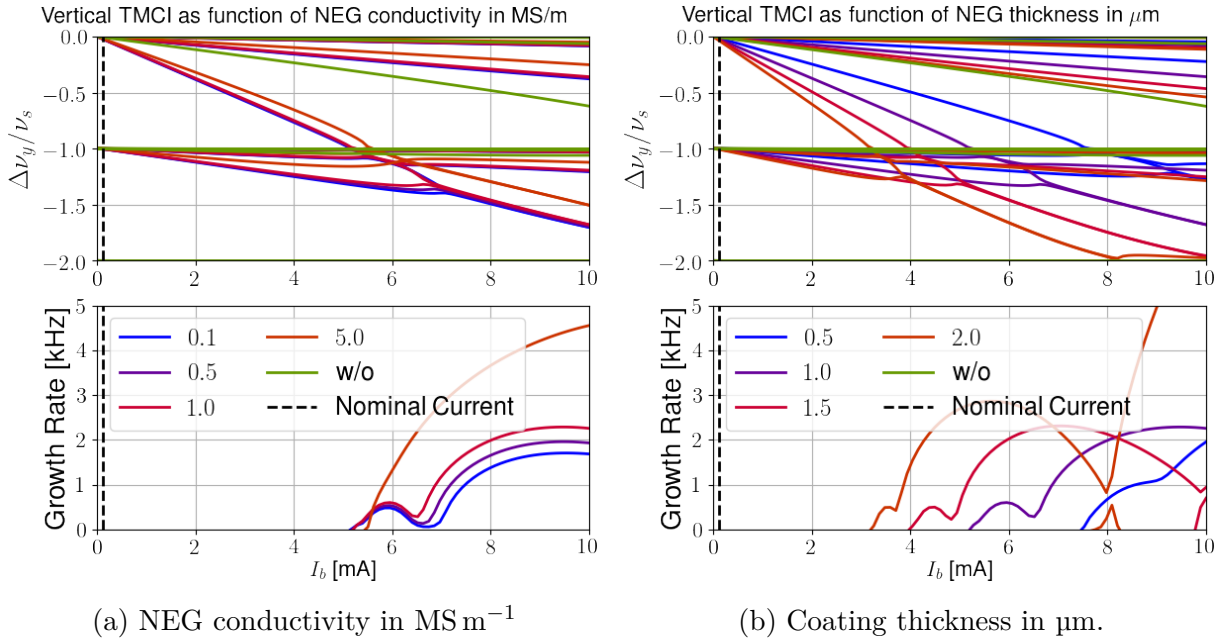


Figure 12 – Simulations of TMCI for single bunch in the machine using the parameters of the first phase of operation of the storage ring, as shown in Table 1, and for several different values of (a) NEG conductivity and (b) coating thickness.

range of interest is very non-linear, being almost saturated for lower conductivities, which means that variations on the conductivity does not have a strong impact on the beam behavior. We can also infer from the figure that the effect of NEG on the impedance is mostly inductive in both planes, where an increase of a factor of 3 in the imaginary impedance is noticeable.

The increase of the imaginary impedance is clearly stands out in Figure 12a, which shows simulations of transverse single-bunch tune shift and the TMCI, and Figure 13, which shows the loss factors and the effective longitudinal impedance.

A study of the impedance dependence on the thickness of the NEG coating was also carried out, as shown in Figure 11b, Figure 12b and Figure 13. Different from the conductivity case, this parameter has strong influence on the value of the impedance, affecting almost linearly the imaginary part in both planes and quadratically the loss factor.

From the analysis of Figure 12 we note that, even though the NEG coating has a strong influence on the impedance, the TMCI threshold induced exclusively by its contribution is much above the nominal single bunch current for uniform filling of the machine and does not compromise the operation. Besides, as will be seen with further details in the next sections, the increased longitudinal inductive impedance will contribute to the bunch lengthening, which helps decreasing IBS effects and improving Touschek lifetime.

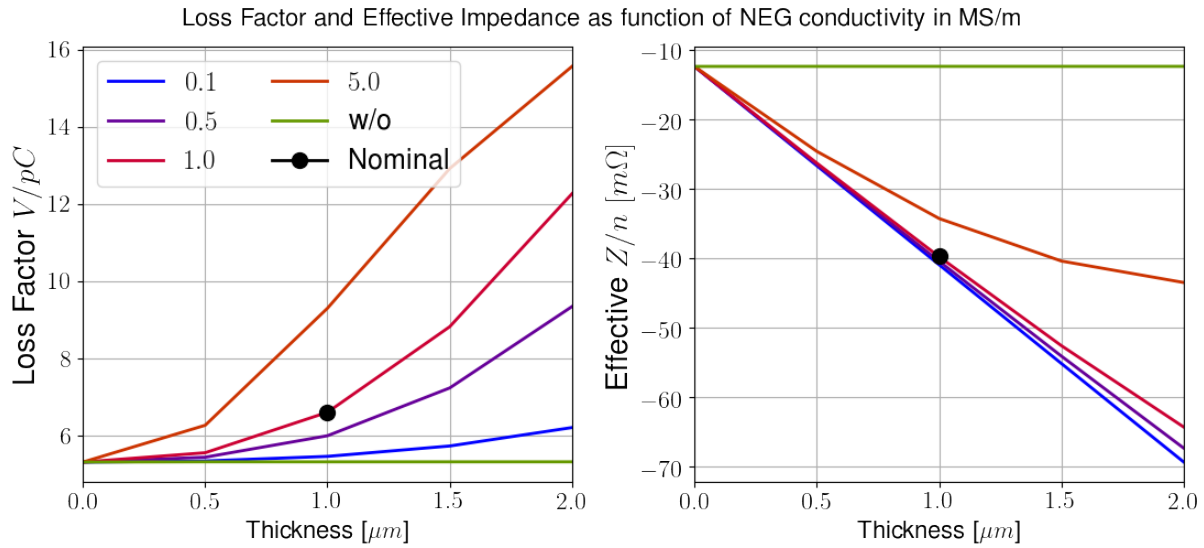


Figure 13 – Loss factor (left) and effective longitudinal impedance (right) for a 2.5 mm bunch as a function of the coating thickness for several different values of NEG conductivity, in MS m^{-1} .

A complete analysis of the impedance of a NEG coated chamber is provided by Shobuda & Chin (2017), who explains the existence of several regimes along the spectrum, where different mechanisms dominate the impedance behavior. For example, the skin depth of NEG at 30 GHz is approximately $3 \mu\text{m}$, which is three times larger than the thickness of the coating used in Sirius chambers, thus, in the frequency range analysed so far, from 1 to 50 GHz, most of the losses happens in the copper chamber and that is why the impedance is mostly inductive. For higher frequencies the NEG contribution will be resistive, and for lower it will not have any effect on the impedance.

5.1.2 Low-Frequency Impedance

One particular frequency range of interest for Sirius is the very low part of the impedance, which goes from 0 Hz to a few MHz, because this range defines two important mechanisms which influence the dynamics of the beam. The first is the traditional resistive-wall instability, defined by the harmonic of the betatron frequency with lowest frequency, being numerically equal to the fractional part of the tune times the revolution frequency. The second is the incoherent tune-shift induced by the quadrupolar impedance, which depends on the direct current (DC) value of the impedance. This mechanism was introduced in section 4.4.2 and is quantitatively described by equation (4.25). Considering that the resistive-wall impedance has a very sharp peak at DC, this term has strong influence on the whole sum that defines the tune-shifts, mainly for multi-bunch operations. Actually the infinitely thick wall theory, from Gluckstern *et al.* (1993) and Yokoya (1993), provides divergent results for this tune-shift. Nagaoka (2001) solved this problem in explaining measurements at ESRF using a method developed by Heifets (1998) and

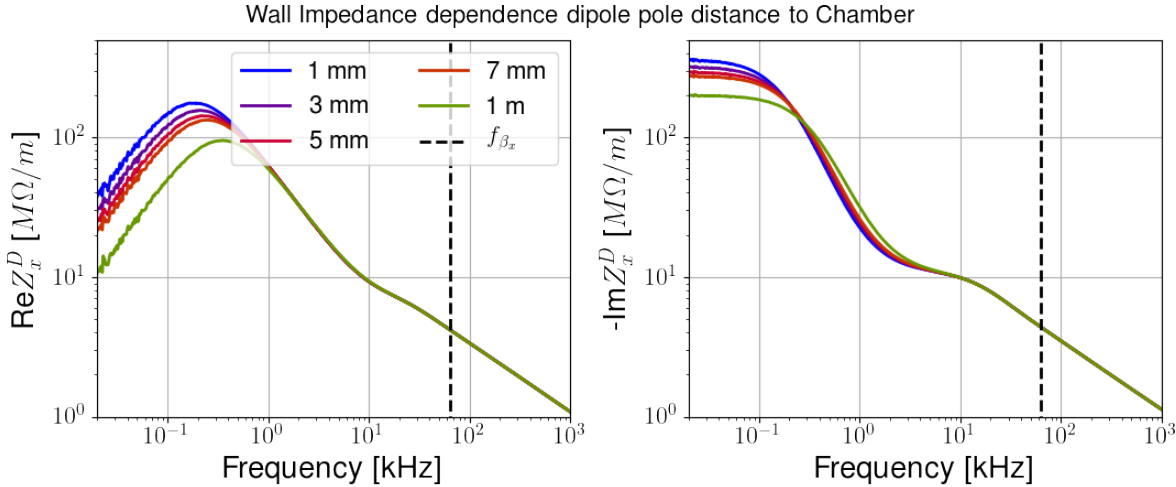


Figure 14 – Low frequency impedance for different values of distance of the magnetic poles of dipoles to the exterior part of the vacuum chamber.

explained in detail by Chao *et al.* (2002), which employed the concept of the diffusion time of the magnetic field in the chamber to truncate the multi-turn effect of this impedance as a way of considering the finite thickness of the wall. Later, Shobuda & Yokoya (2002) showed that such approach is not needed when the impedance already takes into account the finite thickness.

The impedance at very low frequencies is very difficult to calculate because it depends on what is outside the vacuum chamber, due to the increasingly large skin depth. Shobuda & Yokoya (2002) pointed this possibility out when they tried to explain the tune shifts observed in KEKB with their finite-thick wall theory. With the multi-layer formulas used in this work it is possible to see the influence of materials outside the chamber on the impedance, as shown Figure 14, where the infinitely thick layer of air was substituted by a variable gap of air and a layer of FeSi ($\mu_r = 40$), used in the magnetic poles of Sirius magnets. Note that the first betatron line, responsible for the coherent tune-shifts and the resistive-wall instability is completely determined by the copper chamber, but the zero frequency impedance depends on the distance of the magnet to the external part of the wall. One can argue that, since Sirius vacuum chamber is round, this dependence is not important because there is no quadrupolar impedance. However, considering that the impedance at these frequencies depend on the materials outside the chamber, it is reasonable to think it will depend on how they are distributed too. Remembering that the storage ring is filled with magnets with cores made out of ferromagnets, and noticing that only dipoles can generate a quadrupolar impedance because the symmetry of the poles of quadrupoles and sextupoles does not allow such component, we considered this effect on the total budget.

According to Zotter & Kheifets (1998, p. 340) the indirect space-charge impedance

in the ultra-relativistic limit at zero frequency (for penetrating fields) is given by

$$Z_y = i \frac{Z_0 L}{\pi} \left((\varepsilon_1 - \xi_1) \frac{1}{h_1^2} + (\varepsilon_2 - \xi_2) \frac{1}{h_2^2} \right) \quad (5.1)$$

where the indices h_1 and h_2 refer to the electric and magnetic gaps, respectively, ε_i and ξ_i are the Laslett (1963) coefficients for incoherent and coherent tune shifts associated with the electric (1) and magnetic (2) fields, given by

$$\begin{aligned} \varepsilon_1 = \varepsilon_2 = 0, \quad \xi_1 = \xi_2 &= \frac{1}{2} \quad \text{for round chambers,} \\ \varepsilon_1 = \frac{\varepsilon_2}{2} = \frac{\pi^2}{48}, \quad \xi_1 = \xi_2 &= \frac{\pi^2}{16} \quad \text{for flat chambers.} \end{aligned} \quad (5.2)$$

The coherent coefficients ξ_i are a particular case of the dipolar impedance, while the incoherent coefficients ε_i of the quadrupolar impedance. This way, we can interpret the low-frequency limit of the impedances shown in Figure 14 as the sum of the electric and magnetic incoherent space-charge impedance. In fact, a direct evaluation of equation (5.1) for the electric boundary using h_1 equals to the internal radius of the vacuum chamber gives an impedance of $208 \text{ M}\Omega$, which is very similar to the value of $200 \text{ M}\Omega$ taken from the curve where the magnet is far from the beam. The magnetic part gives a contribution of $117 \text{ M}\Omega$ when we consider that the dipole is 16 mm away from the center of the chamber, which corresponds to the 3 mm curve in the plot. This value is also close to the $120 \text{ M}\Omega$, obtained by the subtraction of the 3 mm curve and the 1 m curve. With all the considerations above, we defined the quadrupolar impedance for the Sirius vacuum chambers as¹

$$Z_y^Q(\omega) = -Z_x^Q(\omega) = \left(\left(Z_y^D(\omega) \right)_{\text{round}}^{3 \text{ mm}} - \left(Z_y^D(\omega) \right)_{\text{round}}^{1 \text{ m}} \right) \frac{\varepsilon_2^{\text{flat}}}{\xi_2^{\text{round}}} \frac{L_D}{L_T} \quad (5.3)$$

where L_T is the total length considered for the chamber, L_D is the length covered by dipoles and the fraction involving the Laslett coefficients is the conversion from the round dipole factor to the flat quadrupole factor. Note that if we had used the Yokoya factors in the equation above we would get an impedance a factor of two lower. This approach is not correct since these factors were derived under the assumption of infinitely thick chambers, which means they are only valid in the frequency range where the electric and magnetic fields are shielded at the same place, in other words, when they do not penetrate the material.

5.2 Kicker Chambers

The Sirius storage ring will have two kicker magnets, one standard dipole kicker and one non-linear kicker. While the former will be used for on-axis injection in the

¹ As the Sirius dipoles are straight magnets with inclined poles to produce a quadrupole gradient and the chambers, as well as the beam trajectory, are curved along them, the distance of the poles to the chamber is variable. Nevertheless, 3 mm is a good estimate for the average distance and that is why it was used in the definition above.

Table 3 – Main parameters of the kicker magnet for impedance modeling

Parameter	Symbol	Value	Unit
Capacitance	C_{bb}	30.0	pF
Parasitic resistance	R_s	500	Ω
Pulser circuit resistance	R_e	50.0	Ω
Ferrite permittivity		12	
Ferrite initial permeability	μ_i	1600	
Ferrite saturation frequency	ω_s	20.0	Mrad s^{-1}
Ceramic permittivity		9.3	
Titanium conductivity		1.6	MS m^{-1}
FeSi conductivity		2.0	MS m^{-1}
FeSi permeability		40	

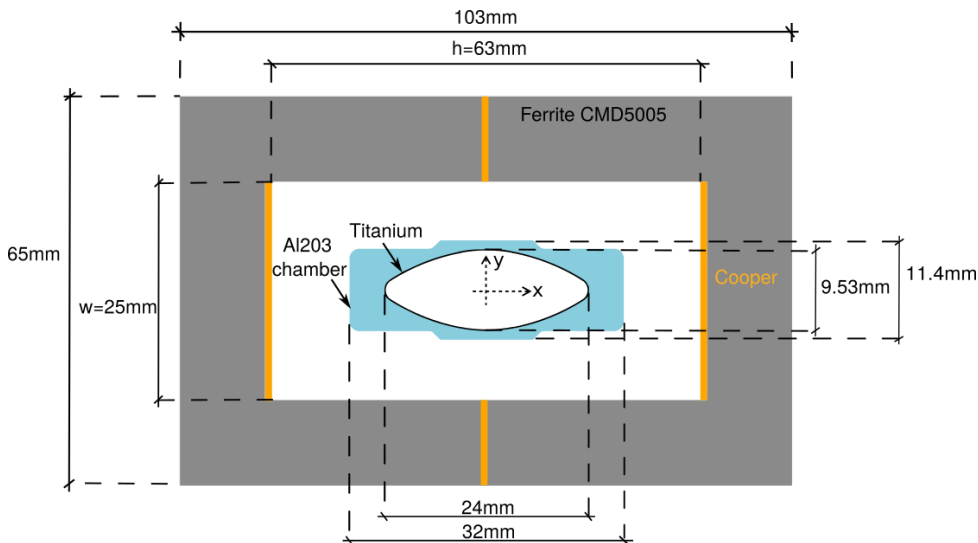


Figure 15 – Cross section of the kicker window-frame magnet that will be used in Sirius storage ring.

commissioning of the light source, and as a pinger magnet for machine studies, the latter will be used for injection in top-up mode (LIU *et al.*, 2016b). Even though the topologies of the two magnets are very different, their vacuum chamber will be identical: a ceramic chamber, coated with 10 μm of Titanium. This means that at high frequencies their impedance will be identical too. Below we describe the considerations on the modeling of the impedance of the dipole kicker magnet and then extrapolate to the case of the non-linear kicker. Table 3 shows the main values of the parameters used to model these components.

Figure 15 shows an schematic drawing of a transverse section of the window-frame dipole kicker magnet that will be used in Sirius storage ring. This type of magnet acts on the beam by the passage of a pulsed current, generated by an external pulser circuit, on the lateral copper plates. This current induces a magnetic field around the plates that is guided by the ferrite to create an almost constant vertical field at the inner gap of the

magnet. The copper plates located at the center of the magnet are important to increase the magnetic impedance for the field lines, forcing them to close the loop by the air gap and not around the ferrite blocks.

There are two main contributions to the impedance of this type of magnet: the losses and resonances defined by the materials of the vacuum chamber and the window-frame itself; and the coupled flux of the beam with the external circuit that feeds the magnet. While the first contribution dominates the high frequency part of the spectrum, the second is important at low frequencies.

The coupled flux, first modeled by Nassibian & Sacherer (1979) and improved by Davino & Hahn (2003), treats the window-frame as a transformer that couples the beam to the external circuit impedance, $Z_g(\omega)$, characterized by the impedance termination of the pulser circuit and the residual capacitances and resistances of the device, which can be accessed via twin wire measurements (MOSTACCI; CASPERS, 2016) with the endplates open and short circuited, as explained by Davino & Hahn (2003). This model predicts impedances for the coupled flux given by

$$Z_{\parallel}^* = \frac{\Delta^2}{h^2} \frac{i\omega L_2 Z_g}{i\omega L_2 + Z_g}, \quad Z_x^D = \frac{c}{\omega \Delta^2} Z_{\parallel}, \quad Z_y^D = Z_x^Q = 0 \quad (5.4)$$

where Δ is a transverse offset of the beam, $L_2 = \mu_0 L h / w$, L is the length of the magnet and h and w are the transverse dimensions as defined in Figure 15.

Equation (5.4) predicts zero vertical impedance and, for a well centered beam, $\Delta = 0$, the longitudinal impedance is zero too. Considering there is no measurements yet for the circuit impedance, $Z_g(\omega)$, of the kicker magnet, the parametric dependency described by Davino & Hahn (2003)

$$Z_g(\omega) = R_e + \frac{1}{\frac{1}{R_s} + i\omega C_{bb}} \quad (5.5)$$

was used for Sirius, where C_{bb} is the busbar capacitance, equal to 30 pF for their kicker, R_s is a resistance in parallel with the capacitance to account for the ferrite losses, equals to 490 Ω in their case, and R_e is the matching impedance of the external circuit, which we considered equal to 50 Ω. Figure 16 shows the coupled flux horizontal impedance for some values of C_{bb} and R_s , where the resonant behavior created by the parallel association of the inductance L_2 with the capacitance C_{bb} is can be noticed. In general, the variation of the parameters influences the positioning, intensity and width of the resonant peaks, all around a few MHz, but do not change the value of the imaginary impedance at lower frequencies. As will be shown below, the Titanium coating in the vacuum chamber shields the beam electromagnetic fields starting from approximately the frequency range of these peaks, thus, their attenuation is expected. The low frequency impedance will not be attenuated, and will influence the coupled-bunch motion, but not the incoherent tune shifts, because there is no quadrupolar impedance associated with this mechanism.

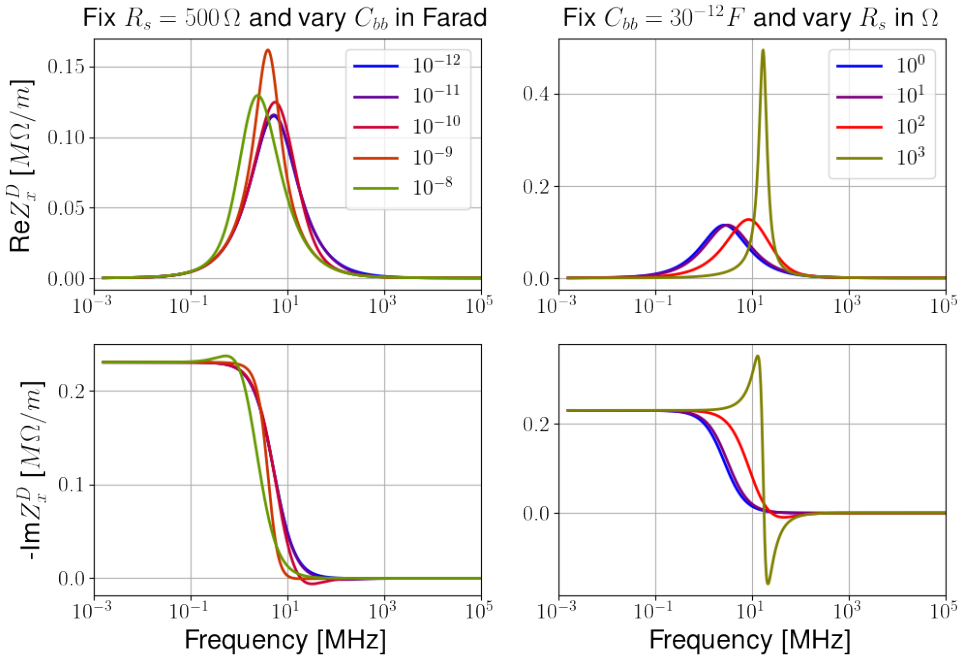


Figure 16 – Coupled flux impedance of the dipole kicker magnet as a function of the frequency for several values of capacitance (left) and resistance (right).

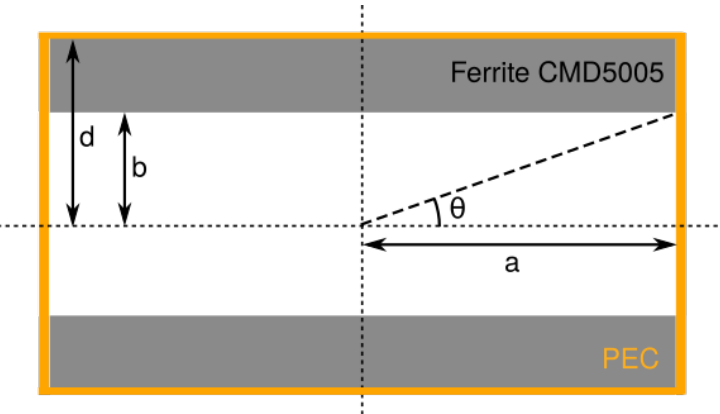


Figure 17 – Tsutsui model for the window-frame kicker magnet.

Regarding the uncoupled flux, there are no formulas in the literature to estimate the impedance of an out-of-vacuum window-frame magnet as the one presented in Figure 15. There is, however, a model for an in-vacuum magnet developed by Tsutsui (2000) for the longitudinal impedance, which was extended to the transverse dipolar impedances by Tsutsui & Vos (2000) and then to the quadrupolar impedance by Salvant *et al.* (2010). These formulas were derived by solving the ME exactly for an ultra-relativistic beam, considering the geometry of Figure 17, which is infinite in the longitudinal direction. Note that in this model the fraction of the fields generated by the beam that are inside the region defined by the angle θ directly interacts with a PEC material, which is an approximated model for the cooper plates of the real magnet, while the rest of the field directly see the ferrite, which is a lossy material. With the exception of the presence of

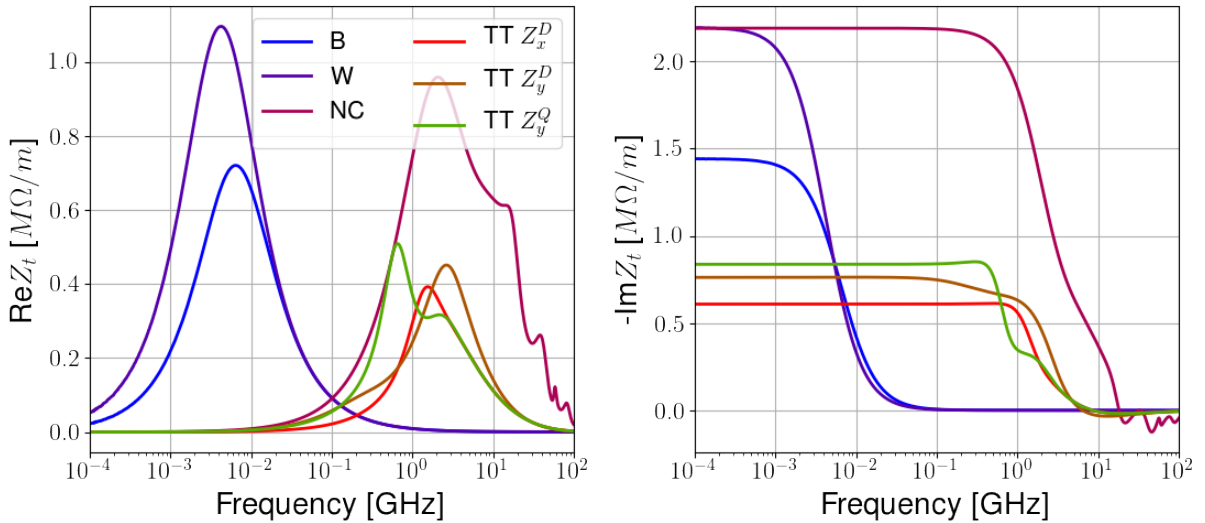


Figure 18 – Transverse impedances of the four models of kicker analysed.

the vacuum chamber, this is what happens in the real magnet, which makes this model a good approximation for the window-frame geometry.

The ferrite that will be used in this magnet is the CMD5005 (Ceramic Magnets, 2017). Its frequency-dependent relative magnetic permeability is modeled by

$$\mu_r(\omega) = 1 + \frac{\mu_i}{1 + i \frac{\omega}{\omega_s}} \quad (5.6)$$

where μ_i is the initial permeability and ω_s is the saturation frequency of the material, which were obtained by fitting the datasheet curve. The values calculated agree well with direct measurements made by Hahn & Davino (2002).

In order to estimate the effect of the vacuum chamber on the impedance, other models based on round multi-layer formulas were analysed. The idea behind the formulation of these models is to try to account for limiting angle θ cases of the Tsutsui geometry, that defines the proportion of the fields that interact with a good conductor. Under these assumptions the models are:

Best case (B): The beam only sees the good conductor: Titanium, ceramic, air and Copper;

Worst case (W): The beam only sees the ferrite. The layers of the round model in this case are composed of: Titanium, ceramic, air, ferrite and Copper;

No Coating (NC): To show the effect of the Titanium coating, this layer was removed from the analysis of the worst case model: ceramic, air, ferrite and Copper.

Figure 18 shows the transverse impedances of the four models analysed. The W curve matches the low frequency limit of the NC case, but at approximately 1 MHz the

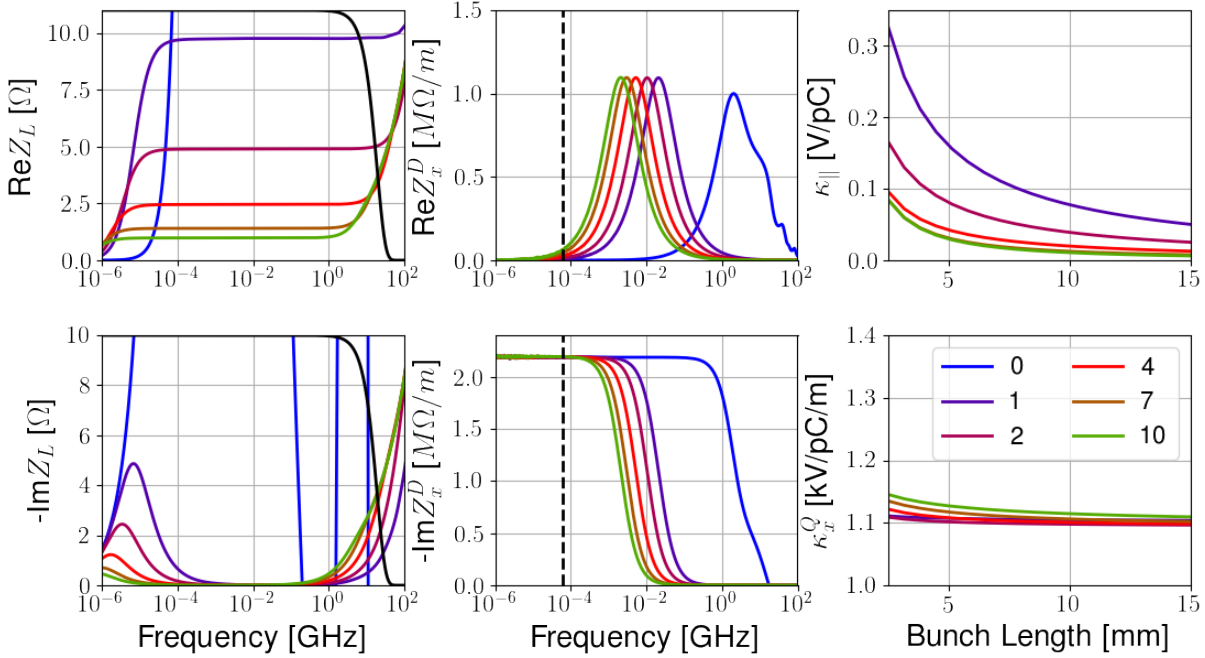


Figure 19 – Longitudinal (left) and dipolar horizontal (middle) impedances as a function of the frequency for several values of coating thickness, in μm . The spectrum of a 2.5 mm bunch is also shown (solid black) in the left to highlight the important part of the frequency spectrum, and the first horizontal betatron line (black dashed) is shown in the middle. In the right is shown the loss factor (above) and quadrupolar kick factor (below) as a function of the bunch length for several values of coating thickness.

coating starts to influence the impedance, damping all of them to very low values. Besides, the impedance predicted by the Tsutsui model (TT) is even lower than the B case, and that the relations between the three of them cannot be described by the constant Yokoya (1993) factors, a fact already pointed out by Salvant *et al.* (2010). Considering that this component have a stronger influence on the total budget due to the low frequency limit of the impedance, the model adopted for the transverse plane was the B case, multiplied by constant factors that matches its impedance to the Tsutsui model. The values used were (0.42, 0.52, 0.58) for the horizontal dipolar, vertical dipolar and vertical quadrupolar impedances, respectively.

For the longitudinal plane it is well known from Zotter (1969a) and Piwinski (1977) that the coating influences the impedance at much lower frequencies than the skin depth of the metal. For this reason the titanium layer thickness was varied in simulations to check if it could be thinner than the nominal value. The results are shown in Figure 19, where we notice by looking at the difference from the result without coating that it is effective since very low frequencies. For almost all the relevant frequency range, the longitudinal impedance is constant, starting to increase only at large frequencies, because in this limit it is dominated by skin-depth effect on the Titanium and the standard resistive wall characteristics apply. However, note that the baseline of the impedance is almost inversely

Table 4 – Main parameters for the fast correctors impedance model.

Parameter	Value	Unit
stainless steel conductivity	1.3	MS m ⁻¹
Chamber thickness	300	μm
Chamber radius	12	mm
Chamber length	100	mm
Number of elements	80	

proportional to the thickness of the coating. This effect is seen in the behavior of the loss factor also shown in Figure 19, which can be used to calculate the power density on the wall through equations (4.10), (4.11), and (4.12). Note that a reduction of the coating thickness to 4 μm would not impact the impedance and heating issues. In the transverse plane, the effect of the coating reduction is only to cause a linear shift of the frequency where the impedance is damped, which does not change its effect on the beam, as can be seen by the quadrupolar kick factor.

Based on the study presented above, we defined the impedance of the non-linear kicker magnet as a round multi-layer chamber with: vacuum, Titanium, ceramic, air, FeSi and Copper. Besides the substitution of the ferrite with the FeSi as the magnet core, this component does not have the parallel copper plates to induce a dipole kick on the beam, creating a much more complex transverse field dependence using copper wires displaced transversely. Such property makes the use of the Tsutsui model inappropriate for this case, and instead of multiplying the resultant impedance of the round chamber by the same factors of the dipole kicker, we decided to use the Laslett coefficients, defined in equation (5.2). This magnet also does not have the coupled flux part of the impedance, because the external circuit does not couple with a beam close to the center of the magnet.

5.3 Fast Correctors Chambers

The fast orbit correctors of the Sirius storage ring will operate at an update rate of 100 kHz in the Fast Orbit Feedback System (FOFB) (TAVARES *et al.*, 2013), requiring special vacuum chambers in order for such high frequency fields to penetrate. The solution adopted is to braze thin stainless steel chambers in the standard copper chamber of the ring. The reduced conductance, only 1 MS, of this material provides a skin depth of 1.6 mm at 100 kHz, which is much larger than the 0.3 mm thickness of the chamber and do not significantly damp or distort the external field of the magnet. The relevant parameters used for modeling of this type of chamber is presented in Table 4.

The small length of these chambers, only 10 cm, raises a question on the validity

Table 5 – Main parameters of the undulators impedance modeling.

Parameter	APU19	APU20	Delta21	Delta52	Unit
Length	2.4	2.4	2.4	3.6	m
Quant. in Phase 1	1	1	2	3	
Quant. in Phase 2	2	3	6	6	
Straight type	low-beta	high-beta	low-beta	low-beta	
Full magnetic gap	5	6.2	7.0	13.8	mm
Chamber thickness	0.10	0.10	0.80	1.00	mm
Hor. beam stay clear	24.0	24.0	8.2	11.2	mm
Vert. beam stay clear	4.8	6.0	5.0	8.0	mm
Transition factor (t)			20		

of the infinitely-long multi-layer chamber formulas used so far. This question is answered by Shobuda *et al.* (2009), who calculated the impedance of a finite resistive insert of finite thickness on an otherwise perfectly conducting and infinitely long round chamber. The authors conclude that even for an insert whose length is smaller than its radius, if the thickness is of the order of 100 µm, the impedance is already equal to the infinitely long chamber counterpart. This result shows that the use of the multi-layer formulas employed so far for the other components are still valid for the fast correctors chambers.

5.4 Undulators Chambers

For the first phase of operation of the Sirius light source the installation of seven IDs on the storage ring is planned. There will be four different types of devices: two Delta-type undulators (TEMNYKH, 2008) and two APU (CARR, 1991). Design details, as well as first experiences with the prototype measurements of the Sirius Delta undulator, are described by Vilela *et al.* (2017) and the information regarding the radiation parameters of such devices can be found elsewhere (SIRIUS, 2013). All the IDs will be out of vacuum and their vacuum chamber will be made of copper and coated with NEG. Regarding the impedance issues, on the one hand this is good because it simplifies the design of the tapers, allowing further optimization of its parameters for impedance reduction, but on the other hand the resistive wall impedance will always be there, regardless of the existence or not of the additional damping provided by radiation emission².

Table 5 shows the main impedance related parameters of each device type. These devices have two main source of impedance that will be modeled separately: one comes from the two tapers at both ends of the device and another from the resistive wall.

² One important remark is that both types of undulators that will be used in Sirius do not have the degree of freedom of changing gap, which means that there will be no way to "turn off" their magnetic fields when the IDs are not used. What is usually done is to change the phases among the Halbach (1985) cassettes in such a way that the field lays down in the longitudinal direction, so the electron beam stops radiating.

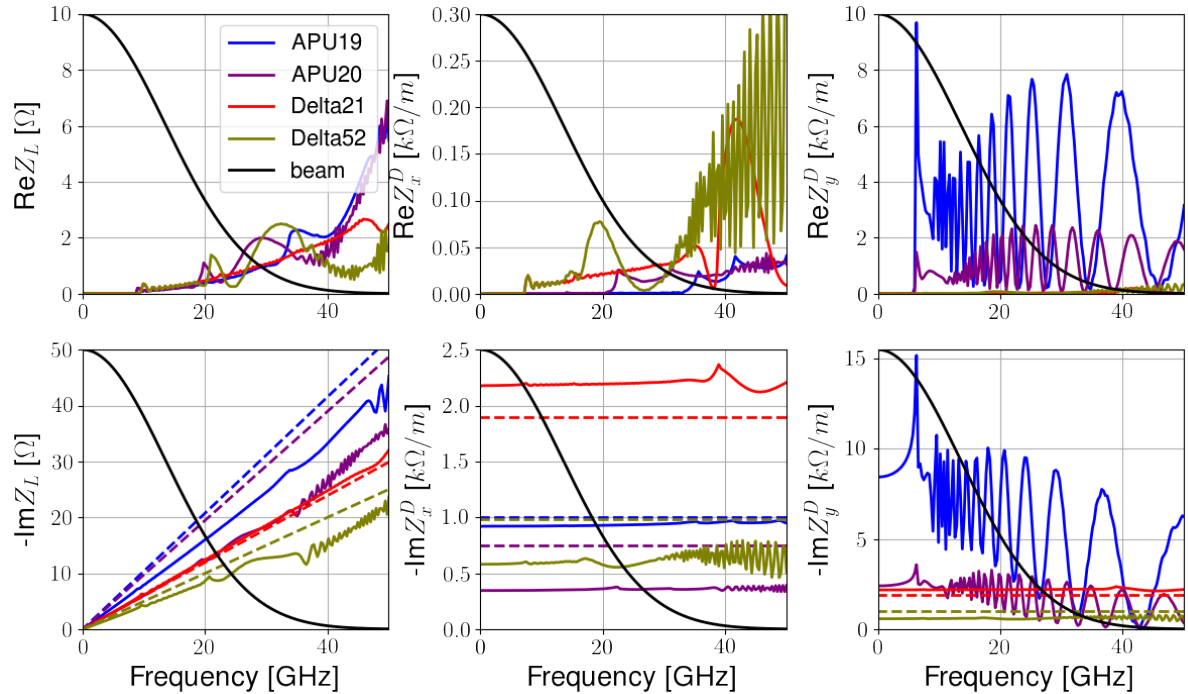


Figure 20 – Geometric impedance from the tapered transitions of the undulators. Solid lines represent numerical calculations performed with ECHOz1 and ECHOz2 for the Delta undulator and with ECHOzR for the APU. Dashed lines are the prediction by the analytic formulas studied in subsection 3.9.1.

The modeling of the tapers was performed with the whole collimator in the simulation, considering perfectly conducting walls and linear transitions with factor³ t equals to 20, which means the angle of the taper is 2.86° (50 mrad), much lower than the rule of thumb of 10° . The APU chambers were calculated with ECHOzR (ZAGORODNOV *et al.*, 2015), being modeled as flat collimators starting from a square chamber of sides equal to the radius of the real chamber and final gap equal to the Vertical BSC defined in Table 5. The Delta-type undulators are a little more complicated to model, because their final chamber geometry is an ellipse with major and minor axes given by the horizontal and vertical BSC presented in Table 5, invalidating the consideration of a flat geometry due to the non-negligible horizontal tapering. We dealt with this problem by simulating a round transition with ECHOz2 (ZAGORODNOV; WEILAND, 2005) and applying numerical factors given by Podobedov & Krinsky (2007, Figures 12a, 13 and 14) to the impedances. Even though their comparisons are valid for tapers with transverse sections composed by confocal ellipses, all the analytic formulas analysed in subsection 3.9.1 suggests that the parts of the tapers with lower gaps contribute more to the total impedance, which corroborates this approach. The form factors used here were $(1, 1.3, 0.5, -0.4)$ for the longitudinal, vertical dipolar, horizontal dipolar and horizontal quadrupolar impedances, respectively.

Figure 20 shows the impedances of the four ID types before the application of

³ Here we recall the notation defined in subsection 3.9.1.

the form factors on the Delta-type undulators. Also shown is the low-frequency analytic expressions discussed in subsection 3.9.1. Note that in general their quantitative agreement with the numerical simulations is not very good, but the qualitative comparisons among all the types of undulators, mainly the differences between the round and flat geometries, are well predicted by the theory. In the case of the longitudinal and horizontal impedances for flat geometries this quantitative difference between theory and numerical simulations could be explained by the fact that the second condition imposed on the validity limits of the expressions ($h \ll w$) is not met in the cases studied here, because the tapers start with a square geometry. Stupakov (2007) provides expressions for impedances for any ratio h/w , which consists on multiplying the integrands of equations (3.50) by form-factor functions that depend on $h(s)/w$. The paper has figures that explicitly show the value of these form-factors and, after a qualitative analysis, it can be concluded that they justify the differences observed here. For the vertical dipolar impedance, this scenario changes because the analytic formula overestimates the impedance by a factor larger than four (they are above the upper limit of the plot and are not shown), which is so large that even the form factors could not account for the difference observed. Maybe this disagreement, if our results are correct, comes from higher-order terms in the taper angle that are not considered in the derivation of the analytic formulas.

Another interesting aspect of the numerically calculated vertical dipolar impedance is the presence of the narrow-band trapped mode studied by Blednykh (2006) for the APU19. Considering that this mode depends strongly on the width of the chamber and the fact that the Sirius undulators are still under study, the complete effect of the this peak was not studied in details, being subject for future work. However, it was verified that it does not induce transverse coupled-bunch oscillations.

Figure 21 shows the vertical dipolar and longitudinal wall impedance of the four types of undulators. They were calculated using the code ImpedanceWake2D (MOUNET, 2011) for flat multi-layer chambers. The layers used in the calculations were: NEG, Copper, air, high μ -material. The last layer was added in an attempt to consider the effect of the magnet blocks of the IDs on the DC impedance, which can be noted in Figure 21b. This figure also shows in dashed lines the results obtained with the calculation of the impedance using the round chamber formulas and posterior application of the Yokoya factors. Note that for the undulators with small gap (APU19, APU20 and Delta21), this method underestimates the impedance, because the sum of the electric and magnetic Laslett coefficients are larger than the factor for the quadrupolar impedance. But for the Delta52 both formulas agree because in this case only the electric coefficient contributes significantly and it is equal to $\pi^2/24$. Blednykh *et al.* (2016) created a more sophisticated model, where the authors considered that a fraction of the surface of the pole of the IDs was composed of the high μ -materials and the other part by saturated ferromagnet blocks with $\mu \approx 1$. With this impedance they successfully explained the incoherent tune-shifts

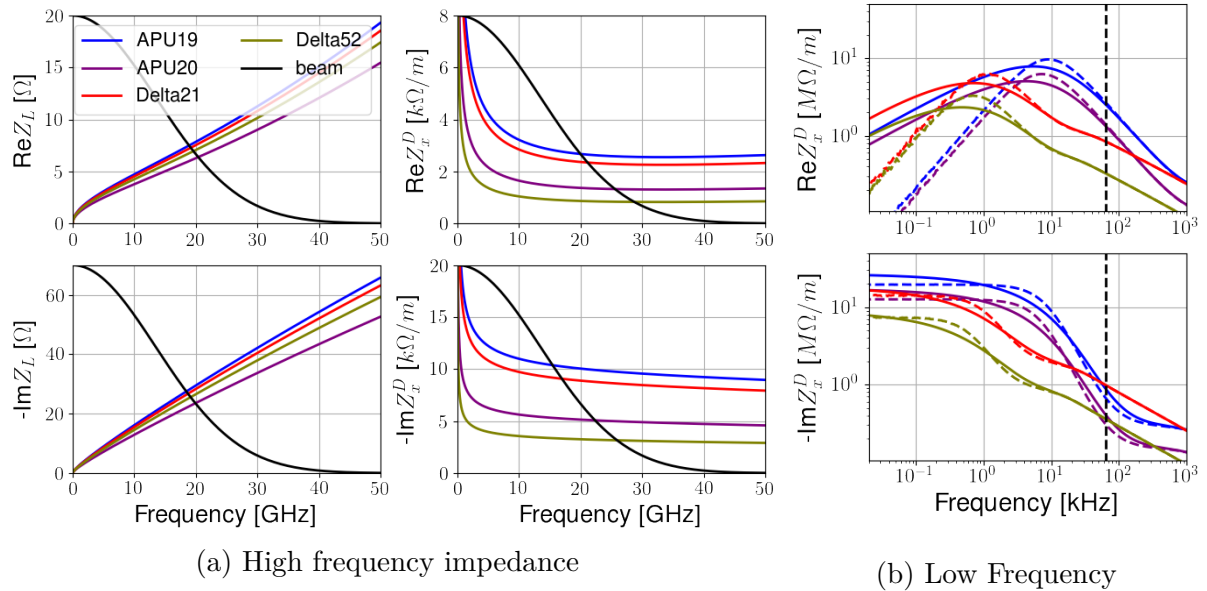


Figure 21 – Wall impedance of the four types of undulators planned for Sirius.

caused by these devices in NSLS-II. Once the detailed model of the IDs are available we intent to improve these components impedance model in a similar way.

The chamber heating is an important aspect to be considered in the design of the undulators, because it is difficult to insert cooling systems in devices with such small gaps. Particularly for the Delta-type undulators, which have small apertures in both transverse directions. To estimate the power density for these devices we used the flat chamber approximation, described in equation (4.12). Even though the undulators chambers are not flat, the estimation of the peak density using this formula is a worst case scenario for the real value. Even in this case it was verified through heating simulations that the power deposited by the wake fields is not an issue.

5.5 BC Chamber

The BC magnet is the central dipole in the arc of the Sirius storage ring unit cell. It is a permanent magnet with longitudinal and transverse gradients and at its center there is a very thin slice that will reach a peak magnetic flux density of 3.2 T which will be used as source for 20 beamlines, providing radiation with critical energy of 19.2 keV. In order to achieve this high flux density, the poles of central part must be very close to the beam, with a full gap of 10 mm.

The initial proposal for the chamber of the central section of this magnet was an elliptical geometry with inner minor semi-axis equal to 4 mm and major semi-axis equal to the radius of the standard chamber, 12 mm, connected by a smooth tapered transition with transition factor equal to 15. Motivated by the analytic formulas of the theory discussed

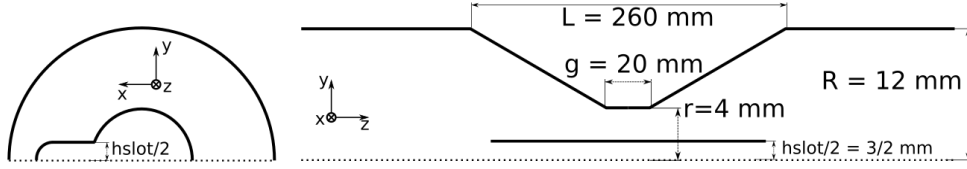


Figure 22 – Scheme of the keyhole-shaped chamber for the BC magnet.

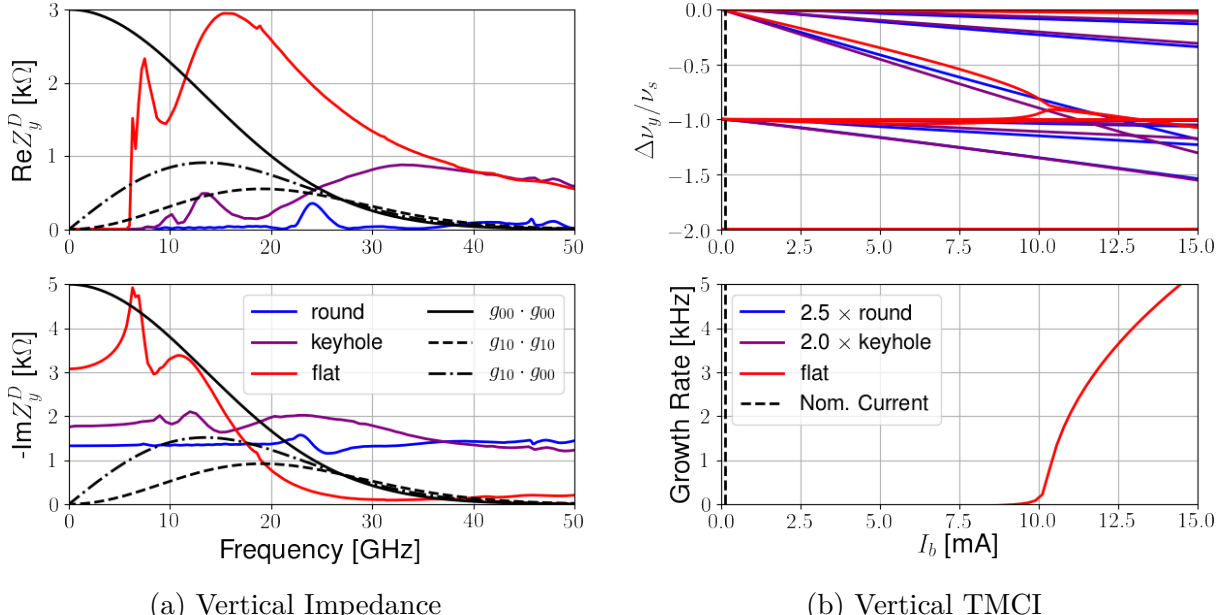


Figure 23 – Comparison of the impedance and its effect on the beam through simulations of mode-coupling instability for different models of impedance. For the TMCI a gaussian single bunch with 2.5 mm root-mean-square (rms) length was considered. The impedance used was that of the 20 components along the ring, multiplied by the average betatron function at the magnet's position.

in subsection 3.9.1, we also investigated the impedance of a round chamber with inner radius equal to the minor radius of the proposed elliptical chamber. For the impedance calculations, the elliptical chamber was approximated by a flat one and simulated using ECHOzR (ZAGORODNOV *et al.*, 2015), while the round chamber was simulated with ECHOz1 and ECHOz2 (ZAGORODNOV; WEILAND, 2005). It was known, however, that the round chamber did not meet the vacuum requirements, because the radiation generated by the upstream dipole would hit strongly the inner part of the transition in the positive (outward the storage ring center) horizontal direction, causing heating problems. For this reason, a chamber which satisfies the requirements, with a "keyhole" shape, as shown in Figure 22, was also proposed and its impedance simulated with GdfdL (BRUNS, 2017).

Figure 23a shows the comparison of the vertical dipolar impedance among the three models analysed. The theory predicts a higher low frequency inductive impedance for the flat-chamber model and we note that this is indeed the case. One interesting fact, however, is that the round chamber remains imaginary for all the frequency range analysed, its real

part only emerges at frequencies larger than 60 GHz, while the flat chamber has a very strong real part at low frequencies, which couples with the beam oscillation mode $g_{10} \cdot g_{00}$. From the theory of mode-coupling instability, discussed in subsection 4.5.2, we know that at zero chromaticity the imaginary part of the impedance causes tune-shifts of the coherent modes and bring them close to each other, in this case the modes 0 and -1, represented in the figure by the spectra $g_{00} \cdot g_{00}$ and $g_{10} \cdot g_{10}$, respectively; but it is the real part of the impedance that couples them causing the instability. We can see this mathematically recalling that the mode-coupling matrix has the following form, when only the modes 0 and -1 are considered:

$$\frac{M}{N} \propto \begin{pmatrix} I_1 - \frac{1}{N} & R_1 \\ -R_1 & I_0 \end{pmatrix} \Rightarrow \frac{\lambda_{1,2}}{N} \propto \frac{I_0 + I_1 - \frac{1}{N}}{2} \pm \frac{1}{2} \sqrt{\left(I_1 - \frac{1}{N} - I_0 \right)^2 - 4R_1^2}, \quad (5.7)$$

where N is the number of particles in the bunch,

$$I_i = \int d\omega \Im \{ Z_y^D \} g_{i0} g_{i0} \quad (5.8a)$$

$$R_1 = \int d\omega \Re \{ Z_y^D \} g_{10} g_{00}, \quad (5.8b)$$

and g_{ml} is given by equation (4.37). Henceforth, it is clear from the eigen-value expression in equation (5.7) that the instability can only happen if the real part of the impedance is strong enough to couple with the beam in such a way that

$$2|R_1| \geq \left| I_1 - \frac{1}{N} - I_0 \right|. \quad (5.9)$$

Note that when the number of particles in the bunch is small, the r.h.s. of the inequality above is very large and when $N \rightarrow \infty$ it tends to $I_1 - I_0$. If R_1 is not larger than this difference, the modes simply cross each other. Note that some mechanism similar to the one explained above is happening in Figure 23b for the round and keyhole chambers, where even after being multiplied by a factor of 2.5 and 2.0, respectively, to match the tune shifts, their real impedances are not strong enough to create the instability.

Figure 24 shows the other impedances for the three models. Note that the imaginary part of the longitudinal impedance of the keyhole and round models are smaller than the one of the flat chamber by a factor of approximately 2, which is in agreement with the theory predictions, and the quadrupolar impedance introduced by keyhole is negligible. The horizontal dipolar impedance was not calculated for this model yet, but a calculation was performed for a keyhole geometry with the *hslot*, defined in Figure 22, equals to 2 mm and it was similar to the transverse impedance of the round model.

5.6 Coherent synchrotron radiation (CSR)

The radiation emitted by one particle can influence other particles in the bunch in a similar way as the wake fields and, for this reason, it is treated with the same formalism

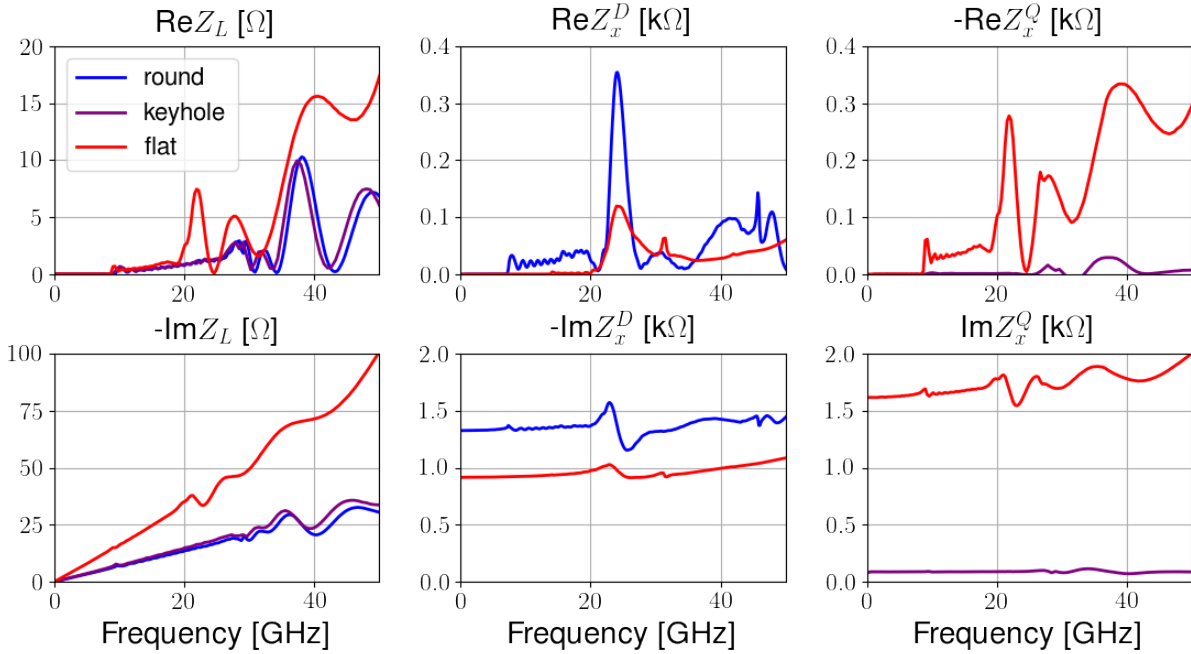


Figure 24 – Longitudinal (left), dipolar horizontal (center) and quadrupolar horizontal (right) impedances for the three models of BC chamber considered. The dipolar horizontal impedance of the keyhole chamber was not calculated yet and the round chamber does no have a quadrupolar impedance.

of impedances and wake functions discussed so far. Such mechanism is often referred to as CSR because its net effect is only relevant for wavelengths of the same order or larger than the bunch length, according to Nagaoka & Bane (2014). The wake function of a source particle moving in circular trajectory in free-space over a witness particle in this same trajectory was calculated by Derbenev *et al.* (1995) and is given by:

$$\frac{W'_0(z)}{L} = \begin{cases} -\frac{Z_0 c}{2\pi 3^{4/3}} \frac{1}{\rho^{2/3} (-z)^{4/3}} & z < 0 \\ 0 & z > 0 \end{cases}, \quad (5.10)$$

where ρ is the radius of curvature of the trajectory, $L = 2\pi\rho$ is the total length of its circle and, contrary to other cases, the wake only affects particles ahead of the source particle. Notice that this formula diverges at the origin and predicts energy gain for all ranges of interaction. This happens because this equation is only the tail of a very short-range and intense wake. This wake starts at $W'_0(0^-) \approx \gamma^4/\rho^2$, crosses zero at $-z \approx 2\rho/9\gamma^2$ and soon after that assumes the value of the asymptotic behavior described by the equation above⁴. A fast calculation shows that the short-range scales of the complete wake ($\rho/\gamma^2 \approx 500$ nm for Sirius) are much smaller than any characteristic length important for the stability analysis in Sirius, which justifies the use of equation (5.10).

Murphy *et al.* (1997) calculated the wake function of the same trajectory described above, but instead of considering the particles were in free space, the authors included two

⁴ Figure 2 of Murphy *et al.* (1997) has a graphic of this function.

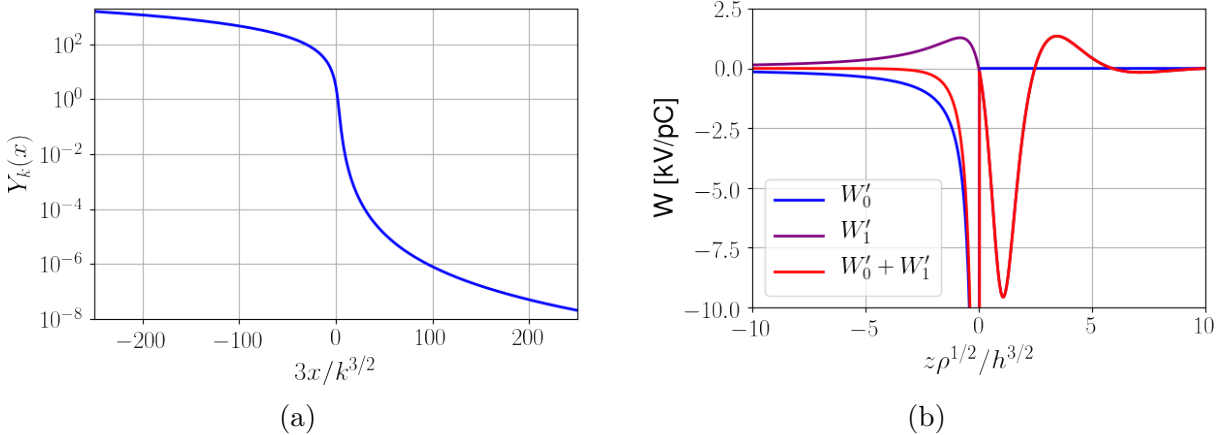


Figure 25 – (a) behavior of $Y_k(x)$ as a function of $3x/k^{3/2}$ showing its smooth dependency.
(b) Sum of the two terms of the CSR impedance: the free-space contribution, W'_0 and the shielding term, W'_1 , where it becomes clear the cancellation of the long tail at positions ahead of the source particle (z negative).

infinite parallel plates equally spaced from the particles trajectory. The asymptotic form of the wake they obtained has, in addition to the term of equation (5.10), a contribution from the radiation of the image charges on the plates, given by

$$\frac{W'_1(z)}{L} = -\frac{Z_0 c}{4\pi} \frac{1}{2\pi h^2} G\left(\frac{\rho^{1/2}}{h^{3/2}} z\right), \quad (5.11)$$

where h is the distance of any one of the plates to the beam trajectory and the function G is given by

$$G(x) = 8\pi \sum_{k=1}^{\infty} \frac{(-1)^{k+1}}{k^2} \frac{Y_k(x) (3 - Y_k(x))}{(1 + Y_k(x))^3}, \quad (5.12)$$

with $Y_k(x)$ being one of the roots of the equation

$$Y_k - \frac{3x}{k^{3/2}} Y_k^{1/4} - 3 = 0. \quad (5.13)$$

According to Bane *et al.* (2010) from the four roots of the equation above, two are complex and two are real and we are interested in the one that gives the larger value for $Y_k(x)$ when $x < 0$, the smallest for $x > 0$ and when $x = 0$ the two real roots are equal to 3. Figure 25a shows $Y_k(x)$ as a function of the term $3x/k^{3/2}$, where we note a smooth and well behaved dependency, guaranteeing fast convergence of the infinite series that defines G . It is necessary to compute only the first 25 to 30 terms for convergence in almost all practical cases. Figure 25b shows the effect of the plates on the total wake, where we can note that, contrary to the free-space term, it is non-zero behind the source particle and that its contribution in the portion ahead is to cancel the long tail of the free-space wake, working as a shield for low frequency terms.

The CSR impedance with and without shielding is known for a long time, see for example the work of Faltens & Laslett (1973). The free-space impedance, corresponding

to the wake given in equation (5.10) is given by (NAGAOKA; BANE, 2014, Eq. 18)

$$\frac{Z(\omega)}{L} = \frac{Z_0}{2\pi} \frac{\Gamma(2/3)}{3^{1/3}} \exp\left(\frac{i\pi}{6}\right) \left(\frac{\omega}{c\rho^2}\right)^{1/3}. \quad (5.14)$$

Calculations of the impedance of the shielded configuration with the parallel plates can be found in Warnock (1990) and Murphy *et al.* (1997). However, recently Cai (2011) presented an approximated result that he built based on the exact equations given by Warnock which is easy to calculate numerically and simply describes the impedance in terms of scaled results

$$\frac{\rho}{h} \frac{Z(n)}{n} = 16Z_0 u_0 \sum_{p=0}^{\infty} (\text{Ai}'(u_p)\text{Ci}'(u_p) + u_p \text{Ai}(u_p)\text{Ci}(u_p)), \quad (5.15)$$

where $n = \omega\rho/c$, Ai and Bi are the Airy functions (Wikipedia Contributors, 2017a) and the prime denotes their derivatives, Ci = Ai - iBi and the variable u_p is given by

$$u_p = \frac{\pi^2(2p+1)^2}{2^{2/3}} \left(n \left(\frac{2h}{\rho}\right)^{3/2}\right)^{-4/3}. \quad (5.16)$$

Using the parallel plates model for the CSR impedance, Bane *et al.* (2010) calculated the threshold for the microwave instability as a function of the plates separation using a Vlasov Fokker Planck (VFP) equation solver developed by Warnock & Ellison (2000) and showed that the CSR-induced instability depends only on two scaled variables: the threshold strength, $(S_{\text{csr}})_{\text{th}}$, and the shielding parameter, Π , given by

$$(S_{\text{csr}})_{\text{th}} = I \frac{\rho^{1/3}}{\sigma_{z,0}^{4/3}}, \quad \Pi = \sigma_{z,0} \frac{\rho^{1/2}}{h^{3/2}} \quad (5.17)$$

where $\sigma_{z,0}$ is the bunch length at zero current and I is a normalized bunch current (with unit of m in the SI) given by

$$I = \frac{Z_0 c}{4\pi} \frac{I_b T_0}{2\pi\nu_{s,0} (E_0/e) \sigma_{\delta,0}}, \quad (5.18)$$

where I_b is the bunch current, $\nu_{s,0}$ is the zero-current synchrotron tune and $\sigma_{\delta,0}$ is the zero-current energy spread. Figure 26 shows their main results with the addition of one line indicating the shielding parameter for Sirius low-field dipoles, where one can note that if the whole ring were composed by only this type of dipole the threshold would be $(S_{\text{csr}})_{\text{th}} = 1.44$, which converted to bunch current gives 0.9 mA.

Note that for most of the simulated shielding parameter range, the threshold follows a simple dependency given by the line

$$(S_{\text{csr}})_{\text{th}} = 0.5 + 0.12\Pi. \quad (5.19)$$

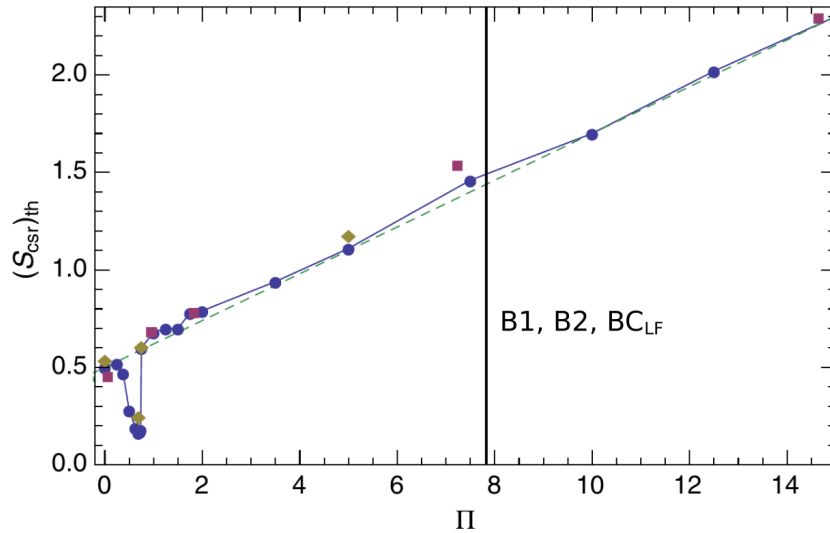


Figure 26 – Plot adapted from Bane *et al.* (2010): CSR threshold strength, $(S_{\text{CSR}})_{\text{th}}$, as a function of the shielding parameter, Π . Blue dots: simulations with the VFP solver. Purple squares: results of the linearized Vlasov equation (does not include damping). Olive diamonds: results with a damping factor two times larger. Dashed line: the scaling $(S_{\text{CSR}})_{\text{th}} = 0.5 + 0.12\Pi$. Black line: shielding parameters for the low field dipoles of Sirius, B1, B2 and the low field part of the BC magnet (BC_{LF}). The shielding for the high field part of this same magnet (BC_{HF}) is larger than the maximum value showed.

Table 6 – Main parameters used for modeling the CSR impedance and effective wake function

Parameter	B1, B2, BC_{LF}	BC_{HF}	Unit
Bending radius	17.2	3.1	m
Magnet length	0.8/1.2/0.4	0.06	m
Total deflection angle	337.6	22.4	°
Vacuum chamber radius	12	4	mm
Shielding parameter	7.8	17.5	
Threshold current	0.9	2.9	mA

Despite the simple model for the impedance used in these calculations, several experiments confirmed the instability predictions above, for example the one performed at the Metrology Light Source by Ries *et al.* (2012) and the more recent results from ANKA, described in Brosi *et al.* (2016). However, the threshold calculated in this way does not take into account the effect of other impedances, requiring a more specific study.

Inspired by these good agreements between theory and measurements we decided to create an initial model for the CSR impedance based on this parallel plate approximation. Table 6 shows the main parameters used for modeling the impedances and wakes for the case of the Sirius storage ring. The impedance was directly calculated from equation (5.15), but the method to obtain the wake was more involving. Instead of the wake

function of the point charge, we convolved the expressions of equations (5.10) and (5.11) with a small gaussian beam of $\sigma = 5 \mu\text{m}$ to avoid the divergence of the free-space wake and used this effective wake function as input for tracking simulations. The convolution with the shielded contribution was done in the standard numeric way, but the one with the free-space part of the wake was performed following Nagaoka & Bane (2014)

$$V_0(z) = \int_{-\infty}^{\infty} dx W'_0(x) \lambda(z - x) = - \int_{-\infty}^{\infty} dx W_0(x) \lambda'(z - x), \quad (5.20)$$

where the divergence of the first integral of the equation above is neglected and the remainder is integrable. This procedure is justified by the fact that what causes this divergence is the approximated expression of the wake; the real physical one is finite. This is just a clever way to remain using the approximation for the free-space wake which does not depend on the particle's energy. The explicit expressions for the integrands are

$$\frac{W_0(z)}{L} = \begin{cases} \frac{-Z_0 c}{2\pi 3^{1/3}} \frac{1}{\rho^{2/3}(-z)^{1/3}} & z < 0 \\ 0 & z > 0 \end{cases} \quad \text{and} \quad \lambda'(z) = -\frac{z}{\sqrt{2\pi}\sigma^3} \exp\left(-\frac{z^2}{2\sigma^2}\right). \quad (5.21)$$

Note that $W_0(z)$ also diverges at the origin, but slower, in such a way that the convolution can be carried out numerically or analytically. The analytic result was obtained with Wolfram Mathematica (Wolfram Research Inc., 2016) and it reads

$$\frac{V_0(z)}{L} = \frac{Z_0 c}{4\pi^{3/2}(3\sqrt{2}\rho^2\sigma^{10})^{1/3}} \left\{ \sqrt{2}\Gamma\left(\frac{5}{6}\right) \left(\sigma^2 {}_1F_1\left(-\frac{1}{3}; \frac{1}{2}; -\frac{z^2}{2\sigma^2}\right) - z^2 {}_1F_1\left(\frac{2}{3}; \frac{3}{2}; -\frac{z^2}{2\sigma^2}\right) \right) + z\sigma\Gamma\left(\frac{4}{3}\right) \left(3 {}_1F_1\left(\frac{1}{6}; \frac{1}{2}; -\frac{z^2}{2\sigma^2}\right) - 2 {}_1F_1\left(\frac{1}{6}; \frac{3}{2}; -\frac{z^2}{2\sigma^2}\right) \right) \right\},$$

where ${}_1F_1$ is the confluent hypergeometric function (Wikipedia Contributors, 2017b). Figure 27a shows the two components of the wake and their sum, while Figure 27b shows the impedance calculated via the inverse Fourier transform and posterior deconvolution of equation (5.20), compared with the calculation using equation (5.15) and the free-space impedance (5.14). Note the very good agreement between the two methods of calculating the impedance, which validates the calculation trick of the effective wake function. Besides, note that the shielding virtually eliminates the resistive part of the impedance up to approximately 100 GHz and changes the sign of the imaginary part from positive, which is generally referred as capacitive in the accelerator community, to negative, often called inductive. However, the impedance in this range of frequencies may depend very strongly on the parameters of the vacuum chamber geometry. For example, Warnock & Morton (1990) calculated the radiation impedance for a beam in a smooth toroidal chamber with rectangular cross-sections and found that the impedance at low frequencies would also be imaginary, but capacitive. The importance of this impedance to the budget is not in the frequency region of the stationary beam spectrum, but the very strong impedance at high frequencies, because the instability arises when modulations in the beam distribution starts radiating coherently, as explained by Stupakov & Heifets (2002).

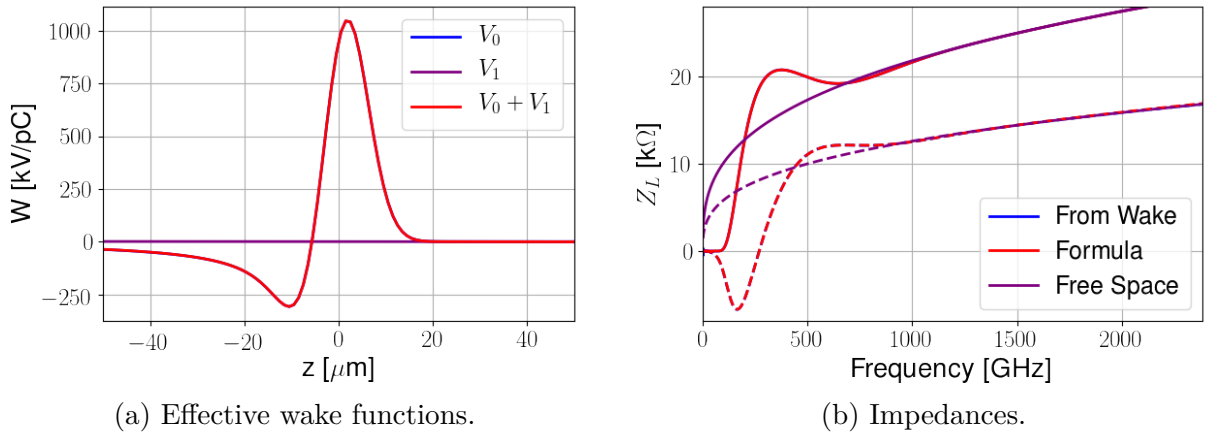


Figure 27 – CSR effective wake functions and impedances calculated using the parameters of the Sirius low-field dipoles. Solid lines represent the real part of the impedance and dashed lines, the imaginary part. In both plots the blue line coincides with the red one and, therefore, it is not visible.

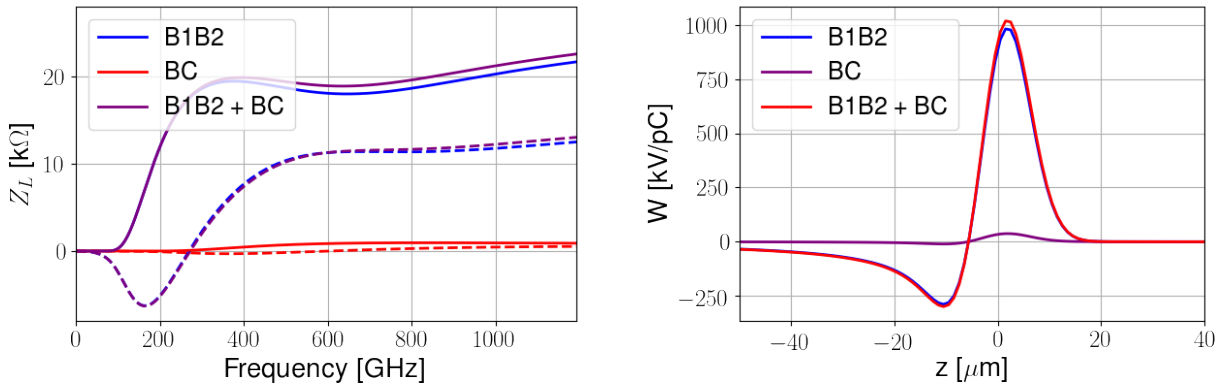


Figure 28 – Total CSR impedance (left) and wake (right) models for Sirius, considering the two types of dipoles. Solid lines represent the real part of the impedance and dashed lines represent the imaginary part.

Figure 28 shows the total impedance considered for Sirius. The contribution from both types of dipoles was calculated considering their total lengths along the ring. Notice that the strong shielding factor of the BC magnet helps reducing the total impedance, in such a way that the threshold predicted by equation (5.19) rises to 1 mA.

As a final remark, we reinforce that this is only the initial model for the impedance, future works could consider the analytic results obtained by Stupakov & Zhou (2016), where the authors developed a general method to calculate the impedance for any planar trajectory in free space, and with the parallel plates shielding, and applied it to some practical cases, including the case of a finite dipole followed by a straight section. Another possibility is to use the results from Stupakov & Kotelnikov (2009), where the authors used a method developed in a previous paper (STUPAKOV; KOTELNIKOV, 2003) to calculate the impedance of a finite dipole in a rectangular chamber. Besides, numerical solvers such as the one developed and described by Zhou *et al.* (2012) based on a method for solving

the parabolic equation by Agoh & Yokoya (2004) could be employed.

6 IMPEDANCE BUDGET

The main aspects of the whole impedance budget of the Sirius storage ring will be discussed in this chapter. Besides the components whose modeling were analysed in Chapter 5, several others are also included. Table 7 shows all the components and important parameters for weighting their contribution to the budget, such as the quantity (Q) of elements and the average betatron function at their locations. The longitudinal parameters, the loss factor, effective impedance and power loss of the beam, were calculated considering multi-bunch operation with uniform filling in all the 864 RF buckets of the ring and, additionally, for the power loss it was considered 100 mA in the machine. The transverse figure of merits, however, were calculated for the single bunch case in order to compare the relative effect of each component on TMCI. Finally, for all the calculations it was considered a 2.5 mm bunch.

Some of these components, precisely the tapers for the superconducting RF cavity and the tapered transitions of the injection straight section, had their impedance calculated following the same methods of the undulators and the BC magnet transitions, discussed in Sections 5.4 and 5.5, respectively. All the others were designed in detail with 3D modeling and calculated with GdfidL¹ (BRUNS, 1997), to minimize issues related to wake heating and avoid the coupled-bunch instabilities. In this work, only the key aspects of these designs will be mentioned and their detailed impedance characterization as well as the design process can be found elsewhere (DUARTE *et al.*, 2013; DUARTE *et al.*, 2017b; DUARTE *et al.*, 2017a).

A closer look to Table 7 reveals that the flanges, which are an important source of impedance for other machines, as described by Nagaoka (2004a), are not included in our budget, because Sirius flanges are virtually free of any impedance. They were based on a modified version of a KEK MO-type flange (SUETSUGU *et al.*, 2005) and, as explained by Seraphim *et al.* (2015), they do not present material transition and the vacuum seal is made at the inner surface, forming a cavity with negligible size. Another type of component missing in the impedance budget is the scraper, which is responsible for limiting the horizontal or vertical acceptance of the storage ring to avoid localized electron losses in other, more delicate, elements by creating transverse obtrusions with variable gap. Generally the impedance of such device is optimized for its nominal position, which is defined by taking into account the BSC at the scraper location, but the abrupt transitions created when it is in any other position, farther or closer from the center of the vacuum chamber, generate a large impedance. The Sirius design, presented by Duarte *et*

¹ All the 3D calculations and optimizations were performed by another member of the LNLS team, Henrique de Oliveira Caiafa Duarte.

Table 7 – Sirius storage ring impedance budget for phase 1. RW stands for Resistive wall and Trans for transitions.

Q	β_x [m]	β_y [m]	κ_L [N/pC]	Multi bunch @ 100 mA			Single bunch [kV/pC]			
				$Z_L/n _{eff}$ [$m\Omega$]	P_w [W]	$\beta_x \kappa_x^D$	$\beta_y \kappa_y^D$	$\beta_x \kappa_x^Q$	$\beta_y \kappa_y^Q$	
Pipe RW	1	6.0	11.0	6.80	-41.43	136.11	-10.11	-18.52	0.02	-0.30
Delta21 RW	2	2.2	2.2	0.31	-1.91	6.27	-1.62	-3.22	1.66	-1.66
Delta52 RW	3	2.6	2.6	0.44	-2.68	8.82	-1.05	-2.09	1.09	-1.09
APU19 RW	1	2.2	2.2	0.16	-0.99	3.27	-0.91	-1.82	0.95	-0.95
APU20 RW	1	17.8	5.0	0.13	-0.79	2.61	-3.78	-2.11	3.95	-1.11
BC RW	20	0.4	5.2	0.05	-0.30	0.98	-0.04	-0.57	0.00	0.00
FOC RW	80	7.2	6.5	0.60	-1.47	12.09	-0.47	-0.42	0.00	0.00
NLK RW	1	18.2	7.3	0.10	-0.11	1.91	-0.48	-0.39	0.49	-0.20
DIPK RW	1	18.0	6.7	0.10	-0.10	1.91	-0.55	-0.22	0.67	-0.25
Delta21 Trans	2	2.4	2.4	0.01	-0.71	0.28	-0.18	-0.46	0.14	-0.14
Delta52 Trans	3	3.0	3.0	0.02	-0.70	0.48	-0.09	-0.23	0.07	-0.07
APU19 Trans	1	2.4	2.4	0.01	-0.45	0.12	-0.07	-0.64	0.10	-0.10
APU20 Trans	1	3.0	3.0	0.01	-0.35	0.15	-0.04	-0.24	0.06	-0.06
BC Trans	20	0.4	5.2	0.10	-4.80	1.98	-0.23	-2.94	0.00	0.00
RF CAV Trans	1	7.3	7.3	5.71	-10.07	114.33	-0.35	-0.35	0.00	0.00
KIKS Trans	1	18.2	7.1	0.00	-0.22	0.10	-0.12	-0.31	0.23	-0.09
BPM Block	120	6.6	8.8	12.81	-28.19	256.30	-6.86	-9.14	0.00	0.00
Bellows	20	6.6	8.8	0.84	-2.08	16.86	-0.49	-0.66	0.00	0.00
Rad. Masks	360	6.6	11.0	2.93	-11.45	53.71	-5.04	-1.22	-4.39	7.31
Valve Block	40	6.6	11.0	9.41	-24.51	183.40	-5.00	-8.33	-0.10	0.17
SL GSL07	1	7.0	7.0	0.34	-0.22	6.77	-0.06	-0.06	0.00	0.00
SL GSL15	1	7.0	7.0	0.14	-0.04	2.86	-0.06	-0.06	0.00	0.00
SL Monitor	2	4.8	14.5	0.19	-0.18	3.87	-0.07	-0.22	0.00	0.00
SL HShaker	1	18.2	7.3	0.53	-0.19	10.67	-0.57	-0.09	-0.21	0.09
SL VShaker	1	2.5	22.0	0.53	-0.19	10.67	-0.03	-0.69	0.03	-0.26
SL HKicker	1	18.2	7.3	0.56	0.07	11.15	-0.59	-0.10	-0.21	0.09
SL VKicker	1	2.5	22.0	0.56	0.07	11.15	-0.03	-0.72	0.03	-0.26
DCCT	2	2.5	22.0	0.76	2.18	15.18	-0.04	-0.36	0.00	0.00
Pump Slots	100	16.0	7.0	0.27	-1.27	5.49	-0.77	-0.34	-0.00	0.00
CSR	1	2.0	25.0	0.00	-0.20	0.00				
Total				44.44	-133.28	889.46	-39.72	-56.52	4.57	1.12

al. (2017a), will not have this problem, presenting negligible impedance for any transverse offset.

In order to simplify the presentation of the results, the components of Table 7 were divided in some groups:

Ring RW: comprises the elements BC RW, Pipe RW (standard chamber), FOC RW (Fast orbit correctors), NLK RW (Non-linear Kicker), DIPK RW (Dipole Kicker). The element that dominates the impedance of this group is the resistive-wall impedance of the standard chamber;

ID RW: composed by the undulators resistive-wall impedance, APU19 RW, APU20 RW, Delta21 RW, Delta52 RW, and the CSR impedance. This last one was included here because it does not fit in any of the groups and its contribution in the frequency range of the equilibrium beam spectrum is too small to have its own category;

Ring Geom: Transitions of chambers with different cross sections along the ring, formed by the RF CAV Trans, BC Trans and KIKS Trans (transitions for both kickers). The resistive longitudinal impedance of this group is dominated by the RF cavity transition impedance, because space limitations in the straight section where it will be installed forced the use of a small transition factor, t , which means larger taper angles and, consequently, impedance too. However, the vertical kick factor is defined mostly by the BC Trans, as can be seen in Table 7;

ID Geom: all the transitions for the IDs;

Vac. & Diag: Composed of all the stripline (SL) kickers and pick ups, SL GSL07, SL GSL15, SL Monitor, SL HShaker, SL VShaker, SL HKicker, SL VKicker, the DCCT² and the Pump Slots.

Blw & BPM: This group contains the isolated bellows and the BPM block, which was simulated as a single piece because all BPMs of the storage ring have two bellows attached, one upstream and another downstream, which means there could be coupling between the resonant modes of each device;

Valve Block: All the valves of the storage ring will have a BPM Block followed by a Radiation Mask in the upstream direction and a bellows downstream. For the same reasons as the previous component, all these elements were simulated as a single block. Duarte *et al.* (2017a) shows a Figure of these components and the impedance comparison of the sum of individual impedances and the block impedance, demonstrating the differences between both approaches.

² Short for Direct Current Current Transformer, it is the current meter of the storage ring.

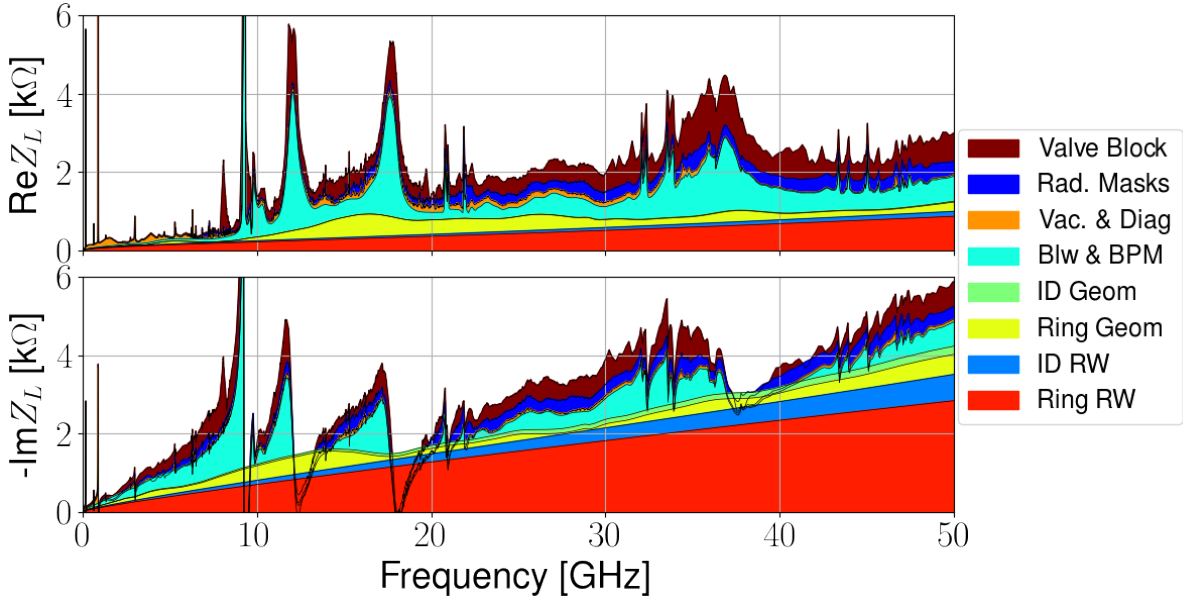


Figure 29 – Longitudinal impedance budget for Sirius.

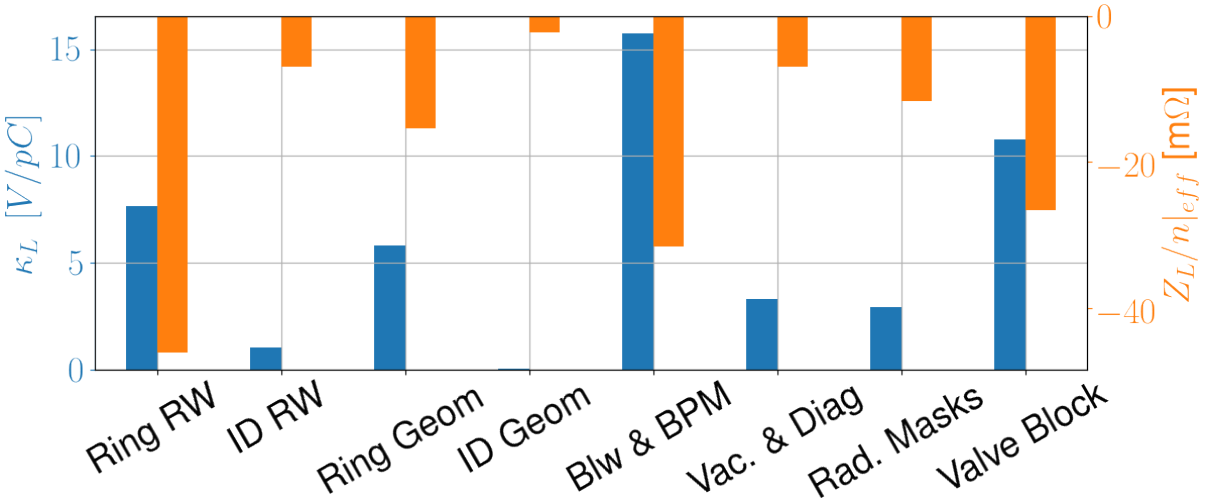


Figure 30 – Single-bunch loss factor (left, blue) and effective impedance (right, orange) calculated for the nominal operation mode of phase1 for Sirius.

Rad. Masks: This group is composed of a single type of component to show its large contribution to the budget and also to highlight the positive impact of its optimization, as described by Duarte *et al.* (2017a).

Figure 29 shows the longitudinal impedance budget of the storage ring for its first phase of operation and Figure 30 shows the single bunch loss factor and effective impedance, which were defined in section 4.2 and subsection 4.5.1, respectively. Note that the imaginary part of the impedance is mostly inductive and is dominated by the resistive-wall impedance of the standard chamber, which we know from section 5.1 that is mostly determined by the NEG coating. This large contribution is responsible for approximately one third of the total effective impedance of the storage ring and, consequently to the

bunch lengthening, which will be discussed in Chapter 7.

The second larger contribution for the imaginary part of the impedance is also the major contributor to the real part. It is common for the bellows and the BPMs to dominate the longitudinal impedance of the ring, as can be noted from Max IV impedance budget analysed by Klein *et al.* (2013) or from Soleil's budget, presented by Nagaoka (2004a) or even in the work of Blednykh & Krinsky (2007) for NSLS-II. Note in Figure 29 the existence of three main peaks in the impedance of these components, one very narrow-band, located at approximately 9 GHz, close but below the cutoff of the chamber, which is due to a trapped mode in the bellows cavity. Increasing the frequency, the next one, close to 12 GHz, also comes from the bellows, and the other, at 18 GHz, is from the BPMs. It is interesting to note that this peak from the BPM is much broader than what was presented by Duarte *et al.* (2013, Figure 4a), due to the resistive wall chamber that is included in the simulation presented here. Duarte *et al.* (2017b) shows a plot comparing simulations with PEC and resistive walls in GdfidL. The feature of performing electromagnetic simulations considering the finite conductivity of the metals of the chamber is reasonably new in most time domain codes, and was not available in GdfidL at the time when that paper was published.

Considering the bellows are made of stainless steel and the BPMs are made of Ti₆Al₄V, the geometric average of the electrical resistivity of these materials is approximately 59 times larger than copper and the average length of each component is 5 cm. Considering there will have 160 BPMs and 360 bellows in the ring, we note that this is roughly equivalent to 26 m of stainless steel chamber, which in turn, because of the $\sqrt{\rho}$ dependence of the resistive wall impedance, is equivalent to 200 m of copper chamber, qualitatively accounting for the large broad band contribution of these components. In fact, this contribution is so large that it could even change significantly the value of the low frequency resistive-wall impedance and affect the thresholds for coupled-bunch instabilities in the transverse plane. It remains a task for future works to estimate this contribution and improve the impedance budget in this direction.

The effect of the resistive-wall of the BPMs and bellows is enhanced by the fact that instead of a smooth chamber, which would distribute the impedance over the whole spectrum because of the $1/\sqrt{\omega}$ dependence of the resistive wall, these components have cavities which increase the effective inner surface and concentrate the impedance around the frequencies of the resonant modes, which are relatively low. However, this is rather inevitable for these components, and it is worth remembering that the Sirius BPM has one of the lowest loss factors among several existent designs due to the bell shaped cavity of its button, as showed by Duarte *et al.* (2013) and its first resonant peak is at a frequency as high as it can be, considering the state of the art for the production of such component.

Another component that is worth mentioning is the radiation mask. As described

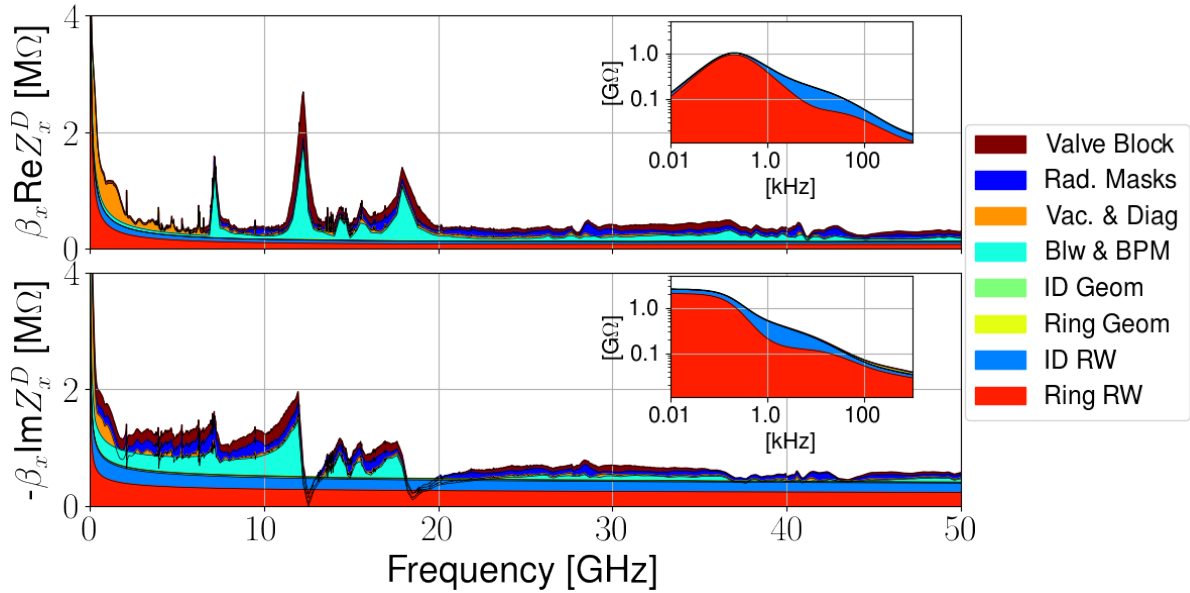


Figure 31 – Horizontal dipolar impedance budget for Sirius.

by Duarte *et al.* (2017a) two proposals were studied, one axially symmetric, which basically creates a bottleneck in the chamber, and one with only a lateral obtrusion in the outer horizontal side of the chamber, where all the radiation is concentrated. While the first design was easier and cheaper to produce, the second had a longitudinal impedance five times smaller and for this reason was chosen as the official model. Looking at Figure 30 we note that if the impedance of this component were five times larger its contribution to the budget would be as large as the one from the BPM for the loss factor, and its effective impedance would be $-58\text{ m}\Omega$, which is much larger than the $-46\text{ m}\Omega$ of the resistive wall. Such significant increase would strongly impact the threshold of the microwave instability, which will be studied in Chapter 7.

Figure 31 and Figure 32 shows the $\beta_{x,y}$ weighted horizontal and vertical dipolar impedance budgets for the first phase of operation of Sirius, and Figure 33 and Figure 34 shows the $\beta_{x,y}$ weighted single-bunch kick factor for the horizontal and vertical dipolar and quadrupolar impedances. The impedance in both planes are very similar to each other, due to the predominating round chamber of the machine. With exception of the IDs, the main differences come from the local betatron functions at the position of the components, being the vertical slightly larger, because on average $\beta_y > \beta_x$. In fact, the average of the vertical betatron function around the ring is 11 m, while the horizontal is only 6 m. Even though the gaps of the IDs are very narrow and the resistive-wall impedance depends on the inverse of the cube of the half gap, the dominating contribution for the kick factors comes from the standard chambers of the ring, but only because both betatron functions at the position of the IDs are very small, of the order of 3 m, as can be noticed in Table 7.

The only components of the ring with quadrupolar impedances with significant

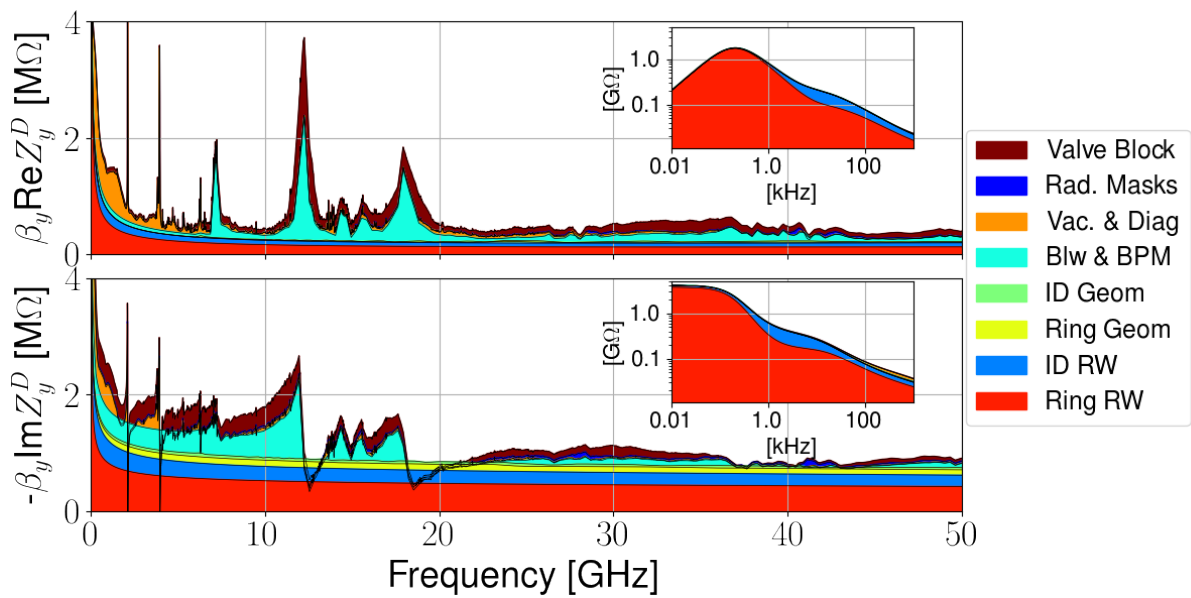


Figure 32 – Vertical dipolar impedance budget for Sirius.

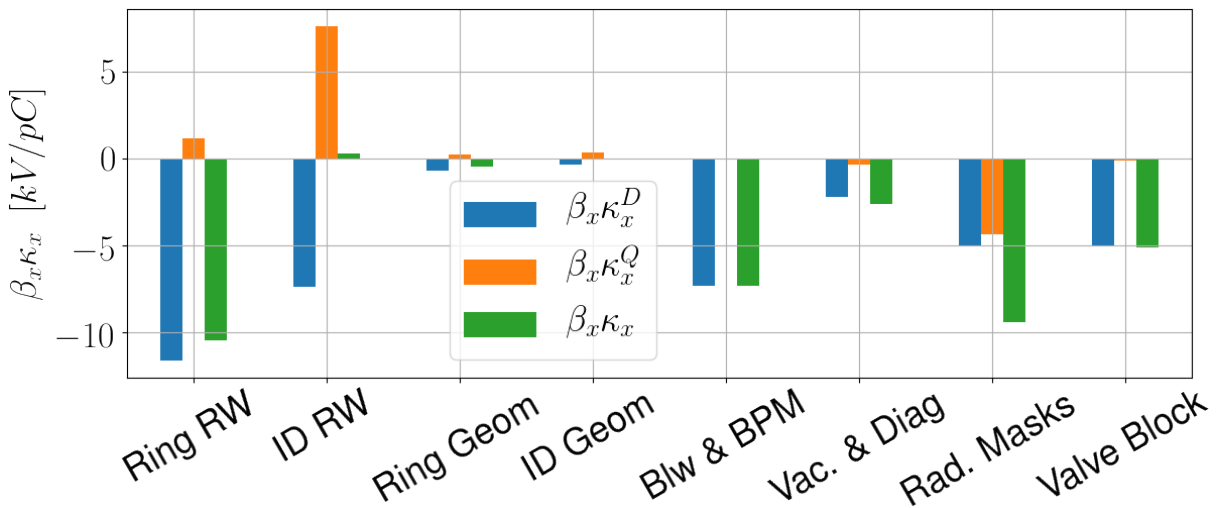


Figure 33 – Horizontal kick factors for single-bunch operation mode.

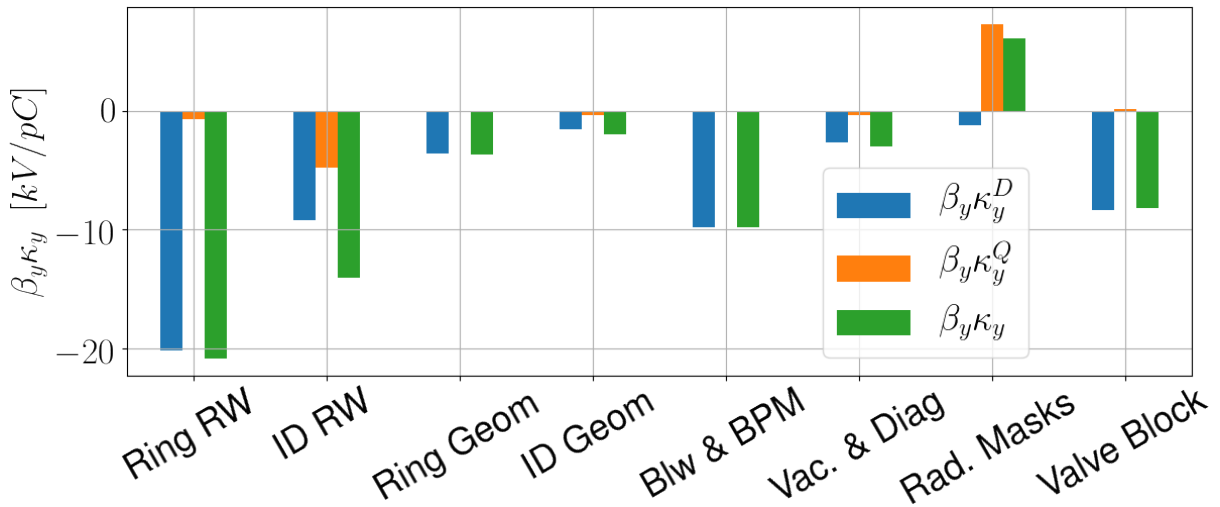


Figure 34 – Vertical kick factors for single-bunch operation mode.

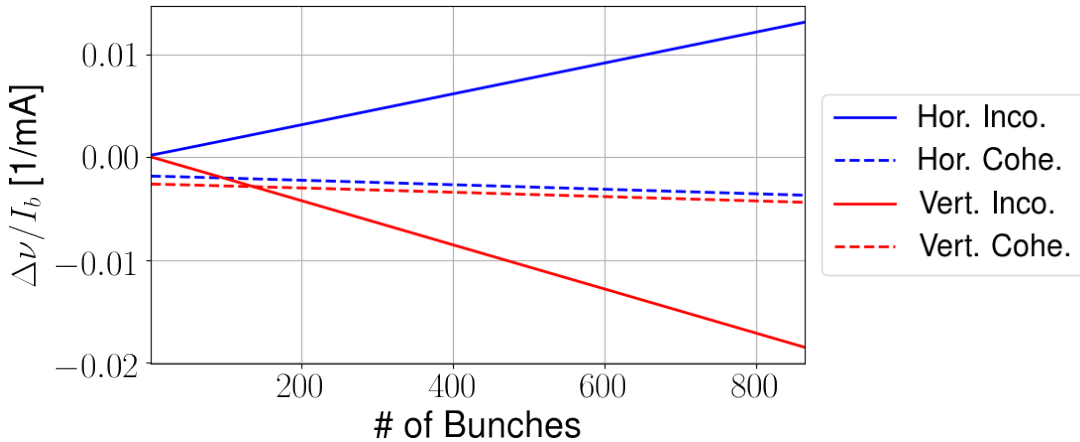


Figure 35 – Tune shift normalized by the bunch current as a function of the number of bunches in uniform filling.

effect on the beam for the single–bunch operation mode are the IDs and the radiation masks, due to the asymmetries in their chambers. Here we recall that the quadrupolar kick factor is what originates the incoherent tune shifts on the beam and the single–bunch dipolar kick factor is related to the coherent tune shifts, which means that their sum is the measurable tune of the machine and that the last one is the main factor that determines the threshold of the TMCI. Considering the vertical dipolar kick factor of the component Ring Geom is dominated by the impedance of the transition of the BC magnet, if the elliptical vacuum chamber were used instead of the keyhole geometry, as discussed in section 5.5, their kick factor would be 2.5 times larger, being the third largest of all the groups presented here. The geometric transitions of the IDs also have a small effect on the impedance because of the low betatron function, as already explained, and due to the large transition factor, t , that was used in the tapers, which was only possible because the IDs are out–of–vacuum.

While the single–bunch tune shifts are mostly defined by the broad–band impedance of the whole spectrum, their multi–bunch counterpart depends mostly on the low–frequency components of the dipolar impedance and on the zero–frequency component of the quadrupolar impedance, because, as shown in Figure 31 and Figure 32, the impedance in this region is two to three orders of magnitude larger than the high–frequency part of the spectrum, being dominated by the resistive–wall contributions from the standard chamber and the undulators. Figure 35 shows the tune shift normalized by the bunch current in uniform filling as a function of the number of filled bunches, which should be an horizontal line if the impedance were broad band. When all the bunches are filled, the incoherent tune shifts are almost five times larger than the coherent ones and, in the vertical plane, most part comes from the Laslett (1963) incoherent tune shifts from the dipole magnets, as modeled in section 5.1.

7 INSTABILITY STUDIES

The impedance budget presented in the last chapter will be used here to calculate some beam parameters at equilibrium, or stationary state, and the thresholds for instabilities as well as the behavior of the beam above the threshold. In the first section of this chapter we will briefly discuss the effect of the PETRA 7–Cell cavity on the coupled–bunch instabilities of Sirius for the commissioning phase; In the second and third sections the longitudinal and transverse dynamics of the storage ring will be studied for the phase one of operation.

7.1 The PETRA 7–Cell Cavity

According to the impedance budget gathered for Sirius, there will be no long–range wake fields capable of generating longitudinal coupled–bunch instabilities. All the elements simulated were tested individually to check whether their impedances could create this type of instability. Actually, this was a criteria adopted in the design of the components, not only for the longitudinal plane, but also for both transverse planes. However, a PETRA 7–Cell cavity will be used in the commissioning phase and it is known that this type of cavity can generate coupled–bunch instabilities, as shown by Bassi *et al.* (2016a) for the case of NSLS-II, for which this same commissioning strategy was adopted. Bassi *et al.* (2016a) presents a table with the simulated values of the longitudinal HOMs of this cavity, which we will use here to estimate the instabilities for Sirius.

The procedure we adopted to perform this analysis was the following: first we identified which of these modes have potential to cause coupled–bunch instabilities in the Sirius storage ring. This was done by finding the minimum value for the impedance as a function of the frequency for which equation (4.39) gives a positive growth rate. Isolating the impedance in that equation we get

$$\left|Z_{\parallel}^{\min}(\omega)\right| = \frac{\omega\alpha_z}{I_T\omega_0\alpha} \frac{2\pi E_0 (\omega_z\sigma_z/c)^2}{h_m^2(\omega)}. \quad (7.1)$$

Figure 36 shows the comparison of the minimum impedance with the impedance of the cavity for different values of current, considering the azimuthal modes $m = \pm 1$. For higher order azimuthal modes, the minimum impedance is much larger than any of the shunt impedances of the cavity. Note that with 10 mA three modes are already larger than the minimum impedance and have potential to create instabilities.

Next, for the modes with shunt impedance larger than the minimum impedance, we found the frequency range, $\Delta\omega_{\parallel}$, in which their impedance is also larger than the

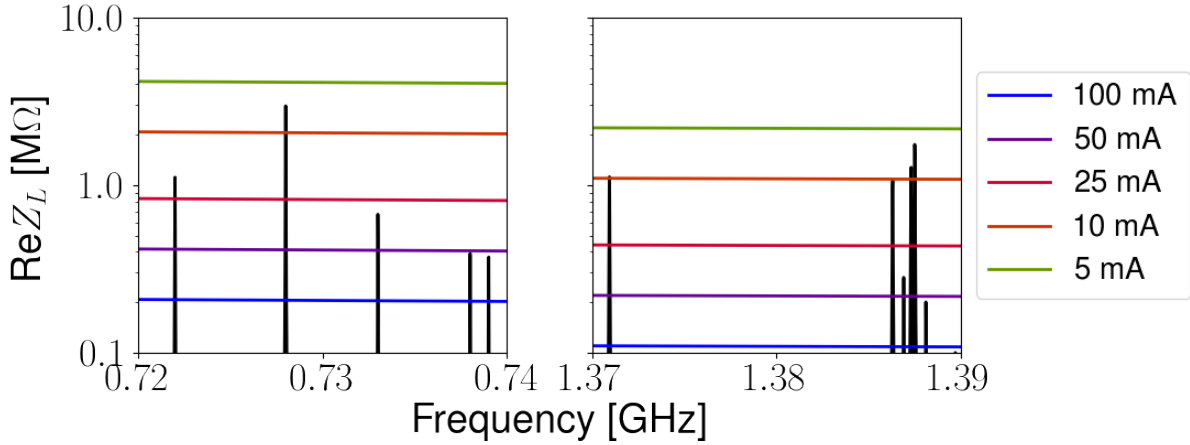


Figure 36 – Longitudinal PETRA 7–Cell cavity impedance compared with the minimum shunt impedance needed to drive coupled–bunch instabilities for several values of total beam current.

minimum impedance, in such a way that, recalling equation (4.39), if the condition

$$\forall p \in \mathbb{Z}, \quad \exists \omega_p \in \Delta\omega \mid \omega_p := (Mp + \mu \pm \nu_z) \omega_0 \quad (7.2)$$

is satisfied, it is very likely that the beam will be unstable. Considering the modes can be represented by the resonator impedance introduced in equation (3.41), we can find $\Delta\omega_{\parallel}$ by solving the inequality

$$|Z_{\parallel}^{\min}| \leq \Re \left\{ \frac{R_s}{1 + iQ \left(\frac{\omega_R}{\omega} - \frac{\omega}{\omega_R} \right)} \right\} \quad (7.3)$$

for positive frequencies. The result can be used to define

$$\Delta\omega_{\parallel} = \left\{ \omega \in \mathbb{R} \mid -\frac{f}{2} \leq \frac{\omega}{\omega_R} - \sqrt{\left(\frac{f}{2} \right)^2 + 1} \leq \frac{f}{2} \right\} \quad (7.4)$$

where $f = 1/Q\sqrt{R_s/Z_{\parallel}^{\min} - 1}$. In order to improve the visualization of the data, it is useful to map the interval $\Delta\omega_{\parallel}$ for all the resonators to the interval $[0, 1)$. This is accomplished with the definition

$$\Delta\nu_{\parallel} = \left\{ \nu \in \mathbb{R}, \omega \in \Delta\omega_{\parallel} \mid \nu = \frac{\omega}{\omega_0} - \left\lfloor \frac{\omega}{\omega_0} \right\rfloor \right\}, \quad (7.5)$$

where $\lfloor \cdot \rfloor$ is the floor function. In this space, the sampling lines for longitudinal instability are equal ν_z for the azimuthal mode $m = 1$ and $1 - \nu_z$ for the mode $m = -1$, which are all very close to the limits of the interval, remembering the synchrotron tune for Sirius is approximately 4×10^{-3} . Figure 37 shows the values of $\Delta\nu_{\parallel}$ as a function of the coupled–bunch mode closest to each resonator,

$$\mu_R \equiv \left\lfloor \frac{\omega_R}{\omega_0} \right\rfloor \bmod(M), \quad (7.6)$$

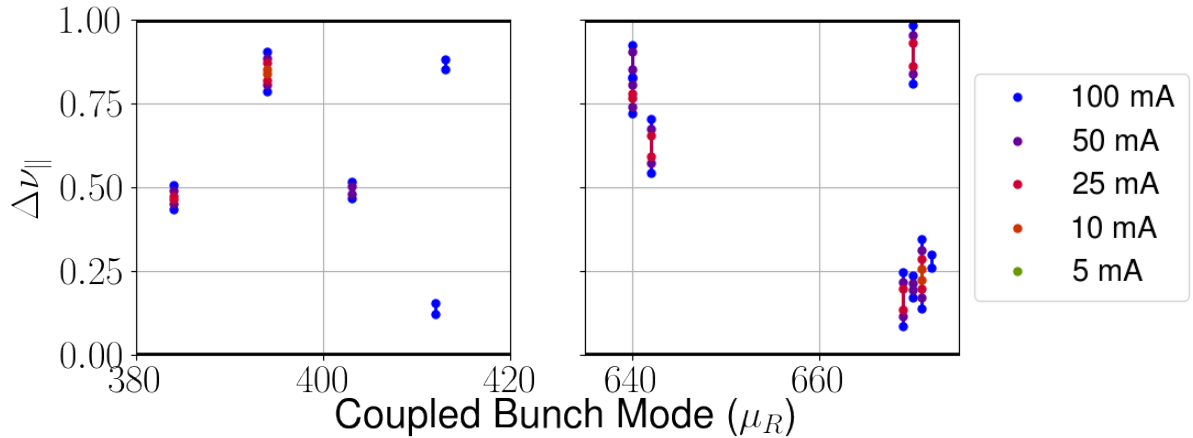


Figure 37 – The horizontal axis indicates the mapping of the RF cavity longitudinal impedance peak frequencies in the coupled–bunch modes. Vertical axis indicates the fractional part of one revolution frequency in the ring. Black horizontal lines are $\pm\nu_z$ and the interval defined by the dots is the interval in which sampling by the synchrotron tune corresponds to instability at the indicated current.

where this is strictly valid only for mode $m = 1$. For mode $m = -1$ the value of $-\omega_R$ should be used, which, due to the fact that floor of negative numbers is the complement of its positive counterpart, for example, $\lfloor -3/5 \rfloor = 2$, the coupled–bunch numbers would be inverted. We highlight that this definition is only useful if the bandwidth of the mode is smaller than the revolution frequency, otherwise the HOM would be able to drive more than one coupled–bunch mode into resonance. In Figure 37, each vertical line indicates the frequency range where instability could be generated if the beam sampled any frequency there and the horizontal black lines are the frequencies sampled by the beam. Analysing the Figure 37 we note that according to this impedance model, the beam will be stable up to 100 mA. This hypothesis was tested with a direct application of the equation (4.39), which confirmed that there would be no positive growth rates.

However, in the real cavity, the resonant frequencies of the HOMs depend on the temperature and have a strong dependence on the geometry of the cavity, which, in turn, will be adjusted to change the frequency of the main mode to be close to the Sirius RF frequency. These frequency changes can be larger than the revolution frequency of the ring, which means that the scenario presented in Figure 37 could change drastically and some of the modes could cross the lines sampled by the beam, close to zero and one. The first analysis, based on the results presented in Figure 36, is more reliable, because the shunt impedance is much less sensitive to small changes in the cavity. For this reason, since we plan to commission the ring with currents up to 30 mA, and also predicting a possible delay in the installation of the superconducting RF cavity, a longitudinal kicker was designed and will be installed in the ring, together with a longitudinal bunch–by–bunch feedback system to control the longitudinal coupled–bunch instabilities.

This kicker will have a shunt impedance, R_K , of 900Ω and an amplifier of 30 W. Considering the losses in the cables, the maximum effective power applied to the beam will be 9 W (DUARTE, 2018). According to Lonza (2007), the relation between the power, P , and the damping time provided by the kicker, τ_K , is given by

$$\alpha_K = \frac{1}{\tau_K} = \sqrt{\frac{R_k P}{2}} \frac{\alpha}{2\pi\nu_z(E_0/e)} \frac{c}{z_{\max}}, \quad (7.7)$$

where z_{\max} is the maximum amplitude of the movement. The requirement for the maximum longitudinal oscillation of the beam for stable operation is 10 % of the beam size, which corresponds to 0.25 mm and, consequently, via the equation above, an additional damping rate of 175 Hz will be provided by the kicker, which is approximately two times larger than the natural damping rate of the storage ring. With this factor of three in the damping, operations with 30 mA will be possible. Actually, the estimative made above is pessimistic, because the measurement of the longitudinal oscillations will be much better than the requirement presented above, which means the instability will be controlled at smaller amplitudes, requiring less power. Besides, if more power were needed it will be possible to install another amplifier in parallel, doubling the total power of the system. Finally, even though Figure 37 is not enough to quantitatively describe the stability of the beam, it shows that there are regions of the $\Delta\nu$ space which are free of HOMs, or at least have weaker ones, in such a way that in principle it will be possible to find more stable regions by adjusting the temperature of the cavity.

A similar study was performed for the transverse couple–bunch instabilities with the impedance model provided by Bassi *et al.* (2016a). In this case, we can use equation (4.43) to isolate the minimum impedance,

$$Z_u^{\min}(\omega) = \frac{(\alpha_u + |m|\alpha_z)}{\beta_u} \frac{4\pi\nu_z E_0}{I_T h_m^2(\omega - \omega_\xi)}, \quad (7.8)$$

where u stands for both, x and y . Figure 38 shows the comparison of the minimum shunt impedance with the cavity impedance for several values of currents in the machine for the azimuthal mode $m = 0$. The azimuthal modes $m = \pm 1$ will be stable at zero chromaticity, but at $\xi_u = 2.5$, currents larger than 50 mA could become unstable. The calculations were performed for the horizontal plane, but the results are identical in the vertical plane, because horizontal and vertical betatron functions at the location of the cavity are equal. In this case, there are fewer modes, but all are strong enough to create coupled–bunch instabilities. Even for a current as low as 5 mA there are modes which could drive the beam unstable. It was verified that the chromaticities only start to influence for values larger than 5, which would degrade the lifetime of the ring and cause instabilities of the modes $m = \pm 1$, as discussed above.

Proceeding with the calculation of the frequency range $\Delta\omega_u$, where the absolute value of the impedance for each HOM is larger than the minimum impedance, we use the

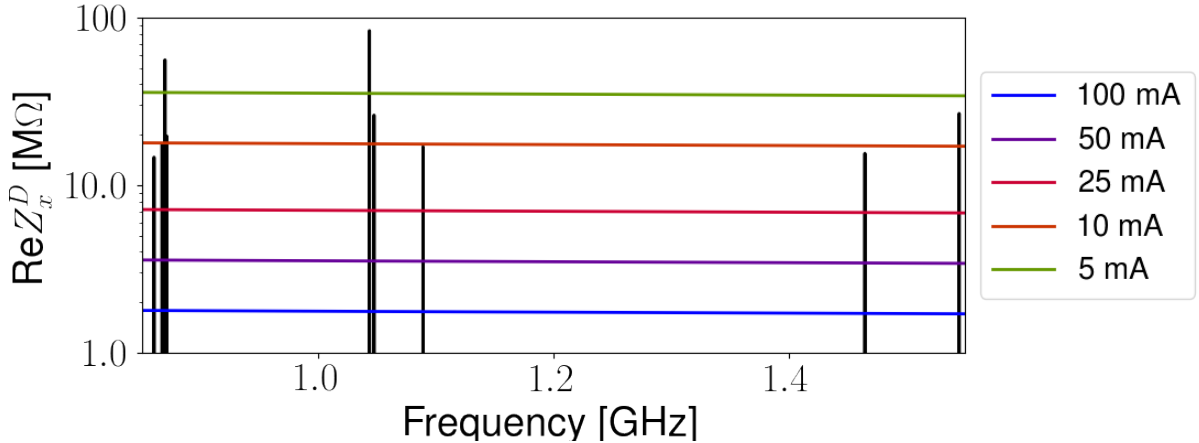


Figure 38 – Transverse PETRA 7–Cell cavity impedance compared with the minimum shunt impedance needed to drive coupled–bunch instabilities for several values of total beam current.

equation (3.44) to model the modes as resonators and get

$$-Z_u^{\min} \geq \Re \left\{ \frac{\omega_R}{\omega} \frac{R_s}{1 + iQ \left(\frac{\omega_R}{\omega} - \frac{\omega}{\omega_R} \right)} \right\}, \quad (7.9)$$

which differs from its analog in the longitudinal plane, because we are interested in negative real impedances, which are responsible for generating instabilities. This equation can be used to define, implicitly,

$$\Delta\omega_u = \left\{ \omega \in \mathbb{R} \mid \omega < 0, \omega^4 + \left(\frac{1}{Q^2} - 2 \right) \omega^2 \omega_R^2 + \frac{R_s}{Z_u^{\min} Q^2} \omega \omega_R^3 + \omega_R^4 \geq 0 \right\}, \quad (7.10)$$

where we point out that now we are looking for negative frequencies, because it is in this region that the real part of the impedance is negative too. The second inequality in the definition of the interval $\Delta\omega_u$ is too complex to be solved analytically and the values were found numerically. With this interval, we can calculate $\Delta\nu_u$ using the exact same definition as in the longitudinal plane, given by equation (7.5), with the remark that, since now we are working with negative frequencies, the floor function should be carefully carried out. On the other hand, the definition of the coupled–bunch mode must be changed, because the transverse tunes are much larger than unit and have to be taken in to account:

$$\mu_R \equiv \left[\frac{-\omega_R - \nu_u}{\omega_0} \right] \text{mod}(M). \quad (7.11)$$

Figure 39 shows the fractional frequency range, $\Delta\nu_u$ as a function of the coupled–bunch mode calculated for the horizontal plane for all the transverse HOMs. Recalling equation (4.43), the sampling of the impedance in the transverse plane when mapped to the space of $\Delta\nu_u$ happens at $\nu_{x,y}$, shown in the figure as black horizontal lines. Note that the threshold for the horizontal and vertical instabilities is slightly below 50 mA. Actually,

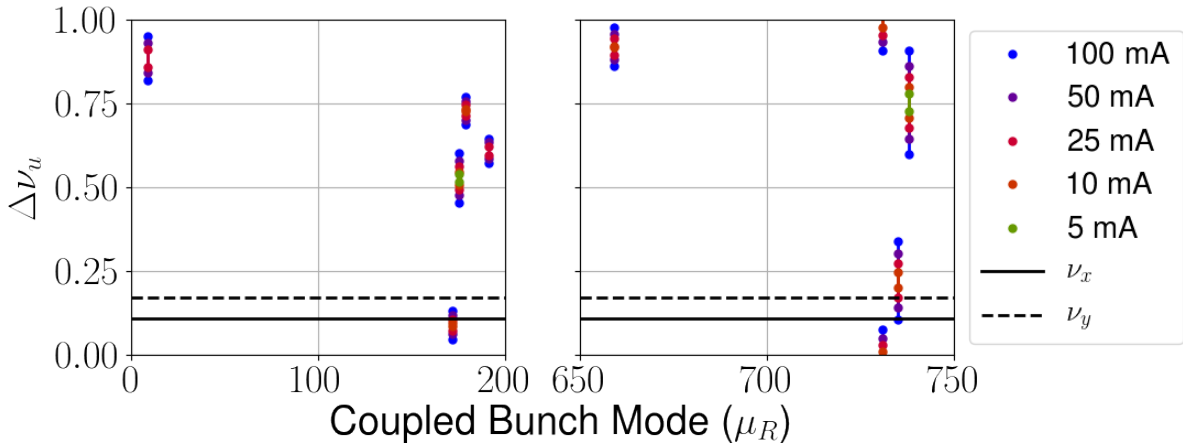


Figure 39 – The horizontal axis indicates the mapping of the RF cavity transverse impedance peak frequencies in the coupled–bunch modes. Vertical axis indicates the fractional part of one revolution frequency in the ring. Black solid horizontal line is the fractional part of ν_x and black dashed line is the fractional part of ν_y . The interval defined by the dots is the range in which sampling by the betatron tune corresponds to instability at the indicated current.

the precise calculation, using equation (4.43), showed that the threshold is coincidentally 30 mA for both planes. Besides, notice that at 100 mA another HOM, the same one driving the vertical plane instability, also starts to influence the horizontal plane. One interesting feature of this figure is that it reveals an island of stability in the region (0.34, 0.44) and, since the difference between the tunes is only 0.07, in principle it would be possible to try to adjust the temperature of the cavity to change the position of the HOMs in such a way that this region coincides with the beam.

However, as discussed for the longitudinal plane, this phasing study is very idealized and it is very likely that the real cavity will have a different configuration. For these reasons the most pragmatic approach is to rely in transverse bunch–by–bunch feedback systems to ensure the stability of the beam. These systems will be available for Sirius in the commissioning.

7.2 Longitudinal Plane

The studies of the longitudinal dynamics of the Sirius storage ring will be presented in this section. First, we will evaluate the effects of the standard impedance budget, without considering the CSR impedance. In the second part we will analyse the noise in tracking simulations induced by high–frequency components of the wake, together with the solutions for this problem that were adopted in this work. In the third part we will present the results of the simulations with CSR, trying to take into account the effect of the other impedance sources and IBS as well.

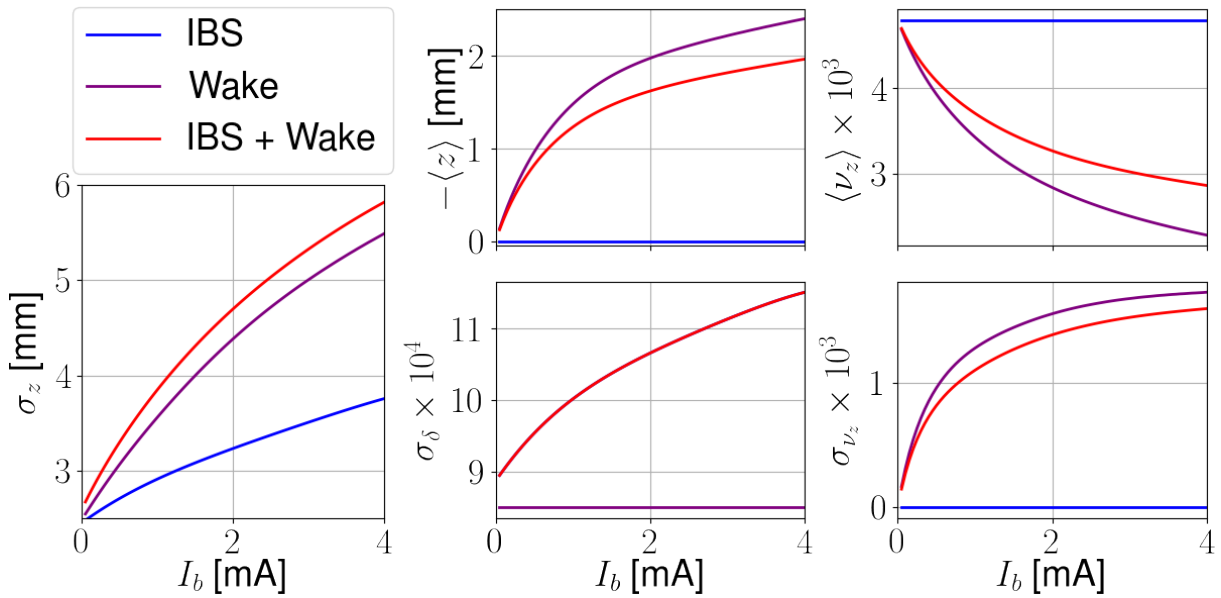


Figure 40 – Stationary parameters of the longitudinal plane, calculated from the solution of the Haissinski equation.

7.2.1 Standard Impedance Budget Effects

Table 1 shows only the natural, or zero-current, values of the equilibrium parameters of the storage ring. When the bunch current increases, the IBS change these parameters due to the temperature rise coming from collisions¹. The main impact of this effect for the wake field induced collective effects is the energy spread increase and the consequent bunch lengthening. Figure 40 shows the equilibrium parameters of the storage ring as a function of current for three situations, where the last one, IBS+Wake, is not self-consistent, because it was obtained by the solution of the Haïssinski equation using the additional energy spread induced by IBS as initial input. It means that the reduction of the IBS effect caused by lengthening of the bunch by the wake is not considered in that curve. While this curve can be considered as a higher limit for the bunch length and energy spread, or optimistic in relation to the threshold of the instabilities which will be studied below, the curve for which only the wake function of the machine is considered can be interpreted as the other extreme limit case. The strong inductance of the impedance budget becomes evident in Figure 40 where we notice that the bunch is lengthened by a factor larger than 2 in the current range analysed, while the synchrotron position, $\langle z \rangle$, only changes by less than 2 mm.

The average synchrotron tune, $\langle \nu_z \rangle$, and the synchrotron tune spread, σ_{ν_z} , shown in Figure 40 were calculated based on a generalization of the synchrotron tune defined in equation 2.37 for a general voltage gap, $V(z)$. Neglecting the damping rate, α_z , in that

¹ The effect of IBS on Sirius equilibrium parameters was not calculated in this work. The values shown here were obtained by Natália Milas and Afonso Haruo Mukai

Table 8 – Broad band resonators model of the Sirius longitudinal impedance budget.

f_R [GHz]	716.2	206.9	138.4	79.6	57.3	35.0	17.5	17.8	11.9	9.2
R_s [$k\Omega$]	30.0	6.5	2.0	2.0	2.5	2.5	1.7	3.0	4.0	20.0
Q	0.7	1.3	4.0	1.0	4.5	3.0	1.0	24.0	24.0	100.0

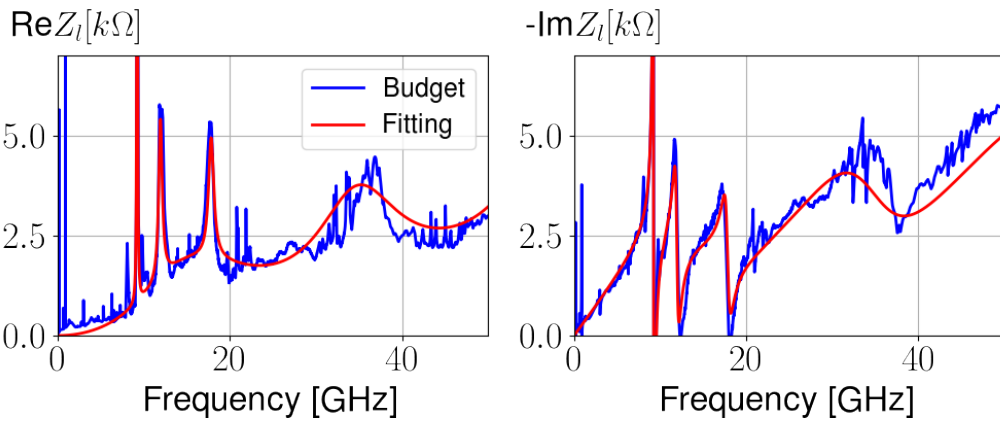


Figure 41 – Comparison of the complete longitudinal impedance calculated for the Sirius storage ring (blue) with the BBRs fitting presented in Table 8 (red).

equation, we can define a z -dependent synchrotron tune as

$$\nu_z(z) = \frac{1}{2\pi} \sqrt{V'(z)\alpha L_0}, \quad (7.12)$$

where $V'(z)$ is the derivative of the effective voltage (RF cavity plus wake) obtained from the Haissinski equation, normalized by the nominal energy of the storage ring, E_0 . This way, the average synchrotron tune and the synchrotron tune spread can be calculated with

$$\langle \nu_z \rangle = \int_{-\infty}^{\infty} dx \nu_z(x) \lambda(x), \quad \sigma_{\nu_z}^2 = \int_{-\infty}^{\infty} dx (\nu_z(x) - \langle \nu_z \rangle)^2 \lambda(x), \quad (7.13)$$

respectively, where $\lambda(z)$ is the equilibrium distribution, solution of the Haissinski equation.

The current threshold for the microwave instability was calculated in frequency domain, using equation (4.35) and by macroparticle tracking. In this process, we also created a model based on BBRs for the whole impedance budget as an attempt to summarize it in a small set of numbers that can be used in future calculations and try to understand the individual contribution of each structure to the behavior of the beam. Such task was accomplished with the 11 BBRs shown in Table 8. Figure 41 shows the comparison between the fitted and original impedances. Even though the agreement is not excellent, and there is still room for improvement, this model explains very well the bunch lengthening, the energy loss, threshold of the instability and the behavior of the beam above the threshold. The very high frequency BBR, the first in the table, is due to the NEG-coated vacuum chamber, which has a very large inductive impedance at low frequencies, being the major contributor for the bunch lengthening. The last three resonators are originated by the bellows and the BPMs of the machine and have a fairly

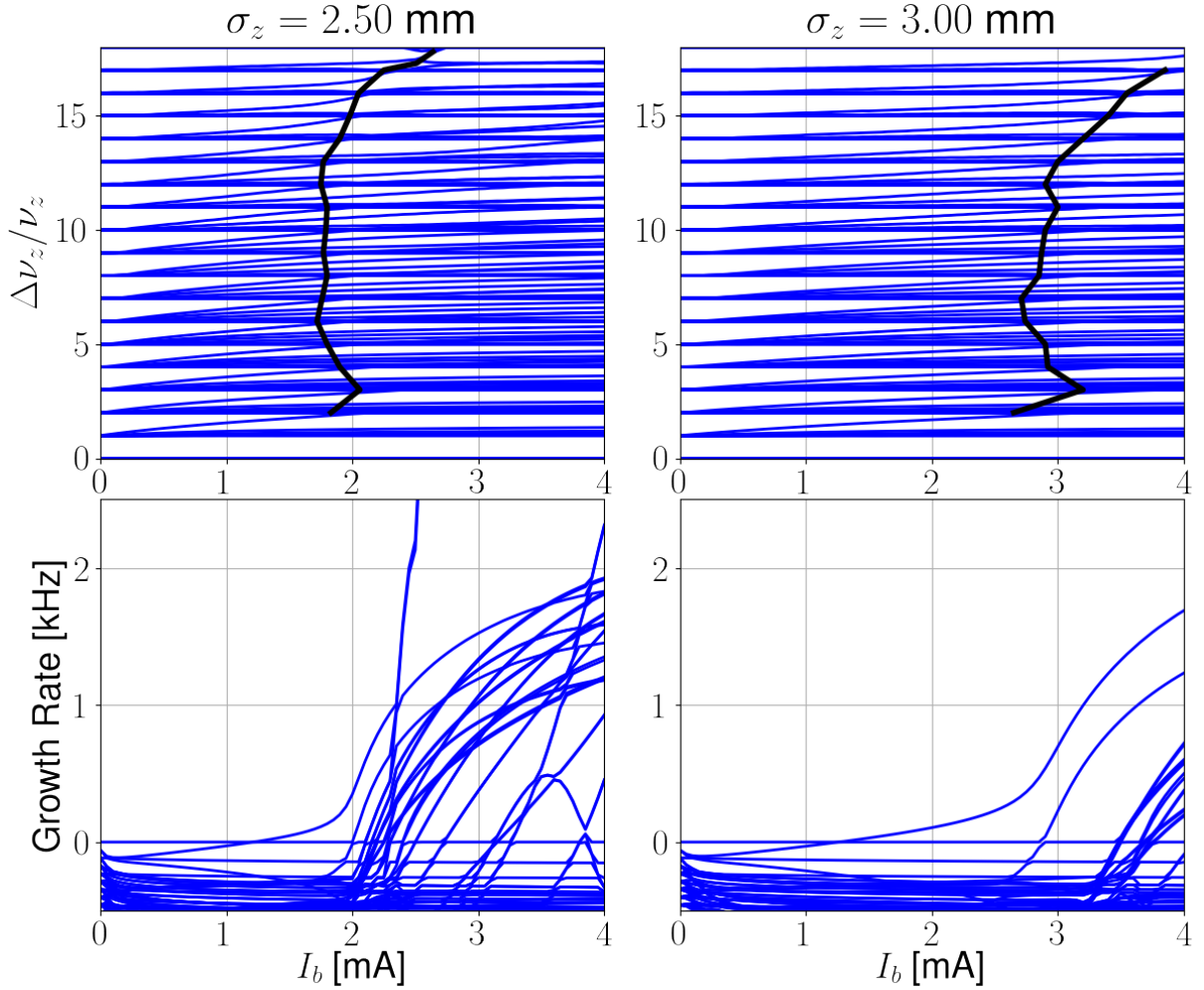


Figure 42 – Mode-coupling instability for two different bunch lengths for phase one of operation. The black lines indicate where different azimuthal modes couple.

large Q factor. Their correct modeling is very important to reproduce the behavior of the beam above the threshold of the microwave instability.

For the frequency domain calculations we did not take into account the IBS effect and, due to the limitation of the theory, the potential well distortion is not included either. We ran the simulations of the mode-coupling instability considering the first 31 radial modes and the azimuthal modes from -30 to 30 , totalizing 1860 modes, for two different bunch lengths: 2.5 mm and 3.0 mm, being the first condition related to zero-current parameters of the first phase of operation of the storage ring and the second was considered only for a better understanding of the physical phenomena, as described below. Figure 42 shows the results, which are amazingly interesting. There is a fierce competition for mode-coupling among modes with azimuthal number up to 17, being the higher order modes driven by the strong high-frequency components of the resistive-wall impedance and the low-order modes driven by the other components of the machine, mainly the BPMs and bellows. In the simulation with bunch length equal to 2.5 mm, several of them couples almost together, being difficult to identify which one goes first.

On the other hand, when a bunch of 3 mm is used, all couplings are shifted to higher currents and the coupling between one dipolar and one quadrupolar mode is the first one to happen. In both simulations there is the prediction of a weak instability, result of the coupling between two radial modes of the same dipolar azimuthal mode, that in fact sets the threshold for the instability at 1.25 mA. The BBR model does not predict this coupling and so far we could not identify which part of the impedance budget is creating it, but it must be some component at the low-frequency part of the spectrum because it is present and unchanged in simulations with bunch lengths up to 5 mm.

Tracking simulations were performed for 3×10^4 turns in the ring, using 10^7 macroparticles and the PIC method was used to apply the wake kicks, where longitudinal direction was segmented in 5×10^4 bins from -5 cm to 5 cm, which corresponds to 2 μm per bin. With these parameters all the wakes of the budget can be completely described, with the requirement of the Nyquist theorem, expressed in equation (4.47), being met for all of them. As will be described in the next section, the Savitzky–Golay filter was applied in the beam distribution before the convolution with wake in every turn, as an attempt to control the effects of numerical noise to acceptable levels. The initial tracking conditions were the stationary results obtained with the Haissinski equation, to minimize the initial oscillations of the beam, which would increase the time needed to observe the instability buildup.

Figure 43 shows the main longitudinal beam parameters obtained from average over all the turns of the simulation. Two different situations were studied, with and without the IBS effects, to account for the best and worst case scenarios, respectively, regarding the instability threshold. A strong instability rises between 2.8 mA and 3.0 mA for the simulation with only the wake effects, and drastically increases the average energy spread as a function of the current. Only 0.5 mA above the threshold, the energy spread reaches values larger than the one where the effects of IBS are considered. Even though their time average are comparable, the behavior of the beam above the threshold is completely different in both situations. This difference is notable in Figure 44 where the time evolution of the energy spread is shown. The coherent energy of the instability drives exponentially increasing oscillations of the beam, deforming the longitudinal distribution of the particles. When this deformation is large, the interaction of the beam with the wake is weakened and radiation damping brings the beam to lower values of energy spread. Even though it is not shown here, simulations with a larger number of turns shows that this process of growth and damping repeats, forming a saw-tooth like pattern. Figure 45 shows the discrete Fourier transform of the time evolution of the average bunch position, where the horizontal axis was normalized by the zero-current synchrotron tune for easy identification of the coherent modes. The dipole mode, as expected, remains fixed at one synchrotron tune, because of the single-bunch nature of the simulation, which carries the potential well distortion together with the bunch. The mode which is driving the instability is the

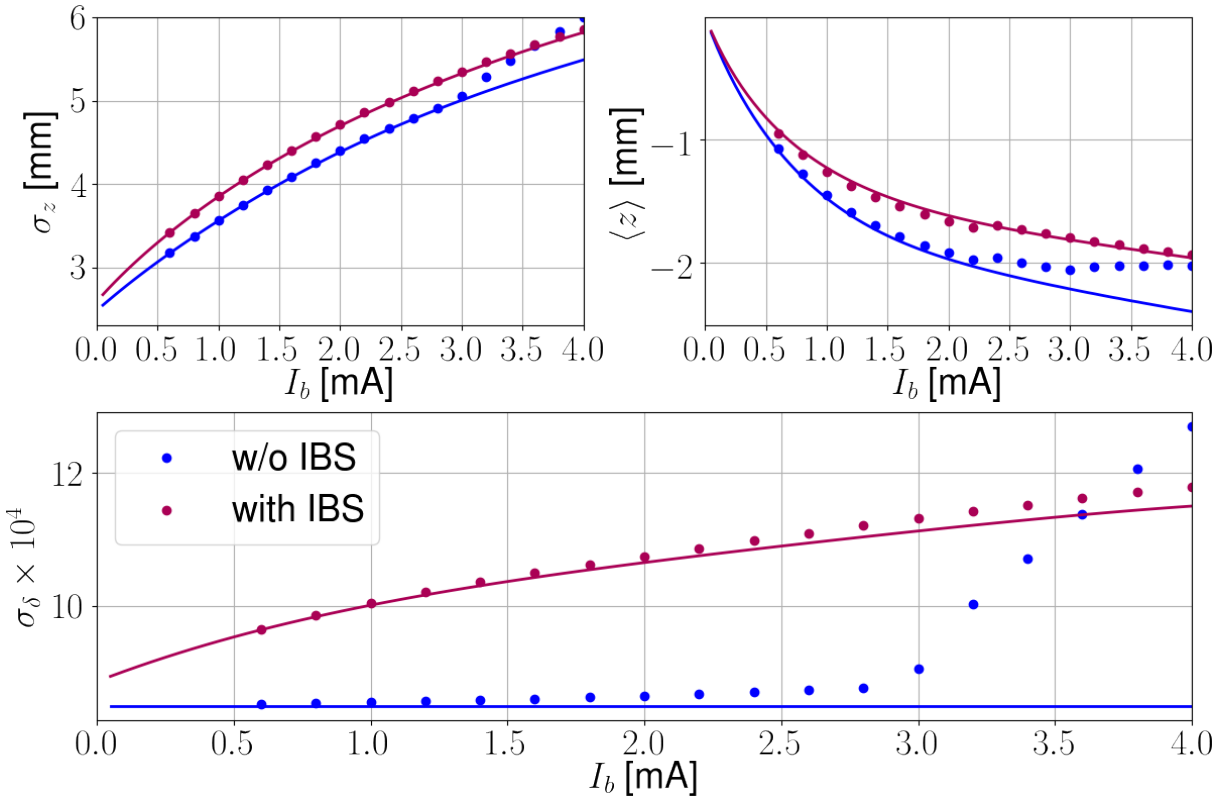


Figure 43 – Main parameters of the beam obtained from tracking (dots) as a function of the current for the simulations with and without the effects of IBS. The values shown here are averages over all the 3×10^4 turns of the simulation. The solid lines are the results obtained from the solution of the Haissinski equation.

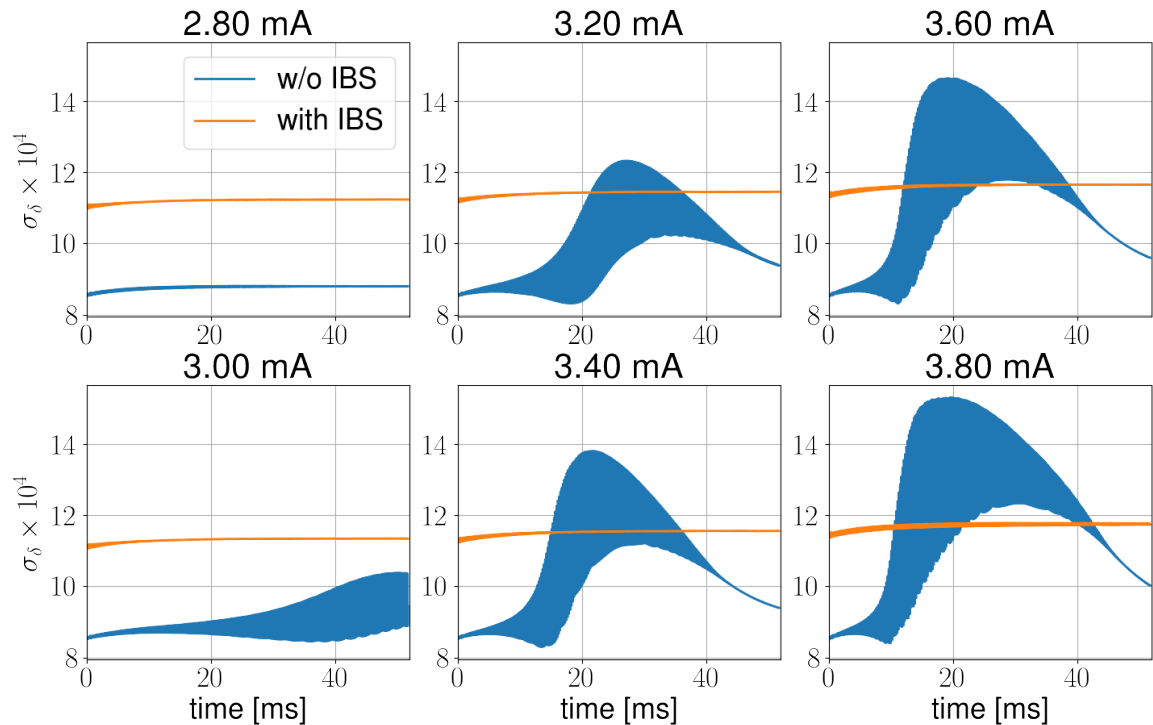


Figure 44 – Time evolution of the energy spread for different bunch currents close to the threshold of the sawtooth-like instability.

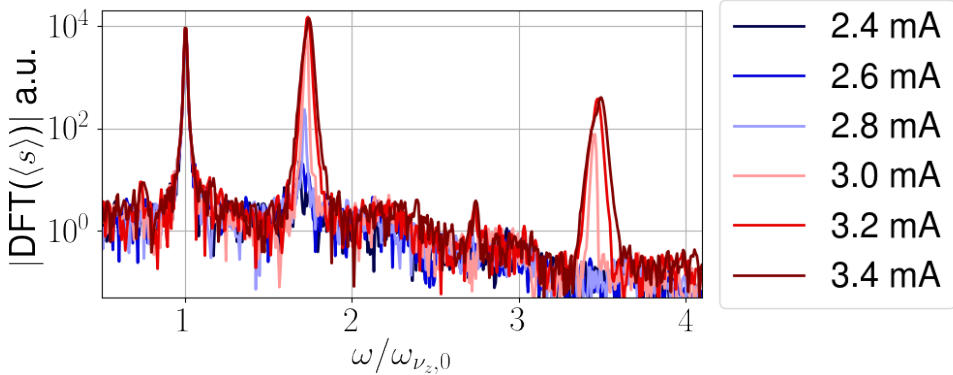


Figure 45 – Discrete Fourier transform of the time-dependent bunch centroid, as a function of frequency in units of the zero-current synchrotron frequency.

quadrupolar mode, close to 1.75. Even though it is present in the spectrum below the threshold, its amplitude increases almost two orders of magnitude from current 2.8 mA to 3.0 mA. The peak at approximately 3.5 is not another coupling of modes, as Figure 42 suggests, but only a multiple of the main mode that is driving the instability, being a result of the non-linearities created by both the radiation damping and the different interaction of the beam with the wake as a function of time.

Figure 43 also reveals a small sudden change in the average longitudinal position of the beam as a function of the current from the simulations with 2.2 mA and 2.4 mA in both simulations presented there. This could be an indication of the weak instability predicted by the frequency domain analysis, but no other result besides this one corroborates such interpretation, and further studies are required to confirm or reject this hypothesis.

Even though the threshold of the instability was not determined properly with the study presented here, because the behavior of the beam in the best and worst case scenarios is completely different, two important conclusions can be drawn. The first is that the lower limit for the current threshold is much larger than any current predicted for operation of the machine. Even the single-bunch operation scenarios are currently limited to 2 mA due to lifetime issues. The second is that, as indicated by the frequency domain analysis, the current threshold is very sensitive to an increase in the bunch length caused by energy spread increase, which suggests the real behavior of the beam will be closer to the simulated IBS+Wake than to the only wake case. It is a work for future endeavors, however, to develop methods to self-consistently simulate the effects of wake fields and IBS together, or at least use some iterations between both isolated simulations to obtain more realistic results.

As a final remark, the tracking code and the Haissinski solver employed in this analysis can be directly applied to determine the single-bunch stability of the storage ring in the second phase of operation, when the Landau cavity will be installed. The calculations were not performed in this work mainly due to lack of time.

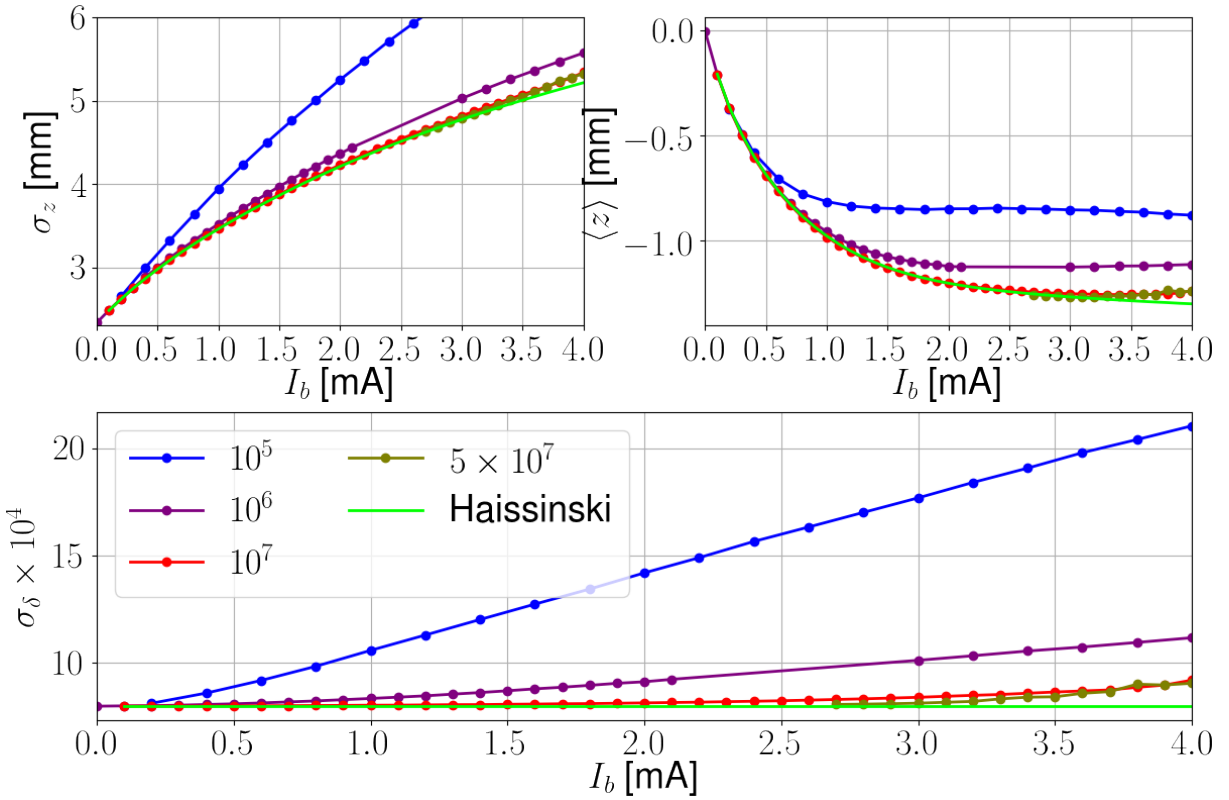


Figure 46 – Tracking results, showing the effect of noise as a function of current for different numbers of macroparticles in the simulation.

7.2.2 Noise in Tracking Simulations

Prior to the study presented above, it was necessary to deal with the problem of noise in tracking simulations in order to extract reliable results. Numerical noise can completely spoil longitudinal simulations, because it provides an additional source of energy spread for the bunch, which is bad for two reasons: first, because this is the main observable that indicates the onset of the instability we want to study; and second, because the increased energy spread lengthens the bunch, which changes, generally weakens, the effect of the wake, preventing the instability from happening. Figure 46 shows an example of this phenomena, where the first tracking results obtained for Sirius are presented. They were performed with a slightly different configuration for the machine than the one presented in last section, and for this reason this figure does not exactly compares to Figure 43. Note that even with a number of particles as large as 10^6 , there still is a strong influence of noise, and only with 10^7 particles the results seem to have converged, where the onset of an instability happens at approximately 3 mA, as already known from the last section results.

This additional energy spread is introduced by the interaction of very high-frequency components of the wake with fluctuations in the beam distribution due to the reduced finite number of simulated particles. There are some methods to avoid this problem, being

the most obvious one to increase the number of particles until this effect is negligible. This approach generally works well. For example, in the benchmarking presented in subsection 4.6 only 10^5 macroparticles were enough to reproduce the results of Elegant (BORLAND, 2000) and SPACE (BASSI *et al.*, 2016b), but in the case of the impedance budget of Sirius, the strong high-frequency components of the resistive-wall and the CSR, makes such approach impracticable. Another method is to increase the size of the grids in the longitudinal plane as a method to abruptly cut the high frequencies of the wake, avoiding the generation of noise. This method is also valid when one knows that the high-frequency components of the wake are not strong enough to generate coherent motion, which again, is not the case of CSR and neither what was being indicated by the frequency-domain analysis for the case of the resistive-wall. Even when the wakes are not strong enough to create instabilities and the application of this method is viable, depending on the parameters of the simulation, convergent results might be difficult to obtain, requiring several simulations with different number of particles and mesh sizes, until optimal parameters are found.

A conceptually similar way of ignoring the high frequencies of the wake and, at least in parts, to avoid the problem of spectral leakage is to convolve the original wake function with a small gaussian distribution, that smoothly filters the undesired frequencies without the need of increasing the mesh size and assuring the convergence of the results depends only on the number of particles. This method was successfully used for Sirius calculations considering the standard impedance budget presented in last section, but completely failed in the CSR simulations. Even the success with the impedance budget is due to the fact that, luckily, the mode which coupled first was the quadrupolar one, as showed in the last section. If the parameters of the simulation were slightly different it could have failed as well. Other filters, which are not as smooth as the gaussian could be a better alternative for handling this problem.

Another method, which is the hard way of dealing with noise, is to filter the noise at the source, i.e. filter the distribution of particles. Terzic & Bassi (2011) shows a very detailed study where the authors compared different methods of performing this task. The study of these advanced methods will be addressed in future works. The solution currently adopted for this problem was the use of 9-point cubic Savitzky–Golay filter (SAVITZKY; GOLAY, 1964), as it is done in Elegant (BORLAND, 2000), according to Borland (2001). The results presented in last section were calculated already using this method and the ones from the next section, where the CSR will be analysed, will use it too.

Considering that the issues with noise are very difficult to be dealt with in tracking simulations, it is useful to know *a priori* what will be its effect on the beam, given a wake function and the number of particles being simulated. This necessity motivated us to try to understand better how this coupling of the wake with the beam creates the additional

energy spread. In the paragraphs below we describe a possible explanation for this process.

7.2.2.1 Estimative of Numerical Noise

Given a longitudinal density distribution $\rho(z)$, the number of particles in a small interval Δz centered at the position z , $N_l(z)$, is a random variable that follows a binomial distribution. Thus, considering that there are N_p macroparticles in the bunch simulation, we have

$$\langle N_l \rangle = \rho(z) \Delta z N_p \quad \text{and} \quad \text{var}(N_l) \approx \rho(z) \Delta z N_p, \quad (7.14)$$

where $\langle \cdot \rangle$ and $\text{var}(\cdot)$ denotes average and variance, respectively, being the latter a measure of the fluctuations in the bunch due to the finite number of particles. If the particles were static, this fluctuation would also be, but, as they are moving due to the longitudinal dynamics of the storage ring, these fluctuations are constantly changing. For very small Δz , the value of $N_l(z)$ changes very fast, but as Δz increases, this characteristic time becomes increasingly large.

It is possible to estimate the length scale where the behavior of the variance changes by considering the number of turns it takes for the stored particles to complete one oscillation in the longitudinal phase space, which is $1/\nu_{z,0}$. This means that, on average, the longitudinal position of each particle differs from its position in the last turn by $\Delta z_L \approx 4\nu_{z,0}\sigma_{z,0}$. Consequently, for scales below or on the order of this length, the fluctuations of the particle distribution changes in a turn-by-turn basis.

Now, let us consider there is a wake function $W(z)$ that is constant in a small interval $\Delta z_W \approx \Delta z_L$ behind the source particle and zero outside this interval. Then, any particle inside the bunch would receive random kicks $K = eI_b T_0 W N_l / N_p$. The average of this kick varies slowly in time, because it depends on the evolution of the density distribution, but the variance, given by

$$\text{var}(K) = (qI_b T_0 W)^2 \frac{\text{var}(N_l)}{N_p^2} \approx (qI_b T_0 W)^2 \frac{\Delta z_W}{\sigma_z N_p \sqrt{2\pi \exp(1)}}, \quad (7.15)$$

varies from turn to turn, where in the last step it was assumed $z \approx \sigma_z$ and that the distribution is gaussian, $\rho(\sigma_z) = 1/(\sqrt{2\pi \exp(1)}\sigma_z)$. Summarizing, this mechanism introduces a random variation of the energy of the particles in a turn-by-turn basis, similarly to the quantum excitation process due to radiation emission. This means that it should change the energy spread of the beam by

$$\begin{aligned} \Delta\sigma^2 &= \sigma_\delta^2 - \sigma_{\delta 0}^2 \approx \frac{4\text{var}(K)/E_0^2}{\alpha_z T_0 (4 - \alpha_z T_0)} = \\ &= \left(\frac{qI_b T_0 W}{E_0} \right)^2 \frac{\Delta z_W}{\sigma_z N_p \sqrt{2\pi \exp(1)}} \frac{4}{\alpha_z T_0 (4 - \alpha_z T_0)}. \end{aligned} \quad (7.16)$$

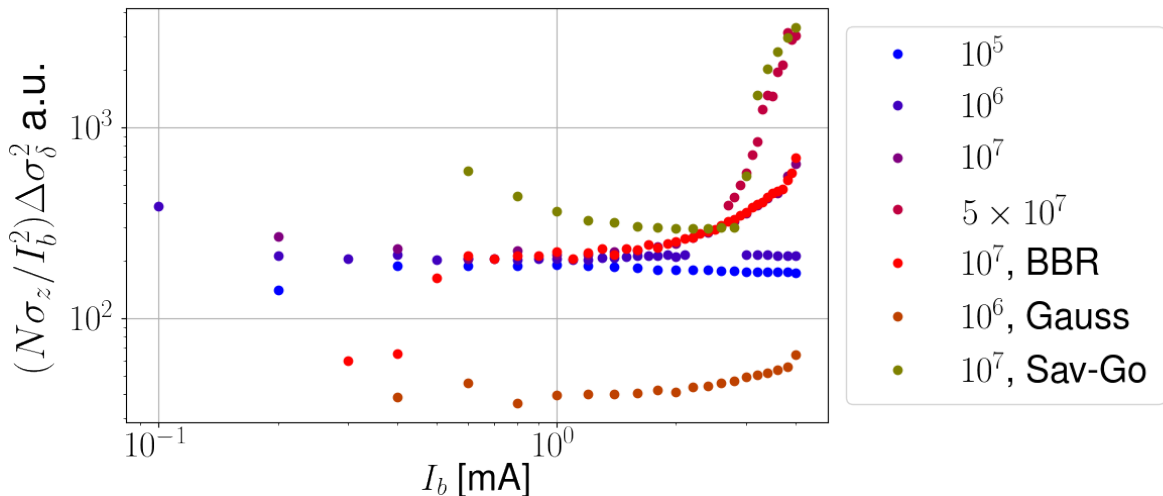


Figure 47 – Energy spread increase in simulations multiplied by $N_p \sigma_z / I_b^2$. The curves 10^5 , 10^6 , 10^7 and 5×10^7 were performed with the same wake function using the PIC method, while for curve $(10^7, \text{BBR})$ the dynamics was simulated using directly the BBRs from the impedance model presented in subsection 7.2.1. For the curve $(10^6, \text{Gauss})$ a convolution with a $40 \mu\text{m}$ gaussian bunch was applied to the wake and a Savitzky–Golay filter was applied in the simulation of the results of $(10^7, \text{Sav-Go})$.

Figure 47 shows the energy spread variation from Sirius tracking simulations multiplied by $N_p \sigma_z / I_b^2$. According to equation (7.16) this quantity should depend only on the storage ring properties and on the wake characteristics, $(W, \Delta z_W)$, and, therefore should be an horizontal straight line in the plot. The curves for 10^5 and 10^6 particles approximately follow this rule, having the same baseline, and the curves for 10^7 and $(10^7, \text{BBR})$, deviate from this behavior above 2 mA , but approach the same baseline of the others for lower currents. This deviation is understood when the simulation with 5×10^7 particles is analysed, where the real microwave instability dominates the scaling. Besides, the fact that the tracking using directly the BBR also follows this pattern, is an indication that this is not an artifact of the PIC method.

The curve $(10^6, \text{Gauss})$ corresponds to the filtering of the wake with a gaussian of $\sigma = 40 \mu\text{m}$. This filtering reduces the strength of the wake at short ranges and consequently changes the baseline of this curve. The curve $(10^7, \text{Sav-Go})$ is the result of using the Savitzky–Golay filter in the simulation, hence it has the same short-range wake of the other curves, and, according to equation (7.16), should follow the same baseline of the other curves below the threshold of the instability. This is not what is happening because the filtering of the distribution changes its interaction with the high frequencies of the wake. Notice, however, that with the Savitzky–Golay filter, a simulation with 10^7 particles have the same behavior above the threshold as an ordinary simulation with 5 times more macroparticles.

While Figure 47 shows that equation (7.16) qualitatively explains the energy

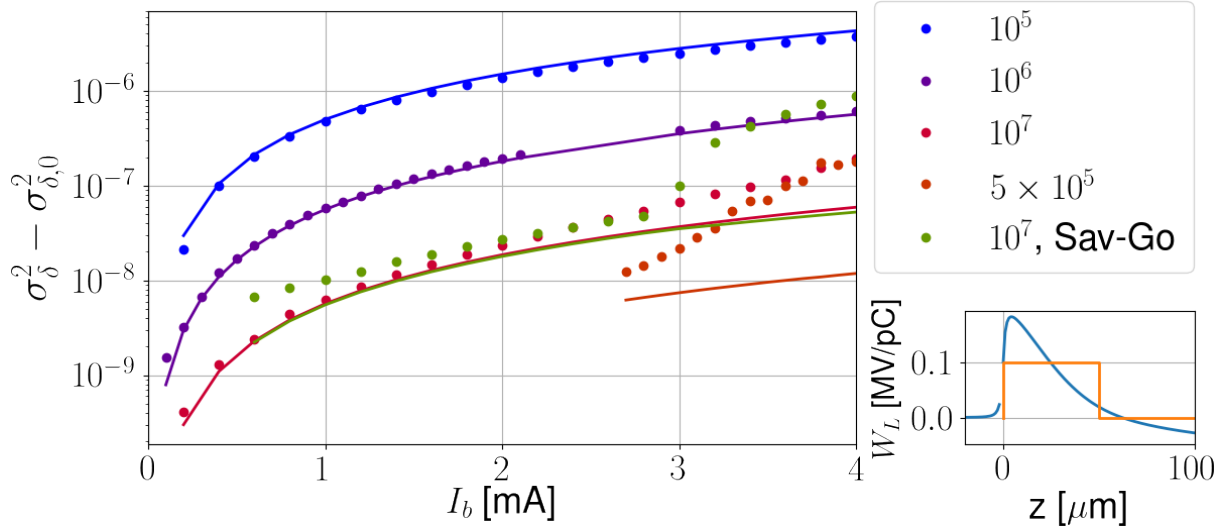


Figure 48 – Dots represents the energy spread increase in simulations with the same wake function (represented by the blue curve in the small graphic) and lines are the prediction of equation (7.16) using a constant model for the wake (orange line in the small graphic), with $W = 1 \text{ MV/C}$ and $\Delta z_W = 80 \mu\text{m}$.

spread increase induced by noise in simulations, Figure 48 shows that, even though several approximations were performed in its derivation, that equation can be used to quantitatively estimate the number of particles needed to avoid such problems. In this figure the behavior of the curve (10^7 , Sav-Go) again differs from the others, presenting a larger energy spread increase than its counterpart without filtering for low currents, but smaller noise close to the threshold. The understanding of this behavior is a subject for further studies.

7.2.3 Inclusion of CSR in the Budget

Before including the CSR in the Sirius impedance budget, we performed simulations using only this source of impedance to test if we could find the same threshold predicted by the theory. We ran the mode–coupling instability simulations using the first 30 radial numbers and azimuthal modes from -40 to 40 , but no instability was predicted up to 4 mA . Simulations with more modes were not performed because of the large computing time they would take. The tracking simulations were performed with the same discretization of the longitudinal direction the same as the one used in subsection 7.2.1, with a grid size of $2 \mu\text{m}$, and the number of macroparticles was increased to 5×10^7 , to ensure convergence. At 1.2 mA , weak modulations of the longitudinal density distribution were already observed, as shown in Figure 49. The peak value of the coherent modes is centered at a wavenumber equal to 7 mm^{-1} and rise three times above the simulation noise level. This wavenumber corresponds to a frequency of 333 GHz , which is close to the first peak of real part of the CSR impedance, at 400 GHz , shown by Figure 28.

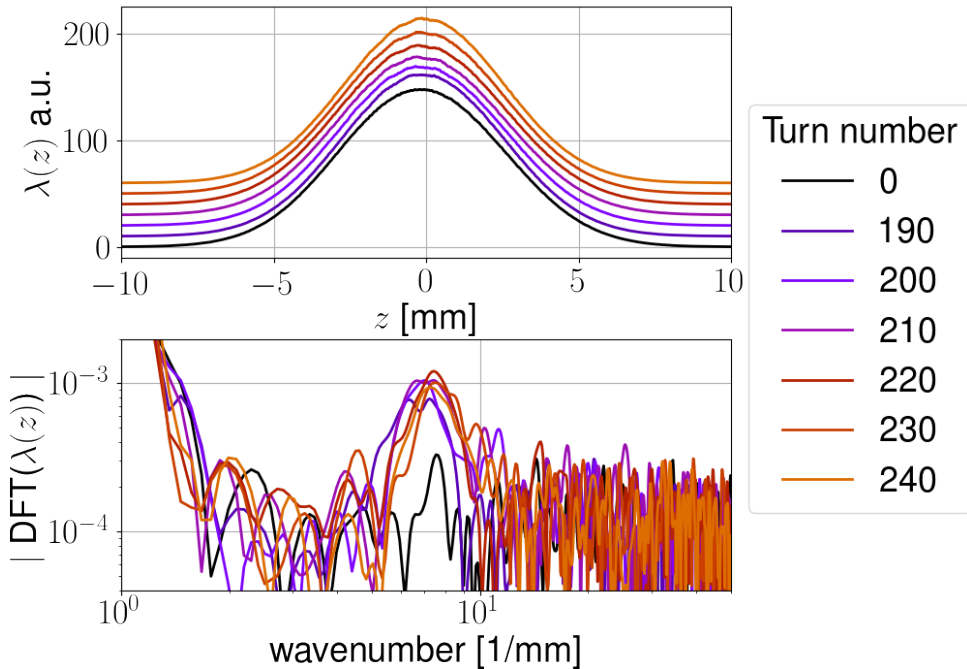


Figure 49 – Longitudinal beam distribution and its discrete Fourier transform for a CSR simulation with beam current of 1.2 mA.

Recalling section 5.6, the threshold predicted by equation (5.19) is 1.0 mA for Sirius, which is below the value found here, considering that a simulation was performed with 1.1 mA and no traces of microbunching were found. However, a closer look at Figure 26 reveals that the threshold obtained with the VFP solver, in the region close to the shielding parameter of the Sirius dipoles, is larger than the line defined by the mentioned equation. Besides, the damping rate used by Bane *et al.* (2010) in that simulation was approximately 3.5 times larger than Sirius longitudinal damping rate. If we consider the strength parameter at threshold given by the linearized Vlasov solver, also shown in that figure, instead of the one predicted by equation (5.19), the current threshold is between 1.1 mA and 1.2 mA, which agrees with the result found here.

Simulations with beam currents above the threshold have shown very good agreement with qualitative explanation of the behavior of the beam given by Venturini & Warnock (2002), where quasiperiodic bursts of CSR are followed by a relaxation of the distributions and damping. For example, Figure 50 agrees well with (VENTURINI; WARNOCK, 2002, Fig. 2), where the discontinuities in the bunch size oscillations are generated when the bursts happen.

The results shown above suggest all the parameters of the simulation are correctly tuned so as to identify the CSR instability and we proceeded with its inclusion in the storage ring impedance budget. The simulations without the effects of IBS show modulations of the beam density starting from a current of 1.4 mA. These modulations have approximately the same strength as the ones shown in Figure 49. However, when only

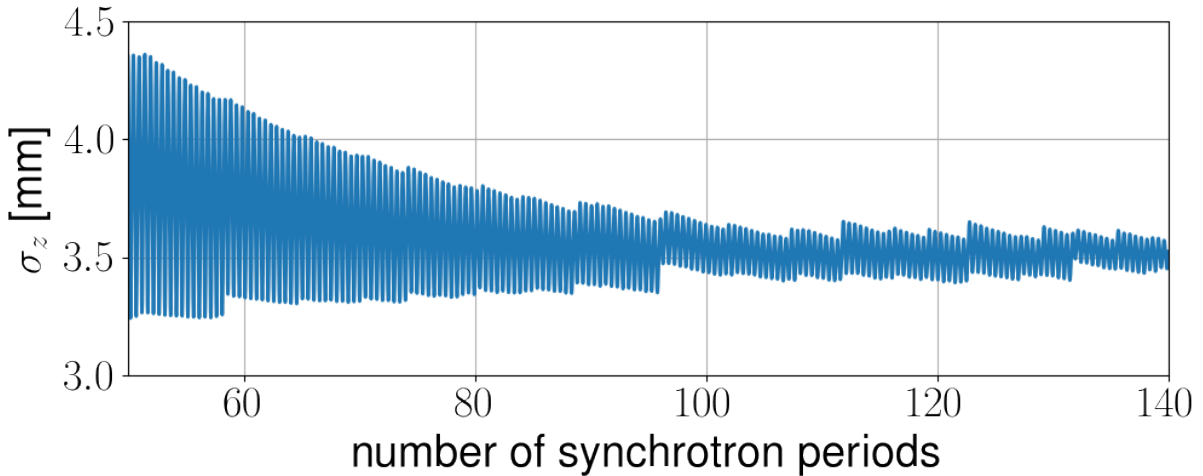


Figure 50 – Time evolution of the bunch size for a beam current of 4.0 mA under the effect of the microbunching instability driven by CSR.

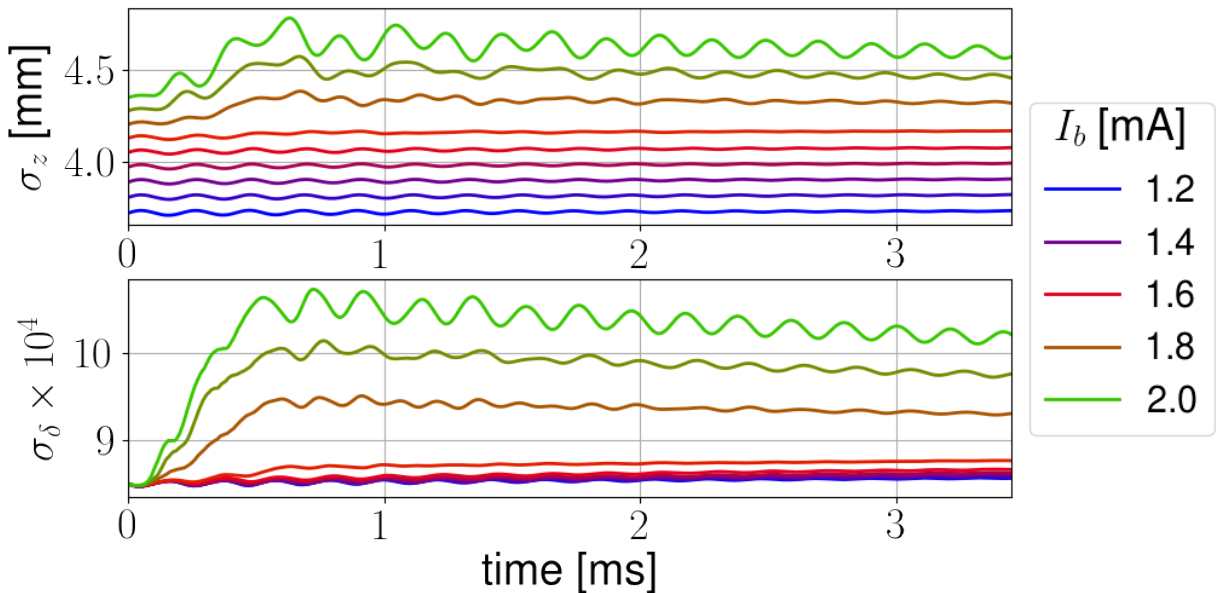


Figure 51 – Time evolution of the energy spread and bunch length for different bunch currents in the simulation with CSR and the machine impedance budget.

the CSR wake is included in the simulation, with a current only 0.1 mA above the threshold, the modulations are strong enough to distort the beam, changing significantly the time evolution of energy spread and bunch length. For the case where both the machine impedance and CSR are considered, the instability remains weak up to 1.7 mA, as shown in Figure 51. The threshold for the simulations with the effect of IBS included is between 3.4 mA and 3.6 mA, but the instability is weak and do not change the equilibrium parameters up to 4.0 mA.

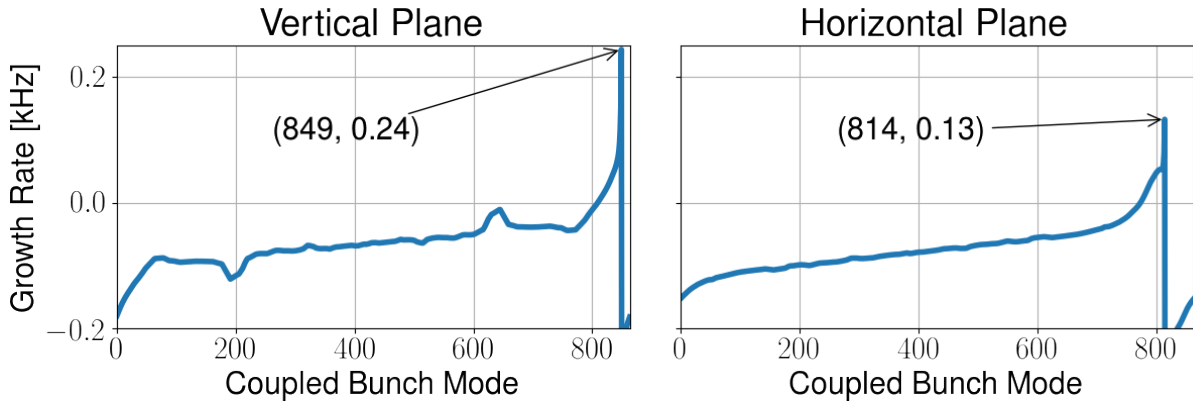


Figure 52 – Transverse coupled–bunch instabilities for the first phase of operation of the Sirius storage ring.

7.3 Transverse Plane

7.3.1 Multi–Bunch Instabilities

Differently from the longitudinal plane, in the transverse plane there will be coupled–bunch instabilities because of the long–range wake field of the resistive–wall impedance. The contribution of the IDs to this instability is two-fold: on the one hand, they increase the long–range impedance of the machine, which decreases the threshold, but on the other hand, the additional energy loss by radiation they introduce increases the damping rate in all planes, and change the equilibrium parameters of the machine, which helps stabilizing the beam. The effects of the additional radiation were calculated for the Sirius storage ring assuming all IDs were in their configuration of maximum vertical field and the main results can be found in (SIRIUS, 2013). In practice, however, the damping rates of the machine will oscillate between the bare machine values and the maximum value presented in the mentioned reference because the IDs will be constantly moving, changing the configuration of their fields. For this reason, we decided to adopt the conservative approach and not to include the effect of the IDs on the damping time to calculate the instability thresholds.

Figure 52 shows the coupled–bunch growth rates at zero chromaticities calculated with equation 4.43 for the phase one of operation of the machine, with the impedance of the IDs included, but without the additional damping they provide. Besides the resistive–wall instabilities, which are characterized by the peaks in the coupled–bunch numbers at $864 - 50 = 814$ in the horizontal plane and $864 - 15 = 849$ in the vertical plane, the effects of other impedances can be seen as well. In the horizontal plane the resistive wall contribution from the kickers is responsible for the slow decay of the growth rate as a function of the coupled–bunch mode close to the most unstable mode. This is due to the large betatron function at the injection straight section, of approximately 18 m. In the vertical plane only the resistive wall is driving the beam unstable, but there is a peak at a

Table 9 – Transverse coupled–bunch instability thresholds at zero chromaticity for the phase one of operation for different assumptions on the IDs effects.

Plane	Threshold Current [mA]		
	with IDs		
	w/o damping	with damping	
Vertical	29.5	21.4	32.0
Horizontal	54.6	37.9	56.8

coupled–bunch number approximately equal to 650, which is being caused by the DCCT impedance. This component is installed in the arc of the lattice, close to the dipole B2, where the vertical betatron function is very large, of the order of 22 m.

Table 9 shows the current thresholds at zero chromaticity for the coupled–bunch instabilities for different assumptions on the effect of the IDs to show their influence on the impedance budget and also the contribution of the additional damping on the stabilization of the beam. The additional damping increases the threshold by a factor of approximately 3/2 in both planes, and, interestingly, almost cancel the effect of the impedance of the IDs for this instability. This is only possible because the betatron functions at the location of the IDs is very low, which implies that their effects on the transverse dynamics is relatively weak, even though their gap is approximately five times smaller than the standard vacuum chamber and the resistive wall goes with $1/b^3$. Table 9 also shows that the vertical threshold is almost twice as large as the one for the horizontal plane, even for the bare machine impedance, which is a consequence of the larger average vertical betatron function of the machine and the fact that the vertical tune is larger than the horizontal.

Figure 53 shows the effect of the chromaticity on the most unstable mode of the coupled–bunch instability calculated with two different approaches. One using the approximate expression of equation 4.43 for the azimuthal modes 0 and 1, which are the diagonal terms of the mode–coupling matrix, given by equation 4.42, and another by solving the mode–coupling matrix, considering the first 7 radial modes and azimuthal modes from -7 to 7 . There is a very good agreement between the two approaches at low chromaticities, when the azimuthal mode 0 dominates the instability, but at larger values, the simplified approach overestimates the thresholds (underestimate the strength of the instability). This study shows that the beam will be stable when the ring is operated with chromaticities above 2.3 and 1.6 in the vertical and horizontal planes, respectively. Such dependency was foresaw a few years ago, which allowed the optimization of the non–linear optics of the storage ring to operate at chromaticity equal to 2.5 in both planes, which we expect will avoid the usual problems of lifetime and dynamic aperture reduction related to this type of operation.

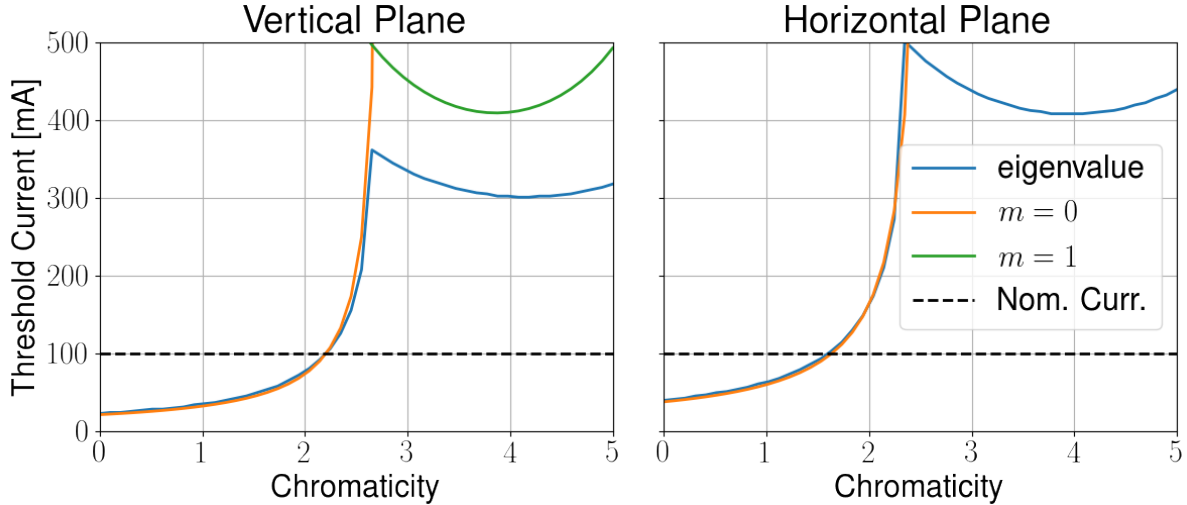


Figure 53 – Effect of chromaticity on the most unstable mode of the transverse coupled–bunch instabilities for the first phase of operation of the Sirius storage ring.

Even though the study above shows the possibility of operating the ring in stable conditions with an increased chromaticity, the most reliable way to solve this problem, which has been demonstrated to be successful in several 3rd GLS for the last two decades, is the use of transverse bunch–by–bunch feedback systems. Sirius will have two of these systems, one for the horizontal plane and another for the vertical. The actuator used will be striplines with shunt impedance, R_K , of $70 \text{ k}\Omega \text{ m}^{-1}$ and the amplifier will have maximum power of 75 W, of which only approximately 30 W will be applicable to the beam, due to cable losses (DUARTE, 2018). According to Lonza (2007), the relation between the power, P , and the damping time provided by the kicker, τ_K , is given by

$$\alpha_K = \frac{1}{\tau_K} = \sqrt{\frac{R_K P}{2}} \sqrt{\beta_K \beta_B} \frac{1}{(E_0/e) T_0} \frac{1}{x_{\max}}, \quad (7.17)$$

where β_K and β_B are the betatron functions at the position of the actuator and the pickup, respectively, and x_{\max} is the maximum amplitude of the movement. The requirement for stability of the beam allows oscillations no larger than 10 % of the beam size, which corresponds to $1.7 \mu\text{m}$ at the pickup position for the vertical plane and $5.5 \mu\text{m}$ in the horizontal plane. These requirements for beam stability are very demanding, so we will assume, as a worst case scenario, that the instability will be controlled at an oscillation ten times larger than the requirement for the vertical plane. Using this value in the equation above, the maximum damping rate the system will be capable of controlling is 170 kHz and 190 kHz in the horizontal and vertical plane, respectively, which are much larger than the thresholds calculated so far. This estimative is, off course, very idealized, because at such large growth rates the total latency of the system, not included in this simplified analysis, becomes a serious issue, reducing the effectiveness of the bunch–by–bunch feedback system. Considering another scenario, where the beam is initially unstable and we want to control this instability with the feedback system, even with an oscillation

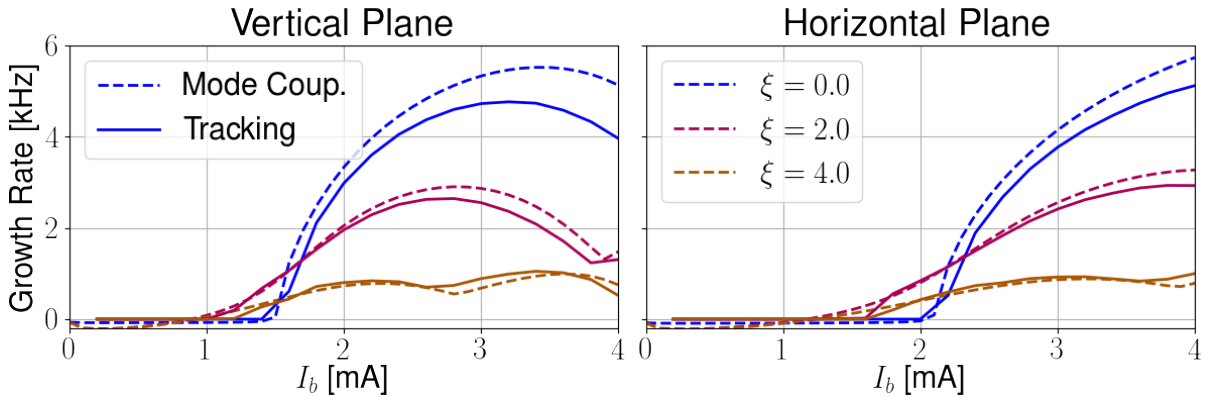


Figure 54 – Transverse single–bunch instabilities for the first phase of operation of the Sirius storage ring, considering the unperturbed longitudinal distribution, without the effects of IBS and potential well distortion.

as large as 5 mm, the maximum damping rate will still be of the order of 0.5 kHz.

The behavior of the beam in the second phase of operation of the storage in the multi–bunch configuration cannot be explained with the frequency domain theory used in this work because of the flattened distribution of the beam, created by the action of the passive Landau cavity, and further investigations are needed. However, based on the work of Cullinan *et al.* (2016) it is expected that the chromaticity will have an even larger effect on the beam, being more efficient to stabilize it.

7.3.2 Single–Bunch Instabilities

Figure 54 shows the growth rate of the single–bunch instability for different values of chromaticity. The solid lines represent the results obtained from tracking and the dashed lines are from the solution of the equation (4.42), considering the first 10 radial modes and azimuthal modes from -10 to 10 , totalizing 231 modes. The tracking simulation was performed with 10^5 macro particles in the bunch for 10^4 turns, using directly the effective wake functions obtained from numerical simulations with ECHO and GdfdL and the wake functions calculated with ImpedanceWake2D (MOUNET; MÉTRAL, 2010b) for the resistive–wall impedance. While the growth rate is a direct result of the frequency domain calculation, being given by the largest imaginary part of all the eigenvalues, for the tracking simulations linear fit of the natural logarithm of the beam size as a function of time was needed and take the angular coefficient in order to extract these values. The good agreement between frequency and time domain simulations shown in the Figure 54 was already expected, considering that the conditions used in tracking perfectly match the assumptions implicit in the mode–coupling theory.

We do not believe that the discrepancies on the prediction of the damping rates are due to the truncation of the mode–coupling matrix, because we have performed con-

vergence tests on the number of modes included in that analysis. They might be due to the fact that the impedance budget only have the kickers' impedance, but not the wake functions yet, which makes the total impedance and wakes of the budget not completely equivalent to each other. Another possibility comes from the fact that in the time-domain simulations the effective wake functions were used, and not the point-charge wakes. This could soften the strength of the short-range wakes, due to the convolution with the gaussian beam used for their calculation in the numerical solvers of the ME. An investigation of better ways to extract and use the information of the effective wake functions in tracking simulations is desirable in future works, maybe by fitting the wakes or the impedances with well-known functions, like resonators, inductors and resistors, for which analytic expressions for the wakes exists, as was done by Nagaoka (2006) for the Soleil impedance budget.

Figure 54 also shows that the chromaticities have a strong effect on the single-bunch instabilities, where positive values reduce growth rates in both planes at the cost of lowering the current threshold too. It is expected that this reduced growth rate will improve the effectiveness of the control of this instability with the bunch-by-bunch feedback system, as shown experimentally at ALS (BYRD; BARRY, 1997) and at Diamond (KOUKOVINI-PLATIA *et al.*, 2017).

It is known from the theory, as explained by Lindberg (2016) for example, that the longitudinal impedance has a two-fold effect on the transverse single-bunch stability because of the potential well distortion: the reduction of the average synchrotron tune tends to decrease the threshold and the creation of synchrotron tune spread induces Landau damping, pushing it to higher currents. The net effect of these two mechanisms at zero chromaticity depends on the particularities of the impedance budget and need detailed analysis. The simulation of this effect on Sirius was done in a simplified manner, where the distorted potential well which generates the equilibrium distribution given by the Haissinski equation is used in the longitudinal plane to simulate the effect of the longitudinal impedance without the need of applying the wake kicks. This was done because below the threshold of the microwave instability all the effects of the longitudinal impedance are described by the distorted potential at equilibrium. This approach speeds up tracking simulations, since, besides the time saved computing the longitudinal wake kicks, it is possible to simulate much less particles without the energy spread increase coming from the coupling of the high frequency components of the wake with the noise in the particle's distribution, which can spoil the whole simulation. This method could be extended to currents higher than the threshold of the microwave instability by also adjusting the energy spread of the ring to the equilibrium energy spread defined by this instability. However, this was not done in the case of Sirius, because, as seen in section 7.2, in the cases where the microwave instability happens it induces deformations in the bunch distribution so strong that it is not likely that a transverse instability could rise. This is

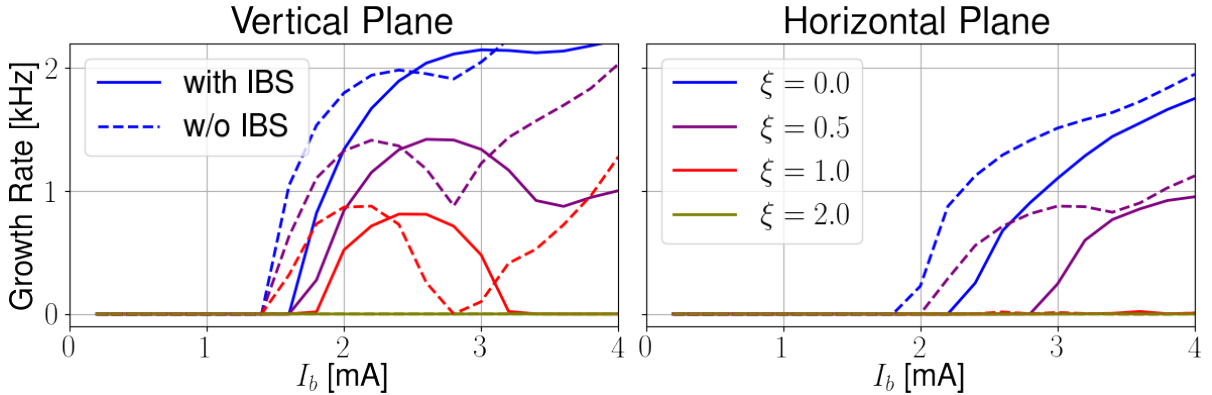


Figure 55 – Transverse single-bunch instabilities for the first phase of operation of the Sirius storage ring, considering effects of IBS and potential well distortion.

an hypothesis that could be easily tested in the future using the same tools developed in this work.

Considering the assumptions above, Figure 55 shows the effect of the longitudinal impedance on the transverse stability of the beam for two different configurations, with and without considering the effects of the IBS, and for different values of chromaticities. In the vertical plane, the potential well distortion alone does not increase the current threshold but helps lowering the growth rates of the instability and increase its sensitivity to chromaticity. In contrast, the additional energy spread introduced by the IBS increases the threshold but does not influence strongly the growth rates. It is interesting to notice the peculiar behavior of the simulation with IBS and potential well distortion at chromaticity equals to 1, where the beam is unstable from 1.8 mA to 3.2 mA and then becomes stable again up to currents higher than 4 mA. This can be understood if one notices that in all the situations presented in both Figure 54 and Figure 55 the instability in the vertical plane is dictated by two independent mode-coupling events, the first being the one responsible for the current threshold at approximately 1.45 mA and the other taking place at higher currents. The qualitative behavior of the first coupling is the same in both figures, first it grows in strength up to a maximum value, which depends on the condition simulated, followed by a decline and a probable decoupling at higher currents. On the other hand, the behavior of the second coupling is very different among the simulations, being completely suppressed for chromaticities larger than 1 with potential well distortion and IBS. The qualitative behavior of the instability in the horizontal plane is similar to the vertical, with the potential well distortion alone not increasing the threshold, but helping to control the strength of the growth rates, and the IBS contributing to the increase of the stable region. Finally, Figure 55 shows that both planes are stable when the ring is operated at a chromaticity equal to 2.0.

CONCLUSIONS

In this work we modeled the impedance of some of the main components of the Sirius storage ring with simplified models and gathered the results for other components whose calculations were done in detail using 3D solvers of Maxwell equations, to form the initial impedance budget of the machine. This data was used to calculate the current thresholds for single and multi-bunch instabilities for Sirius phase 1 of operation, which consists in 100 mA total current (or 120 μ A per bunch in uniform filling), 2 SC RF cavities and no 3HC for bunch lengthening. In Phase 2, although the current is larger, there will be 3HC, which is expected to lengthen the bunch by a factor of 3 to 4.

One of the most important components of the impedance budget is the standard chamber of the storage ring, which has a small transverse cross-section, only 12 mm in radius, and will be NEG-coated along all its extension. In this work we used semi-analytic formulas from literature to compute the impedance of this component, which allowed us to evaluate the effect of NEG under various possible scenarios related to its thickness and electrical conductivity. It was verified that imprecision in the conductivity close to the nominal value of 1 MS m^{-1} , do not have a large impact on the current threshold of the TMCI. On the other hand, small thickness increase above the nominal value of 1 μm , strongly contributes to lowering the threshold of the TMCI. Besides, under nominal conditions of electrical conductivity and coating thickness, the standard chamber resistive wall is the main contributor to the transverse impedance of the machine and is responsible for $\frac{1}{3}$ of the total longitudinal effective impedance, having a large impact on bunch-lengthening. Despite of these effects, the operation of the ring will not be compromised, given that all the thresholds for single-bunch instabilities are much above the nominal current of the ring in uniform filling.

A study of the geometric transition impedance of the BC magnet revealed that the initial proposal for the vacuum chamber, which consisted in a transition from the standard round chamber to an elliptical one, had an impedance 2.5 times larger than a round conical cross section. Based on this study, the design of this component was changed to an intermediate geometry which meets the requirement for radiation power dissipation and have approximately the same impedance of the conical transition.

The insertion devices predicted for phase one of operation of the storage ring will be out-of-vacuum magnets, which allowed us to create a simple model for its geometric transition impedance, consisting on simple tapers in both ends of the device with a very large transition factor. The resistive wall impedance of such components was calculated using the same methods as the standard chamber and, even though the gap of these

devices is very small, of the order of 5 mm to 7 mm full gap, their contribution to the transverse impedance is relatively low, because of the small values of the horizontal and vertical betatron functions at the insertion devices positions.

Regarding the coupled–bunch instabilities, a PETRA 7–Cell RF cavity will be used in the commissioning phase. Even though it is difficult to predict correctly the quantity and peak frequency of the RF cavities higher order modes, in this work we carried out a study of the coupled–bunch instabilities induced by them on Sirius, based on an impedance model found in literature. The studies have shown that, provided the transverse and longitudinal bunch–by–bunch feedback systems are installed and working, these cavities will not compromise the commissioning. Otherwise, a vertical instability will arise at approximately 25 mA in uniform filling. For phase one of operation, the PETRA 7–Cell cavity will be replaced by a superconducting one and the longitudinal kicker will be removed to optimize the impedance of the machine. In this situation, no longitudinal coupled–bunch instabilities are predicted.

The current threshold for the resistive–wall instability are approximately 20 mA in the vertical plane and 35 mA in the horizontal plane, which will require the action of the transverse bunch–by–bunch feedback system to reach the nominal current of 100 mA. However, studies have shown that with chromaticities close to 2.2 and 1.8 in the vertical and horizontal planes, respectively, the beam will be stable up to the nominal current in uniform filling without the action of feedback systems. The prediction of this behavior, a few years ago, enabled us to optimize the operation of the machine with chromaticity of 2.5 in both transverse planes, which will mitigate common problems related to this type of operation, such as dynamic aperture and lifetime reduction.

The calculation of the single–bunch instabilities were performed with frequency domain codes, based on the mode–coupling theory and also with a tracking code developed in-house. It was verified, with good agreement between both methods, that the threshold for microwave instability is at approximately 3.0 mA per bunch, if the effects of energy–spread increase induced by IBS were not taken into account. When this effect is included, the threshold is above 4.0 mA. However, further studies considering the bunch–lengthening induced by the impedance on the calculation of the IBS effects is necessary in order to improve the accuracy of the predictions. The coherent synchrotron radiation impedance was included in the impedance budget of the storage ring and tracking simulations were performed to access the current thresholds. Simulations with only the CSR impedance revealed a threshold of 1.2 mA, which is in good agreement with the predicted value from theory. When the machine impedance is added in the simulations, the threshold increases to 1.4 mA but the instability is weak and does not change significantly the beam parameters up to 1.7 mA. Finally, when IBS effects are included, the threshold is approximately at 3.4 mA and remains weak up to 4.0 mA. Further studies are needed in

order to confirm these results under different simulation parameters and also with a more accurate estimative of the IBS-induced increase of energy spread.

Without considering the potential well distortion caused by the longitudinal impedance transverse single-bunch tracking results have shown an excellent agreement with the frequency domain codes, where the current threshold for the TMCI in the vertical plane was verified to be 1.5 mA and 2.0 mA for the horizontal plane. It is possible to lower the growth rates of the instability above the threshold by increasing the chromaticity at the cost of a small reduction of the current threshold. The potential well distortion was included in the transverse simulations by setting the potential well of the simulated RF cavity with the equilibrium potential well obtained from the Haissinski equation solver, which allowed us to perform tracking with a very reduced number of particles compared to the standard approach of simulating the longitudinal and transverse wake kicks concomitantly. The results have shown that the current thresholds remain approximately unchanged but the sensitivity of the instability with chromaticity increases significantly, in such a way that a chromaticity equal to 2.0 in both planes is enough to increase the threshold up to currents higher than 4.0 mA. When IBS effects are included, the threshold slightly increases, but the sensibility of the growth rates with chromaticity does not change.

Further studies are needed to characterize the behavior of the beam in the second phase of operation, when a Landau cavity will be installed in the ring to lengthen the bunches. For the single-bunch studies the same tracking code and the Haissinski equation solver developed in this work can be used directly, without any addition of new functionalities, but new methods must be investigated for the multi-bunch studies.

BIBLIOGRAPHY

- AGOHI, T.; YOKOYA, K. Calculation of coherent synchrotron radiation using mesh. *Physical Review Special Topics - Accelerators and Beams*, v. 7, n. 5, p. 61–69, 2004. ISSN 10984402. 124
- AL-DMOUR, E. *et al.* Diffraction-limited storage-ring vacuum technology. *Journal of Synchrotron Radiation*, International Union of Crystallography, v. 21, n. 5, p. 878–883, 2014. ISSN 1600-5775. Disponível em: <<http://scripts.iucr.org/cgi-bin/paper?S1600577514010480>>. 34
- AL-KHATEEB, A. M. *et al.* Longitudinal impedance and shielding effectiveness of a resistive beam pipe for arbitrary energy and frequency. *Physical Review E*, v. 71, p. 026501, 2005. ISSN 0094243X. 80
- BANE, K.; STUPAKOV, G.; ZAGORODNOV, I. Impedance calculations of nonaxisymmetric transitions using the optical approximation. *Physical Review Special Topics - Accelerators and Beams*, v. 10, n. 7, p. 074401, 2007. ISSN 1098-4402. Disponível em: <<http://link.aps.org/doi/10.1103/PhysRevSTAB.10.074401>>. 75
- BANE, K. L. F. *The short range resistive wall wakefields*. Stanford, 1991. 26 p. 78
- BANE, K. L. F.; CAI, Y.; STUPAKOV, G. Threshold Studies of the Microwave Instability in Electron Storage Rings. *Physical Review Special Topics - Accelerators and Beams*, v. 13, n. 10, p. 104402, 2010. ISSN 10984402. 12, 119, 120, 121, 150
- BANE, K. L. F.; NG, C. K.; CHAO, A. W. Estimate of the impedance due to wall surface roughness. *Proceedings of PAC 1997*, p. 1738–1740, 1997. Disponível em: <http://ieeexplore.ieee.org/xpls/abs_all.jsp?arnumber=750991>. 100
- BANE, K. L. F.; RUTH, R. D. Bunch Lengthening Calculations for the SLC Dampling Rings. In: *Proceedings of PAC 1989*. [S.l.: s.n.], 1989. p. 789–791. 90
- BASSI, G. *et al.* Analysis of coupled-bunch instabilities for the NSLS-II storage ring with a 500 MHz 7-cell PETRA-III cavity. *Nuclear Instruments and Methods in Physics Research, Section A: Accelerators, Spectrometers, Detectors and Associated Equipment*, Elsevier B.V., v. 810, p. 151–163, 2016. ISSN 01689002. 133, 136
- BASSI, G.; BLEDNYKH, A.; SMALUK, V. Self-consistent simulations and analysis of the coupled-bunch instability for arbitrary multibunch configurations. *Physical Review Accelerators and Beams*, v. 19, n. 2, p. 024401, 2016. ISSN 24699888. 97, 146
- BENGTSSON, J. *Sextupole Scheme for the Swiss Light Source (SLS): An Analytic Approach*. Villigen, 1997. 44, 49
- BENVENUTI, C. A New Pumping Approach for the Large Electron Positron Collider (LEP). *Nuclear Instruments and Methods*, v. 205, p. 391–401, 1983. 34
- BENVENUTI, C. *et al.* Decreasing surface outgassing by thin film getter coatings. *Vacuum*, v. 50, n. 1-2, p. 57–63, 1998. ISSN 0042207X. Disponível em: <<http://www.scopus.com/inward/record.url?eid=2-s2.0-0032058258&partnerID=tZOTx3y1>>. 99

- BERG, J. S. *Coherent modes for multiple non-rigid bunches in a storage ring*. Tese (Doutorado) — Stanford University, 1996. 48, 88
- BERNARDINI, C. *et al.* Lifetime and Beam Size in a Storage Ring. *Physical Review Letters*, v. 10, n. 9, p. 407–409, 1963. 35
- BIRDSALL, C. K.; BREWER, G. R.; HAEFF, A. V. The Resistive-Wall Amplifier. *Proceedings of the IRE*, v. 41, n. 7, p. 865–875, 1953. ISSN 0096-8390. Disponível em: <<http://ieeexplore.ieee.org/lpdocs/epic03/wrapper.htm?arnumber=4051404>>. 78
- BJORKEN, J. D.; MTINGWA, S. Intrabeam Scattering. *Particle Accelerators*, v. 13, p. 115–143, 1983. ISSN 0094243X. 35
- BLEDNYKH, A. Trapped modes in tapered vacuum chambers for a mini-gap undulator magnet. *Nuclear Instruments and Methods in Physics Research, Section A: Accelerators, Spectrometers, Detectors and Associated Equipment*, v. 565, n. 2, p. 380–393, 2006. ISSN 01689002. 77, 114
- BLEDNYKH, A. *et al.* Low-frequency quadrupole impedance of undulators and wigglers. *Physical Review Accelerators and Beams*, v. 19, n. 10, p. 104401, 2016. ISSN 24699888. 61, 114
- BLEDNYKH, A.; FERREIRA, M. J.; KRINSKY, S. Impedance Calculations for the Nsls-II Storage Ring. In: *Proceedings of PAC09*. Vancouver: [s.n.], 2009. D04, p. 4595–4597. 35
- BLEDNYKH, A.; KRINSKY, S. Preliminary impedance budget for NSLS-II storage ring. In: *Proceedings of PAC07*. Albuquerque: [s.n.], 2007. v. 05-D04, p. 4321–4323. ISBN 1424409179. 35, 129
- BORLAND, M. Elegant: A Flexible SDDS-Compliant Code for Accelerator Simulation. In: *Proceedings of ICAP 2000*. Darmstadt: [s.n.], 2000. Disponível em: <http://www.osti.gov/bridge/product.biblio.jsp?osti_id=761286>. 97, 146
- BORLAND, M. Simple method for particle tracking with coherent synchrotron radiation. *Physical Review Special Topics - Accelerators and Beams*, v. 4, n. 7, p. 070701, 2001. ISSN 10984402. 146
- BORLAND, M. *et al.* Lattice design challenges for fourth-generation storage-ring light sources. *Journal of Synchrotron Radiation*, International Union of Crystallography, v. 21, n. 5, p. 912–936, 2014. ISSN 16005775. 34, 41
- BROSI, M. *et al.* Systematic Studies of Short Bunch-Length Bursting At Anka. In: *Proceedings of IPAC 2016*. Busan: [s.n.], 2016. p. 1662–1665. ISBN 9783954501472. 121
- BRUNS, W. GdfidL: a finite difference program with reduced memory and CPU usage. *Proceedings of PAC 1997*, p. 2651–2653, 1997. 84, 125
- BRUNS, W. *GdfidL Web Page*. 2017. Disponível em: <<http://www.gdfidl.de/>>. 84, 116
- BUROV, A.; LEBEDEV, V. TRANSVERSE RESISTIVE WALL IMPEDANCE FOR MULTI-LAYER FLAT CHAMBERS. In: *Proceedings of EPAC2002*. Paris: [s.n.], 2002. v. 12, n. 7, p. 1455–1457. 80

- BUROV, A.; LEBEDEV, V. Transverse Resistive Wall Impedance for Multi-Layer Round Chambers. In: *Proceedings of EPAC2002*. Paris: [s.n.], 2002. v. 1, p. 1452–1454. 80
- BYRD, J. M.; BARRY, W. *Controlling the Vertical Mode Coupling Instability with Feedback in the ALS*. Berkeley, 1997. 156
- BYRD, J. M. *et al.* Observation of Broadband Self-Amplified Spontaneous Coherent Terahertz Synchrotron Radiation in a Storage Ring. *Physical Review Letters*, v. 89, n. 22, p. 224801, nov 2002. ISSN 0031-9007. Disponível em: <<http://link.aps.org/doi/10.1103/PhysRevLett.89.224801>>. 36
- CAI, Y. A Linear Theory of Microwave Instability in Electron Storage Rings. *Physical Review Special Topics - Accelerators and Beams*, v. 14, n. 6, p. 061002, 2011. 120
- CARR, R. Adjustable phase insertion devices as X-ray sources. *Nuclear Inst. and Methods in Physics Research A*, v. 306, n. 1-2, p. 391–396, 1991. ISSN 01689002. 112
- Ceramic Magnets. *CMD5005 Datasheet*. 2017. Disponível em: <<http://www.cmi-ferrite.com/Materials/Datasheets/NiZn/CMD5005.pdf>>. 109
- CHAO, A. W. *Physics of Collective Beam Instabilities in High Energy Accelerators*. 1st. ed. New York: John Wiley & Sons, 1993. 371 p. (Wiley Series in Beam Physics and Accelerators Technology). ISBN 0471551848. 67, 68, 73, 78, 92
- CHAO, A. W.; HEIFETS, S.; ZOTTER, B. Tune shifts of bunch trains due to resistive vacuum chambers without circular symmetry. *Physical Review Special Topics - Accelerators and Beams*, v. 5, n. 11, p. 111001, 2002. 79, 104
- CHIN, Y. Longitudinal Stability Limit for Electron Bunches in a Double RF System. *Nuclear Instruments and Methods*, v. 215, p. 501–509, 1983. 93
- CHIN, Y.; SATOH, K.; YOKOYA, K. Instability of a Bunched Beam With Synchrotron-Frequency Spread. *Part. Accel.*, v. 13, p. 45–66, 1983. ISSN 00312460. 93
- CHIN, Y. H. *User's Guide for ABCI Version 8.7 (Azimuthal Beam Cavity Interaction)*. Geneva, 1994. 1—74 p. Disponível em: <<http://cds.cern.ch/record/259547/files/CM-P00061200.pdf?version=1>>. 82
- COURANT, E.; SNYDER, H. Theory of the alternating-gradient synchrotron. *Annals of Physics*, v. 3, n. 1, p. 1–48, 1958. ISSN 00034916. 45, 53
- COURANT, E. D.; SESSLER, A. M. Transverse coherent resistive instabilities of azimuthally bunched beams in particle accelerators. *Review of Scientific Instruments*, v. 37, n. 11, p. 1579–1588, 1966. ISSN 00346748. 78
- CST. *CST-Particle Studio*. 2017. Disponível em: <<https://www.cst.com/products/cstps>>. 84
- CULLINAN, F. J. *et al.* Transverse coupled-bunch instability thresholds in the presence of a harmonic-cavity-flattened rf potential. *Physical Review Accelerators and Beams*, v. 19, n. 12, p. 1–15, 2016. ISSN 24699888. 155

- DANILOV, V. V. Extended definitions of wake fields and their influence on beam dynamics. *Physical Review Special Topics - Accelerators and Beams*, v. 3, n. 1, p. 1–5, 2000. ISSN 1098-4402. Disponível em: <<http://link.aps.org/doi/10.1103/PhysRevSTAB.3.014201>>. 62
- DANILOV, V. V. *et al.* Experimental Study of Collective Effects in BEP Storage Ring with High Stored Current. In: *Proceedings of PAC 1993*. [S.l.: s.n.], 1993. p. 3711–3713. 62
- DAVINO, D.; HAHN, H. Improved Analytical Model of the Transverse Coupling Impedance of Ferrite Kicker Magnets. *Physical Review Special Topics - Accelerators and Beams*, v. 6, n. 1, p. 012001, 2003. 71, 107
- DENES, P.; SCHMITT, B. Pixel detectors for diffraction-limited storage rings. *Journal of Synchrotron Radiation*, International Union of Crystallography, v. 21, n. 5, p. 1006–1010, 2014. ISSN 16005775. 34
- DERBENEV, Y. S. *et al.* *Microbunch Radiative Tail-Head Interaction*. Hamburg, 1995. 36, 65, 118
- DESTER, P. S.; SÁ, F. H. de; LIU, L. Energy Acceptance and on Momentum Aperture Optimization for the Sirius Project. In: *Proceedings of IPAC2017*. Copenhagen: [s.n.], 2017. v. 05-D02, p. 3041–3044. ISBN 9783954501823. 39
- DUARTE, H. O. C. *private communication*. 2018. 136, 154
- DUARTE, H. O. C.; LIU, L.; MARQUES, S. R. Evaluation and Attenuation of Sirius Components Impedance. In: *Proceedings of IPAC2017*. Copenhagen: [s.n.], 2017. p. 3048–3051. ISBN 9783954501823. 125, 127, 128, 130
- DUARTE, H. O. C. *et al.* Analysis and Countermeasures of Wakefield Heat Losses for Sirius. In: *Proceedings of IPAC2017*. Copenhagen: [s.n.], 2017. v. 05-D04, p. 3052–3055. ISBN 9783954501823. 125, 129
- DUARTE, H. O. C.; SANFELICI, L.; MARQUES, S. R. Design and impedance optimization of the sirius BPM button. In: *Proceedings of IBIC2013*. Oxford: [s.n.], 2013. v. 2, n. 1, p. 365–368. ISBN 9783954501274. Disponível em: <<http://www.scopus.com/inward/record.url?eid=2-s2.0-84903902969&partnerID=tZOTx3y1>>. 125, 129
- ERIKSSON, M.; Van Der Veen, J. F.; QUITMANN, C. Diffraction-limited storage rings-A window to the science of tomorrow. *Journal of Synchrotron Radiation*, International Union of Crystallography, v. 21, n. 5, p. 837–842, 2014. ISSN 16005775. 33, 34
- FALTENS, A.; LASLETT, L. J. Longitudinal Coupling Impedance of a Stationary Electron Ring in a Cylindrical Geometry. *Particle Accelerators*, v. 4, p. 1–24, 1973. Disponível em: <<http://papers2://publication/uuid/9400908E-3087-41D5-9EE9-CA66BB81BF1B>>. 119
- FARVACQUE, L. *et al.* a Low-Emittance Lattice for the E.S.R.F. In: *Proceedings of IPAC 2013*. Shanghai: [s.n.], 2013. p. 79–81. ISBN 9783954501229. 28
- FRENET, F. Sur les courbes à double courbure. *Journal de Mathématiques Pures et Appliquées*, v. 17, p. 437–447, 1852. ISSN 0021-7874. Disponível em: <<http://eudml.org/doc/233946>>. 41

- GLUCKSTERN, R. L. *Analytic methods for calculating coupling impedances*. Geneva, 2000. 73
- GLUCKSTERN, R. L.; ZEIJTS, J. V.; ZOTTER, B. Coupling Impedance of beam pipes of general cross section. *Phys. Rev. E*, v. 47, n. 1, p. 656–663, 1993. Disponível em: <<http://dx.doi.org/10.1103/PhysRevE.47.656>>. 78, 103
- GÜNZEL, T. F. Transverse coupling impedance of the storage ring at the European Synchrotron Radiation Facility. *Physical Review Special Topics - Accelerators and Beams*, v. 9, n. 11, p. 114402, 2006. 74
- GÜNZEL, T. F.; PEREZ, F. Impedance and Instabilities for the ALBA Storage Ring. In: *Proceedings of EPAC08*. Genoa: [s.n.], 2008. v. 05-D04, p. 1622–1624. 35, 74
- HAHN, H. *Matrix solution to longitudinal impedance of multi-layer circular structures*. Upton, 2008. 12 p. 80
- HAHN, H.; DAVINO, D. RHIC Abort Kicker with Reduced Coupling Impedance. In: *Proceedings of EPAC 2002*. Paris: [s.n.], 2002. p. 1502–1504. 109
- HAÏSSINSKI, J. Exact Longitudinal Equilibrium Distribution of Stored Electrons in the Presence of Self-fields. *Il Nuovo Cimento*, v. 18, n. 1, p. 72–82, 1973. ISSN 03693554. 90, 139
- HALBACH, K. Applications of Permanent Magnets in Accelerators and Electron Storage Rings. *Journal of Applied Physics*, v. 57, n. 1, p. 3605, 1985. 112
- HEIFETS, S. *Tune Shift due to Asymmetry of the Resistive Beam Pipe*. Stanford, 1998. 7 p. 103
- HEIFETS, S. A. *On the Direction Symmetry of the Impedance*. Stanford, 1990. 1—5 p. 75, 77
- HEIFETS, S. A.; KHEIFETS, S. A. Coupling impedance in modern accelerators. *Reviews of Modern Physics*, v. 63, n. 3, p. 633–673, 1991. 67, 75
- HETTEL, R. O. Challenges in the Design of Diffraction-Limited Storage Rings. In: *Proceedings of IPAC2014*. Dresden: [s.n.], 2014. v. 02-A16, p. 7–11. ISBN 9783954501328. 34
- HETTEL, R. O. DLSR design and plans: An international overview. *Journal of Synchrotron Radiation*, International Union of Crystallography, v. 21, n. 5, p. 843–855, 2014. ISSN 16005775. 31
- HITCHCOCK, A. P.; TONEY, M. F. Spectromicroscopy and coherent diffraction imaging: Focus on energy materials applications. *Journal of Synchrotron Radiation*, International Union of Crystallography, v. 21, n. 5, p. 1019–1030, 2014. ISSN 16005775. 33
- HUANG, Z. Brightness and Coherence of Synchrotron Radiation and FELs. In: *Proceedings of IPAC 2013*. Shanghai: [s.n.], 2013. p. 16–20. ISBN 9783954501229. Disponível em: <<http://epaper.kek.jp/IPAC2013/papers/moycb101.pdf>>. 31, 33

- JACKSON, J. D. *Classical Electrodynamics*. 2nd. ed. New York: John Wiley & Sons, 1962. 848 p. 51, 60
- JOHANSSON, M.; ANDERBERG, B.; LINDGREN, L. J. Magnet design for a low-emittance storage ring. *Journal of Synchrotron Radiation*, International Union of Crystallography, v. 21, n. 5, p. 884–903, 2014. ISSN 16005775. 34
- JONES, R. M.; KROLL, N. M.; MILLER, R. H. Spectral Function Calculation of Angle Wakes, Wake Moments, and Misalignment Wakes for the SLAC Damped Detuned Structures (DDS). In: *Proceedings of PAC 1997*. [S.l.: s.n.], 1998. p. 551–553. ISBN 078034376X. 62
- KARANTZOULIS, E.; SMALUK, V.; TOSI, L. Broad band impedance measurements on the electron storage ring ELETTRA. *Physical Review Special Topics - Accelerators and Beams*, v. 6, n. 3, p. 36–43, 2003. ISSN 10984402. 100
- KLEIN, M. *et al.* Study of Collective Beam Instabilities for the MAX IV 3GeV Ring. In: *Proceedings of IPAC 2013*. Shanghai: [s.n.], 2013. v. 05-D05, p. 1730–1732. ISBN 9783954501229. 35, 129
- KOUKOVINI-PLATIA, E. *et al.* Study of Single Bunch Instabilities With Transverse Feedback At Diamond. In: *Proceedings of IPAC 2017*. Copenhagen: [s.n.], 2017. v. 05-D06, p. 4489–4492. ISBN 9783954501823. 156
- KOUKOVINI-PLATIA, E.; RUMOLO, G.; ZANNINI, C. High Frequency electromagnetic Characterization of NEG Properties for the CLIC Damping Rings. In: *Proceedings of IPAC2014*. Dresden: [s.n.], 2014. v. 07-T14, p. 3097–3099. ISBN 9783954501687. 100
- KRONIG, R. d. L. On the Theory of Dispersion of X-Rays. *J. Opt. Soc. Am.*, v. 12, n. 6, p. 547—557, 1926. Disponível em: <<http://www.osapublishing.org/abstract.cfm?URI=josa-12-6-547>>. 68
- KUBO, K.; OIDE, K.; INTRODUCTION, I. Intrabeam Scattering in Electron Storage Rings. *Physical Review Special Topics - Accelerators and Beams*, v. 4, n. September, p. 124401, 2001. ISSN 1098-4402. 35
- LANDAU, L. D.; LIFSHITZ, E. *Physical Kinetics (Course of Theoretical Physics, Vol 10)*. [S.l.]: Pergamon Press Ltd., 1981. 452 p. ISBN 0080264808. 55
- LANDAU, L. D.; LIFSHITZ, E. M. *Electrodynamics of Continuous Media (Course of Theoretical Physics, Vol 8)*. Pergamon Press Ltd., 1960. 429 p. ISSN 0002-9505. ISBN 0750626348. Disponível em: <<http://aapt.scitation.org/doi/10.1119/1.1937882>>. 88
- LASLETT, L. J. *On Intensity Limitations Imposed by Transverse Space-Charge Effects in Circular Particle Accelerators*. Upton, 1963. 324–367 p. Disponível em: <<http://lss.fnal.gov/conf/C630610/p324.pdf>>. 36, 99, 105, 111, 114, 132
- LASLETT, L. J.; NEIL, V. K.; SESSLER, A. M. Transverse Resistive Instabilities of Intense Coasting Beams in Particle Accelerators. *Review of Scientific Instruments*, v. 36, n. 4, p. 436–448, 1965. 78

- LEE, S. Y. *Accelerator Physics*. 1st. ed. Singapore: World Scientific Publishing Co. Pte. Ltd., 1999. 491 p. ISBN 981023709X. 41, 42, 43, 44, 55, 56
- LEEMANN, S. C. *et al.* Beam dynamics and expected performance of Sweden's new storage-ring light source: MAX IV. *Physical Review Special Topics - Accelerators and Beams*, v. 12, n. 12, p. 120701, 2009. ISSN 1098-4402. Disponível em: <<http://link.aps.org/doi/10.1103/PhysRevSTAB.12.120701>>. 28, 37
- LINDBERG, R. R. Fokker-Planck analysis of transverse collective instabilities in electron storage rings. *Phys. Rev. Accel. Beams*, v. 19, n. 12, p. 124402, 2016. Disponível em: <<https://link.aps.org/doi/10.1103/PhysRevAccelBeams.19.124402>>. 54, 55, 56, 88, 92, 95, 156
- LINDBERG, R. R.; BLEDNYKH, A. Modeling of Impedance Effects for the APS-MBA Upgrade. In: *Proceedings of IPAC2015*. Richmond: [s.n.], 2015. v. 02-A05, p. 1825–1827. ISBN 9783954501687. 35
- LIU, L. *et al.* Status of Sirius - A New Brazilian Synchrotron Light Source. In: *Proceedings of IPAC2011*. San Sebastián: [s.n.], 2011. v. 02-A05, p. 931–933. 37
- LIU, L. *et al.* Update on Sirius, the New Brazilian Light Source. In: *Proceedings of IPAC2014*. Dresden: [s.n.], 2014. v. 02-A05, p. 191–193. ISBN 9783954501328. 37
- LIU, L. *et al.* a New 5Ba Low Emittance Lattice for Sirius. In: *Proceedings of IPAC2013*. Shanghai: [s.n.], 2013. v. 05-D01, p. 1874–1876. ISBN 9783954501229. 37
- LIU, L.; RESENDE, X. R.; RODRIGUES, A. R. D. Sirius (BR): A New Brazilian Synchrotron Light Source. In: *Proceedings of IPAC'10*. Kyoto: [s.n.], 2010. v. 02-A05, p. 2481–2483. ISBN 9789290833529. 37
- LIU, L. *et al.* Upgraded Optics for Sirius With Improved Matching of Electron and Photon Beam Emittances. In: *Proceedings of IPAC2015*. Richmond: [s.n.], 2015. v. 02-A05, p. 1407–1409. ISBN 9783954501687. 37
- LIU, L.; SÁ, F. H. de; RESENDE, X. R. A New Optics for Sirius. In: *Proceedings of IPAC2016*. Busan: [s.n.], 2016. v. 05-D01, p. 3413–3415. ISBN 9783954501472. 37, 39
- LIU, L. *et al.* Injection Dynamics for Sirius Using a Nonlinear Kicker. In: *Proceedings of IPAC2016*. Busan: [s.n.], 2016. v. 05-D02, p. 3406–3408. ISBN 9783954501472. 40, 106
- LIU, L.; WESTFAHL, H. Towards Diffraction Limited Storage Ring Based Light Sources. In: *Proceedings of IPAC2017*. Copenhagen: [s.n.], 2017. p. 1203–1208. ISBN 9783954501823. 33, 34
- LONZA, M. Multi-Bunch Feedback Systems. In: BRANDT, D. (Ed.). *CAS CERN Accelerator School: Digital Signal Processing*. Sigtuna: [s.n.], 2007. p. 285—340. 136, 154
- MOSTACCI, A.; CASPERS, F. Beam-Coupling Impedance and Wake Field — Bench Measurements. *IFCA Beam Dynamics Newsletter No. 69*, Geneva, p. 88—96, 2016. 107

- MOUNET, N. *ImpedanceWake2D*. 2011. Disponível em: <<https://twiki.cern.ch/twiki/bin/view/ABPComputing/ImpedanceWake2D>>. 80, 114
- MOUNET, N. *The LHC Transverse Coupled-Bunch Instability*. Tese (phdthesis) — École Polytechnique Fédérale de Lausanne, 2012. 80
- MOUNET, N.; MÉTRAL, E. *Electromagnetic field created by a macroparticle in an infinitel long and axisymmetric multilayer beam pipe*. Geneva, 2009. 80
- MOUNET, N.; MÉTRAL, E. *Electromagnetic fields and beam coupling impedances in a multilayer flat chamber*. Geneva, 2010. 80
- MOUNET, N.; MÉTRAL, E. Impedances of Two Dimensional Multilayer Cylindrical and Flat Chambers in the Non-ultrarelativistic Case. In: *Proceedings of HB 2010*. Morschach: [s.n.], 2010. p. 353–357. 80, 155
- MURPHY, J. B.; KRINSKY, S.; GLUCKSTERN, R. L. Longitudinal Wakefield for an Electron moving on a Circular Orbit. *Particle Accelerators*, v. 57, n. BNL-63090, p. 9–64, 1997. 118, 120
- NAGAOKA, R. Impact of Resistive-Wall Wake Fields Generated by Low-Gap Chambers on the Beam at the ESRF. In: *Proceedings of PAC 2001*. Chicago: IEEE, 2001. p. 3531–3533. ISBN 0780371917. 103
- NAGAOKA, R. Numerical Evaluation of Geometric Impedance for Soleil. In: *proceedings of EPAC 2004*. Lucerne: [s.n.], 2004. p. 2041–2043. 35, 125, 129
- NAGAOKA, R. Study of Resistive-Wall Effects on Soleil. In: *Proceedings of EPAC 2004*. Lucerne: [s.n.], 2004. p. 2038–2040. 100
- NAGAOKA, R. Instability Studies Using Evaluated Wake Fields and Comparison With Observations at Soleil. In: *Proceedings of EPAC 2006*. Edinburgh: [s.n.], 2006. v. 05-D04, p. 2847–2849. 88, 156
- NAGAOKA, R.; BANE, K. L. F. Collective effects in a diffraction-limited storage ring. *Journal of Synchrotron Radiation*, v. 21, n. 5, p. 937–960, 2014. Disponível em: <<https://doi.org/10.1107/S1600577514015215>>. 34, 35, 40, 99, 118, 120, 122
- NAGAOKA, R. *et al.* Beam Instability Observations and Analysis at Soleil. In: *Proceedings of PAC 2007*. Albuquerque: [s.n.], 2007. v. 05-D04, p. 2019–2021. ISBN 1424409179. 100
- NAPOLY, O.; Yong Ho Chin; ZOTTER, B. A generalized method for calculating wake potentials. *Nuclear Inst. and Methods in Physics Research A*, v. 334, n. 2-3, p. 255–265, 1993. ISSN 01689002. 83
- NASSIBIAN, G.; SACHERER, F. Methods for Measuring Transverse Coupling Impedances in Circular Accelerators. *Nuclear Instruments and Methods*, v. 159, n. 6, p. 21–27, 1979. 107
- NEIL, V. K.; SESSLER, A. M. Longitudinal Resistive Instabilities of Intense Coasting Beams in Particle Accelerators. *The Review of Scientific Instruments*, v. 36, n. 4, p. 429–436, 1965. 78

- NEUENSCHWANDER, R. T. *et al.* Engineering Challenges of Future Light Sources. In: *Proceedings of IPAC2015*. Richmond: [s.n.], 2015. p. 1308–1313. ISBN 9783954501687. 34
- NG, K.-Y. *Physics of Intensity Dependent Beam Instabilities*. 1st. ed. Singapore: World Scientific Publishing Co. Pte. Ltd., 2006. 776 p. ISBN 981270339X. Disponível em: <http://books.google.com/books?id=pXg1_7m3_UgC&pgis=1>. 92
- NG, K.-Y.; BANE, K. L. F. *Explicit Expressions of Impedances and Wake Functions*. Stanford, 2010. 1—10 p. 74
- NIEDERMAYER, U.; GJONAJ, E. Wake Field and Beam Coupling Impedance Simulations. *Beam Dynamics Newsletter*, v. 69, n. December, p. 78–87, 2016. 81
- PALUMBO, L.; VACCARO, V. G.; ZOBOV, M. *Wake Fields and Impedance*. Rhodes, 1994. 1–70 p. 74, 75
- PERSICHELLI, S. *et al.* Impedance and Collective Effects for the Advanced Light Source Upgrade at LBNL. In: *Proceedings of IPAC2017*. Copenhagen: [s.n.], 2017. v. 05-D04, p. 3192–3195. ISBN 9783954501823. 35
- PIERCE, J. R. Waves in Electron Streams and Circuits. *Bell System Technical Journal*, v. 30, n. 3, p. 626–651, 1951. 78
- PIWINSKI, A. Intra-Beam-Scattering. In: *9th International Conference on High-energy Accelerators*. Stanford: [s.n.], 1974. p. 405–409. 35
- PIWINSKI, A. Penetration of the Field of a Bunched Beam Through a Ceramic Vacuum Chamber With Metallic Coating. *IEEE Transactions on Nuclear Science*, NS-24, n. 3, p. 1364–1366, 1977. 79, 110
- PIWINSKI, A. *Wake Fields and Ohmic Losses in Flat Vacuum Chambers*. Hamburg, 1992. 1—18 p. 88
- PIWINSKI, A. *The Touschek Effect in Strong Focusing Storage Rings*. [S.l.], 1998. 1–22 p. Disponível em: <<http://arxiv.org/abs/physics/9903034>>. 35
- PODOBODOV, B.; KRINSKY, S. Transverse Impedance of Tapered Transitions with Elliptical Cross Section. *Physical Review Special Topics - Accelerators and Beams*, v. 10, n. 7, p. 074402, 2007. ISSN 1098-4402. Disponível em: <<http://link.aps.org/doi/10.1103/PhysRevSTAB.10.074402>>. 77, 113
- PODOBODOV, B.; STUPAKOV, G. Point-Charge Wakefield Calculations from Finite Length Bunch Wake Potentials. *Physical Review Special Topics - Accelerators and Beams*, v. 16, n. 2, p. 024401, 2013. ISSN 1098-4402. Disponível em: <<http://link.aps.org/doi/10.1103/PhysRevSTAB.16.024401>>. 82
- PRODROMIDES, A. *Non-Evaporable Getter Thin Film Coatings for Vacuum Applications*. 180 p. Tese (Tese Doutorado) — Ecole Polytechnique Federale de Lausanne, 2002. 99
- RIES, M. *et al.* THz Bursting Thresholds Measured at the Metrology Light Source. In: *Proceedings of IPAC 2012*. New Orleans: [s.n.], 2012. p. 3030–3033. ISBN 9783954501151. Disponível em: <<http://accelconf.web.cern.ch/Accelconf/IPAC2012/papers/weppr046.pdf>>. 121

- ROCHA, T. M. da. *The vacuum system at the upcoming SIRIUS light source in Brazil*. Karlsruhe: [s.n.], 2017. Disponível em: <<https://indico.gsi.de/event/5393/session/7/contribution/15/material/slides/0.pdf>>. 100
- SÁ, F. H. de; LIU, L.; RESENDE, X. R. Optimization of Nonlinear Dynamics for Sirius. In: *Proceedings of IPAC2016*. Busan: [s.n.], 2016. v. 05-D02, p. 3409–3412. ISBN 9783954501472. 39
- SÁ, F. H. de et al. A New Booster Synchrotron for the Sirius Project. In: *Proceedings of IPAC2014*. Dresden: [s.n.], 2014. v. 02-T12, p. 1959–1962. ISBN 9783954501328. 40
- SÁ, F. H. de et al. Instability Thresholds and Tune Shift Estimation for Sirius. In: *Proceedings of IPAC 2015*. Richmond: [s.n.], 2015. v. 05-D05, p. 70–73. ISBN 9783954501687. 97
- SACHERER, F. J. A Longitudinal stability criterion for bunched beams. *IEEE Transactions on Nuclear Science*, v. 20, n. 3, p. 825–829, 1973. ISSN 15581578. 92
- SACHERER, F. J. Bunch Lengthening and Microwave Instability. *IEEE Transactions on Nuclear Science*, NS-24, n. 3, p. 1393–1395, 1977. 92
- SALVANT, B. et al. Quadrupolar Impedance of Simple Models of Kickers. In: *Proceedings of IPAC 2010*. Kyoto: [s.n.], 2010. v. 05-D05, p. 2054—2057. 108, 110
- SANDS, M. *The Physics of Electron Storage Rings - An Introduction*. Stanford, 1970. 172 p. 41, 56
- SAVITZKY, A.; GOLAY, M. J. Smoothing and Differentiation of Data by Simplified Least Squares Procedures. *Analytical Chemistry*, v. 36, n. 8, p. 1627–1639, 1964. ISSN 15206882. 146
- SERAPHIM, R. M. et al. Vacuum system design for the sirius storage ring. In: *Proceedings of IPAC 2015*. Richmond: [s.n.], 2015. v. 07-T14, p. 2744–2746. ISBN 9783954501687. 100, 125
- SERRET, J.-A. Sur Quelques Formules Relatives à la Théorie des Courbes à Double Courbure. *Journal de mathématiques pures et appliquées 1re séries*, v. 16, p. 193–207, 1851. Disponível em: <<http://eudml.org/doc/235002>>. 41
- SESSLER, A. M.; VACCARO, V. G. *Longitudinal instabilities of azimuthally uniform beams in circular vacuum chambers with walls of arbitrary electrical properties*. Geneva, 1967. 71
- SHOBUDA, Y.; CHIN, Y.; TAKATA, K. Coupling impedances of a resistive insert in a vacuum chamber. *Physical Review Special Topics - Accelerators and Beams*, v. 12, n. 9, p. 094401, sep 2009. ISSN 1098-4402. Disponível em: <<http://link.aps.org/doi/10.1103/PhysRevSTAB.12.094401>>. 112
- SHOBUDA, Y.; CHIN, Y. H. Resistive-wall impedances of a thin non-evaporable getter coating on a conductive chamber. *Progress of Theoretical and Experimental Physics*, v. 2017, n. 12, p. 123G01, 2017. ISSN 2050-3911. Disponível em: <<http://academic.oup.com/ptep/article/doi/10.1093/ptep/ptx167/4746618>>. 103

- SHOBUDA, Y.; HIRATA, K. The Existence of a Static Solution for the Haissinski Equation with Purely Inductive Wake Force. *Particle Accelerators*, v. 62, p. 165–177, 1999. 90
- SHOBUDA, Y.; YOKOYA, K. Resistive wall impedance and tune shift for a chamber with a finite thickness. *Physical Review E*, v. 66, n. 5, p. 056501, nov 2002. ISSN 1063-651X. Disponível em: <<http://link.aps.org/doi/10.1103/PhysRevE.66.056501>>. 104
- SIEWERT, F. *et al.* On the characterization of ultra-precise x-ray optical components: Advances and challenges in ex situ metrology. *Journal of Synchrotron Radiation*, v. 21, n. 5, p. 968–975, 2014. ISSN 16005775. 34
- SIRIUS. *Sirius Web Page*. 2013. Disponível em: <https://wiki-sirius.lnls.br/mediawiki/index.php/Main_Page>. 37, 38, 39, 112, 152
- SOUTOME, K. *et al.* Non-Linear Optimization of Storage Ring Lattice for the SPring-8 Upgrade. In: *Proceedings of IPAC 2016*. Busan: [s.n.], 2016. v. 02-A05, p. 3440–3442. ISBN 9783954501472. 28
- STUPAKOV, G. Using the parabolic equation for calculation of beam impedance. *New Journal of Physics*, v. 8, n. 11, p. 280, 2006. ISSN 1367-2630. Disponível em: <<http://stacks.iop.org/1367-2630/8/i=11/a=280?key=crossref.760948553bf92eaaf4e439da364a2540>>. 74
- STUPAKOV, G.; BANE, K. L.; ZAGORODNOV, I. Optical approximation in the theory of geometric impedance. *Physical Review Special Topics - Accelerators and Beams*, v. 10, n. 5, p. 1–11, 2007. ISSN 10984402. 77
- STUPAKOV, G. *et al.* Effects of beam-tube roughness on x-ray free electron laser performance. *Physical Review Special Topics - Accelerators and Beams*, v. 2, n. 6, p. 060701, jun 1999. ISSN 1098-4402. Disponível em: <<http://link.aps.org/doi/10.1103/PhysRevSTAB.2.060701>>. 100
- STUPAKOV, G. V. Geometrical wake of a smooth taper. *Particle Accelerators*, v. 56, p. 83–97, 1996. 76
- STUPAKOV, G. V. *Wake and Impedance*. Stanford, California, 2000. 61, 63, 67, 82
- STUPAKOV, G. V. Low frequency impedance of tapered transitions with arbitrary cross sections. *Physical Review Special Topics - Accelerators and Beams*, v. 10, n. 9, p. 094401, 2007. ISSN 1098-4402. Disponível em: <<https://link.aps.org/doi/10.1103/PhysRevSTAB.10.094401>>. 76, 114
- STUPAKOV, G. V.; BANE, K. L. F.; ZAGORODNOV, I. Impedance Scaling for Small Angle Transitions. *Physical Review Special Topics - Accelerators and Beams*, v. 14, n. 1, p. 014402, 2011. ISSN 10984402. 74
- STUPAKOV, G. V.; HEIFETS, S. A. Beam instability and microbunching due to coherent synchrotron radiation. *Physical Review Special Topics - Accelerators and Beams*, v. 5, n. 5, p. 054402, 2002. ISSN 10984402. 122

- STUPAKOV, G. V.; KOTELNIKOV, I. A. Shielding and synchrotron radiation in toroidal waveguide. *Physical Review Special Topics - Accelerators and Beams*, v. 6, n. 3, p. 154–165, 2003. ISSN 10984402. 123
- STUPAKOV, G. V.; KOTELNIKOV, I. A. Calculation of coherent synchrotron radiation impedance using the mode expansion method. *Physical Review Special Topics - Accelerators and Beams*, v. 12, n. 10, p. 104401, 2009. ISSN 1098-4402. Disponível em: <<https://link.aps.org/doi/10.1103/PhysRevSTAB.12.104401>>. 123
- STUPAKOV, G. V.; PODOBEDOV, B. High-frequency impedance of small-angle tapers and collimators. *Physical Review Special Topics - Accelerators and Beams*, v. 13, n. 10, p. 104401, 2010. ISSN 10984402. 77
- STUPAKOV, G. V.; ZHOU, D. Analytical theory of coherent synchrotron radiation wake-field of short bunches shielded by conducting parallel plates. *Physical Review Accelerators and Beams*, v. 19, n. 4, p. 1–20, 2016. ISSN 24699888. 123
- SUETSUGU, Y.; SHIRAI, M.; OHTSUKA, M. Application of a Matsumoto-Ohtsuka-type vacuum flange to beam ducts for future accelerators. *Journal of Vacuum Science & Technology A: Vacuum, Surfaces, and Films*, v. 23, n. 6, p. 1721–1727, 2005. ISSN 0734-2101. Disponível em: <<http://avs.scitation.org/doi/10.1116/1.2101808>>. 125
- SUN, Y.; BORLAND, M. Alternate lattice design for advanced photon source multi-bend achromat upgrade. In: *Proceedings of IPAC2015*. Richmond: [s.n.], 2013. p. 1803–1805. ISBN 9783954501687. 28
- SUSINI, J. *et al.* New challenges in beamline instrumentation for the esrf upgrade programme phase ii. *Journal of Synchrotron Radiation*, v. 21, n. 5, p. 986–995, 2014. ISSN 16005775. 34
- SUZUKI, T. Theory of longitudinal bunched-beam instabilities based on the fokker-planck equation. *Particle Accelerators*, v. 14, p. 91–108, 1983. 55, 56, 92, 94
- SUZUKI, T. Fokker-planck theory of transverse mode-coupling instability. *Particle Accelerators*, v. 20, p. 79–96, 1986. 55, 56, 92
- TAVARES, D. O. *et al.* Development of an Open-Source Hardware Platform for Sirius Bpm and Orbit Feedback. In: *Proceedings of ICALEPS 2013*. San Francisco: [s.n.], 2013. p. 1036—1039. ISBN 9783954501397. Disponível em: <<http://accelconf.web.cern.ch/AccelConf/ICALEPS2013/papers/wecob07.pdf>>. 111
- TEMNYKH, A. B. Delta undulator for Cornell energy recovery linac. *Physical Review Special Topics - Accelerators and Beams*, v. 11, n. 12, p. 12072, 2008. ISSN 10984402. 112
- TERZIC, B.; BASSI, G. New density estimation methods for charged particle beams with applications to microbunching instability. *Physical Review Special Topics - Accelerators and Beams*, v. 14, n. 7, p. 070701, 2011. ISSN 10984402. 146
- THIBAULT, P.; GUIZAR-SICAIROS, M.; MENZEL, A. Coherent imaging at the diffraction limit. *Journal of Synchrotron Radiation*, International Union of Crystallography, v. 21, n. 5, p. 1011–1018, 2014. ISSN 16005775. 33

- TSUTSUI, H. *Some Simplified Models of Ferrite Kicker Magnet for Calculation of longitudinal Coupling Impedance*. Geneva, 2000. 1—19 p. 108, 111
- TSUTSUI, H.; VOS, L. *Transverse Coupling Impedance of a Simplified Ferrite Kicker Magnet Model*. Geneva, 2000. 1–6 p. 108
- VACCARO, V. G. *Longitudinal Instability of a Coasting Beam above Transition, due to the action of Lumped Discontinuities*. Geneva, 1966. 67
- VENTURINI, M.; WARNOCK, R. Bursts of Coherent Synchrotron Radiation in Electron Storage Rings: A Dynamical Model. *Physical Review Letters*, v. 89, n. 22, p. 224802, 2002. ISSN 0031-9007. Disponível em: <<https://link.aps.org/doi/10.1103/PhysRevLett.89.224802>>. 150
- VILELA, L. N. P. et al. Studies of Delta-Type Undulators for Sirius. In: *Proceedings of IPAC2017*. Copenhagen: [s.n.], 2017. v. 05-D02, p. 52–54. ISBN 9783954501823. 37, 112
- WANG, L. et al. Beam Ion Instability: Measurement, Analysis, and Simulation. *Physical Review Special Topics - Accelerators and Beams*, v. 16, n. 10, p. 1–14, 2013. ISSN 10984402. 40, 65
- WANG, M. C.; UHLENBECK, G. E. On the Theory of the Brownian Motion. *Reviews of Modern Physics*, v. 17, p. 323–342, 1945. 55
- WANG, N. et al. Studies on Collective Instabilities in HEPS. In: *Proceedings of IPAC2017*. Copenhagen: [s.n.], 2017. v. 05-D05, p. 3763–3766. ISBN 9783954501823. 35
- WANG, N. et al. Development of the Impedance Model in HEPS. In: *Proceedings of IPAC2017*. Copenhagen: [s.n.], 2017. v. 05-D04, n. 11205171, p. 3110–3113. ISBN 9783954501823. 35
- WARNOCK, R. L. *Shielded Coherent Synchrotron Radiation and its Effect on Very Short Bunches*. [S.l.], 1990. v. 1990, n. November, 1–10 p. Disponível em: <<http://inspirehep.net/record/300390/files/slac-pub-5375.pdf>>. 120
- WARNOCK, R. L.; ELLISON, J. *A General Method for Propagation of the Phase Space Distribution, with Application to the Sawtooth Instability*. Stanford, 2000. 120
- WARNOCK, R. L.; MORTON, P. Fields Excited by a Beam in a Smooth Toroidal Chamber. *Particle Accelerators*, v. 25, n. 1, p. 113–151, 1990. Disponível em: <<http://cds.cern.ch/record/1108077/files/p113.pdf>>. 122
- WEILAND, T. On the Computation of Resonant Modes in Cylindrically Symmetric Cavities. *Nuclear Instruments and Methods*, v. 216, n. 3, p. 329–348, 1983. 83
- WIEDEMANN, H. *Particle Accelerator Physics*. 3rd. ed. Berlin: Springer, 2007. 949 p. ISBN 9783540490432. 24, 30, 41, 44, 47, 55, 56
- Wikipedia Contributors. *Airy function — Wikipedia, The Free Encyclopedia*. 2017. Disponível em: <https://en.wikipedia.org/w/index.php?title=Airy_function&oldid=803698177>. 120

- Wikipedia Contributors. *Confluent hypergeometric function — Wikipedia, The Free Encyclopedia*. 2017. Disponível em: <https://en.wikipedia.org/w/index.php?title=Confluent_hypergeometric_function&oldid=815637881>. 122
- Wikipedia Contributors. *Convolution theorem — Wikipedia, The Free Encyclopedia*. 2017. Disponível em: <https://en.wikipedia.org/w/index.php?title=Convolution_theorem&oldid=804485249>. 81
- Wikipedia Contributors. *Frenet–Serret formulas — Wikipedia, The Free Encyclopedia*. 2017. Disponível em: <https://en.wikipedia.org/w/index.php?title=Frenet-Serret_formulas&oldid=814838096>. 41
- Wikipedia Contributors. *Laguerre polynomials — Wikipedia, The Free Encyclopedia*. 2018. Disponível em: <https://en.wikipedia.org/w/index.php?title=Laguerre_polynomials&oldid=819922521>. 94
- Wolfram Research Inc. *Wolfram Mathematica v11.0.1.0*. 2016. 122
- YOKOYA, K. *Impedance of Slowly Tapered Structures*. Geneva, 1990. 1—12 p. 76
- YOKOYA, K. Resistive Wall Impedance of Beam Pipes of General Cross Section. *Particle Accelerators*, v. 41, p. 221–248, 1993. 78, 80, 103, 105, 110, 114
- ZAGORODNOV, I. Indirect methods for wake potential integration. *Physical Review Special Topics - Accelerators and Beams*, v. 9, n. 10, p. 102002, oct 2006. ISSN 1098-4402. Disponível em: <<http://link.aps.org/doi/10.1103/PhysRevSTAB.9.102002>>. 83
- ZAGORODNOV, I.; BANE, K. L. F.; STUPAKOV, G. V. Calculation of wakefields in 2D rectangular structures. *Physical Review Special Topics - Accelerators and Beams*, v. 18, n. 10, p. 104401, 2015. ISSN 1098-4402. Disponível em: <<http://link.aps.org/doi/10.1103/PhysRevSTAB.18.104401>>. 63, 84, 113, 116
- ZAGORODNOV, I.; SCHUHMANN, R.; WEILAND, T. Long-time numerical computation of electromagnetic fields in the vicinity of a relativistic source. *Journal of Computational Physics*, v. 191, n. 2, p. 525–541, nov 2003. ISSN 00219991. Disponível em: <<http://linkinghub.elsevier.com/retrieve/pii/S0021999103003292>>. 83
- ZAGORODNOV, I.; WEILAND, T. TE/TM field solver for particle beam simulations without numerical Cherenkov radiation. *Physical Review Special Topics - Accelerators and Beams*, v. 8, n. 4, p. 73–87, 2005. ISSN 10984402. 83, 113, 116
- ZHOU, D. *et al.* Calculation of Coherent Synchrotron Radiation Impedance for a Beam Moving in a Curved Trajectory. *Japanese Journal of Applied Physics*, v. 51, n. 1R, p. 16401, 2012. Disponível em: <<http://stacks.iop.org/1347-4065/51/i=1R/a=016401>>. 123
- ZOTTER, B. *High Frequency Effects on the Transverse Resistive Wall Instability in Particle Storage Rings*. Geneva, 1969. 53 p. 79, 110
- ZOTTER, B. *Transverse Oscillations of a Relativistic Particle Beam in a Laminated Vacuum Chamber*. Geneva, 1969. 56 p. 79

- ZOTTER, B. Longitudinal instabilities of charged particle beams inside cylindrical walls of finite thickness. *Particle Accelerators*, v. 1, n. 1, p. 311–326, 1970. 79
- ZOTTER, B. *New Results on the Impedance of Resistive Metal Walls of Finite Thickness*. Geneva, 2005. 25 p. 80
- ZOTTER, B.; KHEIFETS, S. *Impedances And Wakes In High Energy Particle Accelerators And Storage Rings*. 1st. ed. Singapore: World Scientific Publishing Co. Pte. Ltd., 1998. 405 p. ISBN 9789810226268. 67, 72, 73, 104
- ZWANZIG, R. *Nonequilibrium Statistical Mechanics*. 1st. ed. New York: Oxford University Press, 2001. 222 p. ISBN 0195140184. 55